

See discussions, stats, and author profiles for this publication at: <https://www.researchgate.net/publication/227160444>

Proton-Coupled Electron Transfer

ARTICLE *in* CHEMICAL REVIEWS · JUNE 2012

Impact Factor: 46.57 · DOI: 10.1021/cr200177j · Source: PubMed

CITATIONS

234

READS

116

10 AUTHORS, INCLUDING:



Christine Murphy

Princeton University

2 PUBLICATIONS 231 CITATIONS

[SEE PROFILE](#)



Amit Paul

Indian Institute of Science Education and Res...

15 PUBLICATIONS 499 CITATIONS

[SEE PROFILE](#)

Proton-Coupled Electron Transfer

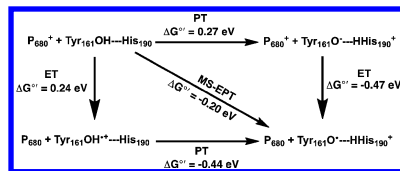
David R. Weinberg,^{†,§} Christopher J. Gagliardi,[†] Jonathan F. Hull,[†] Christine Fecenko Murphy,[‡] Caleb A. Kent,[†] Brittany C. Westlake,^{||} Amit Paul,[†] Daniel H. Ess,[†] Dewey Granville McCafferty,^{*,‡} and Thomas J. Meyer^{*,†}

[†]Department of Chemistry, University of North Carolina at Chapel Hill, Chapel Hill, North Carolina 27599-3290, United States

[‡]Department of Chemistry, B219 Levine Science Research Center, Box 90354, Duke University, Durham, North Carolina 27708-0354, United States

[§]Department of Physical and Environmental Sciences, Colorado Mesa University, 1100 North Avenue, Grand Junction, Colorado 81501-3122, United States

^{||}The American Chemical Society, 1155 Sixteenth Street NW, Washington, District of Columbia 20036, United States



CONTENTS

1. Introduction	4017
1.1. Transferring Electrons and Protons Together: Concerted Electron–Proton Transfer	
1.1.1. Defining Concerted Electron–Proton Transfer	4018
1.1.2. Multiple Site Electron–Proton Transfer	4018
1.2. PCET: Mechanism	4019
1.2.1. Solvent as EPT Proton Donor or Acceptor	4020
1.2.2. Free-Energy Dependence and pH	4022
1.2.3. Related Pathways	4023
1.3. Theory of EPT	4023
1.3.1. Electron Transfer	4024
1.3.2. Electron–Proton Transfer	4025
1.4. PCET: Thermodynamics and Structure	4026
1.4.1. pH Dependence	4027
1.4.2. Redox Potential Leveling	4028
1.4.3. "Missing" Oxidation States	4028
1.4.4. pK _a -Potential Diagrams	4029
1.4.5. PCET, Proton Gradients, and Energy Transduction	4029
2. Theory Behind PCET and EPT	4031
2.1. Marcus-Type Modeling and Predictions	4031
2.2. Kinetic Isotope Effect	4032
2.3. Electrochemical and Electrode–Solution Interface PCET	4032
2.4. HAT versus PCET	4032
2.5. Electronic Coupling in EPT Pathways	4032
2.6. Photochemical EPT	4033
2.7. Biological Systems	4034
2.8. Combined Theory and Experiment	4036
3. Organic PCET	4037
3.1. Phenols	4037
3.1.1. Reactions of Phenols with H-atom Abstractors	4037

3.1.2. Reactions between Oxidant and Pendant Base	4038
3.2. Other	4038
3.2.1. Amines	4038
3.2.2. Hydroxylamines	4039
3.2.3. Debromination of 8-Bromopurine	4039
3.3. Heterocycles as H-atom Donors	4039
4. PCET Involving Metal Complexes	4039
4.1. Oxidation Catalysis	4039
4.1.1. Water Oxidation	4039
4.1.2. Organic Oxidations	4041
4.1.3. Hydrogen Oxidation and Reduction	4043
4.2. Oxygen-Reduction Catalysis	4044
4.3. EPT Reactions Involving Coordinated Ligands	4044
4.3.1. Oxidation by EPT	4044
4.3.2. Reduction by EPT	4045
5. Excited-State PCET	4046
5.1. Excited-State Superacids	4047
5.2. Superbases	4048
5.3. Organic Molecules	4048
5.4. Metal Complexes	4049
5.5. Biological Molecules	4051
6. Electrochemical PCET	4052
6.1. Cyclic Voltammetry	4053
6.2. Rotating-Disk Electrode Voltammetry	4057
6.3. Electrochemical Impedance Spectroscopy	4058
6.4. Spectroelectrochemistry	4058
7. Heterogeneous PCET	4058
7.1. Nonbiological	4058
7.1.1. Liquid–Liquid Interfaces	4058
7.1.2. Solid–Liquid Interfaces	4061
7.2. Biological	4066
7.2.1. Hemes	4066
7.2.2. Biomimetic Membranes	4067
7.2.3. Glucose Oxidase	4068
7.2.4. Arsenite Oxidase	4068
8. PCET in Biology and Model Systems	4069
8.1. Introduction	4069
8.2. Tyrosyl Radicals	4069

Received: May 19, 2011

Published: June 18, 2012

8.3. PCET in Designed Peptides and Redox Cofactors	4070
8.3.1. Peptides	4070
8.3.2. Metal-Binding Heme Proteins	4070
8.4. Photosystem II	4071
8.4.1. Introduction	4071
8.4.2. Structural Updates Related to Water Oxidation and PCET	4073
8.4.3. Mechanism, Kinetics, and Thermodynamics	4074
8.5. Proton-Coupled Electron Transfer in Enzymes	4078
8.5.1. Class I Ribonucleotide Reductase	4078
8.5.2. DNA Photolyase	4079
8.5.3. Azurin	4079
8.5.4. Soybean Lipoxygenase	4079
8.5.5. Superoxide Dismutase	4080
8.5.6. Cytochrome c Peroxidase	4081
8.6. Proton-Gated Electron Transfer in Cytochrome <i>c</i> Oxidase	4081
8.7. PCET in Biology is Everywhere	4083
Author Information	4084
Corresponding Author	4084
Notes	4084
Biographies	4084
Acknowledgments	4086
References	4086

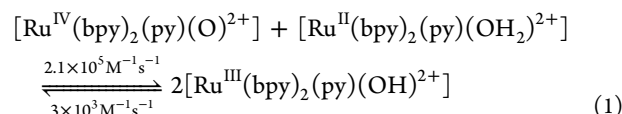
1. INTRODUCTION

An initial review (PCET1) on proton-coupled electron transfer (PCET) by Huynh and Meyer appeared in *Chemical Reviews* in 2007.¹ This is a follow-up on the original. It was intended for the special *Chemical Reviews* edition on Proton-Coupled Electron Transfer that appeared in December, 2010 (Volume 110, Issue 12, pp 6937–7100). The reader is referred to it with articles on electrochemical approaches to studying PCET by Costentin and co-workers,² theory of electron/proton transfer reactions by Hammes-Schiffer and Stuchebrukhov,³ proton-coupled electron flow in proteins and enzymes by Gray and co-workers,⁴ and the thermochemistry of proton-coupled electron transfer by Mayer and co-workers.⁵

Coverage for the current review is intended to be broad, covering all aspects of the topic comprehensively with literature coverage overlapping with the later references in PCET1 until late 2010. There is a growing understanding of the importance of PCET in chemistry and biology and its implications for catalysis and energy conversion. This has led to a series of informative reviews that have appeared since 2007. They include: “The possible role of proton-coupled electron transfer (PCET) in water oxidation by Photosystem II” by Meyer and co-workers in 2007,⁶ “Theoretical studies of proton-coupled electron transfer: Models and concepts relevant to bioenergetics” by Hammes-Schiffer and co-workers in 2008,⁷ “Electrochemical Approach to the Mechanistic Study of Proton-Coupled Electron Transfer” by Costentin in 2008,⁸ “Proton-Coupled Electron Transfer in Biology: Results from Synergistic Studies in Natural and Model Systems” by Reece and Nocera in 2009,⁹ and “Integrating Proton-Coupled Electron Transfer and Excited States” by Meyer and co-workers in 2010.¹⁰

In 1981 the term proton-coupled electron transfer (PCET) was introduced to describe an elementary step, like electron

transfer or proton transfer, but in which electrons and protons transfer together. It was coined to describe the concerted e⁻/H⁺ transfer process that occurs in the comproportionation reaction between Ru^{IV}(bpy)₂(py)(O)²⁺ (Ru^{IV}=O²⁺) and Ru^{II}(bpy)₂(py)(OH)₂²⁺(Ru^{II}–OH₂²⁺) in eq 1. In this reaction an electron and proton are transferred simultaneously from Ru^{II}–OH₂²⁺ to Ru^{IV}=O²⁺ to give 2 Ru^{III}–OH²⁺. Comproportionation is favored by 0.11 eV and occurs with transfer of a single proton with a *k*(H₂O)/*k*(D₂O) kinetic isotope effect (KIE) of 16.1.¹¹

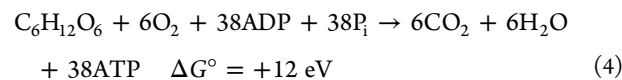
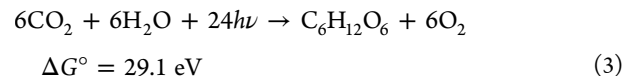


The term PCET has come to be used more broadly to describe reactions and half reactions in which both electrons and protons are transferred without regard to mechanism. Water splitting into H₂ and O₂ should seemingly be a pH-independent reaction. However, it is composed of separate PCET half reactions, one for water oxidation (eq 2a) and one for proton/water reduction (eq 2b), both of which are pH-dependent.

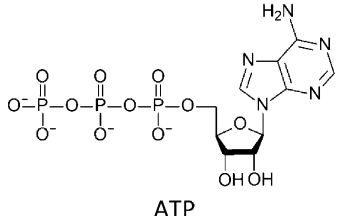


Multielectron, multiproton PCET half reactions are ubiquitous in energy conversion and storage reactions in chemistry and biology. In biology, key half reactions for energy storage and production exploit PCET and the high energy content in the C–H bonds of hydrocarbons, sugars, or other oxygenates by indirect reactions with oxygen at physically separated half reactions. Quintessential examples include carbohydrate formation by light-driven reduction of CO₂ by water in photosynthesis (eq 3) and the reverse, oxidation of glucose by oxygen, which releases energy in respiration. In photosynthesis, CO₂ reduction, coupled with water oxidation, occurs in a reaction that stores 29.1 eV, 1.22 eV/redox equivalent. The stored energy is released in respiration (eq 4) with the indirect oxidation of glucose by oxygen used to drive oxidative phosphorylation in mitochondria, which combines inorganic phosphate, P_i, and ADP to give ATP (eq 5). ATP and the energy released by phosphate hydrolysis to give ADP provide a key “chemical battery” used to power cells for biosynthesis, motion, and signaling.

Photosynthesis is a spectacular example of PCET in action with the transfer of 24 e⁻ and 24 H⁺ driven by at least 48 photons. It is also impressive in energy storage, with ~10¹¹ tons of carbon stored annually, ~10¹⁸ kJoules of energy.



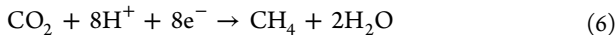
In the half reactions of photosynthesis and respiration, there are significant changes in electron content (and oxidation state) between reactants and products. These changes trigger changes



in proton affinities with charge compensation provided by proton gain or loss and covalent bond formation.

In contrast to direct oxidation with oxygen, as it occurs in combustion (e.g., $\text{CH}_4 + 2\text{O}_2 \rightarrow \text{CO}_2 + 2\text{H}_2\text{O}$), as noted above, energy conversion in biology, or in a fuel cell, occurs at physically separated PCET half reactions. The half reactions are multielectron/multiproton PCET in character and impose critical demands on mechanism and how electrons and protons are transferred. PCET is at the heart of successful energy conversion strategies in chemistry and biology. PCET and concerted electron–proton transfer (EPT) influence energetics and mechanism. PCET allows for the buildup of multiple redox equivalents at single sites or clusters. EPT provides reaction pathways in which electrons and protons are transferred simultaneously avoiding high-energy intermediates.

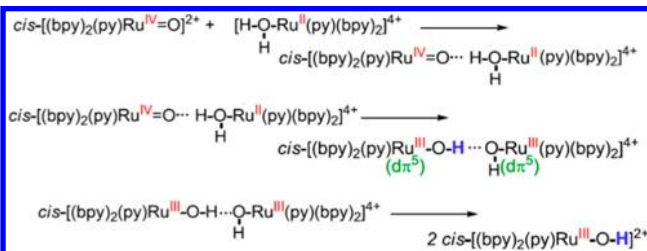
In PCET half reactions, variations in pH influence driving force. For example, for the half reactions of methane oxidation by oxygen, E° for the $\text{O}_2/\text{H}_2\text{O}$ couple in eq 2b decreases by 0.59 mV/pH unit at 25 °C and 1 atm from 1.23 V at $a_{\text{H}_2\text{O}} = 1$ –0.82 V at pH = 7. Similarly, for the CO_2 to CH_4 half reaction in eq 6, E° decreases from 0.17 V under standard conditions to –0.24 V at pH = 7.



1.1. Transferring Electrons and Protons Together: Concerted Electron–Proton Transfer

A three-step mechanism for comproportionation in eq 1 is shown in Scheme 1. It consists of (i) hydrogen-bond

Scheme 1

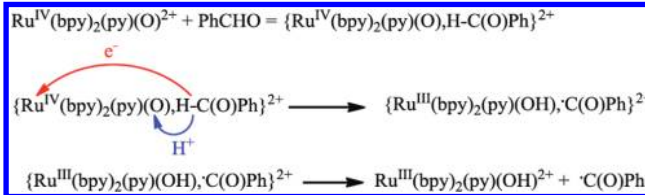


preassociation of the reactants, (ii) concerted electron–proton transfer (EPT), and (iii) separation of the products. Preassociation with H-bonding is required because of the short-range nature of proton transfer (section 1.3.2). In the key EPT step, concerted e^-/H^+ transfer occurs with electron transfer from a metal-based $d\pi$ orbital (t_{2g} in O_h symmetry) at $\text{Ru}^{\text{II}}-\text{OH}_2^{2+}$ to a $d\pi$ acceptor orbital at $\text{Ru}^{\text{IV}}=\text{O}^{2+}$. Proton transfer occurs from a $\sigma(\text{O}-\text{H})$ orbital at Ru(II) to an O-based lone-pair orbital at $\text{Ru}^{\text{IV}}=\text{O}^{2+}$.^{11a,b}

The use of different orbitals for transferring the e^-/H^+ pair distinguishes EPT from H-atom transfer (HAT). In HAT, e^-/H^+ transfer occurs to or from the same orbital in one of the

reactants. An example of HAT, in the oxidation of benzaldehyde by $\text{Ru}^{\text{IV}}(\text{bpy})_2(\text{py})(\text{O})^{2+}$, is shown in Scheme 2. Concerted e^-/H^+

Scheme 2



H^+ transfer also occurs from benzaldehyde, but both the transferring electron and proton come from the $\sigma(\text{C}-\text{H})$ bond of the aldehyde. In this reaction, the orbital pathway at $\text{Ru}^{\text{IV}}=\text{O}^{2+}$ remains the same with electron transfer occurring to the $d\pi$ electron-acceptor orbital and H^+ to a lone pair in a proton-acceptor orbital at $\text{Ru}^{\text{IV}}=\text{O}^{2+}$. This is an example of a mixed orbital pathway.

1.1.1. Defining Concerted Electron–Proton Transfer.

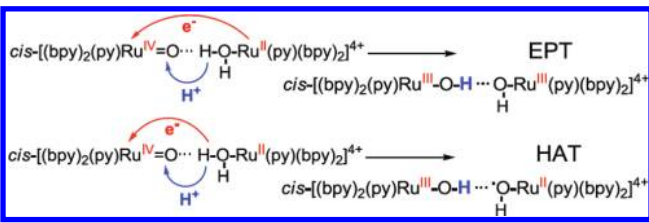
As proposed in PCET1, in an EPT elementary step *electrons and protons transfer from different orbitals on the donor to different orbitals on the acceptor*. Both HAT and EPT are elementary steps by which PCET reactions can occur. In H-atom transfer (HAT), both the transferring electron and proton come from the same bond in one of the reactants. In EPT, the e^-/H^+ donor orbitals and e^-/H^+ acceptor orbitals interact electronically, enabling simultaneous transfer. Simultaneous means rapid relative to the periods for coupled vibrations (tens of femtoseconds) and solvent modes (~ 1 ps). In EPT there is no discrete ET or PT intermediate equilibrated with its surroundings. If there were, the underlying thermodynamics would be those of the intermediate and not those of the final EPT products.

Unfortunately, the nomenclature used to describe concerted electron–proton transfer has not been standardized with different terms used to describe the same elementary step. Alternate terms from the literature include concerted proton–electron transfer (CPET),⁸ electron transfer proton transfer (ET-PT),¹² and concerted electron–proton transfer (CEP).¹³ The use of EPT follows straightforwardly from ET to describe electron transfer and PT to describe proton transfer as fundamental elementary reactions. It is descriptive, consistent with existing terminology, and, as described below, provides a systematic nomenclature for a family of reactions that differ considerably in microscopic detail but in all of which concerted electron–proton transfer is the defining redox event.

As discussed in PCET1 and in section 2 in this review, the distinction between EPT and HAT can be subtle and even equivocal especially in cases involving strong electronic coupling between reactants and products. Nonetheless, in many cases it is important to make the distinction because the difference between the two can be mechanistically profound.

This is illustrated by the comparison in Scheme 3 between EPT and HAT pathways for the redox step in eq 1. EPT leads to the final, energetically stable $\text{Ru}^{\text{III}}-\text{OH}^{2+}$ products and is thermodynamically favored with $\Delta G^\circ' = -0.11 \text{ eV}$.^{11f} For the HAT pathway, e^-/H^+ transfer occurs from a $\sigma(\text{O}-\text{H})$ orbital at $\text{Ru}^{\text{II}}-\text{OH}_2^{2+}$ to electron($d\pi_{\text{Ru}}$)/proton (p_{O}) acceptor orbitals at $\text{Ru}^{\text{IV}}=\text{O}^{2+}$, giving $\text{Ru}^{\text{III}}-\text{OH}^{2+}$ and the high-energy (~ 2.1 eV) charge transfer intermediate, $\text{Ru}^{\text{II}}-\text{O}^\bullet-\text{H}^{2+}$. The latter is

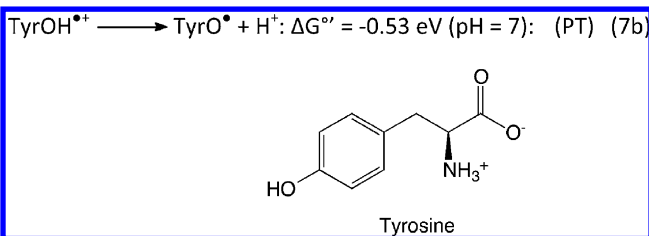
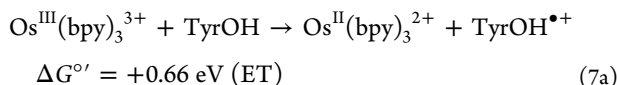
Scheme 3



accessible by UV excitation of $\text{Ru}^{\text{III}}-\text{OH}^{2+}$, $\text{Ru}^{\text{III}}-\text{O}-\text{H}^{2+} \xrightarrow{h\nu} \text{Ru}^{\text{II}}-\text{O}^{\bullet}-\text{H}^{2+}$, with λ_{max} at ~ 320 nm.

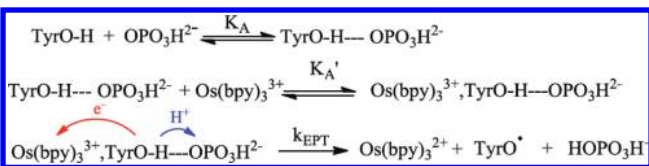
1.1.2. Multiple Site Electron–Proton Transfer. There are multiple redox pathways in which the characteristic feature is concerted electron–proton transfer. A systematic nomenclature is needed to describe them. In the EPT step in Scheme 1, concerted e^-/H^+ transfer occurs from a single donor to a single acceptor. There is another class of EPT reactions, multiple site electron–proton transfer (MS-EPT), in which concerted electron–proton transfer also occurs, but to different acceptors, or electron–proton transfer occurs from different donors to a common acceptor.

An example occurs in ET-PT oxidation of tyrosine (TyrOH) by $\text{Os}^{\text{III}}(\text{bpy})_3^{3+}$ ($E^\circ(\text{Os}^{3+/2+}) = 0.80$ V, eq 7). This reaction is relatively slow because the initial ET step gives the high-energy tyrosine radical cation ($E^\circ(\text{TyrOH}^{\bullet+}/\text{TyrOH}) = 1.5$ V), which is also a strong acid, $pK_a(\text{TyrOH}^{\bullet+}) = -2$ ¹⁴, and under some conditions subsequently dimerizes.



With added proton-acceptor bases OAc^- , histidine, HPO_4^{2-} , and Tris, the oxidation of tyrosine is greatly accelerated. Kinetic studies show that this is a buffer base effect and not a pH effect.¹⁵ As illustrated by the mechanism in Scheme 4 with

Scheme 4



HPO_4^{2-} as the base, initial adduct formation occurs with H-bond association. Preassociation between the adduct and $\text{Os}^{\text{III}}(\text{bpy})_3^{3+}$ is then followed by concerted electron–proton transfer. In this EPT step, electron transfer occurs to $\text{Os}^{\text{III}}(\text{bpy})_3^{3+}$ and proton transfer occurs to the base, and the two are spatially separated. The first experimental examples of this kind came from studies on the reduction of the triplet

excited state of C_{60} , ${}^3\text{C}_{60}$, by phenols by Linschitz and co-workers.¹⁶

In MS-EPT: (i) An electron–proton donor transfers electrons and protons to spatially separated acceptors or (ii) an electron–proton acceptor accepts electrons and protons from spatially separated donors. The number of electrons and protons that are transferred further characterizes MS-EPT pathways. For example, in the concerted step in Scheme 4, single electron–single proton transfer occurs, $1e^-/1\text{H}^+$ MS-EPT.

MS-EPT is microscopically more complex than electron or proton transfer. It shares with electron transfer requirements for medium and intramolecular reorganization (section 1.3.1), but with the additional complexity of a coupled proton transfer. At a common driving force, electron transfer is expected to dominate because of its lower barrier.

MS-EPT pathways intervene because of favorable energetics. This can be seen for tyrosine oxidation by electron transfer in eq 7. For initial electron transfer, $\Delta G^\circ = +0.66$ eV. For MS-EPT oxidation in Scheme 4, $\Delta G^\circ = -\{E^\circ(\text{Os}(\text{bpy})_3^{3+/2+}) - E^\circ(\text{TyrOH}^{\bullet+}/\text{TyrOH})\} + 0.059\{pK_a(\text{TyrOH}^{\bullet+}) - pK_a(\text{HPO}_4^{2-})\} = +0.12$ eV.

MS-EPT and the role of energetics appear in Photosystem II (PSII) in dramatic fashion (section 8.4). In PSII, light absorption by an antenna apparatus sensitizes the singlet excited state of chlorophyll P_{680} ($\text{Chl}_{\text{D}1}$ in Figure 1), ${}^1\text{P}_{680}^*$. ${}^1\text{P}_{680}^*$ undergoes oxidative quenching with electron transfer to pheophytin and then to quinone Q_A (Figure 1). Oxidation gives the powerful oxidant P_{680}^{+} with $E^\circ(\text{P}_{680}^{+}/0) \approx 1.26$ V, and it drives water oxidation at the CaMn_4 cluster of the oxygen evolving complex (OEC). Oxidative activation of the OEC occurs through intervening Y_Z as an electron transfer relay. Y_Z consists of a tyrosine and an associated histidine base, His(190). Removal of His(190) by mutagenesis shuts down photosynthesis! Loss of a single base is sufficient to disrupt an enormously complex apparatus with multiple linked functional elements and hundreds of thousands of atoms.

The utilization of a MS-EPT pathway has been invoked to explain the histidine base effect. As shown in Figure 1, in the sequence of reactions following formation of ${}^1\text{P}_{680}^*$, without histidine electron transfer is highly unfavorable. Oxidation of tyrosine is too slow to compete with back electron transfer from $\text{Q}_\text{A}^{\bullet-}$ to P_{680}^{+} .^{1,6,17} With His(190) in place and MS-EPT available, the energetics are favorable by ~ 0.2 eV.

MS-EPT pathways play a major role in biological PCET (section 8). Structural motifs have evolved that exploit the relatively long-range nature of electron transfer coupled with intricate local proton transfer channels engineered for site-to-site hopping, sometimes over long distances (section 8). This type of proton-hopping mechanism has been studied by Voth and co-workers where the role of proton transfer through two proton-uptake pathways in Cytochrome *c* oxidase was explored. Their calculations were based on available X-ray diffraction (XRD) data and the results of mutagenesis studies that revealed the role of the underlying molecular architecture.¹⁹

An example, also from Photosystem II, is the proposed $1e^-/2\text{H}^+$ MS-EPT reaction in the initial oxidative activation step of the OEC, the $\text{S}_0 \rightarrow \text{S}_1$ transition in the Kok cycle (section 8.4). In this step, long-range (~ 6 Å) electron transfer occurs from the Mn(4) site in the Mn_4Ca cluster to Y_Z^{\bullet} . As illustrated in eq 8, it has been proposed that two coupled EPT events occur in this step: (i) EPT oxidation of $\text{Mn}(4)-\text{OH}_2$ (or $\text{Mn}^{\text{III}}(4)-\text{OH}$) with long-range electron transfer to Y_Z^{\bullet} , which occurs in

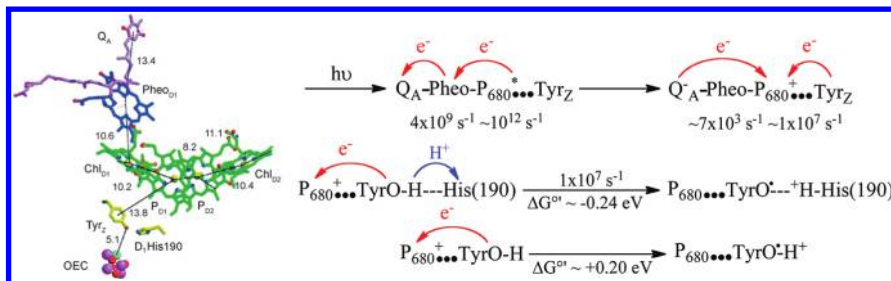
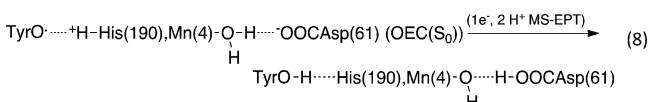


Figure 1. Structure of the reaction center of Photosystem II illustrating terminal chlorophyll P₆₈₀, pheophytin_{D1}, quinone acceptor Q_A, Y_Z (Tyrz-His(190)), the oxygen evolving complex (OEC), and the sequence of electron transfer events induced by light absorption and sensitization. The critical energetic role proposed for His(190) as EPT acceptor base is also shown.¹⁰ Reproduced in part with permission from ref 18. Copyright 2004 American Association for the Advancement of Science.



concert with proton transfer to neighboring base Asp61; (ii) EPT at TyrO^{·-}-H-His190 with electron transfer from Mn(4)-OH₂ (or Mn^{III}(4)-OH) in concert with proton transfer from ⁺H-His(190) to TyrO[·]. We note that other mechanistic proposals for this reaction exist, and they are discussed in section 6.

The proton transferred from Tyr161 to His190 with oxidation of Y_Z by P₆₈₀⁺ in Figure 1 is transferred back in eq 8, possibly by the “proton-rocking” mechanism proposed by Renger and co-workers.²⁰ MS-EPT is required for tyrosyl radical water oxidation, $E^{\circ'} = 0.88$ V (section 8.4.3). For the TyrO[·]/TyrO^{·-} couple, $E^{\circ'} = 0.73$ V, with $E^{\circ'} = 0.88$ V required for water oxidation. For the EPT couple, TyrO^{·-}-H-His190/TyrO-H---His, $E^{\circ'} \approx 1.0\text{--}1.2$ V versus a normal hydrogen electrode (NHE) (see section 8.4.3).²¹

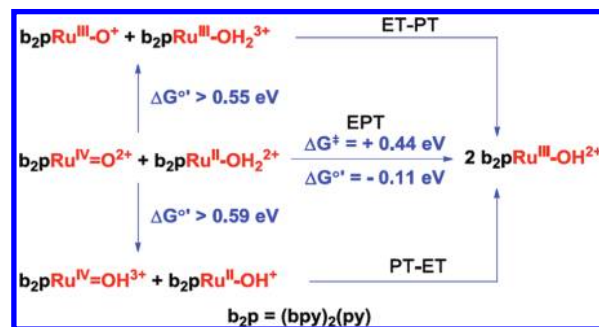
Asp61 is the entryway to a long-range (~30 Å) proton exit channel to the lumen with proton release occurring on the lumen surface in as little as 12 μs. One proposed proton exit channel consists of a cluster of titratable residues beginning with D1Asp61 and terminating at the lumen surface in a series of PsbO residues (section 8.4.3).²²

1.2. PCET: Mechanism

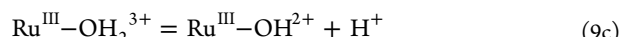
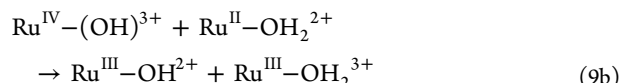
ET, PT, EPT, MS-EPT, HAT, and hydride transfer (with simultaneous transfer of 2e⁻/1H⁺) are all elementary steps available for carrying out PCET reactions. In general, PCET reactions occur by more than one multistep mechanism with a competition between mechanisms and their relative importance dictated by reaction conditions: temperature, pH, etc.

Three mechanisms are illustrated in Scheme 5 for the comproportionation reaction in Scheme 1: ET-PT, PT-ET, and EPT. As noted above, the extent to which each of the three contribute depends on the conditions. At pH = 7, EPT dominates comproportionation because it avoids high-energy intermediates. For initial electron transfer and the stepwise ET-PT mechanism, $\Delta G^{\circ'} > 0.55$ eV for the initial step: Ru^{IV}=O²⁺ + Ru^{II}-OH₂²⁺ → Ru^{III}-O⁺ + Ru^{III}-OH₂³⁺. For initial proton transfer and PT-ET, $\Delta G^{\circ'} > 0.59$ eV for the initial step: Ru^{IV}=O²⁺ + Ru^{II}-OH₂²⁺ → Ru^{IV}(OH)³⁺ + Ru^{II}-OH⁺. The minimum values of $\Delta G^{\circ'}$ cited for PT or ET in Scheme 5 are also minimum free energies of activation for the initial ET or PT steps. These values are larger than the experimental free energy of activation, $\Delta G^* = 0.44$ eV, ruling them out as major contributors.

Scheme 5. (At pH = 7)



Other mechanisms are available for this reaction. For example, in acidic solutions near the pK_a for Ru^{IV}(OH)³⁺, prior protonation of Ru^{IV}=O²⁺ followed by electron transfer is a viable mechanism (eq 9).

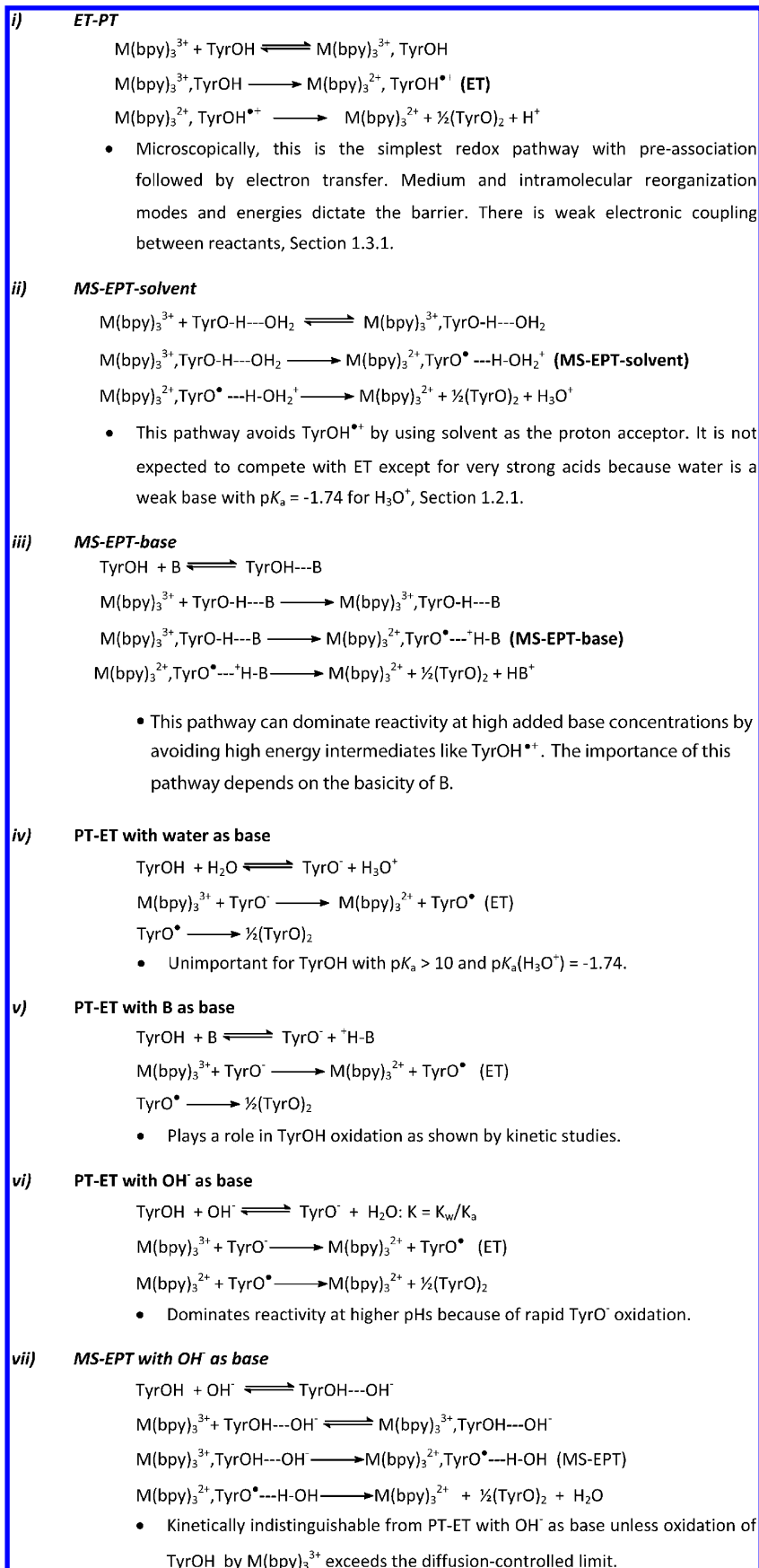


MS-EPT: For a MS-EPT pathway in a protein, the acceptor base is dictated by local structure and proximity to the transferring proton. In solution, MS-EPT is indiscriminate with regard to base. For Os(bpy)₃³⁺ oxidation of tyrosine in Scheme 4, OAc⁻, histidine, HPO₄²⁻, Tris, and others have all been shown to act as proton-acceptor bases. Their ability to contribute depends on the initial H-bond interaction and their strength as an acceptor base as measured by $-RTpK_a$ (section 1.3.2).

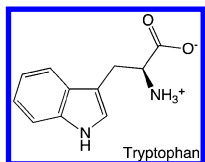
The indiscriminate nature of MS-EPT in solution with regard to oxidant and base can lead to significant mechanistic complexity and ambiguity as to the oxidant/base combination or combinations that dominate reactivity. An annotated listing of MS-EPT mechanisms for oxidation of tyrosine by M(bpy)₃³⁺ with added base, B, is included in the mechanistic summary in Scheme 6. The redox step is shown as rate-limiting in all cases.

Appearance of pH-dependent rate laws are generally assumed to arise from prior proton loss, (mechanism (vi) in Scheme 6). However, MS-EPT with OH⁻ as the EPT base in mechanism (vii) is kinetically equivalent and may play a role. It appears in the M(bpy)₃³⁺ oxidation of tryptophan (TrpN-H) with $pK_a > 16$ for the indolic N-H proton and a pathway first order in OH⁻. PT-ET can be ruled out in this case because initial PT

Scheme 6. PCET Pathways for the Oxidation of Tyrosine by $M(bpy)_3^{3+}$ in Water with Added Buffer, ${}^+HB/B$



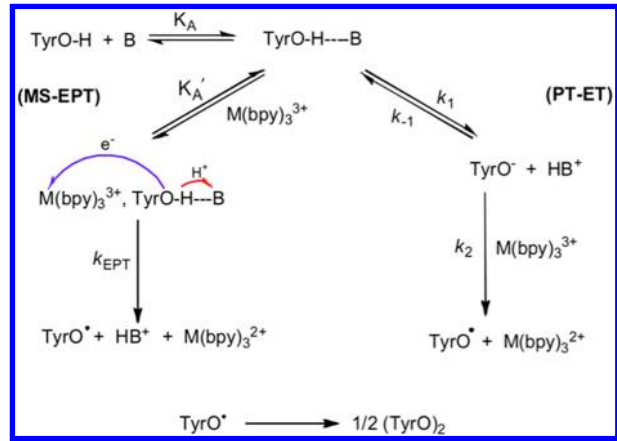
followed by oxidation of TrpN^- would have to exceed the diffusion-controlled limit for the ET step.²³



Kinetics: Kinetic complexity follows from mechanistic diversity. In the oxidation of TyrOH by M(bpy)₃³⁺, kinetic studies under a variety of conditions have revealed pH regions where ET-PT ((i) in Scheme 6) and PT-ET (iv) dominate. Significant rate accelerations are observed with added proton acceptor bases acetate, histidine, HPO₄²⁻, and Tris. Over a wide range of solution conditions in added bases and buffer ratios, the observed rate law for oxidation of tyrosine is shown in eq 10 with M(III) = M(bpy)₃³⁺ and B being a general proton-accepting base. Equation 10 is consistent with the mechanism in Scheme 7. The rate and equilibrium constants are defined in the scheme.

$$-\frac{d[\text{M(III)}]}{dt} = \left[\frac{K_A[B][\text{TyrOH}]_T}{1 + K_A[B]} \right] \left(K_A' k_{\text{Red}} + \frac{k_1 k_2}{k_{-1}[{}^+ \text{HB}] + k_2[\text{M(III)}]} \right) [\text{M(III)}] \quad (10)$$

Scheme 7



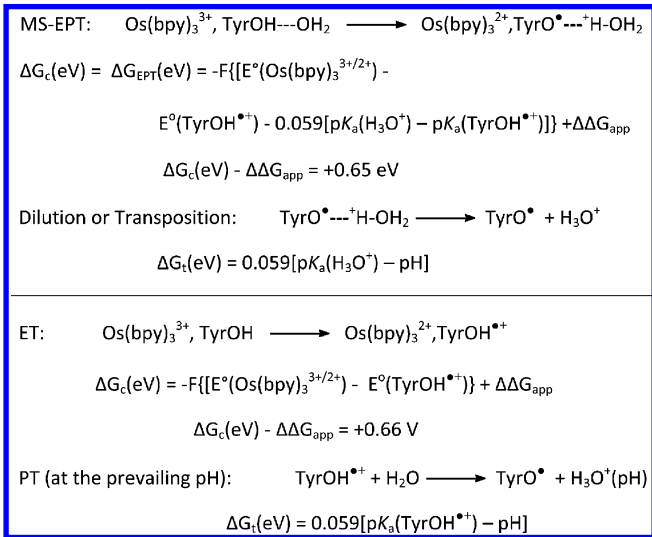
In the rate expression in eq 10, the initial term inverse in [B] is observed experimentally in the appearance of saturation kinetics at high concentrations of B. The first term, $k_{\text{EPT}}K_A'$, arising from MS-EPT (Scheme 7), dominates at high buffer ratios, $[{}^+ \text{HB}]/[\text{B}]$. The second term, arising from PT-ET, dominates at low buffer ratios.

1.2.1. Solvent as EPT Proton Donor or Acceptor. In a protic solvent, particularly in water, proton transfer to or from individual water molecules or water clusters provides a basis for solvent involvement in MS-EPT; note mechanism (ii) in Scheme 6. The state of the proton in water is complex with two different water cluster structures proposed. One is the Zundel cation H₅O₂⁺ (H₂O---H⁺---OH₂)²⁴ and the other is the Eigen cation H₉O₄⁺ (H₃O⁺·3H₂O)²⁵ that undergo rapid dynamical interchange.²⁶ There is also experimental evidence for proton transfer through individual solvent molecules acting as bridges.²⁷

Use of the solvent for MS-EPT is limited by its acid–base properties. Individual water molecules or water clusters are neither good proton donors nor good acceptors. At 25 °C, pK_a(H₂O) = 15.7 for the equilibrium H₂O = H⁺ + OH⁻ and pK_a = −1.74 for H₃O⁺ and the equilibrium H₃O⁺ = H₂O + H⁺.²⁸ Given the weak acidity and basicity of H₂O in water, ET followed by PT is favored over MS-EPT-solvent pathways, except for the strongest acids and bases.

Thermodynamics for ET-PT and MS-EPT-solvent pathways for oxidation of tyrosine by Os(bpy)₃³⁺ are compared in Scheme 8. In this scheme, $\Delta\Delta G_{\text{app}}$ is the difference in free

Scheme 8. MS-EPT with H₂O as the H⁺ Acceptor Compared to ET-PT (25 °C, STP)



energy of formation between the association complex for the EPT reactants (Os(bpy)₃³⁺ + TyrOH---OH₂ = Os(bpy)₃³⁺, TyrOH---OH₂) and products (Os(bpy)₃²⁺, TyrO[•]---H-OH₂ = Os(bpy)₃²⁺, TyrO[•]---H-OH₂) at the configuration appropriate for EPT to occur. $\Delta G_c = \Delta G_{\text{EPT}}$ is the free-energy change for the MS-EPT step, and ΔG_t is the free energy for transposition. The latter is the entropically driven free-energy change for equilibration of the local pH with the bulk following proton transfer in the MS-EPT event.

Driving forces for ET-PT and MS-EPT in Scheme 8 are comparable, and they are kinetically indistinguishable. Which, if either, dominates can sometimes be inferred from kinetic isotope effects or by rate constant and activation parameter comparisons. As noted above, ET-PT is expected to dominate for comparable ΔG values because of increased demands on the reaction barrier from proton transfer in MS-EPT.

1.2.2. Free-Energy Dependence and pH. The role of pH in EPT dynamics has been a source of confusion in the PCET literature. Thermodynamic quantities— E° , ΔG , and K —for PCET couples are pH-dependent as predicted by the Nernst equation (section 1.4.1). However, these quantities reflect thermodynamic differences between initial and final states and are independent of how the interconversion between states occurs.

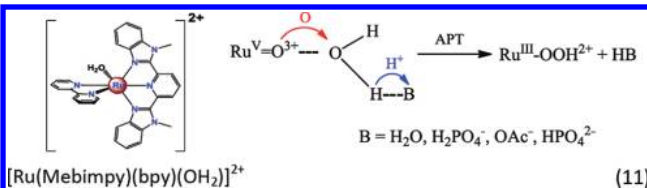
Barriers and rate constants for concerted electron–proton transfer are also free-energy-dependent (section 1.3.2). However, the free-energy dependence for the elementary step arises from the microscopic demands for this step and not from steps preceding or following EPT. In an EPT reaction both

electrons and protons are transferred simultaneously. Except for generalized medium effects, there is no microscopic basis for the barrier to be influenced by variations in external pH. The same is true for electron transfer. When pH-dependent rate terms do appear for PCET reactions, there may be a variety of origins, most typically from protonation or deprotonation equilibria prior to or following electron transfer in PT-ET mechanisms.

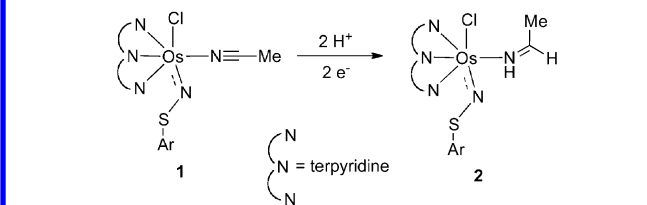
1.2.3. Related Pathways. Utilization of EPT, especially MS-EPT, is ubiquitous in biology to avoid high-energy intermediates and for long-range electron transfer in membranes. Related redox pathways, important in catalysis, have also been identified involving coupled proton transfer but in concert with atom or hydride transfer.

Atom-Proton Transfer (APT). A family of single-site Ru metal complex catalysts for water oxidation has been identified, an example being $[\text{Ru}(\text{Mebimpy})(\text{bpy})(\text{OH}_2)]^{2+}$ (Mebimpy = 2,6-bis(1-methylbenzimidazol-2-yl)pyridine; bpy = 2,2'-bipyridine) (section 4.1.1). In these complexes water oxidation occurs following oxidation from $\text{Ru}^{\text{II}}-\text{OH}_2^{2+}$ to $\text{Ru}^{\text{V}}=\text{O}^{3+}$. Subsequent O---O bond formation occurs by O-atom attack on H_2O . In propylene carbonate-water mixtures, the reaction is first order in complex and first order in H_2O .²⁹

The O---O bond-forming step is catalyzed by added bases— H_2PO_4^- , OAc^- , and HPO_4^{2-} . Quantum mechanics/molecular mechanics (QM/MM) simulations have identified a pathway described as atom-proton transfer (APT) with O-atom transfer occurring in concert with proton transfer to the added base B (eq 11). APT has the advantage of avoiding the intermediate H_2O_2 complex from the reaction, $\text{Ru}^{\text{V}}=\text{O}^{3+} + \text{H}_2\text{O} \rightarrow \text{Ru}^{\text{III}}-\text{OOH}_2^{3+}$.³⁰



Hydride-Proton Transfer (HPT): Reduction of the sulfilimido complex *cis*-[Os^{IV}(tpy)(Cl)(NCCH₃)(NSAr)]⁺ (Ar = 3,5-Me₂C₆H₃SH) to *cis*-[Os^{III}(tpy)(Cl)(NCCH₃)(NSAr)] occurs at 0.24 V versus NHE (1:1 (V:V) H₂O/MeCN-1.0 M in NH₄PF₆) followed by reversible, pH-dependent, 2e⁻/2H⁺ ligand-based reduction to the Os^{III}-imine, [Os^{III}(tpy)(Cl)-(NH=HCCH₃)(NSAr)] (eq 12). The ligand-based couple



undergoes reversible redox chemistry with alcohols and aldehydes or ketones, a reactivity shared with the enzyme liver alcohol dehydrogenase.³¹ As illustrated in eq 13 and figure 2 for reduction of formaldehyde to methanol, quantum mechanical analysis has identified concerted hydride-proton transfer (HPT) in the key redox step.³²

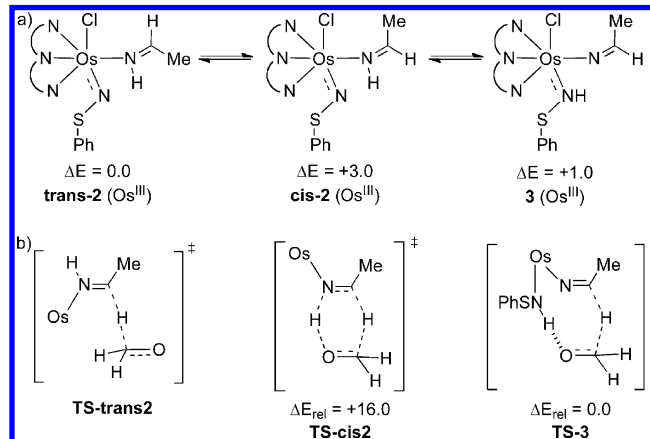
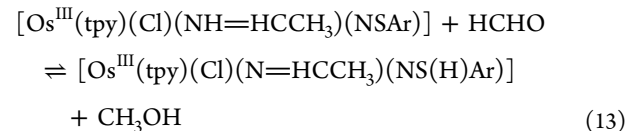


Figure 2. (a) Thermodynamics of possible two-electron reduction products. (b) Transition states for formaldehyde reduction ($\text{Os} = [\text{Os}^{\text{III}}(\text{tpy})(\text{Cl})]$ or $[\text{Os}^{\text{III}}(\text{tpy})(\text{Cl})](\text{NSPh})$).

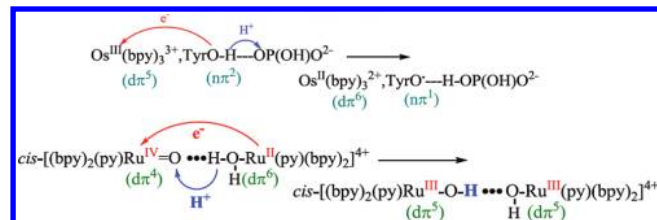


It is different from a Noyori concerted transfer hydrogenation mechanism³³ but is related to multicomponent or bifunctional hydrogenation.³⁴

1.3. Theory of EPT

The EPT elementary steps for comproportionation in Scheme 1 and MS-EPT in Scheme 4 are compared in Scheme 9. They share common features that define reaction barriers and rates.

Scheme 9



Preassociation with H-bond Formation: Because of the proton's heavier mass, $\nu(\text{E-H})$ wave functions fall off with distance much more rapidly than electronic wave functions, by $\lambda_e/\lambda_H \approx 40$. The decrease in radial extension necessitates hydrogen bonding to minimize the proton transfer distance (proton tunneling distance) in EPT.

Both hydrogen bonding and EPT require energetically accessible orbital binding sites at both the proton donor and acceptor. The strength and symmetry of the donor-H---acceptor H bond play an important role. The proton tunneling distance increases as asymmetry increases, decreasing rate and increasing kinetic isotope effects. Nearly symmetric hydrogen bonds between highly electronegative atoms (found in biological structures, for example) minimize the proton transfer distance enhancing EPT rates.

Proton Transfer: Proton motion along the proton transfer coordinate is described by a linear combination of the high frequency (2000–4000 cm⁻¹) $\nu(\text{E-H})$ vibrational modes before and after proton transfer occurs.^{3,7,35} Because of the high quantum spacings between these vibrational levels, proton

transfer occurs by quantum mechanical tunneling not classical barrier crossing.

Electron Transfer: As for electron transfer (see section 1.3.1), the electron transfer part of EPT is induced by an electrostatic perturbation between electron donor and acceptor. The perturbation causes the donor and acceptor electronic wave functions to mix. H-bonding can also promote $d\pi-d\pi$ electronic coupling along the H-bond as in $\text{Ru}^{\text{IV}}=\text{O}-\text{H}-\text{O}(\text{H})\text{Ru}^{\text{II}}$ EPT in Scheme 1. For MS-EPT, as in $\text{Os}(\text{bpy})_3^{3+}$ oxidation of $\text{TyrOH}-\text{OP(O)OH}^{2-}$ in Scheme 4, electron transfer and proton transfer are spatially isolated. There is a secondary impact of the hydrogen bond on electronic coupling by its influence on the electron donor electronic wave function at TyrOH .

In summarizing EPT theory, it is useful to first consider electron transfer. The two are closely related. In the introduction below, it is assumed that electronic coupling between electron donor and acceptor sites is relatively weak. In this limit, the resonance energy arising from donor–acceptor wave function mixing, H_{ab} (see later), is small compared to the reorganization energy (λ), $H_{\text{ab}} \ll \lambda$. More general treatments incorporate the effect of electronic delocalization.³⁶

1.3.1. Electron Transfer. In diffusional electron transfer, preassociation between reactants, D and A (eq 14), is followed by electron transfer and separation of products, D^+ and A^- . Preassociation and close contact enhance electronic wave function mixing between the electron donor (D) and acceptor (A) and also minimize the solvent–medium barrier.^{1,37} In eq 14, K_A is the association constant for the reactants before electron transfer and K_A' is the constant for the products after electron transfer occurs. The free-energy change for the ET step, ΔG_{ET} , is related to the overall free-energy change as in eq 15. In this equation, $\Delta G^\circ = F\{E^\circ(\text{D}^{+/0}) - E^\circ(\text{A}^{-/0})\}$ (25 °C, STP).



$$\Delta G_{\text{ET}} = \Delta G^\circ - RT \ln(K_A/K_A') \quad (15)$$

For intramolecular electron transfer (eq 16a) or electron transfer in a preformed structure with electron transfer donor and acceptor spatially arrayed as in a protein (eq 16b), there is no preassociation, but changes in local orientation can influence k_{ET} by their impact on electronic coupling.



In the classical limit, the rate constant for electron transfer, k_{ET} , is given by eq 17. In eq 17, λ is the classical reorganization energy. It is the sum of solvent (λ_o , medium) and intramolecular (λ_i) reorganization energies with $\lambda = \lambda_o + \lambda_i$.

The reorganization energies arise from the effect of changes in electron content on intramolecular structure and from polarization changes in the medium. They can be resolved into a collection of coupled intramolecular and medium modes, those for which there is a change in equilibrium displacement, or frequency, between reactants and products.³⁷

In eq 17, ν_{ET} is the frequency factor for electron transfer. In the limit of weak electronic coupling (tens of cm^{-1} , the *Marcus*

nonadiabatic limit), ν_{ET} is given by eq 18 with H_{ab} being the electron transfer matrix element and ν_e the electron tunneling frequency. H_{ab} is the resonance energy arising from electronic wave function mixing between the reactant and product electronic wave functions induced by the perturbation between sites, $H_{\text{ab}} = \langle \Psi_p | \hat{H} | \Psi_r \rangle$ with Ψ_r and Ψ_p the reactant and product electronic wave functions, respectively. \hat{H}_{ab} is the perturbation operator.

With weak to moderate electronic coupling, the electron is always at equilibrium with the coupled nuclear motions (*Marcus adiabatic limit*). In this limit the barrier-crossing frequency is dictated by the rate at which the slowest mode or modes reaches the intersection region between reactant and product energy–coordinate curves (eqs 19), which is $\sim 10^{12} \text{ s}^{-1}$ for a coupled solvent mode. In the intermediate regime, electron and nuclear motion are dynamically coupled and ν_{ET} is given by eq 19b.

The Marcus nonadiabatic–adiabatic transition for electron transfer occurs with very weak electronic coupling. The situation is different for EPT (see section 1.3.2).

$$k_{\text{ET}} = \nu_{\text{ET}} (4\pi RT\lambda)^{-1/2} \exp - \left[\frac{(\Delta G_{\text{ET}} + \lambda)^2}{4\lambda RT} \right] \quad (17)$$

$$\nu_{\text{ET}} = \nu_e = \frac{2\pi}{\hbar} H_{\text{ab}}^2 \quad (18)$$

$$\nu_{\text{ET}} = \nu_n \quad (19a)$$

$$\nu_{\text{ET}}^{-1} = \nu_n^{-1} + \nu_e^{-1} \quad (19b)$$

The exponential term in eq 17 describes the classical barrier to electron transfer. It gives the fractional population of preassociated donor–acceptor pairs in which the coupled modes, intramolecular and medium, are in configurations in which electron transfer can occur with energy conservation. For a single classical mode this occurs at the intersection between the reactant and product energy–coordinate curves. The pre-exponential term $(4\pi RT\lambda)^{-1/2}$ is the classical density of states. It defines the number of reaction channels available for barrier crossing in the classical limit.

Quantum Modes: Contributions from coupled medium or high frequency modes can also be included explicitly. With a single coupled quantum mode, and the remaining coupled intramolecular and solvent modes treated classically, electron transfer can be treated as the sum of vibronic transitions from initial quantum levels ν to final quantum levels ν' (Figure 3).

For a single coupled quantum mode with quantum spacing $\hbar\nu = \hbar\omega \gg k_B T$, only level $\nu = 0$ is appreciably populated and k_{ET} is given by eq 20. This result assumes no change in quantum spacing between reactants and products ($\hbar\omega' = \hbar\omega$). The rate constant is the sum of individual vibronic transitions from initial level $\nu = 0$ in the reactants (D,A) to levels ν' in the products (D^+, A^-). All other coupled intramolecular and medium modes are treated classically and included in the classical barrier crossing term as in eq 17 with $\lambda = \lambda_o + \lambda_i$.

$$k_{\text{ET}} = \nu_{\text{ET}} \sum_{\nu'} \langle \chi_{\nu'} | \chi_{\nu=0} \rangle^2 (4\pi RT\lambda)^{-1/2} \times \exp - \left[\frac{(\Delta G_{\text{ET}} + \nu' \hbar\omega + \lambda)^2}{4\lambda RT} \right] \quad (20)$$

The square of the vibrational overlap integral, $\langle \chi_{\nu'} | \chi_{\nu=0} \rangle^2$, gives the extent to which the initial and final states are

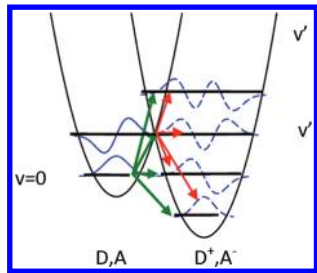


Figure 3. Energy–coordinate curves, vibrational levels, and vibrational wave functions illustrating electron transfer as the sum of vibronic transitions from initial level $\nu = 0$ to final levels ν' .

coincident along the normal coordinate (Q) for the coupled quantum mode. It is the quantum analogue of the intersection between energy curves in a classical barrier crossing. Its origin is the probabilistic uncertainty in spatial coordinates for interacting particles at the quantum level.

For a harmonic oscillator with no change in frequency between the initial and final states, the vibrational overlap integral is given by eq 21a. S is the electron-vibrational coupling constant or Huang–Rhys factor. It is related to the reduced mass, M , and angular frequency, ω , as shown in eq 21b. ΔQ_{eq} is the change in equilibrium normal coordinate for the quantum mode between initial (reactant) and final (product) states.

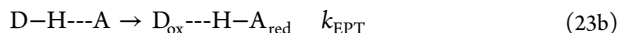
$$\langle \chi_\nu | \chi_{\nu=0} \rangle^2 = \exp(-S) \frac{S^{\nu'}}{\nu'!} \quad (21a)$$

$$S = \frac{1}{2} \left(\frac{M\omega}{\hbar} \right) (\Delta Q_{\text{eq}})^2 \quad (21b)$$

The final expression for k_{ET} including a single coupled quantum mode is given in eq 22. In this equation, λ is the sum of solvent (medium) and reorganization energies for the remaining coupled intramolecular modes treated classically. The result in eq 22 can be generalized to multiple quantum modes and to include contributions from initial vibrational levels above $\nu = 0$.

$$k_{\text{ET}} = \nu_{\text{ET}} \sum_{\nu'} \exp(-S) \frac{S^{\nu'}}{\nu'!} (4\pi RT\lambda)^{-1/2} \times \exp - \left[\frac{(\Delta G_{\text{ET}} + \nu' \hbar\omega + \lambda)^2}{4\lambda RT} \right] \quad (22)$$

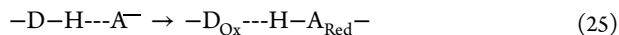
1.3.2. Electron–Proton Transfer. For diffusional reactions, EPT also occurs by preassociation. As noted previously, H-bond preassociation between electron transfer donor (D–H) and acceptor (A) (eq 23) is essential to minimize the proton transfer distance. In eq 23, the preassociation constants K_A and K_A' include the H-bond interaction. The free-energy change for the EPT step, ΔG_{EPT} , is related to the overall free-energy change, ΔG° , as shown in eq 24.



$$\Delta G_{\text{EPT}} = \Delta G^\circ - RT \ln(K_A/K_A') \quad (24)$$

In a preformed protein structure or molecular framework with EPT donor and acceptor at fixed sites spatially (eq 25),

preassociation is not a factor but local orientation and its effect on hydrogen bonding play a role.



In EPT, electrons and protons transfer in a single, concerted step. Because of the high frequency E–H (O–H, N–H) modes involved in the proton transfer act, the PT part of EPT must be treated quantum mechanically with discrete vibrational levels characterized by energy levels, frequencies, and equilibrium displacements. As discussed in section 2, there have been several contributors to EPT theory, but the work of Hammes-Schiffer and her group has been the most comprehensive. She has treated the problem in general, but of most value in treating many chemical and biological EPT reactions is the “adiabatic” (strong electronic coupling) limit for proton transfer combined with the “non-adiabatic” (weak electronic coupling) limit for electron transfer. For the results of more general treatments, including strong electronic coupling, see section 2.4.

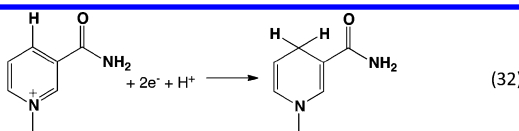
In the Hammes-Schiffer treatment, strong electronic coupling across the D–H---A hydrogen bond leads to extensive mixing of the initial diabatic $\nu(\text{D}-\text{H})$ and final $\nu(\text{A}-\text{H})$ vibrational states and their energy–coordinate curves. A new ground state energy–coordinate surface results with associated vibrational wave functions for the initial (χ_μ) and final vibrational states (χ_ν) including the hydrogen-bond interaction. This strong coupling limit for proton motion is in contrast to the quantum mode treatment for electron transfer in the previous section, where electronic coupling is weak and initial and final vibrational states are relatively unperturbed.

In the quantum view, transfer of the proton in EPT along the D–H---A proton transfer coordinate is described by the square of the vibrational overlap integral, $\langle \chi_\mu | \chi_\nu \rangle^2$. As noted for quantum mode participation in electron transfer, vibrational overlap provides a quantitative measure of the extent to which the initial and final states coexist, in this case along the D–H---A proton transfer coordinate.

In the limit of strong electronic coupling across the hydrogen bond and weak electronic coupling, between electron donor and acceptor orbitals, k_{EPT} is given by the sum over states result in eq 26. It describes a series of vibronic transitions from initial level $\mu = 0$ in the proton transfer mode to final levels ν in the EPT product state and is analogous to the electron transfer result in eq 20. This is a sum over states result describing transitions from initial level μ to final levels ν . The free-energy change for each channel is $\Delta G_{\text{EPT}} + \nu \hbar\omega$ with ΔG_{EPT} being the overall free-energy change. λ is the sum of the solvent (medium) reorganization energy and the reorganization energy for the remaining coupled intramolecular modes treated classically. The summation over ν typically truncates rapidly with only those levels that minimize the classical exponential barrier term playing an important role.

$$k_{\text{EPT}} = \frac{2\pi H_{\text{ab}}^2}{\hbar} \sum_{\nu} \langle \chi_\mu | \chi_\nu \rangle^2 (4\pi RT\lambda)^{-1/2} \times \exp - \left[\frac{(\Delta G_{\text{EPT}} + \nu \hbar\omega + \lambda)^2}{4\lambda RT} \right] \quad (26)$$

The solvent contribution to λ is more complex than for electron transfer because it includes contributions from both transferring electron and proton. As for electron transfer, additional coupled medium and high frequency modes can be included and treated explicitly.



Contributions also exist from vibronic channels from vibrational levels above $\mu = 0$. Even though populations in these levels fall off rapidly with $\hbar\omega$, there can be a considerable compensation due to enhanced vibrational wave function overlap in levels above $\mu = 0$. Including the fractional population above $\mu = 0$, $p(\mu)$, gives the final result in eq 27. In this equation, the first summation is over the vibrational levels in the initial state. As in eq 22, the second summation is over all levels ν .

$$k_{\text{EPT}} = \frac{2\pi H_{ab}^2}{\hbar} \sum_{\mu} p(\mu) \sum_{\nu} \langle \chi_{\mu} | \chi_{\nu} \rangle^2 (4\pi RT \lambda_{\mu\nu})^{-1/2} \times \exp \left[-\frac{(\Delta G_{\mu\nu} + (\mu - \nu)\hbar\omega + \lambda)^2}{4\lambda RT} \right] \quad (27)$$

$$\nu_{\text{EPT}} = \frac{2H_{ab}^2}{\hbar} \sum_{\mu} p(\mu) \sum_{\nu} \langle \chi_{\mu} | \chi_{\nu} \rangle^2 \quad (28)$$

The magnitude of the squared vibrational overlap integral in eq 28 can be very small. Vibrational overlaps for the comproportionation reaction between *cis*-[Ru^{IV}(bpy)₂(py)(O)]²⁺ and *cis*-[Ru^{II}(bpy)₂(py)(OH₂)]²⁺ for the $\mu = 0 \rightarrow \nu = 0$ vibronic transition for both the protio and deuterio aqua complex are shown in Figure 4.^{11a} The decrease in overlap for

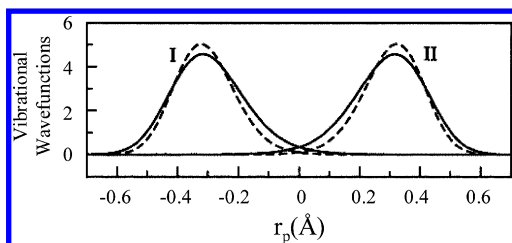


Figure 4. Illustrating reactant (I) and product (II) vibrational wave functions, H (solid curve) and D (dashed curve), for the $\mu = 0 \rightarrow \nu = 0$ vibronic channel for the *cis*-[Ru^{IV}(bpy)₂(py)(O)]²⁺/*cis*-[Ru^{II}(bpy)₂(py)(OH₂)]²⁺ comproportionation reaction in Scheme 3. The plots for *cis*-[Ru^{IV}(bpy)₂(py)(O)]²⁺/*cis*-[Ru^{II}(bpy)₂(py)(OD₂)]²⁺ illustrate the decrease in vibrational overlap for the --OD_2 complex, which is the origin of the H₂O/D₂O KIE of 16.1. Reproduced with permission from ref 11a. Copyright 2002 American Chemical Society.

the --OD_2 complex is the origin of the H₂O/D₂O kinetic isotope effect of 16.1. It arises from the effect on vibrational overlap of the decrease in zero point energy, $\{m_{\text{H}}(m_{\text{o}} + m_{\text{D}})/m_{\text{D}}(m_{\text{o}} + m_{\text{H}})\}^{1/2}$, of 0.7 between H and D.

The pre-exponential term in eq 28 assumes the Condon approximation and the separation of nuclear and electronic motion. It includes the electron transfer matrix element arising from electronic wave function mixing, H_{ab} , and the square of the vibrational overlap integral for proton transfer for each EPT channel. For EPT, the barrier crossing frequency, ν_{EPT} , depends on both the electron transfer matrix element, H_{ab} , and the magnitude of the vibrational overlap integral with $\nu_{\text{EPT}} \propto \langle \Psi_f | \hat{H} | \Psi_i \rangle^2 \langle \chi_{\mu} | \chi_{\nu} \rangle$. With small vibrational overlap, the EPT

equivalent of the Marcus “nonadiabatic” limit in electron transfer is predicted to persist even with moderate electronic coupling. The transition to adiabatic EPT, analogous to eq 19 for electron transfer, is predicted to occur for H_{ab} values of considerably higher magnitude depending on the magnitude of the vibrational overlap integral. In the sum over states result in eq 27, the individual transitions between states could differ in the degree of adiabatic or nonadiabatic character.

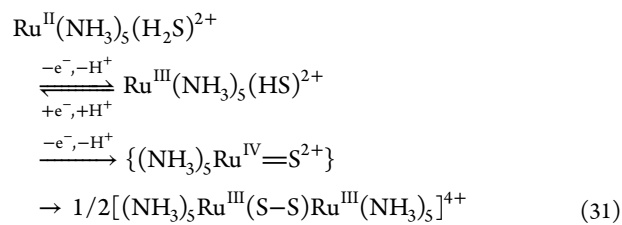
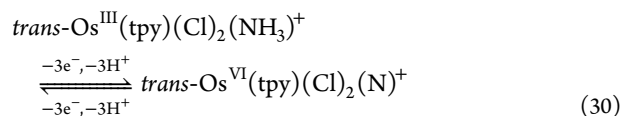
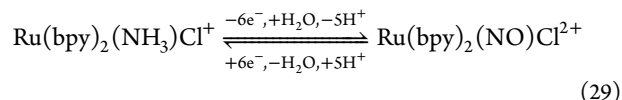
The formalism inherent in the general result in eq 27 and the underlying theory provide a comprehensive, conceptual basis for understanding and quantifying EPT at the microscopic level. It includes a quantitative description of temperature dependence, isotope effects, etc. The formalism has been successfully applied to a variety of EPT reactions in solution, at electrodes, and in the inverted region; note the summary in section 2. In evaluating specific reactions, additional features at the microscopic level have emerged such as the role of coupled “promoting modes” in minimizing the proton transfer distance and increasing the extent of vibrational overlap.³⁸

1.4. PCET: Thermodynamics and Structure

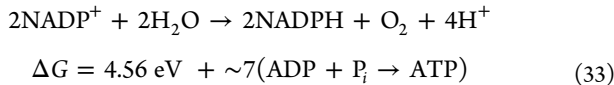
PCET originates in the impact on acid–base properties of changes in electron content at single sites or clusters. Oxidation enhances acidity, and reduction decreases acidity. Changes with electron content can be dramatic. pK_a values for tyrosine and tyrosine radical cation (TyrOH^{•+}) are 10.1 and -2 , respectively. Hupp and co-workers have estimated that $pK_a = -10$ to -18 for protonation of the oxo group in a series of *trans*-[Re^{VI}(L)₄(O)(OH)]³⁺ complexes (L = pyridine or substituted pyridine) and $pK_{a,1} = 22$ – 26 for the hydroxyl groups in *trans*-[Re^{III}(L)₄(OH)₂]⁺.³⁹

Stabilization of higher oxidation states by multiple bond formation plays a major role in PCET couples for main group element couples, e.g., $\text{NH}_3 + 3\text{H}_2\text{O} \rightarrow \text{NO}_3^- + 9\text{H}^+ + 8\text{e}^-$, and for transition metal complexes. Oxidation and loss of $d\pi$ electrons creates an orbital basis for multiple bond formation by electron donation from ligands. For transition metal complexes, this is especially important for H₂O as a ligand as illustrated by oxidation of Mn^{III}(OH₂)₆³⁺ to Mn^{VI}O₄²⁻ or of Cr^{III}(H₂O)₆³⁺ to Cr^{VI}O₄²⁻.

PCET also appears for N- and S-based ligands containing dissociable protons. Examples are known of reversible oxidation of coordinated NH₃ to N³⁻ (eq 29).^{11f,40} With other than O-based ligands, there is a tendency for nucleophilic addition to occur to electron-deficient N or S atoms. This leads to water addition, proton loss, and net ligand oxidation (eq 30)⁴¹ or S---S or N---N bond formation (eq 31).⁴²



Reversible PCET couples based on C–H bonds are also known. An important example is the pyridinium/dihydropyridine couple of NAD⁺/NADPH in biology (eq 32). Light-driven reduction of NADP⁺ to NADPH is the reductive half reaction in Photosystem I (eq 33). Its reductive equivalents are used to reduce CO₂ to carbohydrates in the Calvin cycle.



1.4.1. pH Dependence. PCET half reactions are pH-dependent with variations in E° predicted by the Nernst equation. For a 1e⁻ half reaction with a 1H⁺ change in proton content on reduction, Ox + H⁺ + e⁻ → Red–H, the reduction potential for the couple, E , varies with pH as shown in eq 34. E° is the standard potential for the couple Ox–H⁺ + e⁻ → Red–H.

$$E = E^\circ + (2.303RT/F)\log(a_{\text{ox}}a_{\text{H}^+}/a_{\text{Red}-\text{H}})$$

$$= E^\circ + 0.059 \log(a_{\text{ox}}a_{\text{H}^+}/a_{\text{Red}-\text{H}}) \quad (\text{STP}, 25^\circ\text{C}) \quad (34)$$

In eq 34, the a_{Red} , etc. are activities with $a_i = \gamma_i m_i$. γ_i is the activity coefficient of component i , and m_i is the molality. In dilute solutions, $a_{\text{Ox}} = \gamma_{\text{Ox}} m_{\text{Ox}} \approx \gamma[\text{Ox}]$ and eq 34 is given by eq 35. The formal potential (E') is the commonly measured quantity in electrochemical experiments. It includes both E° and the log of the activity coefficient ratio (eq 36).

$$E = E^\circ + 0.059 \log(\gamma_{\text{Ox}}/\gamma_{\text{Red}-\text{H}}) + 0.059 \log[\text{Ox}]/[\text{Red}-\text{H}] - 0.059\text{pH} \quad (35)$$

$$E = E' + 0.059 \log[\text{Ox}]/[\text{Red}-\text{H}] - 0.059\text{pH}$$

$$E' = E^\circ + 0.059 \log(\gamma_{\text{Ox}}/\gamma_{\text{Red}-\text{H}}) \quad (36)$$

In voltammetry the quantity that characterizes the couple is the “half-wave potential”, $E_{1/2}$.⁴³ It is measured by potentiometry, voltammetry, cyclic voltammetry, etc. as the potential of zero current flow for a chemically reversible reaction; the potential of zero current flow for a chemically reversible reaction is reached when the bulk concentrations of oxidized and reduced species are identical. For an electrochemically reversible reaction (rapid, chemically reversible, diffusion-limited), $E_{1/2}$ is related to E' as shown in eq 37. In this equation $m_{\text{Ox}-\text{H}^+}$ and m_{Red} are mass transfer coefficients in cm/s.

$$E_{1/2} = E' - \frac{RT}{nF} \ln\left(\frac{m_{\text{Ox}\text{H}^+}}{m_{\text{Red}}}\right) \approx E' \quad (37)$$

The Nernst equation predicts a pH dependence for PCET couples in pH ranges where there is a change in proton content between oxidized and reduced forms. As an example, the pH dependence of the Ru^{III/II} couple for *cis*-Ru^{II}(bpy)₂(py)(OH)₂²⁺ ($pK_{a,1} = 0.85$ for Ru^{III}–OH₂³⁺, 10.6 for Ru^{II}–OH₂²⁺, and $E' = 1.04 \text{ V}$) from pH = 0–10 is given by eq 38. Above pH 10.6 with pH > pK_a(Ru^{II}–OH₂²⁺), the couple becomes *cis*-Ru^{III}(bpy)₂(py)(OH)^{2+/+} and is pH-independent with $E' = 0.45 \text{ V}$. Over the entire range of accessible pH's in water, E' is given by eq 39. Similarly, for the Ru^{IV/III} couple, a 1e⁻/2H⁺ transfer interrelates *cis*-Ru^{IV}(bpy)₂(py)²⁺ and *cis*-Ru^{III}(bpy)₂(py)(OH)₂³⁺

at pH < 0.85 followed by a 1e⁻/2H⁺ dependence at pH < 0.85.

$$E(\text{Ru}^{\text{III/II}}) = E' + (2.303RT/F)\log(a_{\text{ox}}a_{\text{H}^+}/a_{\text{Red}-\text{H}}) - 0.059(\text{pH} - pK_{a,1})$$

$$= 1.04 - 0.059(\text{pH} - pK_{a,1}) \quad (38)$$

$$E(\text{Ru}^{\text{III/II}}) = E' + (2.303RT/F)\log(a_{\text{ox}}a_{\text{H}^+}/a_{\text{Red}-\text{H}}) - 0.059\{\log(K_{a,1}^{\text{III}} + [\text{H}^+]) - \log(K_{a,1}^{\text{II}} + [\text{H}^+])\}$$

$$= 1.04 - 0.059\{\log(K_{a,1}^{\text{III}} + [\text{H}^+]) - \log(K_{a,1}^{\text{II}} + [\text{H}^+])\} \quad (39)$$

In general, for a couple in which m protons and n electrons are transferred, Ox + mH⁺ + ne⁻ → Red(H)_m^{(m-n)+}, E varies with pH as shown in eq 40 with pH > pK_a. This dependence results in characteristic variations of E with pH with the slopes in E versus pH plots of 59 mV/pH unit for a 1e⁻/1H⁺ couple, 118 mV/pH unit for a 1e⁻/2H⁺ couple, and 29 mV/pH unit for a 2e⁻/1H⁺ couple, for example.

$$E = E' + \frac{0.059m}{n} \text{pH} \quad (40)$$

$E_{1/2} \approx E'$ values for the Ru^{III/II} and Ru^{IV/III} couples of *cis*-Ru^{III}(bpy)₂(py)(OH)₂³⁺ are shown plotted versus pH in the E versus pH or Pourbaix diagram in Figure 5. The dominant half

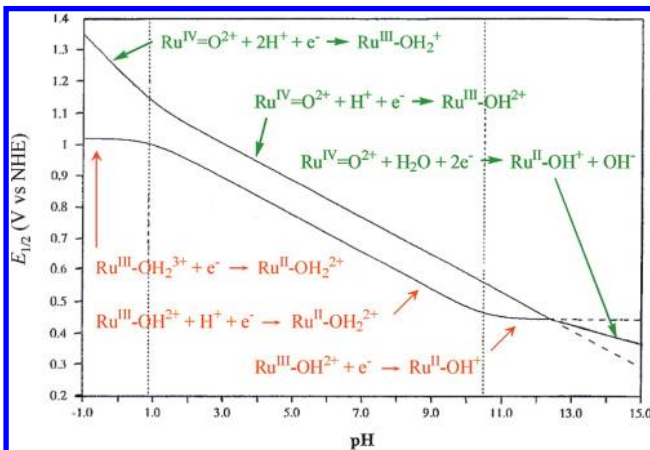


Figure 5. $E_{1/2}$ versus pH diagram for the Ru^{IV/III} and Ru^{III/II} couples of *cis*-Ru^{II}(bpy)₂(py)(OH)₂²⁺, (Ru^{II}–OH₂) at 25 °C, $I = 0.1 \text{ M}$, versus NHE. The vertical dotted lines correspond to $pK_{a,1}$ for Ru^{II}–OH₂⁺ ($pK_a = 10.6$) and $pK_{a,1}$ for *cis*-[Ru^{III}(bpy)₂(py)(H₂O)]³⁺ (Ru^{III}–OH₂³⁺, $pK_a = 0.85$). The remaining abbreviations are *cis*-[Ru^{IV}(bpy)₂(py)(O)]²⁺ (Ru^{IV}=O²⁺) and *cis*-[Ru^{III}(bpy)₂(py)(OH)]²⁺ (Ru^{III}–OH₂⁺). The half-cell reactions for the individual couples in the various pH regions are indicated as are the sixth ligands and whether they are O²⁻, OH⁻, or H₂O. The $E_{1/2}$ –pH curves were calculated from the Nernst equation by using the pK_a values and $E_{1/2}(\text{cis}-[\text{Ru}^{\text{II}}(\text{bpy})_2(\text{py})(\text{H}_2\text{O})]^{3+/2+}) = 1.02 \text{ V}$ and $E_{1/2}(\text{cis}-[\text{Ru}^{\text{II}}(\text{bpy})_2(\text{py})(\text{OH})]^{2+/1+}) = 0.46 \text{ V}$.^{1,11b,44} Reproduced with permission from ref 1. Copyright 2007 American Chemical Society.

reactions in different pH–potential regimes are indicated. The vertical lines correspond to pK_a values for Ru^{III}–OH₂³⁺ and Ru^{II}–OH₂²⁺. The data are of interest in illustrating a number of points about PCET couples: (1) Regions corresponding to OH⁻/1e⁻, 1e⁻/1H⁺, and 1e⁻/2H⁺ all appear in the data. (2) There is a significant decrease in E' for the Ru^{III/II} couple from 1.04 V for the Ru^{III}–OH₂³⁺/Ru^{II}–OH₂²⁺ couple to 0.45 V for

the Ru^{III}–OH²⁺/Ru^{II}–OH⁺ couple due, in part, to the decrease in charge (section 1.4.2). The difference in potentials between couples that differ by a single proton can be calculated from the corresponding pK_a values by use of eq 41.

$$\begin{aligned} E(\text{Ru}^{\text{III}/\text{II}}) &= E^{\circ'}(\text{Ru}^{\text{II}}-\text{OH}_2^{3+/2+}) \\ &\quad - 0.059 \log(K_{\text{a},1}^{\text{III}}/K_{\text{a},1}^{\text{II}}) E(\text{Ru}^{\text{III}/\text{II}}) \\ &= E^{\circ'}(\text{Ru}^{\text{II}}-\text{OH}_2^{3+/2+}) \\ &= 1.04 - 0.059(pH_{\text{a},1}^{\text{II}} - pK_{\text{a},1}^{\text{III}}) \\ &= 0.45 \text{ V} \end{aligned} \quad (41)$$

For transition metal complexes with access to multiple oxidation states and stabilization of higher oxidation states by metal oxo formation, pH-dependent PCET behavior can be complex. Oxidation of *cis*-Ru^{II}(bpy)₂(OH₂)₂²⁺ to *cis*-Ru^{VI}(bpy)₂(O)₂²⁺ involves four oxidation state changes and four different pK_a's from pH 1 to 9.⁴⁵

Related pH-dependent behavior exists for organic and biological couples and even for metal oxide semiconductors. A plot of $E^{\circ'}$ versus pH for 1e⁻ oxidation of tyrosine is shown in Figure 6. As for other metal oxide semiconductors,

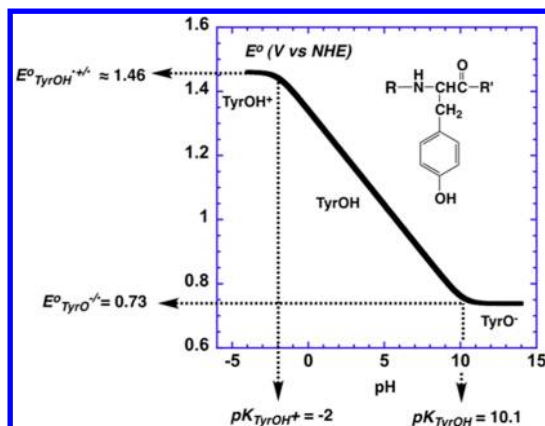


Figure 6. Calculated $E^{\circ'}$ –pH diagram for the 1e⁻ oxidation of tyrosine at 25 °C, $I = 0.1$ M. The structure of tyrosine as it would occur in a peptide is also shown, where R and R' represent the polypeptide chain.

conduction band potential for TiO₂, E_{CB} , displays a Nernstian pH dependence from pH = −8 to 23. Quartz crystal microgravimetric studies have demonstrated that changes in potential are accompanied by proton uptake or loss with PCET and protonation/deprotonation changes coupled to Ti(IV/III) oxidation state changes.⁴⁶

1.4.2. Redox Potential Leveling. A striking feature in the data in Figure 5 and Scheme 11 is the small (110 mV) difference in $E^{\circ'}$ values between the Ru^{IV/III} and Ru^{III/II} couples from pH = 1 to 10. This is in contrast to typical metal complex couples where charge buildup occurs on oxidation or reduction. For the Ru(IV/III)–Ru(III/II) couple of *cis*-Ru^{IV/III}(bpy)₂Cl₂^{2+/+} and *cis*-Ru^{III/II}(bpy)₂Cl₂^{+/-}, $\Delta E^{\circ'} = E_{1/2}(2) - E_{1/2}(1) = 1.7$ V (I = 0.1 M, CH₃CN).^{1,11f,47}

The phenomenon of multiple oxidation states and multiple redox couples in transition metal chemistry is a characteristic feature of early to midtransition metal complexes. It arises from the relatively closely spaced, sequential ionization energies for the 3d, 4d, and 5d levels and efficient screening of the nuclear charge by the d electrons.⁴⁸ The use of PCET, to avoid charge

buildup, further decreases differences in E° values between adjacent couples. This “redox potential leveling” effect enables the buildup of multiple redox equivalents at single sites or clusters. This is seen in the adjacent Ru^{IV}(bpy)₂(py)(O)²⁺/Ru^{III}(bpy)₂(py)(OH)²⁺–Ru^{II}(bpy)₂(py)(OH₂)²⁺ couples in Figure 5, where from pH ≈ 1–10, $\Delta E_{1/2}$ between the Ru^{IV}=O²⁺/Ru^{III}–OH²⁺ and Ru^{III}–OH²⁺/Ru^{II}–OH₂²⁺ couples is only 110 mV.

A major contributor to “redox potential leveling” is revealed in the results of a thermochemical analysis based on a simple Born solvation model. The result is shown in eq 42 for the generalized couples $\text{Ox}_2^{(n+1)+}/\text{Red}_2^{(n+1)+}$ and $\text{Ox}_1^{(n+2)+}/\text{Red}_1^{n+}$ with associated reduction potentials $E_2^{\circ'}$ and $E_1^{\circ'}$. In eq 42, the ionization energy is factored into a promotion energy required to promote the ionizing electron to the surface of a sphere enclosing the complex (I) and a charging term, $(ne)^2/rD_s$. In this expression, e is the unit electron charge, D_s is the static dielectric constant, and r is the radius of Ox/Red assumed to be spherical. Without PCET and an increase in charge between couples (eq 42), $\Delta E^{\circ'}$ is increased by the charging term $2e^2/rD_s$. For a PCET couple (eq 43), the charge types are the same and this term is 0. Charge effects are predicted to be especially important in media of low polarity such as the hydrophobic thylakoid membrane of photosynthesis.

For couples $\text{Ox}_2^{(n+2)+}/\text{Red}_2^{(n+1)+}$ ($E_2^{\circ'}$) and $\text{Ox}_1^{(n+2)+}/\text{Red}_1^{n+}$ ($E_1^{\circ'}$):

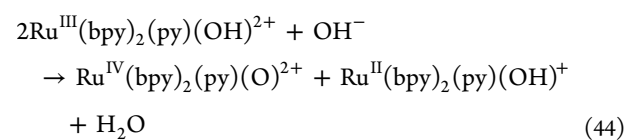
$$\Delta E^{\circ'} = E_2^{\circ'} - E_1^{\circ'} = \left(\frac{2e^2}{rD_s} \right) + I'_{n+1} - I'_n = \left(\frac{2e^2}{rD_s} \right) + \Delta I' \quad (42)$$

For couples $\text{Ox}_2^{n+}/\text{Red}_2^{n+}$ ($E_2^{\circ'}$) and $\text{Ox}_1^{n+}/\text{Red}_1^{n+}$ ($E_1^{\circ'}$):

$$\Delta E^{\circ'} = E_2^{\circ'} - E_1^{\circ'} = \Delta I' \quad (43)$$

The small difference in $\Delta E^{\circ'}$ values for PCET couples is essential for multielectron catalysis driven by single-electron transfer. It enables the sequential gain and loss of multiple electrons and the buildup of multiple redox equivalents at single sites or clusters without local charge buildup. In Photosystem II (section 8.4), water oxidation occurs at the CaMn₄ cluster of the “oxygen-evolving complex”. Oxygen evolution is triggered by a series of four sequential photon absorption events at a nearby antenna array. Each photon that is absorbed and delivered to the reaction center results in 1e⁻ oxidation of the OEC. Following buildup of four oxidative equivalents at the OEC, O₂ evolution occurs (section 8.4). Oxidation is accompanied by proton loss and release from the OEC through a proton exit channel that avoids local charge buildup.

1.4.3. “Missing” Oxidation States. From the $E_{1/2}$ –pH plots in Figure 5 for *cis*-Ru^{II}(bpy)₂(py)(OH₂)²⁺, a difference in pH dependence between the Ru^{IV}=O²⁺/Ru^{III}–OH²⁺ and Ru^{III}–OH²⁺/Ru^{II}–OH⁺ couples is triggered past pH = pK_a(Ru^{II}–OH₂²⁺) = 10.6 (Scheme 11). This causes it to intersect with the pH-independent Ru^{III}–OH²⁺/Ru^{II}–OH⁺ couple at pH = 12.8.^{1,11b} As the pH is increased further, $E_{1/2}(\text{Ru}^{\text{III}/\text{II}}) > E_{1/2}(\text{Ru}^{\text{IV}/\text{III}})$ and *cis*-Ru^{III}(bpy)₂(py)(OH)²⁺ is unstable with respect to disproportionation (eq 44).¹



Disproportionation is driven by PCET, the difference in pH-dependent behavior between adjacent couples, and the stabilization of higher oxidation state Ru(IV) by Ru=O multiple bonding. Remarkable examples of “missing” oxidation states have been identified. The $E_{1/2}$ versus pH diagram for $\text{Os}(\text{tpy})(\text{H}_2\text{O})_3^{2+}$ is shown in Figure 7. For this complex over

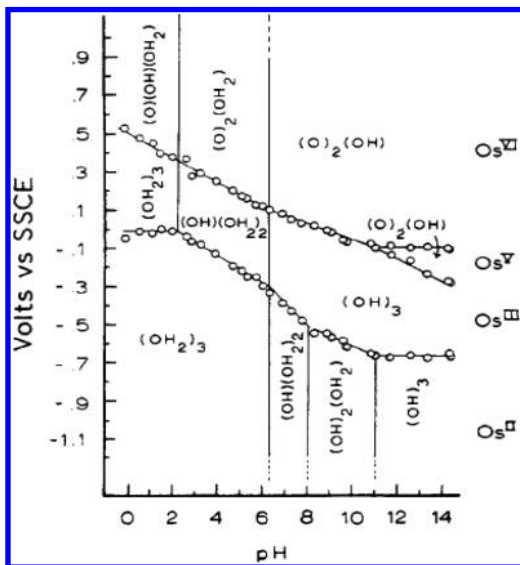
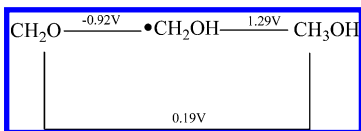


Figure 7. $E_{1/2}$ -pH diagram for $\text{Os}(\text{tpy})(\text{H}_2\text{O})_3^{2+}$ (versus sodium chloride saturated calomel electrode (SSCE); +0.236 V versus NHE) illustrating the $3e^-$ oxidation of Os(III) to Os(VI) over a wide pH range and the instability toward disproportionation of intermediate oxidation states Os(IV) and Os(V). Dominant forms of the complex in the various E -pH regions are indicated on the diagram, for example, $(\text{OH})_3$ for $\text{Os}^{\text{III}}(\text{tpy})(\text{OH})_3$.

an extended pH range, a single $3e^-/3\text{H}^+$ oxidation of Os(III) to Os(VI) occurs. Intermediate oxidation states Os(IV) and Os(V) are unstable with respect to disproportionation over this entire pH range.

Disproportionation and instability of intermediate oxidation states is a common phenomenon in main group chemistry as well. It is induced by electron configuration and bonding changes. Examples are the instability of intermediate oxidation states such as Sn(III) and Tl(II). An example from carbon chemistry is shown in Scheme 10 in the instability of methanol

Scheme 10. E° Values versus NHE for the $1e^-$ Couples Interrelating Formaldehyde and Methanol⁴⁹

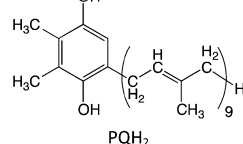
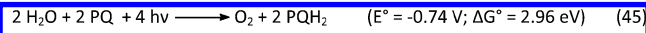


radical, which is unstable with respect to disproportionation into formaldehyde and methanol by $E^\circ = 2.31$ V. Methanol radical is both a powerful oxidant and a reductant.

1.4.4. pK_a -Potential Diagrams. pK_a -potential diagrams provide a useful way to display pK_a and E° data at fixed pH. Diagrams for *cis*-Ru^{II}(bpy)₂(py)(OH₂)²⁺ and quinone/hydroquinone, both at pH = 7 versus NHE, are shown in Schemes 11 and 12.

In these diagrams the impact of electron content and structure on pK_a values, the high E values for forming intermediates in ET-PT or PT-ET mechanisms, and the effect of PCET on redox potential leveling in Ru(IV/III)-Ru(III/II) couples all appear. For the quinone/hydroquinone couple, the intermediate oxidation state semiquinone, QH^\bullet , is stable with respect to disproportionation into QH^+ and QH^- by $E_2^\circ - E_1^\circ = -0.30$ V, but at pH = 7, where the dominant forms are Q and H_2Q , disproportionation is favored by $E_2^\circ - E_1^\circ = +0.28$ V.

1.4.5. PCET, Proton Gradients, and Energy Transduction. As noted in section 8.4, light absorption in Photosystem II results in water oxidation coupled with reduction of plastoquinone (PQ or Q_B) to plastoquinol (PQH_2), eq 45. Water oxidation occurs stepwise in the Kok cycle by sequential absorption of four photons and stepwise oxidative activation of the oxygen-evolving complex.

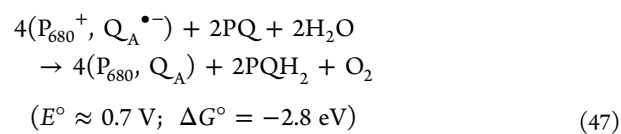


Water oxidation, $2\text{H}_2\text{O} \rightarrow \text{O}_2 + 4\text{H}^+ + 4e^-$ ($E^\circ = -0.82$ V at pH = 7), and PQ reduction, $\text{PQ} + 2e^- + 2\text{H}^+ \rightarrow \text{PQH}_2$ ($E^\circ/\text{PQ}/\text{PQH}_2 \approx 0.08$ V at pH = 7),⁵¹ occur at sites separated by ~50 Å in the thylakoid membrane. Protons for quinone reduction enter the thylakoid membrane from the outside, the stroma. The water oxidation half-reaction occurs at the CaMn_4 cluster of the oxygen-evolving complex (OEC). It is light-driven and releases protons to the inside, the lumen. Under light-saturating conditions, light-driven proton transfer builds up a proton gradient of ~3.5 pH units across the membrane, creating a transmembrane potential of ~0.2 eV (eq 46). The proton gradient is used to drive phosphorylation of ADP to ATP.

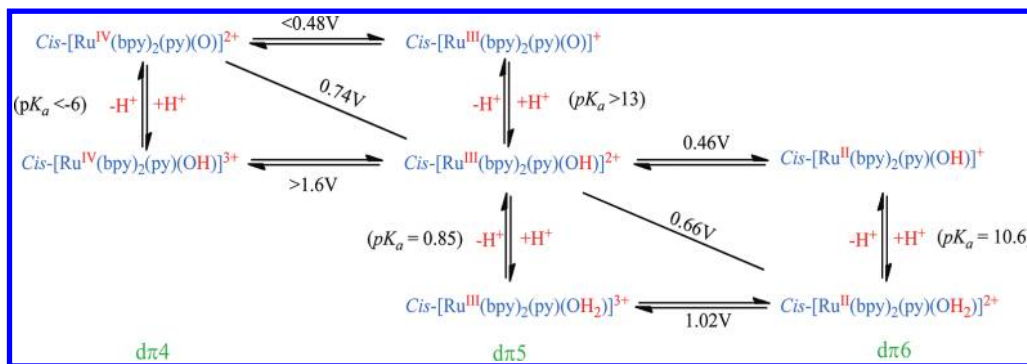
$$\begin{aligned} \Delta G^\circ(\text{eV}) &= -2.303RT(\text{pH}(2) - \text{pH}(1)) \\ &= -0.059\Delta\text{pH} \quad (\text{STP}) \end{aligned} \quad (46)$$

The sequence of reactions from light absorption to transmembrane pH gradient is a striking example of “energy transduction”—interconversion between different forms of energy. It is informative to map how light absorption at the antenna unit in PSII ends up creating a pH gradient that drives transmembrane “proton pumping”.

The driving force comes from free energy left over from photochemical water oxidation by PQ in eq 45. The photochemical reaction is initiated by antenna light absorption and sensitization of chlorophyll-based excited-state ${}^1\text{P}_{680}^*$ (1.8 eV), Chl_{D1} in Figure 1. ${}^1\text{P}_{680}^*$ undergoes oxidative quenching and electron transfer to give P_{680}^+ ($E^\circ/\text{P}_{680}^+/\text{P}_{680} \approx 1.26$ V) and $\text{Q}_A^\bullet-$ ($E^\circ/\text{Q}_A^\bullet-/ \text{Q}_A \approx -0.13$ V), creating ~1.4 eV of transiently stored redox energy (~5.6 eV for four absorbed photons). Following oxidation of water (eq 47), there is ~0.7 V of driving force left for driving the proton gradient.

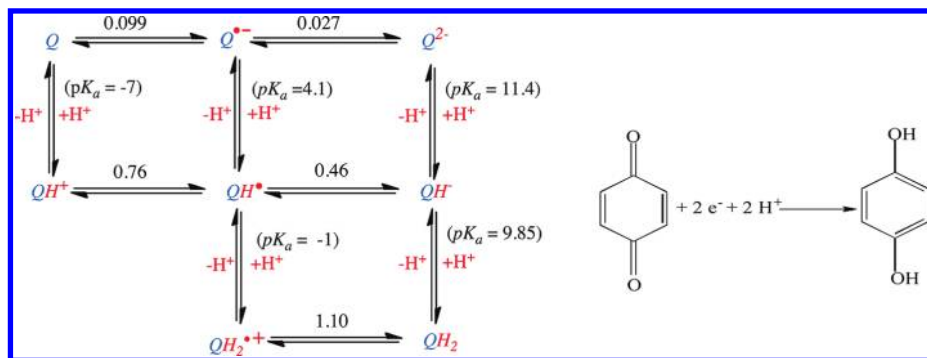


Scheme 11. Acid–Base Redox Potential (pK_a – $E^{\circ'}$) Diagram for the Ru(IV/III) and Ru(III/II) Redox Couples of *cis*-Ru^{II}(bpy)₂(py)(OH₂)²⁺ with Values Taken from Figure 5, Showing the dπ Electron Configurations at the Metal^{1,11b,a}



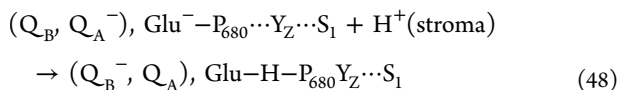
^aPotentials are versus NHE at 25 °C, $I = 0.1$ M. The vertical lines give pK_a values, and the slanted lines give the $E^{\circ'}$ values for the pH-dependent PCET couples at pH 7.

Scheme 12. As in Scheme 11 with Potentials in V versus NHE, pH 7 at 25 °C, $I = 0.1$ for the Quinone/Semiquinone/Hydroquinone (Q/HQ[•]/H₂Q) Couples^{1,50}



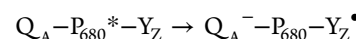
H⁺ Addition from the Stroma—Reduction of PQ: Proton transfer from the stroma into the membrane is driven by Q_A^{•-} reduction of PQ (Q_B), $2Q_A^{•-} + PQ + 2H^+ \rightarrow 2Q_A^- + PQH_2$, with $E^{\circ'} \approx 0.2$ V, $\Delta G^{\circ'} = -0.4$ eV. Reduction of PQ and enhanced basicity create a local driving force for proton transfer into the membrane from the stroma with $\Delta G^{\circ'} = -0.059\{(pK_{a,1}(PQH_2) - pH(\text{stroma})) + (pK_{a,2}(PQH_2) - pH(\text{stroma}))\}$. As an example, for 2e⁻ reduction of quinone to Q²⁻ at pH = 7, $pK_{a,1} = 9.8$ and $pK_{a,2} = 11.4$, giving $\Delta G^{\circ'} = -0.42$ eV.

Reduction of PQ to PQH₂ occurs in two separate reductive steps. The first electron transfer is triggered by absorption of the first photon in the Kok cycle to give PQ^{•-} (Q_B^{•-}). A coupled proton transfer occurs from the stroma but to a neighboring glutamate, Glu⁻ in eq 48. Absorption of a second photon, and a second electron transfer from Q_A^{•-}, coupled with proton transfer from the stroma gives PQH₂ (H₂Q_B): (Q_B^{•-}, Q_A^{•-}), Glu-H + H⁺ → (Q_A⁻, Glu⁻) + H₂Q_B. PQH₂ is translationally labile and diffuses through the membrane, ultimately providing reductive equivalents for CO₂ reduction at PSI. After oxidation and additional proton release, it translates back to PSII as PQ for additional PCET cycles.



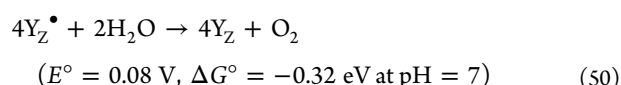
H⁺ Loss to the Lumen—Water Oxidation: Once formed, P₆₈₀⁺ oxidizes Y_Z, the tyrosine–histidine pair in Figure 1, to Y_{Z'}[•]

with $E^{\circ'}(Y_Z^{\bullet}/Y_Z) \approx 0.90$ V. The sequence from excited state to Q_A^{•-}–Y_{Z'}[•] is shown in eq 49.



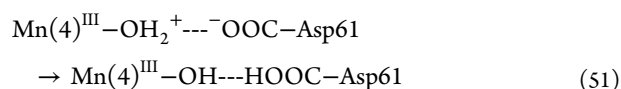
$$\Delta G_{ES} \approx 1.8 \text{ eV} \quad \Delta G^{\circ'}(\text{stored}) \approx -1.3 \text{ eV} \quad (49)$$

Y_{Z'}[•] subsequently delivers oxidative equivalents to the OEC for water oxidation, a reaction that is favored by ~0.08 V, $\Delta G^{\circ} = -0.32$ eV (eq 50).



It has been proposed that, in the first step in the Kok cycle ($S_0 \rightarrow S_1$, section 8.4.3), oxidation of Mn^{II}–OH₂ to Mn(III) occurs in the CaMn₄ cluster. On the basis of XRD data, the most likely site for oxidation is Mn(4), which lies closest to tyrosine Y_Z. It also lies near the carboxylate proton acceptor, aspartate 61 with $pK_a \approx 3.9$. Asp61 is the entryway to a proton exit channel that extends over 30 Å through the membrane to the lumen.

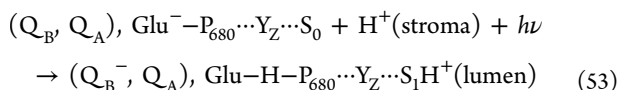
Oxidation of Mn(4)^{II}–OH₂ to Mn(4)^{III}–OH₂⁺ is expected to greatly decrease the pK_a for a bound water; $\Delta pK_a = 10.7$ between Mn(OH)₆²⁺ and Mn(OH)₆³⁺.^{6,10,39c,52} The increase in acidity at Mn(4) would provide the driving force for proton release to the lumen with proton transfer first to Asp61,



with $\Delta G^\circ = -0.059\{(pK_a(\text{Asp}(61)\text{COOH})) - pK_{a,1}(\text{Mn}^{\text{III}} - \text{OH}_2)\}$, followed by proton transfer to the lumen through the proton exit channel,



with $\Delta G^\circ = -0.059 \{pH(\text{lumen}) - (pK_a(\text{Asp}(61)\text{COOH}))\}$. The overall mechanism for proton pumping for the $S_0 \rightarrow S_1$ transition is shown in eq 53.



2. THEORY BEHIND PCET AND EPT

Several recent reviews have been published summarizing advances in theoretical models used to treat PCET reactions.^{7,8,53} For a review of fundamental equations, e.g., Marcus-type and Fermi's golden rule formalisms, we refer the reader to the Introduction (section 1), to these reviews, and to our *Chemical Review* article, "Proton-Coupled Electron Transfer".¹

2.1. Marcus-Type Modeling and Predictions

In the classical Marcus ET theory (section 1.3), the free-energy dependence of k_{ET} on free-energy change, ΔG° , is parabolic with $\ln k_{\text{ET}}$ varying as $\lambda/4 + (\Delta G^\circ/2)(1 + (\Delta G^\circ/2\lambda))$ and the maximum rate constant occurring when $-\Delta G^\circ = \lambda$. λ is the total reorganization energy, both intramolecular and solvent or medium. Parabolic dependences have been observed for ET and PT,⁵⁴ but more complicated behavior is predicted for concerted EPT because of the quantum nature of the proton transfer (section 1.3).

The Hammes-Schiffer group has analyzed the free-energy dependence of the rate constant for EPT, k_{EPT} ,⁵⁵ by utilizing vibronically adiabatic or nonadiabatic electron transfer with the coupled proton transfer treated as an adiabatic process.^{53b,56} For a model system with vibronically nonadiabatic ET, the rate constant reached a maximum when $-\Delta G^\circ = \lambda$. However, for both PT and PCET with quantum effects included for proton transfer, the maximum rate constant did not occur at $-\Delta G^\circ = \lambda$ but rather was significantly shifted to a much larger $-\Delta G$ value, and the inverted parabolic function became unsymmetric (Figure 8).^{54a-c} This was interpreted as a consequence of

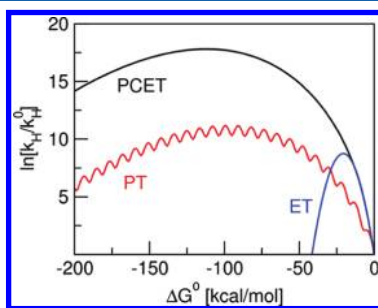


Figure 8. Plot of free-energy dependence versus $\ln(k_H/k_H^0)$, with k_H^0 being the rate constant at $\Delta G^\circ = 0$, for ET, PT, and PCET. See paper by Edwards et al. for parameter details of each model.⁵⁵ Reproduced with permission from ref 55. Copyright 2009 American Chemical Society.

enhanced vibrational wave function overlap between the initial vibronic state and higher vibronic levels in the product energy

surface where vibrational amplitudes are greater toward the energy curves.^{54d} It suggests that very negative ΔG values may be required for experimental observation of an inverted region for PCET and PT.

The dependence of k_{EPT} on ΔG in the "normal region" was explained by the behavior of the vibronic overlap integrals, which cause the rate constant to continue to increase because the excited product states with higher vibrational overlap become accessible. Within this model, the predicted difference in behaviors between ET and PT/PCET is the result of the high-frequency proton mode and a larger shift between the reactant and product proton vibrational wave function. A plausible explanation for this discrepancy between this model and the experimentally observed PT inverted region was given by consideration of oscillations within the PT rate curves (Figure 9), which are predicted to become less observable in

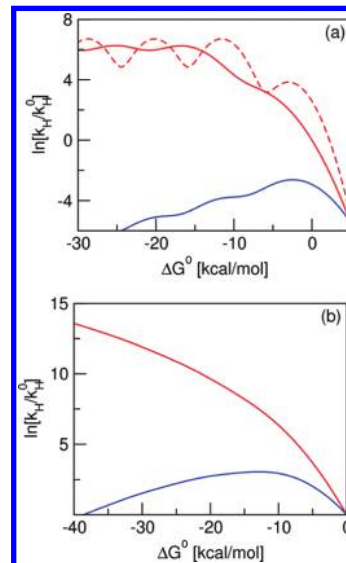


Figure 9. As in Figure 8, plots of $\ln(k_H/k_H^0)$ versus ΔG° for electronically adiabatic (a) PT and (b) PCET models. The red curves correspond to a fixed proton transfer barrier, and the blue curves are from a model based on an increase in barrier as $-\Delta G^\circ$ increases.⁵⁵ In (a), the reorganization energy is 8 kcal/mol for the two solid curves and 3 kcal/mol for the dashed curve. In (b), the reorganization energy is 20 kcal/mol for both curves. Reproduced with permission from ref 55. Copyright 2009 American Chemical Society.

highly polar solvents with large reorganization energies. Alternatively, the driving force could be impacted by the proton donor–acceptor distance, which, as pointed out by Hammes-Schiffer, is highly dependent on the pK_a and bond strength. Incorporation of an increase in intrinsic proton transfer barrier as $-\Delta G$ is increased into an electronic adiabatic PT model then shows inverted region behavior (Figure 9). A similar modification gives the same result for a PCET model curve. In these modified models, there is an initial increase in rate with $-\Delta G$ despite longer proton donor–acceptor distances. When the donor–acceptor distance becomes very large, the rate constant eventually decreases. It was speculated that an inverted region could be observed experimentally for PT and PCET reactions if the driving force changes in a way that also influences the properties of the proton transfer interface.

In PCET reactions two charged particles fluctuate between reaction sites, and the microscopic details of their solvation may

differ. Tully and co-workers have recently outlined a multi-dimensional Marcus approach that uses 3D parabolic functions, rather than the standard 2D functions.⁵⁷ In this treatment the intersection is an infinite line of points, and in order to identify the unique transition state, the free energy must be minimized over the line that connects positions at the negative of the internal energies (Figure 10). The authors also show that, in

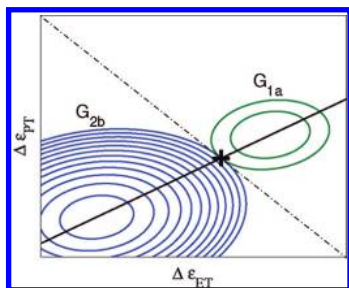


Figure 10. Generalized 2D free-energy surfaces with the transition state along the dash-dotted line. Reproduced with permission from ref 57. Copyright 2008 American Chemical Society.

the limit of linear response by the solvent, the multidimensional problem can be reduced to 1D. For nonlinear solvent response the free energy cannot be obtained by sampling around the minimum with extrapolation of a parabolic function.

2.2. Kinetic Isotope Effect

Using previously derived rate constant expressions for non-adiabatic EPT reactions, Hammes-Schiffer and co-workers recently explored model systems to understand how the proton donor–acceptor distance, solvent reorganization energy, temperature, and driving force affect KIE values.⁵⁸ One surprising finding was that KIEs are virtually unaffected by differences in reorganization energies in the 10–40 kcal/mol range. Their explanation for this was that the magnitude of the KIE does not change monotonically with λ because of changes in relative contributions from higher vibrational levels. KIE values can either increase or decrease with proton donor–acceptor distance. Temperature effects on KIE were found to depend on the magnitude of the quantum spacing for the transfer mode relative to $k_B T$. In the so-called “low-frequency” regime, KIE decreases with increasing temperature as higher vibrational levels are thermally populated in which there are higher vibrational overlaps. In the “high-frequency” limit, EPT is dominated by transitions from the lowest $v = 0$ level and the KIE is temperature-independent. They also showed that both an increase and a decrease in driving force result in asymmetric parabolic functions for the transferring proton, which leads to greater contributions from excited vibrational levels, leading to a maximization of the KIE when the driving force is near zero. Wander and co-workers have utilized Nelsen’s four-point methodology, which involves separate calculation of reorganization energies of oxidants and reductants⁵⁹ to estimate relative barrier heights and isotope effects for Fe^{2+} reduction of superoxide by EPT.⁶⁰

2.3. Electrochemical and Electrode–Solution Interface PCET

In a recent contribution, the Hammes-Schiffer group has derived rate constant expressions for electrochemical proton-coupled electron transfer. They interpolate between the golden rule, nonadiabatic (weak electronic coupling, rapid solvent

relaxation), and solvent-controlled (strong electronic coupling, rate-limiting solvent relaxation) limits.⁶¹

The Hammes-Schiffer group has also recently published two theoretical analyses of PCET reactions at metal electrode–solution interfaces. In one formulation, heterogeneous rate constants and current densities were calculated from transition probabilities.⁶² The expressions that are derived are related to similar results obtained by Savéant and co-workers but with a significant difference in the form of the prefactor.⁶³ In the Hammes-Schiffer treatment, current densities are obtained by integrating over the solute–electrode separation distance, which accounts for long-range electron transfer.

In an alternate formulation, this group has extended the Anderson–Newns–Schmickler Hamiltonian for electrochemical PCET.⁶⁴ This new model Hamiltonian, which is based on the master equations for the reduced density matrix of the electron–proton subsystem, is advantageous because it can describe adiabatic and nonadiabatic electrochemical PCET reactions, potentially even including effects for breaking and forming other chemical bonds.

2.4. HAT versus PCET

Several definitions have been offered to distinguish between HAT and EPT (section 1). The initial suggestion was that HAT be reserved for PCET reactions in which both proton and electron are transferred from the same bond. EPT was used to describe a PCET pathway in which the transferring proton and electron are transferred from different orbitals. Although this distinction is straightforward and useful in most cases, it can be ambiguous and offers no insight into the adiabaticity or nonadiabaticity of the reaction.

Beginning with diabatic representations, it has been proposed that the extent of nonadiabaticity be used as the diagnostic quantity for HAT versus PCET.^{7,8,53} Tishchenko, Truhlar, and co-workers have recently introduced the concept of describing a HAT–PCET continuum in terms of topographic features of the potential energy surfaces and diabatic state coupling, which give insight into the electronic adiabaticity or nonadiabaticity of the reaction.⁶⁵ With strong interactions at the intersection between energy curves defining the reaction pathway, the reaction will be largely nonadiabatic in character. These nonadiabatic surface-crossing events would occur through a small energy gap between the two lowest energy states along the reaction pathway through a conical intersection that lies close to a saddle point.

The saddle point serves as the lowest-energy point on the conventional hypersurface separating reactants from products for the electronically adiabatic HAT mechanism. The minimum-energy crossing point likewise provides a reasonable starting point for estimating the probability of a nonadiabatic reaction. In this diabatic-state description, a large energy difference between the saddle point and the minimum-energy crossing point (conical intersection, CI) results in HAT, whereas a small energy difference is more likely to occur by PCET. Figure 11 depicts a More O’Ferrall–Jencks-type diagram for HAT and PCET regions mapped against the hydrogen nuclear coordinate and the nature of the electronic wave function showing the four extreme limiting mechanisms.

2.5. Electronic Coupling in EPT Pathways

In a series of papers, DiLabio and co-workers have computationally (UB3LYP-DFT calculations) examined and described the iminoxyl/oxime self-exchange reaction (Figures 12 and 13).⁶⁶ Although a transoid (bottom, Figure 13) transition state

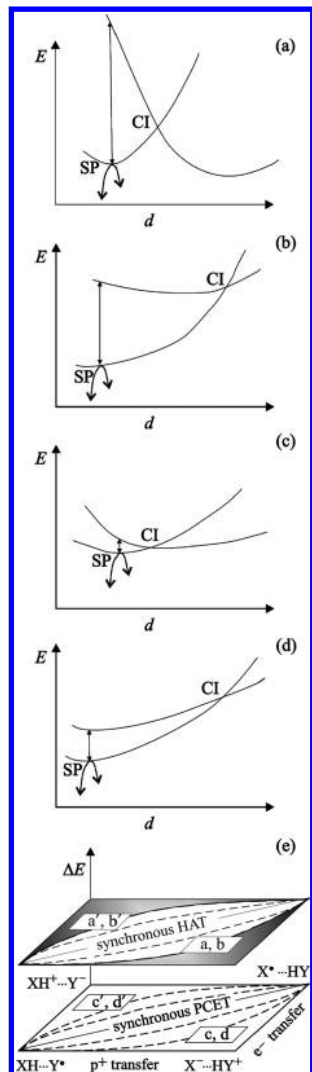


Figure 11. (a–d) Possible relationships between saddle points and CI points involving simultaneous electron and proton transfer. (e) More O'Ferrall–Jencks-type diagram for a possible HAT–PCET continuum. Reproduced with permission from ref 65. Copyright 2008 American Chemical Society.

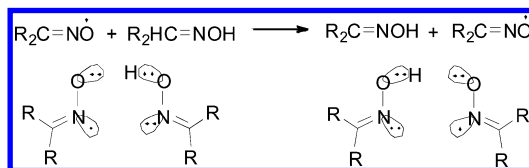


Figure 12. Iminoxyl/oxime self-exchange reaction. Reproduced in part with permission from ref 66. Copyright 2007 American Chemical Society.

minimizes steric and dipole repulsion, the lowest-energy transition state for proton transfer occurs in a cisoid (Figure 12 and top of Figure 13) geometry, attributed to the N–N bonding interaction in HOMO-2 (3-electron–2-center bonding interaction). For the cisoid transition state, the PCET mechanism is described as EPT with proton transfer between oxygen atoms and electron transfer between nitrogen lone pairs (Figure 12). This PCET example, with electron and proton transfer occurring in the same σ -framework, is different from the EPT mechanism for phenoxy/phenol self-exchange. Li et al.

identified a similar EPT pathway in the self-exchange reaction between NO and NOH.⁶⁷ Similarly, a cisoid transition state and EPT have been proposed for the reaction between sulfenic acid peroxy radicals.⁶⁸

DiLabio has also pointed out the importance of lone pair– π and π – π interactions in PCET transition states. For the *tert*-butylperoxy/phenol reaction in Figure 14, this interaction lowers the energy of the cisoid transition state and opens up a new pathway for ET that involves ET from the oxygen lone pair to the phenolic π -system. The benzyl/toluene reaction was also re-examined. By using the UMP2/6-311++G (2d,2p) method, which is capable of describing π – π interactions, DiLabio identified a lower-energy C_2 transition state that is different from the C_{2h} structure identified by Mayer.⁶⁹ Figure 15 shows this C_2 transition state along with the highest occupied molecular orbital (HOMO) and singly occupied molecular orbital (SOMO). The HOMO points to a new bonding overlap between π -systems. DiLabio contends that it is possible for the hydrogen atom to transfer between carbon atoms while ET occurs between π -rings.

For PCET involving peptide bond protons, Chen and Bu used density functional theory (DFT) to study radical exchange between an acylamide unit and its oxidative lesion-generated radical.⁷⁰ Figure 16 shows HOMO and SOMO orbitals for the formamide–formamide radical transition state. The presence of $3\text{e}^- - 2\text{H}^+$ -centered bonding across the oxygen–oxygen interaction points to PCET facilitated by intramolecular charge transfer from oxygen to nitrogen. Lewis acid–water hydrate binding between the oxygen atoms was also shown to influence whether a HAT or PCET mechanism is preferred. High oxidation state metal oxidants that interact strongly promote HAT whereas low oxidation state oxidants that weakly bind favor EPT.

Bu and co-workers have also shown computationally that the reaction of uracil-N3-dehydrogenated radical with uracil proceeds by an EPT mechanism.⁷¹ Here again, complexation of bridging hydrated Lewis acid metal ions can alter the orbital that the transferring electron occupies and change the lowest energy pathway from EPT to HAT.

O'Malley and co-workers have utilized the B3LYP DFT functional to explore transition states for the reaction of substituted phenols with hydroperoxy radical. On the basis of low atomic volumes and high hydrogen atom charge, it was concluded that these reactions are better described as EPT than HAT.⁷²

2.6. Photochemical EPT

It has been proposed by de Lucas and co-workers that photochemically induced, excited-state hydrogen transfer between isopropyl alcohol and *ortho*-quinones proceeds by EPT.⁷³ To provide computational support for the suggestion, these authors also studied radical reactions of *t*-butoxyl and methyl radicals with isopropanol by application of Bader's atoms-in-molecules theory. They found that the transferring hydrogen atom had unique properties in EPT transition states compared to HAT transition states. For example, in HAT transition states, the transferring hydrogen atom has a significantly larger (roughly 50%) atom volume, significantly reduced charge, and more spherical charge distribution. Because the properties of the reaction between *t*-butoxyl radical and isopropyl alcohol were related to reactions involving *ortho*-quinones, it was classified as EPT.

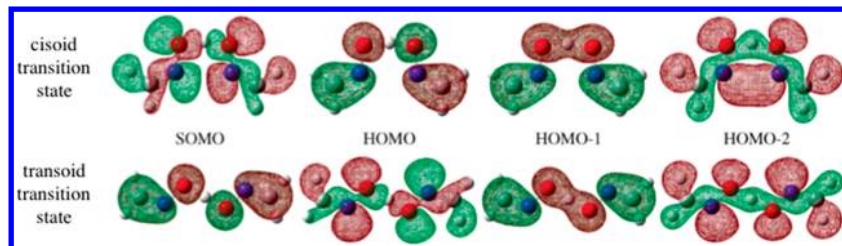


Figure 13. Transition-structure molecular orbitals for iminoxyl/oxime self-exchange by EPT. Reproduced with permission from ref 66. Copyright 2005 American Chemical Society.

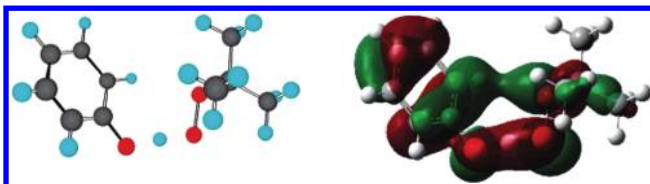


Figure 14. Transition state and HOMO orbital for *tert*-butylperoxy/phenol hydrogen atom transfer. Reproduced with permission from ref 66. Copyright 2007 American Chemical Society.

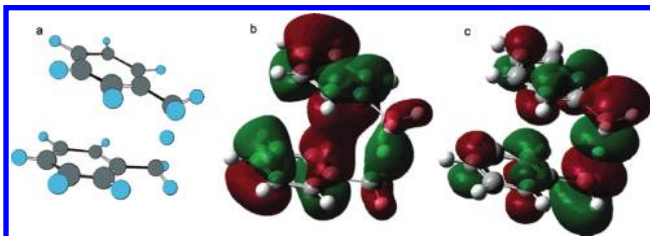


Figure 15. C₂ transition state and orbitals for benzyl/toluene hydrogen transfer. Reproduced with permission from ref 66. Copyright 2007 American Chemical Society.

Because photoinduced EPT reactions are nonequilibrium processes, the Hammes-Schiffer group has recently developed a model based on the reduced density matrix formalism that allows for studying the time evolution of electronic states after photoexcitation with the accompanying proton vibrational dynamics.⁷⁴ This model has also been extended to describe the dynamics of photoinduced EPT reactions at semiconductor interfaces.⁷⁵ Their model is designed for application to photoexcited dye molecules at semiconductor surfaces or photoexcitation from semiconductor band defects to a molecular adsorbate overlayer.

2.7. Biological Systems

Kramer and co-workers recently found that oxidation of ubiquinol by cytochrome *bc*1 and biomimetic models demonstrate an increase in KIE with temperature with $\Delta G_{(H)}^\ddagger < \Delta G_{(D)}^\ddagger$. Plastoquinol oxidation does not show this novel behavior with KIE decreasing with temperature.⁷⁶ Spurred by this experimental result, Yamamoto and Kato utilized QM/MM methodology to study the EPT reaction of an ubiquinol analogue (2,3-methoxyl 5,6-methyl *p*-benzoquinol) with phenoxy radical in acetonitrile.⁷⁷ The V representation, with

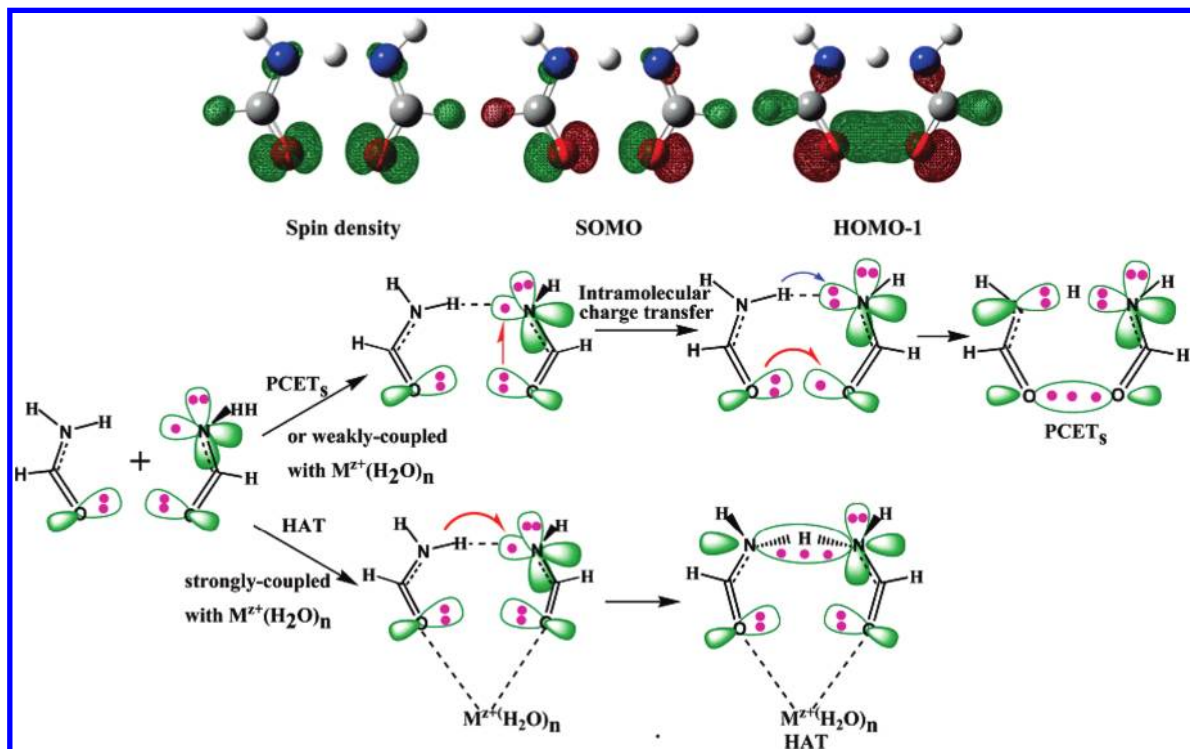


Figure 16. Transition states and orbital interactions for formamide–formamide radical EPT and HAT pathways. Reproduced with permission from ref 70. Copyright 2007 American Chemical Society.

V being the solvent electrostatic potential represented as a collective solvent variable, gives the free energy as a function of nuclear coordinates and external potential. On the basis of an approximate transition state located by estimating the minimum free-energy crossing point in reduced coordinate and V space, the KIE was approximated by application of a transition state-like theory. They concluded that a stiffer proton potential in the transition state may be responsible for this unique experimental KIE.

Subsequently, Hammes-Schiffer and co-workers used numerical modeling in conjunction with approximate proton potentials generated from truncated quantum chemical calculations on metal-to-ligand charge transfer (MLCT) excited-state oxidant $[\text{Ru}(\text{bpy})_2(\text{pbim})]^{*+}$ ($\text{pbim} = 2-(2\text{-pyridyl})\text{benzimidazolate}$) in its reaction with 2,3-dimethoxy-5-methyl-1,4-benzoquinol (UQH_2) and 2,3,5-trimethyl-1,4-benzoquinol (PQH_2).⁷⁸ They concluded that the KIE for UQH_2 could be explained by invoking a stiff hydrogen bond, small inner sphere, and solvent reorganization energies, with the $0 \rightarrow 0$ reactant/product vibronic transition occurring in the inverted region and the $0 \rightarrow 1$ transition occurring in the normal region and being rate-controlling. In this model, the KIE temperature dependence was explained as arising due to the rate being dominated by the UQH_2 $0 \rightarrow 1$ vibronic transition. In the PQH_2 reaction, multiple vibronic transitions contributed significantly to the rate constant.

Kumar and Kozlowski have carried out DFT (BP86 and B3LYP) calculations on model systems of the active site of methylmalonyl CoA mutase and glutamate mutase enzymes.⁷⁹ These calculations suggest that a tyrosine residue acts as a redox center by EPT to facilitate Co–C bond cleavage. Yanai and Mori have utilized UB3LYP Kohn–Sham orbitals to suggest that in the isomerization of prostaglandin H₂ to prostacyclin catalyzed by cytochrome P450 the isomerization proceeds through EPT.⁸⁰

By use of a 3-(5-imidazolyl)propionylhistamine ligand model for the His13His14 section of the amyloid β peptide ($\text{A}\beta$),⁸¹ Hewitt and Rauk have proposed that EPT occurs during the catalytic production of H_2O_2 by a Cu(II) complex with $\text{A}\beta$. The proposed cycle is shown in Figure 17. In the first step, a Cu(II)

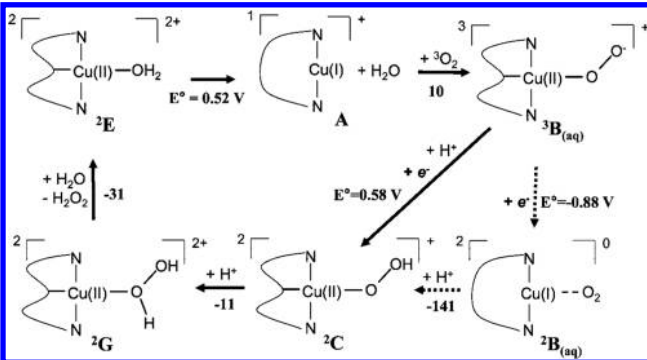


Figure 17. Proposed mechanism for H_2O_2 production from a model $\text{Cu}(\text{II})\text{A}\beta$ and $^3\text{O}_2$. Reproduced with permission from ref 81. Copyright 2009 American Chemical Society.

aqua complex (^2E) is reduced by an external reagent, such as ascorbate or glutathione with $E^\circ = 0.52$ V followed by water displacement and reaction with triplet oxygen to give ^3B , a Cu(II) superoxide depicted in Figure 17. From this intermediate, stepwise reduction and protonation require a

low reduction potential $E^\circ (^3\text{B}/^2\text{B}) = -0.88$ V, and the more favorable EPT route occurs with $E^\circ = 0.58$ V. After EPT a second protonation step and water displacement of hydrogen peroxide regenerate the catalytic species, ^2E .

Yoshioka and co-workers have analyzed the mechanism of two-electron oxidation of ubiquinol (UQH_2 , but modeled as hydroquinone) by cytochrome bc_1 complex.⁸² DFT modeling of an energy scan along the hydrogen–nitrogen forming bond shows that a proton is first transferred from QH_2 to anionic Glu272 followed by EPT to form the NH bond and reduce the Fe center, giving the quinone radical anion (Figure 18). After

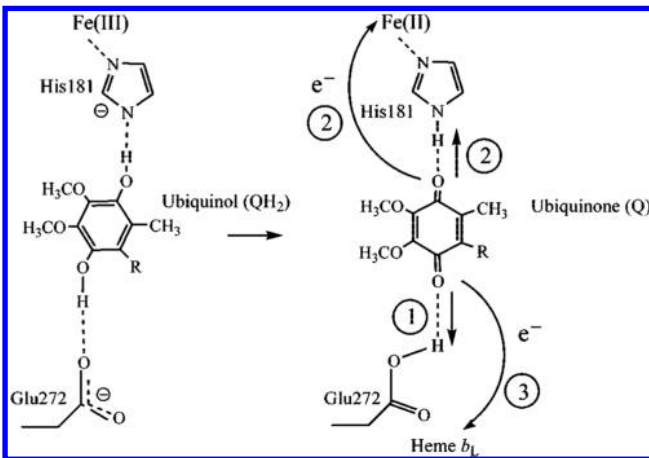


Figure 18. Schematic representation of predicted mechanism of oxidation at the Q_p site. Reproduced with permission from ref 82. Copyright 2008 American Chemical Society.

this process, the quinone radical anion transfers an electron to the heme b_L . Evidence for EPT is shown in the change in the SOMO along the reaction path scanned (Figure 19). In the approximate transition state the SOMO is delocalized over the quinone and [2Fe–2S] motifs.

Shaik and co-workers have postulated that an EPT pathway initiates the C–C bond reaction in the transformation of chromopyrrolic acid (CPA) to staurosporine catalyzed by P450 StaP.⁸³ They utilized DFT in a QM/MM investigation and found that electron transfer from CPA^{2-} , in which the two carboxylic acid groups of CPA are deprotonated, occurs to the iron–oxo center of Compound I (Cpd I) with simultaneous water–histidine–water-bridged shuttling of the NH proton. This step was found to have a lower barrier than the first C–C bond formation (see Figures 20 and 21).

EPT has also been implicated in the O–O bond-cleavage mechanism in formation of Cpd I, the active form in the chloroperoxidase enzyme, a hydrogen peroxide complex, $\text{Fe}^{\text{III}}-\text{HOOH}$. In addition, EPT is predicted, by QM/MM calculations, to occur in the arginine hydroxylation pathway of nitric oxide synthase.⁸⁴

There are several other noteworthy theory-based studies of biological reactions. Tureček et al. have carried out theoretical studies on peptide cations;⁸⁵ Iyengar et al. have studied EPT reaction tunneling in enzymes;⁸⁶ dos Santos et al. have also studied 2,2-diphenyl-1-picrylhydrazyl (DPPH) and 4-hydroxy-2,2,6,6-tetramethylpiperidene-1-oxyl (TEMPO);⁸⁷ and, Young et al. have studied amide–carboxylic acid reactions.⁸⁸ Lastly, Heinze and co-workers have also used DFT to propose a concerted EPT pathway in a biomimetic molybdenum oxotransferase analogue.⁸⁹

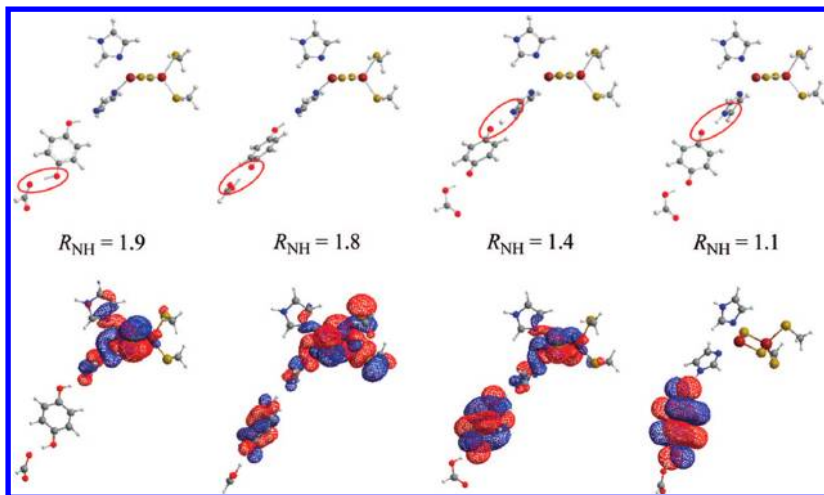


Figure 19. Change in SOMO along the NH bond-forming reaction path for oxidation of hydroquinone by cytochrome *bc*₁ complex in complex III. R_{NH} corresponds to the N-H distance in Å. The transition state corresponds to $R_{\text{NH}} = 1.4$. Reproduced with permission from ref 82. Copyright 2008 American Chemical Society.

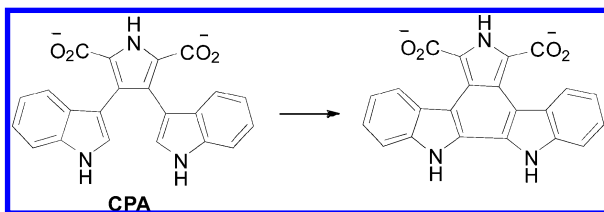


Figure 20. Initial C-C bond formation in CPA catalyzed by P450 StaP (CYP24SA1).

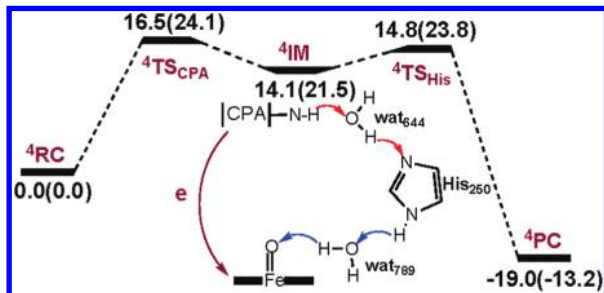
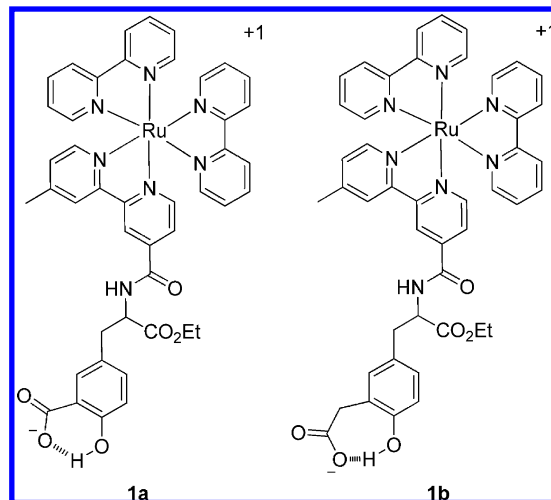


Figure 21. QM/MM reaction profile for EPT in CPA. Reproduced with permission from ref 83b. Copyright 2008 American Chemical Society.

2.8. Combined Theory and Experiment

The effects of internal hydrogen bonding on EPT rates were explored in Ru^{II}(bpy)-tyrosine complexes **1a** and **1b** (Scheme 13). Please note that a variety of experiments related to tyrosine oxidation will be described in section 8.2. In these particular complexes a phenolic proton is hydrogen-bonded to an internal carboxylate group.³⁸ In **1a** the carboxylate group was directly attached to the aromatic ring whereas in **1b** there was a methylene linker. Intramolecular EPT oxidation of the tyrosine group following oxidative quenching of the MLCT excited states was monitored by transient absorption measurements. From temperature-dependent measurements, E_a was ~5 kJ/mol higher for **1a** than for **1b**. The computed hydrogen-bond strengths with B3LYP/6-311++G(d) with a polarizable continuum (PCM) solvation model showed that the hydrogen bond in **1a** is weaker than that in **1b**. Numerical modeling of the kinetic data clearly showed the necessity of incorporating

Scheme 13



promoting vibrations (vibrational modes that decrease the proton transfer distance) to satisfactorily fit the experimental data. These vibrations were also responsible for significantly lowering the KIE from ~40 without intervention of the promoting vibration to 2–3. In contrast to other proposals,^{14b,90} Johannissen et al. propose that a weaker hydrogen bond in **1a** leads to a rate enhancement due to softer promoting vibrations with shorter average proton-tunneling distance and strong proton coupling. The origin of the lower rate for EPT in **1a** is the lower carboxylic acid pK_a value, which creates a smaller driving force. These authors also suggest a distinction between short, strong, and stiff hydrogen bonds with proton tunneling facilitated by short hydrogen bonds. Strong hydrogen bonds are, in general, also stiffer, which reduces the effect of promoting vibrations.

The multiple pH-dependent redox couples for Ru(Q)(tpy)-(OH₂)²⁺ (Q = 3,5-di-*tert*-butyl-1,2-benzoquinone; tpy = 2,2':6',2''-terpyridine), which is a monomeric model complex for the “Tanaka dimer” water oxidation catalyst, have been characterized, and formal oxidation states have been assigned by applying electronic structure theory. The results of a theoretically derived Pourbaix ($E_{1/2}$ -pH) diagram were in good

agreement with experimental data (Figure 22), and the technique may be useful in assigning redox couples in even more convoluted Pourbaix diagrams.⁹¹

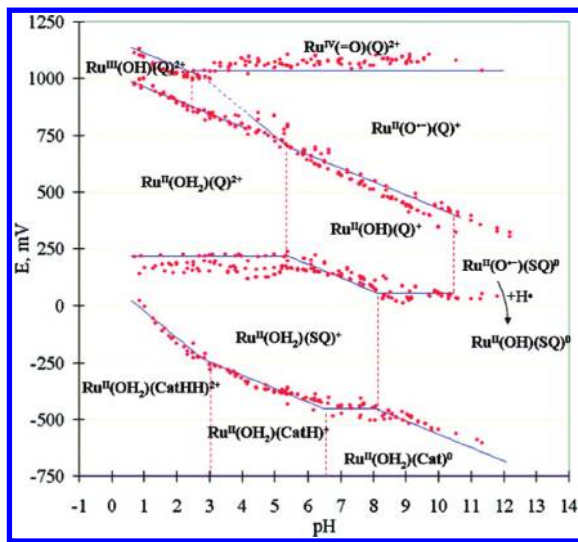


Figure 22. Experimental and theoretical Pourbaix diagram for $\text{Ru}(\text{OH}_2)(\text{Q})^{2+}$ as $E_{1/2}$ values relative to the SCE. The red dashed and solid blue lines correspond to the experimental pK_a and redox potentials. The abbreviation “Cat” stands for catecholate, the reduced form of Q. Reproduced with permission from ref 91. Copyright 2009 American Chemical Society.

The two-electron oxidation of 2-[6-(4'-amino)phenoxy-3H-xanthen-3-on-9-yl]benzoic acid (APF) gives fluorescein and *p*-benzoquinone by reaction with NO_2 and CO_3 radicals. Wong and co-workers utilized MPW1K computations to show that EPT may occur in the first oxidation step in the reaction of APF with NO_2 radical to give HONO.⁹² Borden and co-workers have also established the superiority of MPW1K methodology for computing energies of PCET reactions compared to the popular B3LYP method.⁹³

3. ORGANIC PCET

3.1. Phenols

Interest in phenols stems from their extensive role as PCET reagents including tyrosine in PS II, as flavonoids and their role

as biological antioxidants, and as radical traps in industrial processes. Recent theoretical⁹⁴ and electrochemical⁹⁵ studies of phenols have appeared, but this section will focus on chemical reactions.

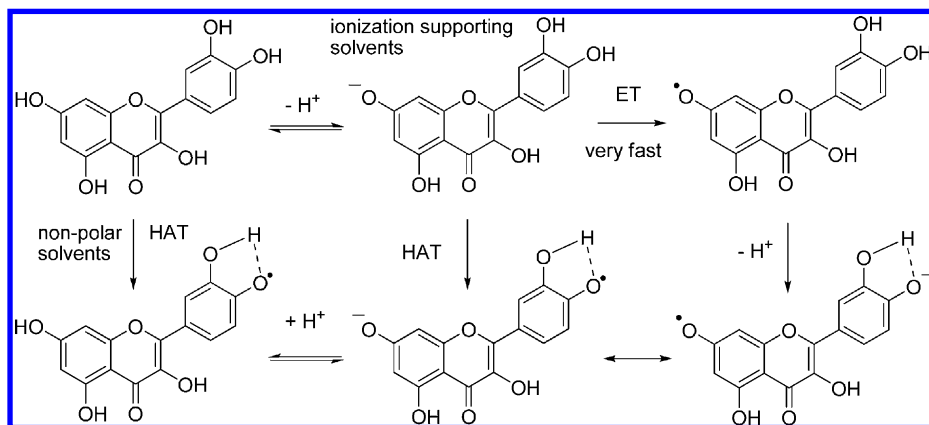
3.1.1. Reactions of Phenols with H-atom Abstractors.

From the results of kinetic and mechanistic studies on what are regarded as hydrogen atom abstraction reactions from a variety of phenols⁹⁶ and flavonoids⁹⁷ by 2,2-diphenyl-1-picrylhydrazyl radical (dpph^\bullet shown in Scheme 14), three distinct and, in some cases competitive, pathways have been invoked: HAT, EPT, and PT-ET. Structure–acidity and structure–activity relationships for 10 flavonoids were explored, and the results show that it is not possible to correlate phenol acidity with rates without considering the solvent. Mechanism and lowest-energy pathway are governed by (i) the hydrogen-bond-accepting and anion-solvating abilities of solvents, (ii) the electron affinities and bond-dissociation enthalpies of the initial radicals, and (iii) the electronic influence of the phenol ring substituents. Changes in these parameters can alter reaction mechanism from coupled (HAT, EPT) to sequential (PT-ET). For example, hydrogen atom abstraction from quercetin by dpph^\bullet (Schemes 14 and 15) occurs by HAT in nonpolar solvents. In polar solvents, enhanced rates are observed and attributed to simultaneous contributions from HAT and PT-ET.

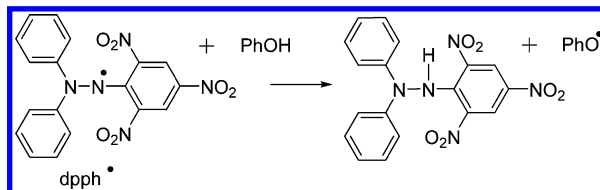
Solvent dependence is manifested in the reactivity of peroxy radicals with phenols in ionizable solvents, depicted in Scheme 16. A 16-fold increase in the reactivity of peroxy radical with a phenol derivative was observed upon the addition of acid and attributed to preprotonation of the peroxy radical cation, HOOH^+ , which is easier to reduce. There may be implications for this reactivity in the role of acid in increasing the efficiency of the antioxidant properties of phenols with possible industrial applications.⁹⁸

The ubiquitous bioreductant, ascorbic acid or vitamin C, functions as a redox cofactor that is oxidized to ascorbyl radical and then to dehydroascorbate. On the basis of thermodynamic and kinetic results, ascorbate oxidation by nitrosobenzene appears to occur by EPT. From a square-scheme analysis, PT-ET and ET-PT would have minimum activation energies of 121.5 kJ/mol and 73.8 kJ/mol, respectively, both of which are significantly higher than the experimentally determined value of 53.3 kJ/mol. A relatively low KIE of 2.20–2.63 was calculated for a concerted mechanism, but observed enthalpies and entropies of activation differ from expected semiclassical values,

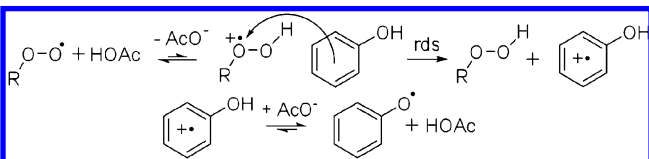
Scheme 14. Possible Mechanisms for Quercetin Oxidation by dpph Radicals^a



^aAdapted with permission from ref 97. Copyright 2009 American Chemical Society.

Scheme 15. HAT Oxidation of a Phenol by dpph^{\bullet} ^a

^aAdapted with permission from ref 97. Copyright 2009 American Chemical Society.

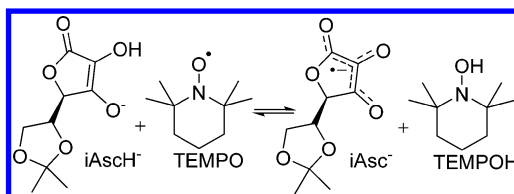
Scheme 16. Proposed Mechanism for Acid-Catalyzed Oxidation of Phenols by Peroxyl Radicals; Rds is Rate-Determining Step^a

^aAdapted with permission from ref 98. Copyright 2009 Wiley.

suggesting that proton transfer occurs by tunneling. A large increase in KIE from 2.4 in water to 9.6 in a 1:1 mixture of water and dioxane was observed.⁹⁹

This same effect was observed for the oxidation of ascorbate by 2,2,6,6-tetramethylpiperidinyl-1-oxy (TEMPO) radical but with an even larger KIE. The kinetic isotope effect at 298 K is 24.2 in water and increases to 31.1 in a 1:1 mixture of water–dioxane. Temperature-dependent studies were performed showing a range of KIEs from 27.3 at 285.4 K to 19.1 at 317.4 K in water and from 34.3 to 24.6 at the same temperatures in a 1:1 water–dioxane mixture. Additionally an isotope effect was observed in both the Arrhenius prefactor and the enthalpy of activation in the two-solvent systems.¹⁰⁰

Ascorbyl radicals can also be generated in EPT oxidation of ascorbate by phenoxy or nitroxyl radicals, as shown in Scheme 17, and are stable for hours in anhydrous acetonitrile. A

Scheme 17. Mechanism of Oxidation of an Ascorbic Acid Derivative to Ascorbyl Radical by the Nitroxyl Radical TEMPO ($i\text{AscH}_2$ Is an Organic Soluble Analogue of Ascorbic Acid)^a

^aAdapted with permission from ref 101. Copyright 2008 American Chemical Society.

thermodynamic analysis shows that free-energy changes for PT-EPT (40 kcal mol⁻¹) and ET-PT (35 kcal mol⁻¹) are significantly higher than the observed value of 13 kcal mol⁻¹.¹⁰¹

3.1.2. Reactions between Oxidant and Pendant Base. Hammarström and co-workers studied the MS-EPT reactions of phenols with a pendant carboxylate group, depicted below in Figure 23. This system acts as a model to understand the reaction dynamics in enzymes that utilize hydrogen-bond interactions to access low-energy pathways. Oxidation was

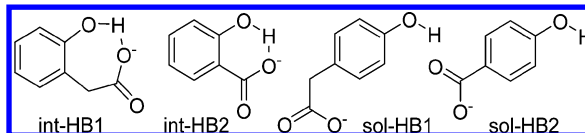


Figure 23. Structure of the substituted phenols in their carboxylate forms.

initiated photochemically by oxidative quenching of $\text{Ru}(\text{bpy})_3^{2+*}$ by methyl viologen, giving $\text{Ru}(\text{bpy})_3^{3+}$. The Ru(III) complex oxidizes the phenol with the proton either transferred to the solvent or a pendant carboxylate depending on structure. The rate of the reaction is pH-dependent when water acts as the proton acceptor, but in phenol derivatives with an internal hydrogen bond there was no pH dependence. The KIE was 2.1 with water acting as a base for sol-HB1 and sol-HB2, but for compounds with an internal hydrogen bond, the KIE fell to 1.6 and 1.2 for int-HB1 and int-HB2, respectively.^{14b}

In a series of papers, Mayer and co-workers examined the role of driving force and of the structure of pendant amine bases on MS-EPT oxidation. The study was conducted on phenol derivatives generated either electrochemically or with one-electron chemical oxidants (Figure 24). Concerted electron–proton transfer was

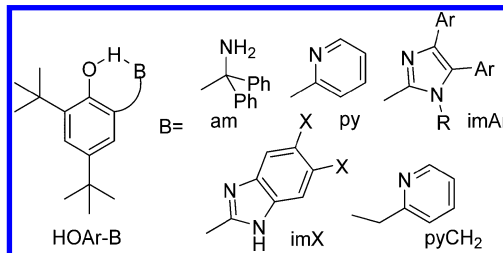


Figure 24. Structure of 4,6-di-tert-butylphenol with a variety of prepositioned bases.^{90,102}

inferred based on the magnitude of primary KIEs, which ranged from 1.6 to 2.8 for compounds HOAr-am and HOAr-py, and ΔG^\ddagger values less than ΔG^o values for formation of competing ET or PT intermediates. While the application of the “Marcus equation” to EPT reactions has been suggested, the quantum nature of MS-EPT requires a modified Marcus treatment with the proton transfer treated quantum mechanically; see section 2.^{90a}

Rate constants for oxidation of a series of substituted 4,6-di-tert-butyl-2-(4,5-diarylimidazolyl)phenols and related benzimidazole compounds (HOAr-imAr, HOAr-imX) by chemical oxidants were measured. This work supports the observations of Fecenko et al., showing that the driving force is the dominant factor determining the rate. It follows that, to reach conclusions about tunneling or intrinsic barriers based on structure or substituent comparisons, the driving force of the reactions must be nearly the same or taken into account.^{15,102}

The rate constant for EPT oxidation of the conjugated phenol pyridine derivative, HOAr-py, in acetonitrile by chemical oxidants was ~100 times faster than the amine analogue, HOAr-am, with a similar driving force. The rate constant for oxidation of a pyridine base with a methylene spacer, HOAr-pyCH₂, was comparable to HOAr-am, suggesting an important role for conjugation in EPT.^{90b}

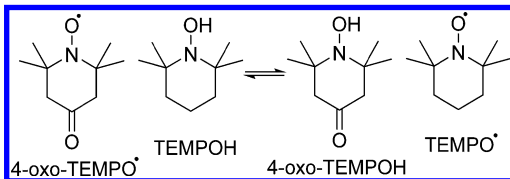
3.2. Other

3.2.1. Amines. Oxidation of 4-X-substituted *N,N*-dimethylanilines (X = OMe, OPh, CH₃, H) by dpph^{\bullet} leads to

N-demethylation of the *N,N*-dimethylaniline. Rate constants correlated with the electron-donating ability of the substituent. On the basis of intramolecular and intermolecular KIE effects, ranging between 2.8 and 4.0 and 2.9–3.6, respectively, the reaction likely proceeds by HAT through the N–C–H bond to dpph[•].¹⁰³

3.2.2. Hydroxylamines. Mayer and co-workers studied the role of tunneling in pseudo-self-exchange kinetics for HAT in several hydroxylamines based on TEMPO derivatives, as depicted in Scheme 18, in MeCN or CH₂Cl₂ at 298 K. For

Scheme 18. Pseudo-Self-Exchange Reaction Based on TEMPO Derivatives^a



^aAdapted with permission from ref 104. Copyright 2009 American Chemical Society.

dialkylhydroxylamine self-exchange, KIEs of 21–23 ± 4 are observed in marked contrast to arylhydroxylamines. The latter have lower free energies of activation, by 9–10 kcal mol^{−1}, have KIE values < 2, and may involve ET-PT. The barrier for arylhydroxylamines is lower, and as a result they react more rapidly with tunneling playing a smaller role.¹⁰⁴

3.2.3. Debromination of 8-Bromopurine. The mechanisms of debromination of 8-bromoguanosine (8BG) and 8-bromoxanthosine (8BA) were studied by reduction of the corresponding 8-bromopurine by pulse radiolysis and by hybrid meta DFT calculations. It was found that the charge on the parent bromopurine dictates the reaction pathway. As shown in Figure 25,

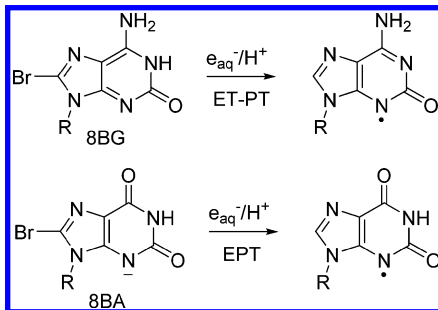


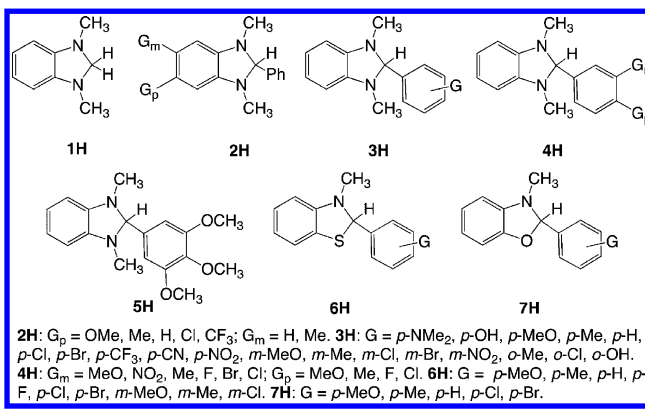
Figure 25. Reaction pathway for the debromination of 8-bromopurines (8BG is 8-bromoguanosine and 8BA is 8-bromoxanthosine). Adapted with permission from ref 105. Copyright 2010 American Chemical Society.

the neutral compounds 8BG and the protonated form of 8BA favor sequential ET-PT but anionic 8BA undergoes a concerted EPT step to avoid a high-energy dianion.¹⁰⁵

3.3. Heterocycles as H-atom Donors

Enthalpy values for electron transfer, proton transfer, HAT, and hydride transfer in acetonitrile for a family of 47 five-membered heterocycles, shown in Scheme 19, were tabulated with data derived from titration calorimetry, electrochemistry, and Hess' law. The change in enthalpy, evaluated by relative thermodynamic cycles, ranged from 71.8 to 91.4 kcal/mol for HAT from

Scheme 19. Structures of the Heterocycles^a



^aReproduced with permission from ref 106. Copyright 2008 American Chemical Society.

neutral donors and from 27.2 to 52.4 kcal/mol for the oxidized forms. The library of heterocyclic data provides a useful thermodynamic reference for future studies.¹⁰⁶

4. PCET INVOLVING METAL COMPLEXES

The essential role of PCET in important bioenergetic reactions, often involving metalloenzymes, is well-documented. Examples include hydrogen oxidation in hydrogenase, nitrogen fixation in nitrogenase, oxygen reduction in cytochrome *c* oxidase, and water oxidation to oxygen in PSII that are reviewed in section 8. Studies on biomimetic metal complexes have been used to approximate the reactive sites in these elaborate enzymes. Recent notable examples in the PCET literature that will not be elaborated here include a Mo model complex used to probe the mechanism of sulfite oxidase¹⁰⁷ and a review on structure/reactivity relationships in Mo and W enzymes.¹⁰⁸

4.1. Oxidation Catalysis

4.1.1. Water Oxidation. Photosystem II is the archetype for water oxidation, but synthetic examples of water oxidation catalysts have appeared based on Ru, Mn, and Ir metal complexes, polyoxometallates, and nanoparticle/films of Co₂O₃, IrO₂, and In₂O₃. A series of recent reviews have appeared that cover this rapidly evolving area.¹⁰⁹

Of relevance to the Mn-based Mn₄Ca cluster in PSII, Magnuson et al. examined structure–property relationships for several dinuclear Mn complexes (Mn–N₃O₃ and Mn–N₂O₄), depicted in Figure 26, that model the dimer of dimers structure in the oxygen-evolving complex. Structural variations in the bridge occurred with successive oxidations, and in both cases μ -oxo bridging occurred near 1 V versus SCE. This may be relevant to PSII because it prevents large overpotentials from building up as multiple oxidative equivalents required for oxygen evolution are accumulated.¹¹⁰ In complex Mn–N_{2.5}O_{3.5}, redox potential leveling was also observed, but the effect has a different origin. In this case the acetate ligands dissociate in water and are replaced with aqua ligands. Subsequent deprotonation of the aqua ligands decreases the difference between successive oxidation potentials by avoiding charge buildup. Oxidation was driven by photosensitized oxidation of the MLCT excited state of Ru(bpy)₃²⁺. Ligand variations were used to tune potentials and stabilize high Mn oxidation states in the dimers while retaining the oxidative strength for water oxidation.¹¹¹

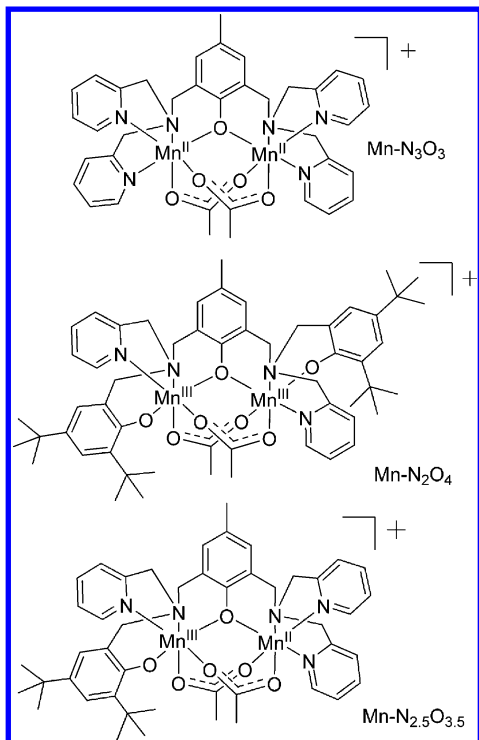


Figure 26. Structure of model Mn clusters of the oxygen-evolving complex. Adapted with permission from refs 110 and 111. Copyright 2006 American Chemical Society and 2006 Wiley.

Theoretical results on the mixed-valence, μ -oxomanganese complex $[(\text{bpy})_2\text{Mn}^{\text{III}}(\mu\text{-O})_2\text{Mn}^{\text{IV}}(\text{bpy})_2]^{3+}$, depicted in Figure 27, by B3LYP DFT correlate well with experimental

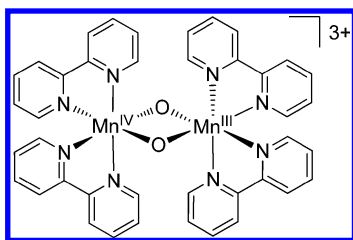


Figure 27. Structure of the mixed-valence μ -oxo-manganese complex $[(\text{bpy})_2\text{Mn}^{\text{III}}(\mu\text{-O})_2\text{Mn}^{\text{IV}}(\text{bpy})_2]^{3+}$.

results with drastic changes in pK_a occurring between oxidation states. The pK_a of the Mn(III)–Mn(IV) dimer changes from near 2 to \sim 12 upon reduction to Mn(III)–Mn(III).¹¹²

The blue Ru dimer, *cis,cis*- $[(\text{bpy})_2(\text{H}_2\text{O})\text{Ru}^{\text{III}}\text{ORu}^{\text{III}}(\text{H}_2\text{O})-(\text{bpy})_2]^{4+}$, was the first designed water oxidation catalyst. It utilizes PCET with combined electron–proton loss to avoid charge buildup to reach its highest oxidation state, $[(\text{bpy})_2(\text{O})\text{Ru}^{\text{V}}\text{ORu}^{\text{V}}(\text{O})(\text{bpy})_2]^{4+}$. This high-energy intermediate then undergoes rapid O-atom transfer to water to give a peroxidic intermediate. Electronic structure and the results of theoretical calculations on the blue dimer are discussed elsewhere.¹¹³ Continuing work on the characterization of intermediates and deactivation pathways is being actively pursued in the Meyer and Hurst groups.¹¹⁴

The Ru–Hbpp dimer shown in Figure 28 undergoes a series of oxidations from the initial Ru(II)–Ru(II) form to the catalytically active Ru(IV)–Ru(IV) bisoxo form. Unlike the blue dimer, the mechanism proceeds predominately through intramolecular

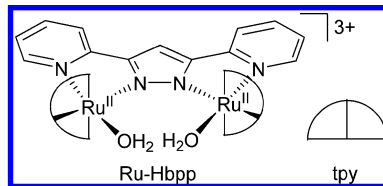


Figure 28. Structure of the Ru–Hbpp dimer water oxidation catalyst.

oxygen–oxygen bond formation instead of by nucleophilic water attack. This mechanism is supported by a combination of kinetics, oxygen-labeling experiments, and DFT calculations.¹¹⁵

A detailed mechanistic analysis of blue dimer oxidation led to the recent development of single-site water oxidation catalysts.¹¹⁶ Catalysis of Ce(IV) water oxidation by Ru(tpy)–(bpm)(H₂O)²⁺ and Ru(tpy)(bpz)(H₂O)²⁺ (ligand abbreviations are shown in Figure 29) was investigated by a detailed

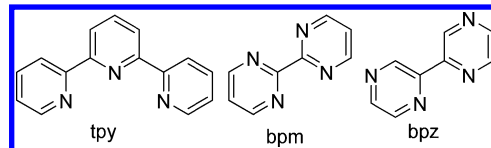
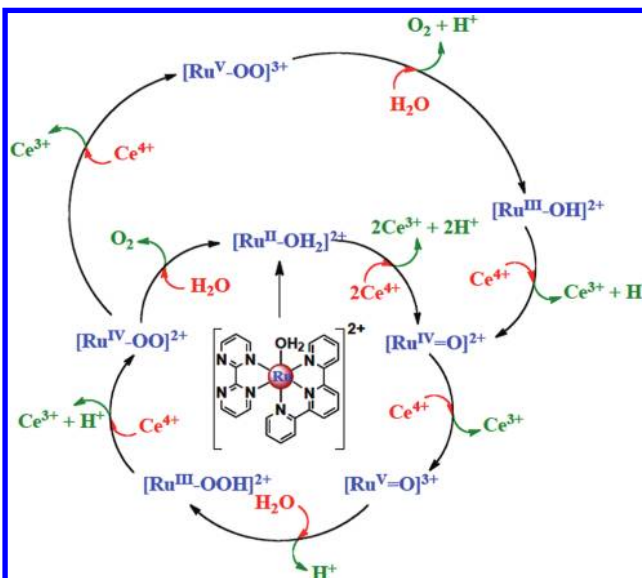


Figure 29. Polypyridyl ligands.

kinetic and mechanistic analysis including DFT calculations on key intermediates.^{117,118} A systematic report of water oxidation by monomeric Ru complexes was given by Thummel and co-workers,¹¹⁹ and the Berlinguette group studied the effects of electron-donating and -withdrawing substituents on the rate and stability of Ru(tpy)(bpy)(H₂O)²⁺ derivatives.¹²⁰

Oxidative activation of these monomeric complexes occurs by PCET with stepwise oxidation of Ru^{II}–OH₂²⁺ to Ru^{IV}=O²⁺ through Ru^{II}–OH²⁺ without an increase in charge (Scheme 20).

Scheme 20. Proposed Single-Site Water Oxidation Mechanism^a

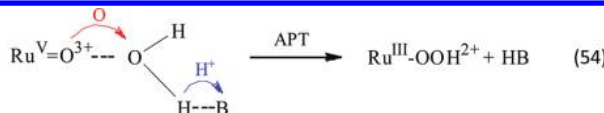


^aReproduced with permission from ref 29. Copyright 2010 American Chemical Society.

Further 1e⁻ oxidation to Ru^V=O³⁺ is followed by O-atom attack on solvent H₂O and O–O bond formation with additional loss of

a proton to solvent to give $\text{Ru}^{\text{III}}-\text{OOH}^{2+}$. Further oxidation of the peroxidic intermediate occurs by PCET to give $\text{Ru}^{\text{IV}}(\text{OO})^{2+}$ with parallel pathways leading to oxygen evolution. In one, dioxygen is displaced by H_2O in $\text{Ru}^{\text{IV}}(\text{OO})^{2+}$ to regenerate $\text{Ru}^{\text{II}}-\text{OH}_2^{2+}$. In the other, $\text{Ru}^{\text{IV}}(\text{OO})^{2+}$ is further oxidized to $\text{Ru}^{\text{V}}(\text{OO})^{3+}$, which rapidly loses oxygen to give $\text{Ru}^{\text{III}}-\text{OH}^{2+}$, reentering the catalytic cycle.

In a further electrochemical mechanistic study, a pathway for water oxidation was identified that was first order in added proton-acceptor base— H_2PO_4^- , OAc^- , and HPO_4^{2-} .³⁰ The appearance of this pathway was attributed to a concerted process with O-atom transfer to a water molecule occurring simultaneously with proton transfer to a H-bonded base molecule (eq 54). This pathway was



termed “atom-proton transfer” (APT) by analogy with EPT for concerted electron–proton transfer.

Rate enhancements of up to 1400 were observed with HPO_4^{2-} as the acceptor base. A DFT-molecular mechanics calculation concluded that even water can act as the proton-acceptor base with $B = \text{H}_2\text{O}$ in eq 54. KIEs from 2.3 for HPO_4^{2-} as base to 6.6 for H_2O were observed with the trend consistent with greater proton transfer distances as the base strength decreases. The appearance of APT as the dominant pathway in water oxidation is attributable to avoidance of a high-energy peroxide intermediate, $\text{Ru}^{\text{V}}=\text{O}^{3+} + \text{H}_2\text{O} \rightarrow \{\text{Ru}^{\text{III}}-\text{OOH}_2^{3+}\}$.

The development of new catalysts has been rapid since this breakthrough with an extensive series of monomeric Ru aqua complexes with one tridentate and one bidentate ligand synthesized and characterized as catalysts. The general mechanism described above appears to be applicable to the series with water oxidation rates varying systematically with ligand-tuned redox potentials, in particular, with E°' values for $\text{Ru}^{\text{V}/\text{IV}}$.^{117,118,121}

An alternate pathway for water oxidation has been suggested for the seven-coordinate complex $\text{Ru}^{\text{IV}}(\text{L})(\text{pic})_2(\text{OH})^+$ shown in Figure 30. The complex has been characterized by X-ray

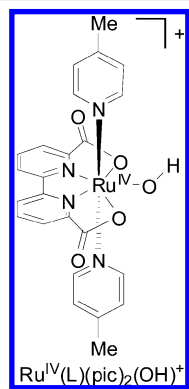


Figure 30. Structure of seven-coordinate $[\text{Ru}^{\text{IV}}(\text{L})(\text{pic})_2(\text{OH})]^+$. The abbreviation “pic” stands for 4-picoline.

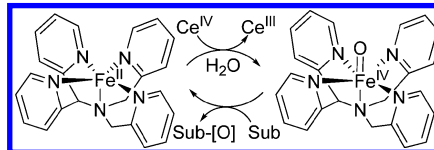
diffraction. The anionic carboxylate ligands facilitate stabilization of high oxidation states, and the distorted octahedral geometry in the precursor creates a coordination site at Ru(IV) for nucleophilic attack of water with release of a proton. It is

proposed that the carboxylate groups can then act as proton acceptors during the oxygen–oxygen bond-forming step, but mechanistic details are unclear.¹²²

4.1.2. Organic Oxidations. Organic PCET oxidations are typically thermodynamically favored but difficult to control because initial oxidized products are often more reactive than the initial reactants and careful management of protons and electrons is a prerequisite. Recent reviews on C–H bond activation by transition metal complexes¹²³ and metal–oxo complexes^{123,124} provide examples.

Iron Complexes: High-valent, active Fe(IV)–oxo complexes play an important role in catalytic oxygen activation cycles by heme and nonheme Fe enzymes. Related reactivity exists for synthetic metal–oxo complexes as well, including intervention of HAT and EPT pathways.¹²⁵ The biomimetic, mononuclear nonheme Fe(IV)–oxo complex in Scheme 21 is generated by

Scheme 21. Catalytic Oxygenation of Organic Substrates with a Mononuclear Nonheme Iron(IV)–Oxo Complex^a



^a Adapted from ref 126.

Ce(IV) oxidation and serves as a catalyst for organic oxidations with water as the oxygen source. Up to 95 turnovers were observed in the oxidation of thioanisole to methyl phenyl sulfoxide.¹²⁶

Redox reactions of a blue dimer analogue based on Fe, $[(\text{phen})_2(\text{OH}_2)\text{FeOFe}(\text{OH}_2)(\text{phen})_2]^{4+}$, were studied in water with added hydroquinone and excess phenanthroline. Under these conditions the dimer was reduced to Fe(II) with rapid formation of $\text{Fe}(\text{phen})_3^{2+}$. Reaction rates were greatly diminished in D_2O , pointing to EPT in the rate-determining step.¹²⁷ In a subsequent paper it was demonstrated that the Fe dimer quantitatively oxidizes pyruvic acid to acetic acid and CO_2 .¹²⁸

The pentadentate pyridyl iron complex, $\text{Fe}(\text{PYS})(\text{H}_2\text{O})^{2+}$ (PYS is depicted in Figure 31), was investigated as a mimic of

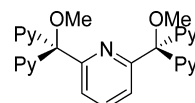


Figure 31. Structure of PYS.

lipoxygenase and is suggested to react through an Fe(IV)–oxo intermediate. Its reactivity was compared to previously studied lipoxygenase models based on Mn(III)OH and Fe(III)OMe complexes. Bond-dissociation energies, entropies of activation, and enthalpic driving forces were compared to explain differences in rates of oxidation of dihydroanthracene.¹²⁹

Mn Complexes: The basicity of metal oxo ligands has been demonstrated to play an important role in oxidation by C–H bond cleavage by lowering the redox potential required for catalysis. The rate of oxidation of dihydroanthracene (DHA) increased by more than an order of magnitude for the Mn(III)oxo complex $[(\text{Mn}^{\text{III}}(\text{H}_3\text{buea})(\text{O}))^{2-}]$ compared to $[\text{Mn}^{\text{IV}}(\text{H}_3\text{buea})(\text{O})]^-$ (both depicted in Figure 32), even

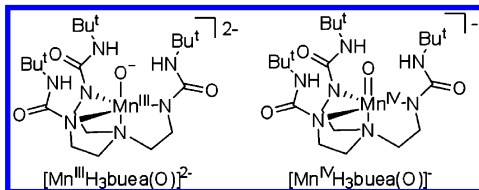


Figure 32. Mn oxo monomers that participate in C–H bond cleavage. Adapted with permission from ref 130. Copyright 2009 American Chemical Society.

though the driving force is less by ~ 1 kcal/mol. The difference in rates occurs as a result of a change in mechanism from PT-EET in the Mn(III)oxo form, with $\Delta pK_a < 2$ for DHA, to EPT for the Mn(IV)oxo form with $\Delta pK_a \approx 15$.¹³⁰

This effect has also been observed in the Mn corrolazine complex shown in Scheme 22. With F^- or CN^- coordinated in the axial position, the basicity of $[Mn^{IV}(O)]^{2-}$ is the leading factor in the increased reactivity of dihydroanthracene oxidation, not the oxidizing power of $Mn^{V}(O)^-$.¹³¹

Ru Complexes: The Ru(IV)–oxo complex, $[Ru^{IV}(\text{tpa})(\text{H}_2\text{O})(\text{O})](\text{PF}_6)_2$ (depicted in Figure 33), is an efficient catalyst for the oxidation of hydrocarbons with water as the solvent and oxygen source using Ce^{IV} as a sacrificial oxidant. For example, cyclohexene was oxidized to adipic acid by a series of PCET oxidation steps. The higher oxidation states $\text{Ru}^{\text{V}}\text{O}$ or $\text{Ru}^{\text{VI}}(\text{O})_2$ are also accessible at higher pHs for oxidation of more electron-deficient substrates.¹³²

The carbene complex, *cis*-Ru(tpip)₂(CHPh)(PCy₃) (tpip is depicted in Figure 34), was shown to act as a molecular mimic of known Ru oxide heterogeneous catalysts in catalyzing oxidation of alcohols and olefins with *N*-methylmorpholine *N*-oxide and iodosylbenzene, respectively.¹³³

The Ru acetate clusters, $[\text{Ru}_3\text{O}(\text{H}_3\text{CCO}_2)_6(\text{py})_2(\text{L})]\text{PF}_6$ (depicted in Figure 35, L = methanol or dimethyl sulfoxide), can be activated by O-atom donors toward catalytic oxidation of cyclohexane or cyclohexene by oxygen atom transfer. These clusters are also capable of olefin epoxidation and C–H bond cleavage similar to oxidative catalysis by metal porphyrins.¹³⁴

Cu Complexes: The permethylated-amine-guanidine bis(μ -oxo)copper dimer, shown in Figure 36, was synthesized and found to mimic Cu-based dioxygen activating enzymes by replicating the tyrosinase enzyme reaction of hydroxylating phenolates to catecholates.¹³⁵

The (μ - η^2 : η^2 -peroxy)dicopper(II) complex $[\text{Cu}_2(\text{H}-\text{L})(\text{O}_2)]^{2+}$ (the structure of the H–L ligand is shown in Figure 37) is oxidatively active, oxidizing the xylyl linker of the supporting

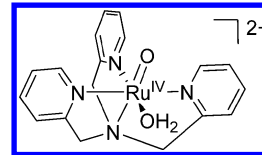


Figure 33. $[Ru^{IV}(\text{tpa})(\text{H}_2\text{O})(\text{O})]^{2+}$.

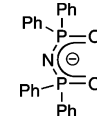


Figure 34. Structure of tpip ligand.

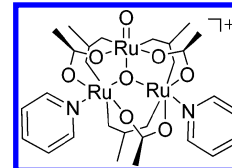


Figure 35. Structure of the Ru acetate cluster $[\text{Ru}_3\text{O}(\text{H}_3\text{CCO}_2)_6(\text{py})_2(\text{O})]^{+}$.

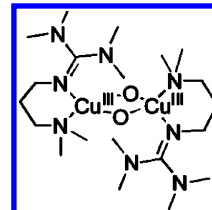
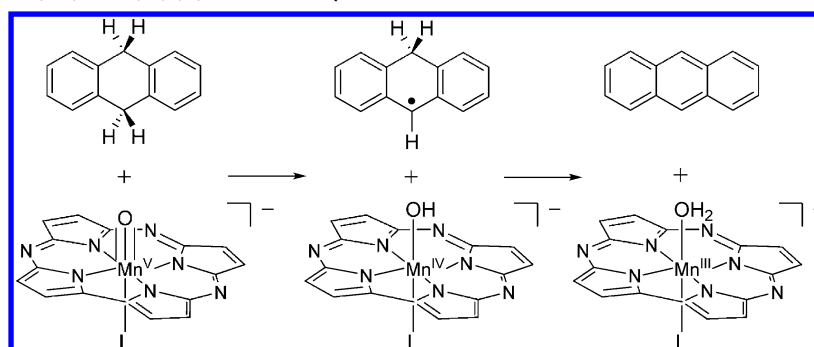


Figure 36. Structure of permethylated-amine-guanidine bis(μ -oxo)-copper dimer.

ligand, styrene, and aliphatic C–H bonds with bond dissociation energies (BDEs) in the range 75–92 kcal mol⁻¹. Large KIEs were observed consistent with HAT/EPT mechanisms.¹³⁶

The triazamacrocyclic Cu(II) complex (Scheme 23) can facilitate C–H activation under mild conditions based on a three-center, three-electron C–H–Cu(II) interaction. The paramagnetic metal–hydrocarbon interaction was studied with EPR and DFT. Kinetics data obtained from spectroscopic measurements, including isotope-labeling, point to a concerted EPT event in the rate-limiting step. This differs from the Ni(II) analogue where Ni(III) is inaccessible. When the Cu(II) complex is reacted with TEMPO, an aryl proton and Cu

Scheme 22. Reactivity of $[(\text{Cz})\text{Mn}^{\text{V}}(\text{O})(\text{L})]^-$ with Dihydroanthracene with $\text{L} = \text{F}^-$ or CN^- ^a



^aAdapted with permission from ref 131. Copyright 2010 Wiley.

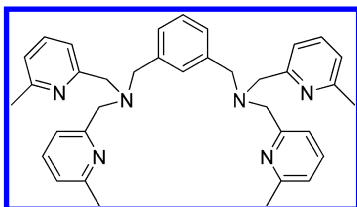


Figure 37. Structure of the dinucleating ligand H-L (1,3-bis[bis(6-methyl-2-pyridylmethyl)aminomethyl]benzene).

electron are removed. The TEMPO–H bond dissociation energy is 72 kcal/mol, showing that the C–H–Cu(II) interaction significantly alters the strength of the C–H bond.¹³⁷

A study of ligand effects on heme-copper–oxygen reactivity relevant to cytochrome *c* oxidase dioxygen reduction demonstrated that the $[\text{Fe}-(\text{O}_2^{2-})-\text{Cu}]^+$ complex shown in Scheme 24 is capable of H-atom abstraction from phenols. The O–O bond is cleaved, forming a Fe(IV)oxo complex, and the resulting phenol radical subsequently dimerizes.¹³⁸

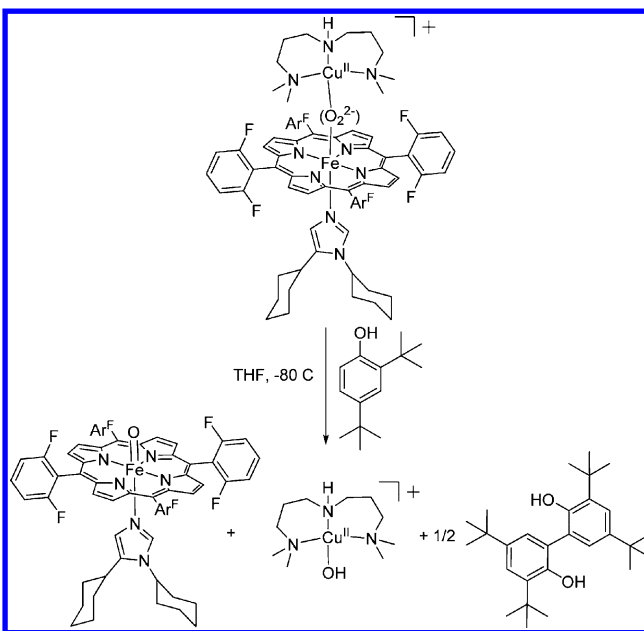
V Complexes: The vanadium salt $\text{V}(\text{O})_2^-$, shown in Scheme 25, oxidatively dehydrogenates activated alcohols to aldehydes. In the proposed mechanism, the rate-determining step is HAT from the C–H bond of the alcohol to $\text{V}(\text{O})_2^-$, which is reoxidized by O_2 to give a peroxidic intermediate. The intermediate also oxidizes the substrate.¹³⁹

The complex, $\text{V}(4,4'-t\text{-butylbpy})_2(\text{O})_2^+$, abstracts a hydrogen atom from TEMPO, hydroquinone, and dihydroanthracene. Rates are relatively slow, which has been attributed to a large intramolecular reorganization energy.¹⁴⁰

Ir Complexes: General base catalysis is observed in the oxidation of phenols by IrCl_6^{2-} at high pH, but it is unclear in acidic conditions, pH 1–3, whether the mechanism proceeds by a stepwise or concerted mechanism. KIE values up to 3.5 suggest MS-EPT with water as the proton acceptor.¹⁴¹ Oxidation of hydroxylamine is also observed from this substitutionally inert Ir(IV) complex. Under acidic conditions the mechanism is likely a concerted event with water functioning as the base.¹⁴²

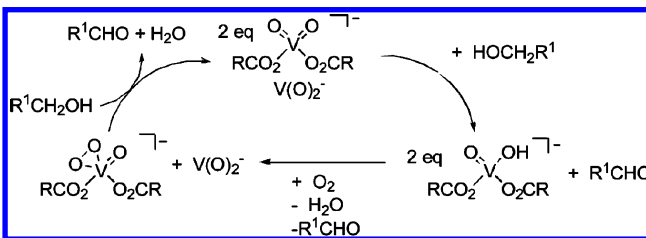
4.1.3. Hydrogen Oxidation and Reduction. Hydrogen oxidation and reduction are fundamental PCET reactions of interest because they involve multiproton, multielectron transfers. Hydrogen is an essential reductant in organic synthesis, in ammonia production, and as a fuel in PEM fuel cells. Solar production of hydrogen is of increasing importance

Scheme 24. $[\text{Fe}-(\text{O}_2^{2-})-\text{Cu}]^+$ H-Atom Abstraction from a Phenol Derivative^a



^aAdapted with permission from ref 138. Copyright 2010 American Chemical Society.

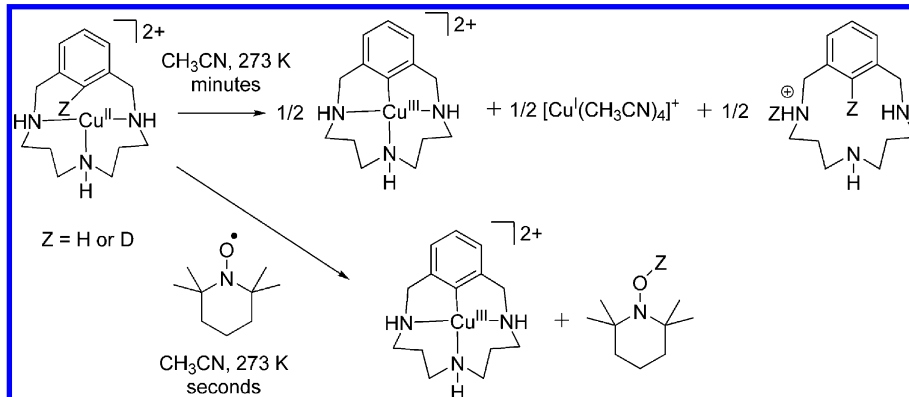
Scheme 25. Oxidative Dehydrogenation of Alcohols by $\text{V}(\text{O})_2^-$ ^a



^aAdapted with permission from ref 139. Copyright 2010 Wiley.

because of its potential for using the sun and water as a hydrogen source.¹⁴³ Heterogenous catalysis of hydrogen oxidation/reduction is well-known and highly studied; detailed mechanistic insight is available for a family of $[\text{Ni}(\text{diphosphine})_2]^{2+}$ complexes that showcase the role of pendant

Scheme 23. C–H Activation by a Triazamacrocyclic Cu(II) Complex^a



^aAdapted with permission from ref 137. Copyright 2010 American Chemical Society.

bases as proton relays for the oxidation of hydrogen and/or reduction of protons.¹⁴⁴

The hydrogenase enzymes are a remarkable example of utilization of PCET in proton reduction to hydrogen. They also provide insight into reaction pathways for catalysis of H⁺/H₂ interconversion in general.¹⁴⁴ The symmetrical (Fe^I)₂ complex model for the enzyme in Figure 38 can be protonated to form a

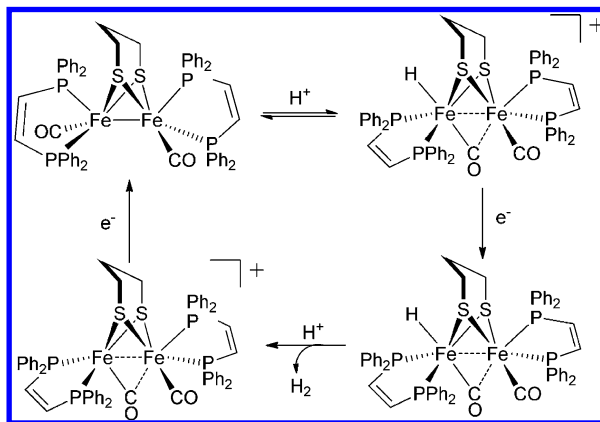


Figure 38. Proposed mechanism of hydrogen evolution. Adapted with permission from ref 146. Copyright 2008 American Chemical Society.

terminal hydride that catalyzes proton reduction at 200 mV below the potential for catalysis with the isomeric bridging hydride.¹⁴⁶ Hydrogen evolution occurs upon reduction to the neutral hydride complex because of the enhanced hydridic character of the Fe–H.¹⁴⁶ Catalysis by a terminal hydride supports the idea that proton reduction occurs at a single Fe site.

Rates for dihydrogen oxidation by the Ni(II) complex NiP₄–N and a previously reported analogue with two pendant bases NiP₄–N₂ have been compared. NiP₄–N functions as an

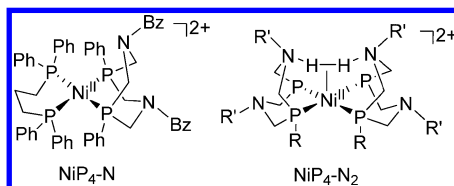


Figure 39. Structure of Ni phosphine complexes with positioned pendant bases for dihydrogen oxidation.

electrocatalyst for hydrogen oxidation with added bases. The mechanism proceeds through a dihydrogen adduct, followed by H–H cleavage to give an intermediate Ni(IV) dihydride that can be observed spectroscopically (Scheme 26). The PCET reactions in this case occur by sequential PT-ET with PT to the pendant amine base and then to an external base followed by electron transfer oxidation. When two pendant bases are positioned to stabilize the transition state, as in the complex NiP₄–N₂, the rate of H₂ oxidation is 20 times faster in spite of less-favorable thermodynamics.¹⁴⁷

The role of proton relay abilities of pendant amines in Fe and Ni functional analogues of the Fe–S cluster in the hydrogenase enzymes have been analyzed. As for the Ni(II) complexes mentioned previously, the model complexes contain internal bases—phosphines and amines—arranged appropriately to act

as proton shuttles from the metal center to enhance rates of PCET.¹⁴⁸

Proton reduction by cobaloximes has been studied chemically, electrochemically, and photochemically.¹⁴⁹ The reaction mechanism proceeds either through a homolytic pathway where two Co^{III} hydrides react to form H₂ or by a heterolytic pathway by protonation of a Co^{III} hydride (Scheme 27). A thermodynamic analysis of the barriers and driving forces of the pathways suggest that homolytic mechanism is favored largely because of the barrier for Co^{III}–diglyoxime formation.¹⁵⁰

4.2. Oxygen-Reduction Catalysis

The Fe complex [N4Py^{2R}Fe^{II}(OTf)]⁺, depicted in Figure 40, reduces dioxygen. It has been suggested that the mechanism proceeds by utilization of PCET and both first- and second-coordination sphere involvement. The unique stability of the complex in strong acids and bases enables characterization of Fe(III)OH and Fe(II)OH intermediates and PCET reduction to Fe(II)(OTf). Isotopic-labeling experiments demonstrate involvement of inner-sphere oxygen atoms and a role for synergistic first- and second-coordination sphere effects. The catalyst can be regenerated with cobaltocene with added triflic acid or by PCET reduction with ascorbic acid.¹⁵¹ The role of the second coordination sphere in dioxygen activation was the subject of a recent forum article.¹⁵²

Oxygen reduction by the reduced heteropolytungstate anion $\alpha\text{-PW}_{12}\text{O}_{40}^{4-}$ occurs by either stepwise ET-PT or multisite EPT (MS-EPT), depending on pH, to give the one-electron reduced heteropolytungstate anion $\alpha\text{-PW}_{12}\text{O}_{40}^{3-}$. At high pH the reaction proceeds through an outer-sphere electron transfer followed by proton transfer. At low pH the process is concerted with a deuterium KIE of 1.7 (Scheme 28). The direction of proton and electron transfer are opposite from MS-EPT oxidation of tyrosine, where the metal complex acts as an electron acceptor rather than an electron donor.¹⁵³

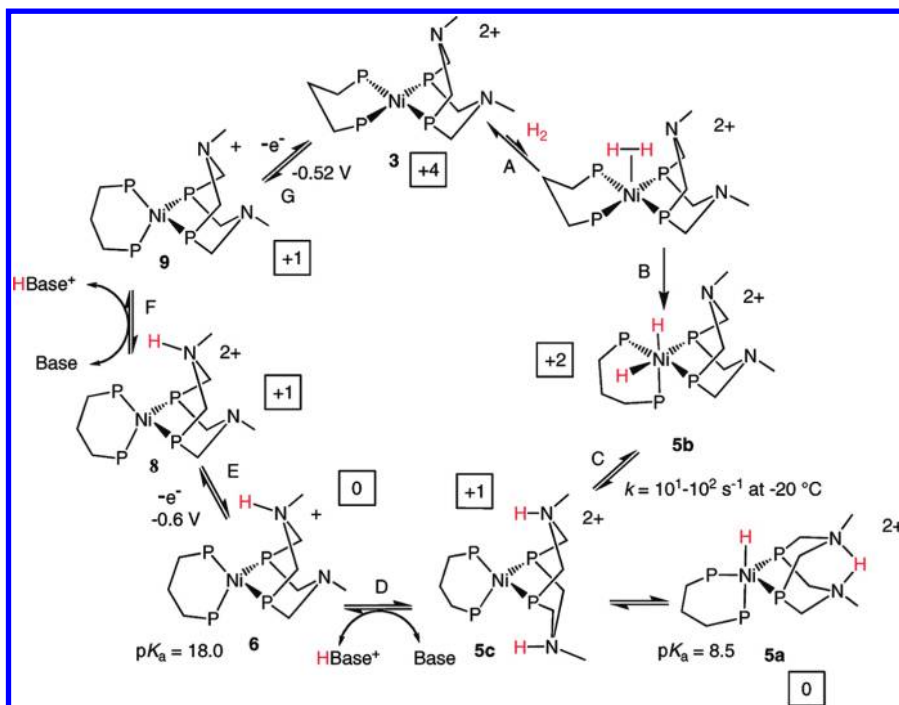
4.3. EPT Reactions Involving Coordinated Ligands

4.3.1. Oxidation by EPT. PCET reactions between [Fe^{II}(H₂bip)(bpy)₂]²⁺ and [Fe^{II}(H₂bim)(bpy)₂]²⁺ (H₂bip and H₂bim are depicted in Figure 41) with TEMPO occur with large negative entropies of activation, $-30 \pm 2 \text{ cal mol}^{-1} \text{ K}^{-1}$ for both. This is not accounted for with hydrogen bonding, solvent effects, ion pairing, or spin-state equilibria and primarily arises from the vibrational entropy difference between the oxidized and reduced forms of the complexes. This result demonstrates the limitations in using only bond dissociation energies in explaining EPT rate phenomena without including entropy changes. In correlations involving HAT and EPT reactions of transition metal complexes, bond-dissociation free energies should be used instead of bond-dissociation enthalpies.¹⁵⁴

Investigation of the role of entropy change in PCET was extended to related reactions involving Co, Fe, and Ru complexes. A correlation exists with electron transfer half-reaction entropies in aprotic solvents allowing for predictions of these effects in other reactions.¹⁰⁴ A review on Ru(II)-(bpy)₂pyridylimidazole complexes provides considerable insight into the properties of these protic, redox-active complexes.¹⁵⁵

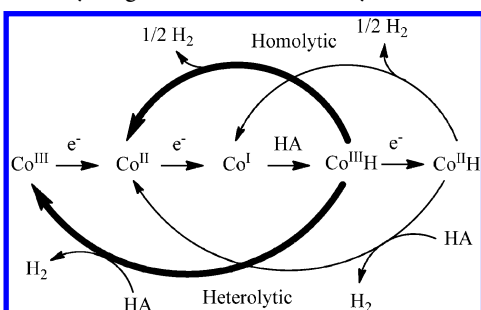
The oxidation of Ru^{II}(py-imH)(acac)₂ by TEMPO (Scheme 29) occurs by EPT with significant tunneling based on the KIE of 23 and a semiclassical analysis of the energy of activation. Application of the Marcus cross-reaction relation does not explicitly include tunneling, which limits its application to

Scheme 26. Proposed Mechanism for Electrocatalytic Oxidation of Hydrogen; Relative Free Energies Are Shown in the Squares in kcal/mol (1.0 atm of H₂, pH 8.5)^a



^aReproduced with permission from ref 146. Copyright 2008 American Chemical Society.

Scheme 27. Hydrogen-Evolution Pathways^a



^aAdapted with permission from ref 149. Copyright 2009 American Chemical Society.

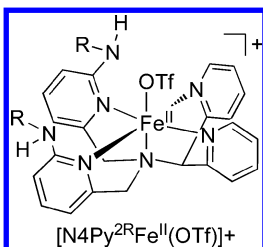
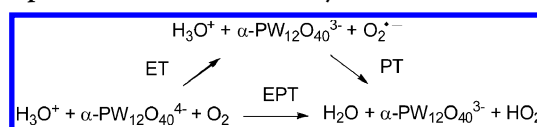


Figure 40. Structure of [N4Py^{2R}Fe^{II}(OTf)]⁺.

reactions in which the coupled modes can be treated classically.¹⁵⁶

The octaaza dinucleating macrocyclic ligand, LH₄, shown in Scheme 30, undergoes a self-oxidation reaction when bound to Cu(II). In the bimolecular reaction, four Cu(II) centers are reduced to Cu(I) and two of the amine ligands are oxidized to give the corresponding imines without added oxidant or base. DFT predicts a two-step mechanism with proton transfer

Scheme 28. pH-Dependent Reduction of O₂ by α-PW₁₂O₄₀⁴⁻ by Stepwise or Concerted Pathways^a



^aAdapted with permission from ref 153. Copyright 2010 American Chemical Society.

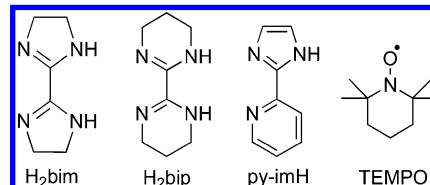
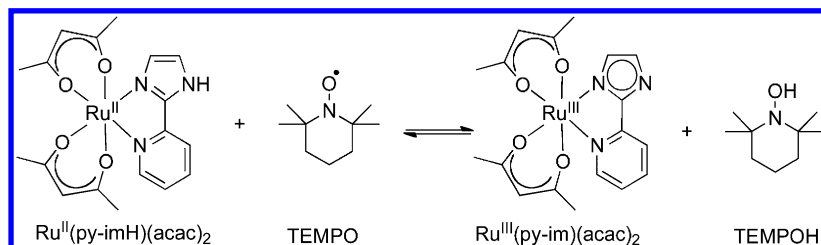


Figure 41. Structures of H₂bim, H₂bip, py-imH, and TEMPO.

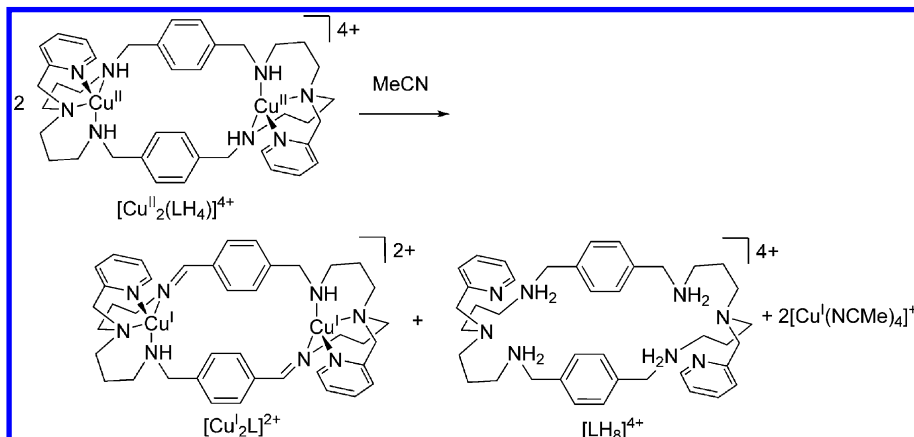
occurring first followed by a net HAT. The mechanism of this amine to imine oxidation appears to be distinct from standard amine to imine oxidations by transition metal catalysts.¹⁵⁷

4.3.2. Reduction by EPT. The tetraphenylporphyrin (TPP) imidazole complexes, TPPFe^{III}Im and TPPFe^{II}ImH (Scheme 31), function as models for the reactivity of histidine ligated hemes with oxy radical and hydroxyl substrates. Reactivity was observed with an ascorbate derivative, hydroquinone and benzoquinone, phenoxy and nitroxyl radicals, and a hydroxylamine. Reactions with ascorbate and TEMPO occur by EPT (HAT) and demonstrate the possibility that EPT plays a role in histidine-ligated heme cofactors.¹⁵⁸

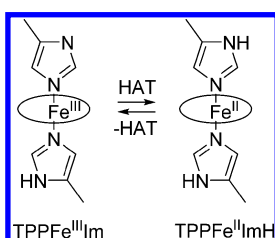
Multistep PT, ET, and PCET processes were demonstrated for complexes containing the pterin ligand (a redox-active heteroaromatic coenzyme) in [Ru^{III}(dmp)⁻(TPA)]²⁺ and

Scheme 29. Oxidation of $\text{Ru}^{\text{II}}(\text{py-imH})(\text{acac})_2$ by TEMPO^a

^aAdapted with permission from ref 156. Copyright 2008 American Chemical Society.

Scheme 30. Self-Oxidation of the Octaaza Ligand LH_4 ^a

^aAdapted with permission from ref 157. Copyright 2010 American Chemical Society.

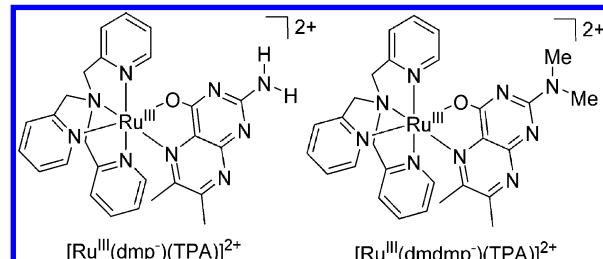
Scheme 31. HAT Interconversion of $\text{TPPFe}^{\text{III}}\text{Im}$ and $\text{TPPFe}^{\text{II}}\text{ImH}$ ^a

^aAdapted from ref 158. Copyright 2008 American Chemical Society.

$[\text{Ru}^{\text{III}}(\text{dmdmp}^-)(\text{TPA})]^{2+}$ (Figure 42). The coordinated pterin ligand can be doubly protonated and undergo PCET oxidation to give a coordinated monohydroopterin radical intermediate. The pK_a values and redox potentials were determined, and N–H bond-dissociation energies were estimated. The latter was invoked as the dominant factor in the rate of PCET.

EPT was investigated for concerted e^-/H^+ from a series of substituted phenol derivatives with electron transfer to Ru(III) in $[\text{Ru}^{\text{III}}(\text{dmp}^-)(\text{TPA})]^{2+}$ and $[\text{Ru}^{\text{III}}(\text{dmdmp}^-)(\text{TPA})]^{2+}$. Rate constants typically increased by 1–2 orders of magnitude for dmp^- as a result of the stronger hydrogen-bond association with the phenol, demonstrating the importance of preassociation and “stabilization of the transition state”. Another explanation is the decrease in proton-tunneling distance in more nearly symmetric H-bonds.¹⁵⁹

The roles of distance and decreased electronic communication between the electron and proton transfer sites on EPT were explored in the complexes illustrated in Figure 43. With the phenyl spacer ($\text{Ru}^{\text{III}}\text{PhCOO}$) there is a 10-bond, 11.2 Å

**Figure 42.** Structures of $[\text{Ru}^{\text{III}}(\text{dmp}^-)(\text{TPA})]^{2+}$ and $[\text{Ru}^{\text{III}}(\text{dmdmp}^-)(\text{TPA})]^{2+}$.

separation distance between the Ru^{III} electron transfer acceptor and carboxylate proton acceptor sites. Cyclic voltammetry and UV–visible absorption measurements suggest that there is almost no interaction between sites. Reactions with TEMPOH occur by EPT in both cases, with the rate constant decreasing by a factor of 2 for the longer ligand even though the driving force for EPT is larger with the phenyl spacer. With 2,6-di-*tert*-butyl-4-methoxyphenol as the H-atom donor, initial ET or PT cannot be ruled out but the rate constant decreases by a factor of 1000 due to diminished electronic communication. This demonstrates that distance and conjugation between redox and base sites play a role in EPT.¹⁶⁰

5. EXCITED-STATE PCET

Excited-state PCET reactions play an important role in chemical and biological processes.^{53b,58,66b,161} A better understanding of the kinetics, dynamics, and role of driving forces in excited-state PCET reactions are important in the design of artificial photosynthetic devices for the production of solar fuels.^{10,74}

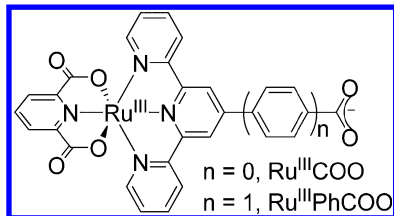


Figure 43. Structure of $\text{Ru}^{\text{III}}\text{COO}$ and $\text{Ru}^{\text{III}}\text{PhCOO}$.

Changes in reactivity and reaction dynamics often appear for excited states with a significant difference in electronic structure between ground and excited states. This is a common observation for protic molecules with light absorption inducing significant changes in acid–base properties that can trigger PCET.¹⁶² PCET provides a basis for photoprotection in many organic and biological molecules following UV absorption with excited-state energy being discharged by proton transfer. Releasing excitation energy prevents dissociation and other deleterious excited-state reactions.¹⁶³ Investigation of excited-state PCET reactions has also given insight into how photosynthetic reactions are driven following light excitation.¹⁶⁴

At the microscopic level, excited-state PCET reactions are influenced by a number of factors including local changes in molecular and solvent structure and changes in the local hydrogen-bonding environment. The roles that these factors play in excited-state kinetics and thermodynamics are being explored both experimentally and theoretically.^{53b,58,65,66b,74,165} In one approach, the quantum nature of proton nuclear motion and electrostatic coupling with surrounding polar solvent determines whether the proton motion is electronically adiabatic or nonadiabatic.^{53b,65,165g} Rate constants are predicted to increase with increasing driving force as excited vibronic product states become accessible.⁵⁸

Electronic structural changes accompanying light absorption can greatly affect proton affinity and excited-state pK_a values. This is common for intramolecular charge transfer (ICT) excited states of weak organic acids such as phenols or the coumarin dyes.^{165a,166} An estimate of excited state pK_a is available by application of the Förster equation (eq 55), in which $h\nu_{\text{HA}}$ is the absorption energy of the protonated acid and $h\nu_{\text{A}-}$ of the corresponding base.^{162b} Application of DFT has allowed the estimation of the pK_a values for many organic acids in a variety of solvents.¹⁶¹

$$pK_a^* = pK_a - \frac{(h\nu_{\text{HA}} - h\nu_{\text{A}-})}{2.3RT} \quad (55)$$

Distinguishing whether transfer of an electron and a proton are sequential or concerted in excited-state PCET can be difficult.^{53b} Photochemically driven EPT (*photo*-EPT), with concerted electron–proton transfer occurring during optical excitation, would appear to be ruled out on fundamental grounds. Application of the Franck–Condon principle shows that electronic excitation occurs rapidly on the time scale for nuclear motions, including proton transfer. However, evidence for *photo*-EPT has been obtained by a combination of femtosecond pump–probe and coherent Raman measurements following ICT excitation of hydrogen-bonded adducts (1) and (2) in Figure 44. On the basis of the ultrafast Raman measurement on $\nu(\text{O}-\text{H})$ and $\nu(\text{N}-\text{H})$ modes, proton transfer is coincident with excitation in these adducts.

These results were rationalized as follows. Immediately following excitation, the proton in the optically prepared ICT

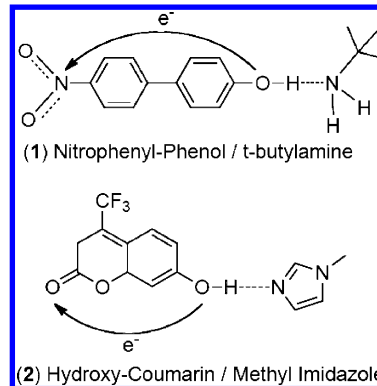


Figure 44. Structures of hydrogen-bonded adducts: (1) 4-hydroxy-4'-nitrobiphenyl (*para*-nitrophenylphenol) and *t*-butylamine (TBA) in 1,2-dichloroethane (DCE); (2) 7-hydroxy-4-(trifluoromethyl)-coumarin and 1-methylimidazole in toluene.

excited state is located at the equilibrium coordinate of the $\text{A}-\text{O}-\text{H}$ ground state, $(\bullet^-\text{A}-\text{O}^*-\text{H}^-\cdots\text{B})^*$. In a conventional proton transfer event, H^+ motion occurs after or during excited-state equilibration in the coupled vibrational and solvent modes. Such a stepwise process is analogous to ET-PT with excitation (ET) followed by proton transfer and has been studied by several groups by ultrafast methods.¹⁶⁷

However, the same configuration produced by vertical excitation could also be viewed as an “ICT-EPT” photoproduct state. In this state the proton is transferred to the nitrogen base in concert with formation of the ICT excited state but with a highly elongated $^+\text{H}-\text{N}$ bond, i.e., $(\bullet^-\text{A}-\text{O}^*\cdots^+\text{H}-\text{B})^*$. The instantaneous appearance of a H^+-N vibrational mode in femtosecond resonance Raman experiments was consistent with this interpretation.¹⁶⁸

5.1. Excited-State Superacids

Superacids are a class of molecules that undergo dramatic decreases in pK_a upon excitation.^{162b} Enhanced acidity accompanying changes in electronic structure dramatically affect pK_a values and can significantly influence reaction dynamics for proton transfer events. Enhanced acidity is common for charge-transfer excited states in protic molecules. The example of 2-naphthol is illustrated in Figure 45 in which the acidity of the phenolic proton

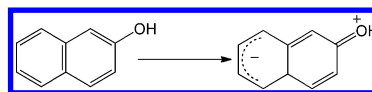


Figure 45. Illustration of charge redistribution between ground state and excited state for 2-naphthol. Reproduced with permission from ref 169a. Copyright 2008 American Chemical Society.

increases by 6.4 pK_a units in the ICT excited state.¹⁶⁹ For molecules with preformed H-bonds, proton transfer is in competition with excited-state decay.

Photoacids can be used as optical triggers to rapidly increase local acidity and induce chemical reactions.^{162a} An ideal photoacid should have $pK_a = 8$ and $pK_a^* < 2$, deprotonate in a few nanoseconds in aqueous solutions following electronic excitation, and undergo slow reprotonation.^{162b}

Utilization of optically controlled proton donors requires initial hydrogen-bond formation. The importance of prior H-bonding has been demonstrated in excited-state proton transfer reactions with 8-hydroxy-1,3,6-pyrenetrisulfonic acid (HPTS), a

common photoacid, with acetate added as acceptor base.^{162a} HPTS and acetate associate in the ground state, creating a hydrogen-bonding network that sets the stage for proton transfer following excitation of the photoacid. If the network is broken by addition of bromide salts, proton transfer is inhibited. The importance of H-bonding is due to the importance of vibronic wave function overlap in order for proton transfer to occur. This overlap decreases exponentially with the proton transfer distance (section 2).^{165g}

HPTS and other pyrene photoacids with related structures, shown in Figure 46, have been extensively studied,^{162a,169a,170}

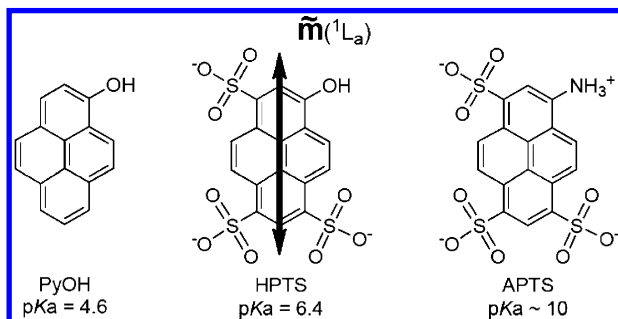


Figure 46. Structures of pyrene excited-state photoacids that have been investigated by Stark spectroscopy. The ${}^1\text{L}_\text{a}$ transition dipole is shown. It lies along the molecular axis for all three molecules. Reproduced with permission from ref 169a. Copyright 2008 American Chemical Society.

including the role of changes in pK_a induced by substituent changes. For HPTS, charge redistribution is followed by proton dissociation due to enhanced acidity in the excited state. For APTS, deprotonation occurs first, followed by charge rearrangement, leading to a decrease in basicity of the deprotonated state relative to the ground state.^{169a}

Stark spectroscopy was used to probe charge transfer in the pyrene photoacids in Figure 46. The ${}^1\text{L}_\text{a}$ transition dipole for the excited state of HPTS is illustrated in the figure.

5.2. Superbases

The converse of superacids, superbases, has also been observed in excited states in which charge transfer excitation creates a basic site. Chen and Tureček found evidence for superbase reactivity (Figure 47) following excitation of an arginine amide containing peptide.¹⁷¹ The electronic excitation is delocalized over the amide group in the π^* orbital, which leads to N–C $_\alpha$ bond cleavage forming C radical fragments.

MS-EPT was observed in reductive fluorescence quenching by three isomeric free-base *meso*-(pyridyl)porphyrins by phenols. In these reactions, quenching occurs by electron transfer to the porphyrin excited state and proton transfer to the hydrogen-bound pyridine (Figure 48). The distance and driving force for electron transfer were tuned, and rate enhancements greater than a factor of 10 were observed.^{165b}

5.3. Organic Molecules

There is an extensive literature on PCET and excited-state hydrogen-bond dynamics in organic molecules. Aromatic molecules can have “highly polar charge-transfer states of ${}^1\pi\pi^*$, ${}^1\text{n}\pi^*$, or ${}^1\pi\sigma^*$ character which drive proton transfer”¹⁶⁶ Computational studies designed to gain an understanding of the conical intersections that couple S_1 and S_0 surfaces and allow for ultrafast internal conversion to the ground state were conducted on indole H-bonded to both pyridine and

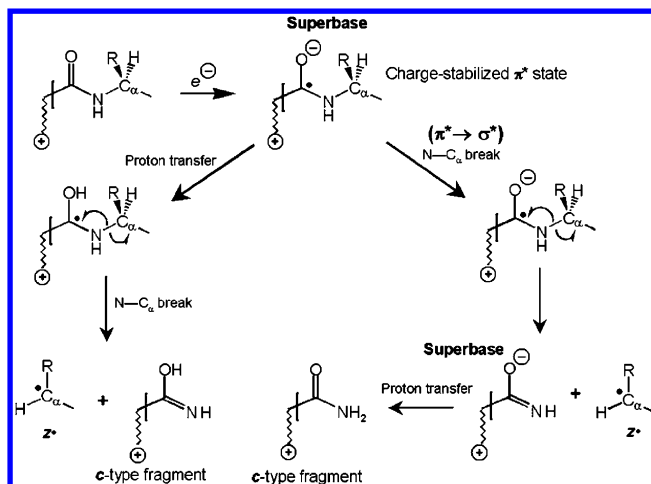


Figure 47. Arginine superbase mechanism for C–N bond cleavage. Reproduced with permission from ref 171. Copyright 2006 American Chemical Society.

ammonia.¹⁶⁶ The results of calculations on these molecules highlight the importance of hydrogen bonding prior to excitation. Fast proton transfer triggered by electronic excitation is dependent on vibronic overlap between the proton donor and acceptor as noted above.

Pyridine–pyrrole hydrogen-bonded assemblies have been widely studied as models for the Watson–Crick base pairs guanine/cytosine (G/C) and adenine/thymine (A/T). Recent calculations generated the intersecting energy-coordinate diagram in Figure 49. It was discovered that two crossings, an avoided crossing and a conical intersection, are important in understanding excited-state hydrogen-bond dynamics involved in photoinduced electron-driven proton transfer in the pyridine–pyrrole system.^{163a,165a}

Femtosecond pump–probe electron-ion coincidence spectroscopic measurements were performed on 2-aminopyridine dimers.^{163c} They display two reaction channels for proton/hydrogen transfer, ultrafast (sub-50 fs) and slower (~75 ps) components.^{163c} Similar to related molecules, this molecule undergoes internal conversion to the charge transfer state, which corresponds to electron transfer from the proton donor to the proton acceptor and a net hydrogen transfer reaction.^{163c}

There is considerable debate concerning whether excited-state double proton transfer (ES-DPT) in 7-azaindole dimers (7AI_2) is a concerted or stepwise process; both possibilities are depicted in Figure 50.¹⁷² Excitation-wavelength dependent fluorescent experiments conducted by Takeuchi and Tahara show high-energy transients with a biexponential decay (0.2 and 1.1 ps) and lower-energy transients with a single exponential decay (1.1 ps).^{172c} The 0.2 ps decay at higher energy is attributed to a ${}^1\text{L}_\text{b}$ (S_2) ${}^1\text{L}_\text{a}$ (S_1) transition, whereas the 1.1 ps decay is assigned to double proton transfer from the ${}^1\text{L}_\text{a}$ (S_1) state. Thus, a concerted process takes place and the biexponential time components can be explained by electronic relaxation.^{172c}

Oxidation of oligodeoxynucleotide residue, 5-methyl-2'-deoxycytidine ($d^{\text{m}}\text{C}$), by photosensitized 2-methyl-1,4-naphthoquinone (NQ) is illustrated in Figure 51. When excited at 355 nm, NQ forms triplet ${}^3(\text{NQ})^*$. Once formed, it reacts to create a $d^{\text{m}}\text{C}$ radical that, based on solution conditions, undergoes either reversible or irreversible deprotonation. The product distribution is pH-dependent; 5-formyl-2'-deoxycytidine

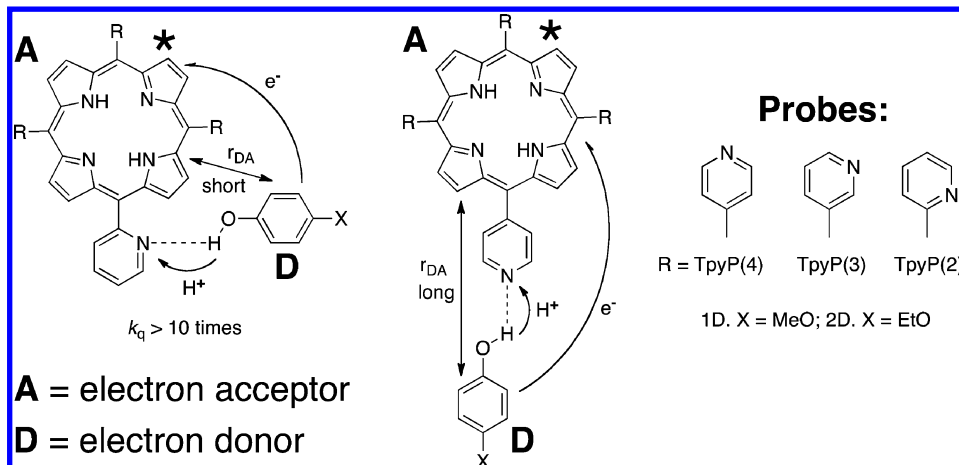


Figure 48. Excited-state reductive quenching by MS-EPT in free-base *meso*-(pyridyl)porphyrins. Reproduced with permission from ref 165b. Copyright 2009 Royal Society of Chemistry.

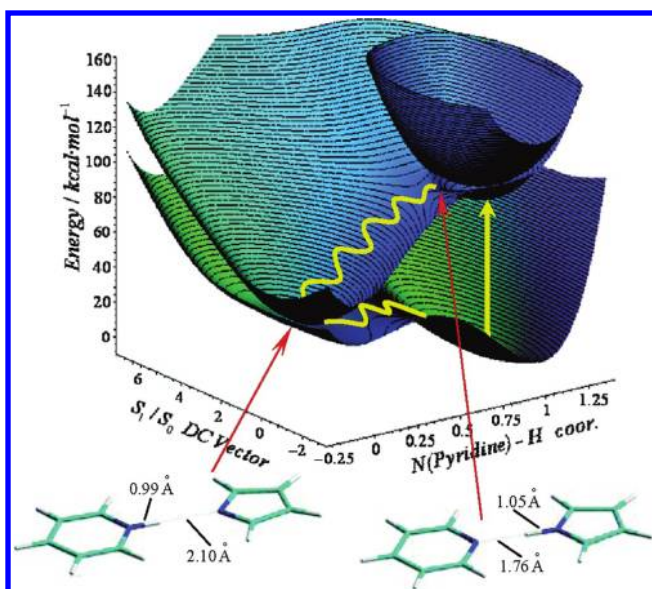


Figure 49. Potential energy surface diagrams (S_2 , S_1 , S_0) involved in radiationless deactivation of the lowest $^1\pi\pi^*$ excited state of the H-bonded pyrrole-pyridine adduct. Illustrative classical paths (in yellow) illustrate Franck-Condon excitation (arrow) and relaxation on the S_1 and S_0 surfaces, restoring the initial ground-state configuration. Reproduced with permission from ref 163a. Copyright 2007 American Chemical Society.

is formed at pH 5, and below pH = 4.5 the N3 position is protonated and one-electron oxidation hindered.¹⁷³

5.4. Metal Complexes

The emitting metal-to-ligand charge transfer excited state of the complex $\text{Ru}(\text{bpy})_2(\text{bpz})^{2+}$ (bpz is 2,2'-bipyrazine) undergoes EPT reduction with added hydroquinone (H_2Q). In the lowest excited state, a bpz radical is formed with an increase of 6 p K_a units compared to the ground state. In the quenching mechanism (Figure 52), excited-state preassociation occurs between H_2Q and the bpz ligand followed by EPT, which is favored over reductive electron transfer to give $\text{Ru}^{II}(\text{bpy})_2(\text{bpz}\cdot\text{H}--\text{HQ}\cdot)^{2+}$ by 0.6 eV.¹⁷⁴

A related mechanism was proposed in the reductive quenching of the emitting MLCT excited state of $[\text{Ru}(\text{bpy})_2(\text{pbim})]^+$, which oxidizes ubiquinol or plastoquinol

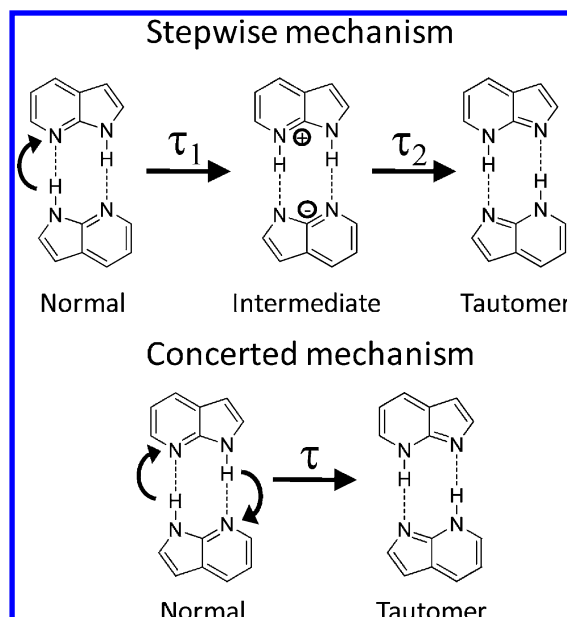


Figure 50. Illustration of concerted and stepwise excited-state double proton transfer in 7-azaindole dimers. Reproduced with permission from ref 172b. Copyright 2008 Elsevier.

analogues in acetonitrile by PCET. The mechanism for this process is shown in Figure 53 for the $[\text{Ru}(\text{bpy})_2(\text{pbim})]^+$ ubiquinol example.⁷⁸ Theoretical calculations were used to investigate the associated EPT pathway.⁷⁸ These calculations predict that the kinetic isotope effect (KIE) will increase for ubiquinol but decrease for plastiquinol.

PCET involvement has also been invoked in the photodimerization of $[\text{Ru}^{II}(\text{bpy})_2(\text{L}-\text{L})]^{2+}$ [$\text{L}-\text{L}$ = *trans*-1,2-bis(4-(4'-methyl)-2,2'-bipyridyl)ethane] in solutions between pH 7 and pH 12. In the proposed mechanism (Figure 54), MLCT excitation is followed by intramolecular oxidative quenching by the remote bipyridinium to give the bipyridinium radical. The radical induces cyclodimerization with a second complex followed by reoxidation by the Ru(III) formed by excited-state quenching.¹⁷⁵

As a model for sensitized electron transfer in Photosystem II, PCET reactions were also investigated in polypyridyl Ru(II) and Re(I) complexes with tyrosine-like ligands (Figure 55).

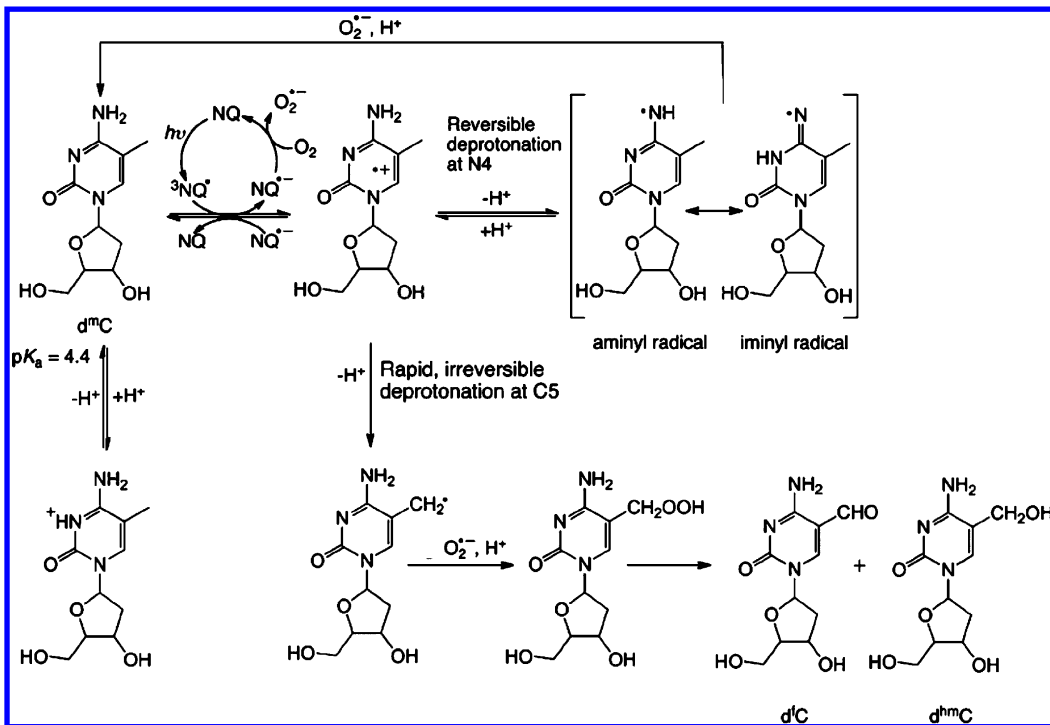


Figure 51. Proposed reaction mechanism for photosensitized 2-methyl-1,4-naphthoquinone oxidation to d^mC . Reproduced with permission from ref 173. Copyright 2008 Wiley.

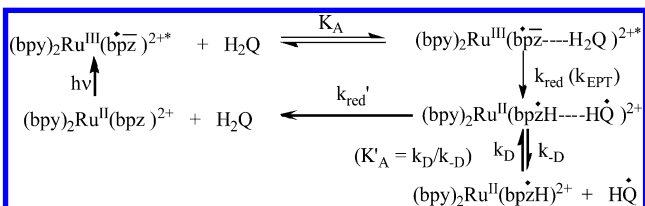


Figure 52. Mechanism for EPT reductive quenching of $[(bpy)_2Ru^{III}(bpz^{\bullet-})^{2+}]$ by H_2Q . Reproduced with permission from ref 174a. Copyright 2007 American Chemical Society.

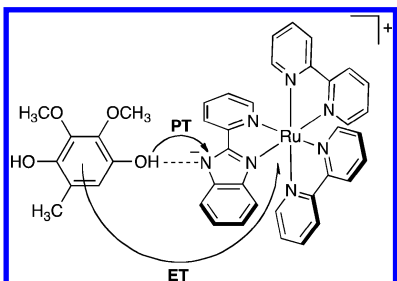


Figure 53. Illustration of reductive EPT quenching of the emitting MLCT excited state of $[Ru(bpy)_2(pbim)]^+$ by a ubiquinol analogue. Reproduced with permission from ref 78. Copyright 2009 American Chemical Society.

Also, note section 8.2. In these experiments, oxidation of intramolecularly bound tyrosine was investigated by laser flash photolysis following oxidative quenching of the Ru- and Re-based MLCT excited states.^{165f} These experiments explored the pH dependence of the PCET oxidation of the tyrosine-like ligands to address a literature debate concerning the proposed role of changes in driving force induced by pH (section 8.2). For an EPT pathway there is no microscopic basis for changes in ΔG , induced by pH changes, to effect the EPT barrier.

However, a pH dependence was observed for intramolecular oxidation in both $Re^{II}(P-Y)$ and $Ru^{III}(P-Y)$.

In a related study, on the basis of a series of Ru-tyrosine analogues, rates and mechanism of PCET were varied depending on the strength of hydrogen bonding to the dissociating proton (Figure S6). For RuY, proton loss to an external base occurred. In the case of Ru-SA and Ru-PA, the ligand functioned as an internal base for proton transfer. For Ru(Y) and Ru-SA, pH-dependent rates occur in discrete steps. Each step in the rate ladder represents a different mechanism, and the rates vary by 5 orders of magnitude over the pH range 2–10.¹⁷⁶

In a related experiment, Freys et al. investigated concerted excited-state EPT in a H-bonded molecular assembly between the iridium complex $IrbiumH_2^+$ and 3,5-dinitrobenzoate anion (dnb^-) as the electron–proton acceptor as shown in Figure S7.^{165c} This complex forms a hydrogen-bonded 1:1 adduct with benzoate anions, and “proton delocalization can be monitored directly by optical spectroscopy due to the close proximity of the acidic N–H protons to the metal center”.^{165c} Following photoexcitation, the spectroscopic changes in the $IrbiumH_2^+$ complex and formation of dnb were used to monitor proton release to the base.

Photochemically induced PCET has been studied in metal porphyrins including temperature- and isotope-dependence studies,^{165e} ligand-field dependence studies,¹⁶⁵ⁱ and the influence of spacers between amidinium–amidine acid–base electron transfer acceptors and the porphyrin.^{165h} Concerted electron–proton transfer was observed following excitation of the porphyrin, by monitoring the transient absorption growth and decay of the porphyrin cation. Temperature-dependent studies on zinc porphyrin dyads (Figure S8) illustrate the importance of vibrational overlap in concerted EPT reactions by highlighting the effects of bath-induced changes in the proton coordinate.^{165e}

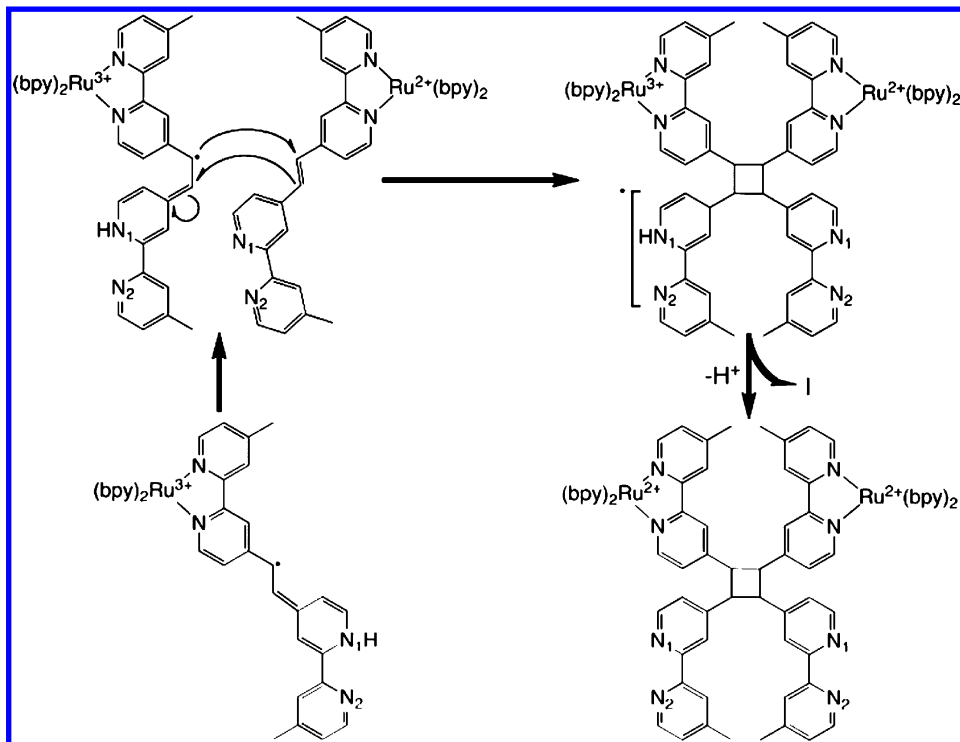


Figure 54. Photodimerization of $[\text{Ru}^{\text{II}}(\text{bpy})_2(\text{L}-\text{L})]^{2+}$ [$\text{L}-\text{L} = \text{trans-1,2-bis}(4\text{-}(4'\text{-methyl)-2,2'\text{-bipyridyl})ethane}$] in aqueous solution. Reproduced with permission from ref 175. Copyright 2008 American Chemical Society.

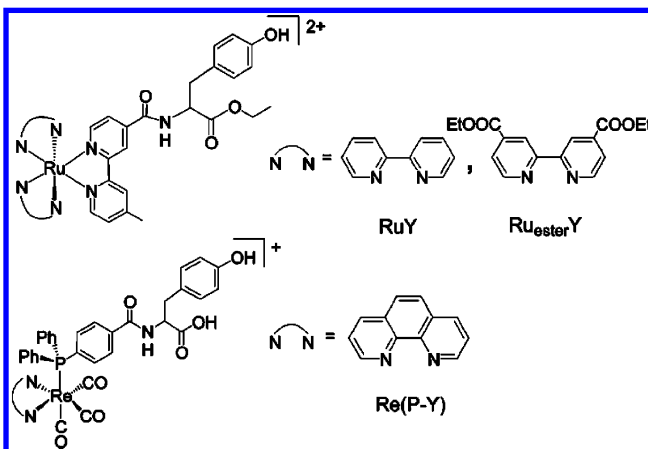


Figure 55. Structures of RuY, Ru_{ester}Y, and Re(P-Y) complexes with appended tyrosinyl groups. Reproduced with permission from ref 165f. Copyright 2007 American Chemical Society.

Experiments with porphyrin frameworks having spacer modifications that maintain π -conjugation but extend the distance between the hydrogen-bonded amidinium–amidine base and the porphyrin demonstrate that concerted EPT occurs between the porphyrin and the hydrogen-bound ligand. The spacer between the amidine and the porphyrin creates a more significant wavelength dependence between the amidinium/amidine protonation states due to the added rotational dimensions between the proton acceptor and donor. This makes experimental observation of changes in electron and proton motion more spectroscopically accessible. The added spacer introduces an additional degree of freedom along the rotational plane of the porphyrin–amidinium pair.^{165h}

Photochemically initiated EPT has been shown to occur from thin films of adsorbed dimethylformamide (DMF) to the

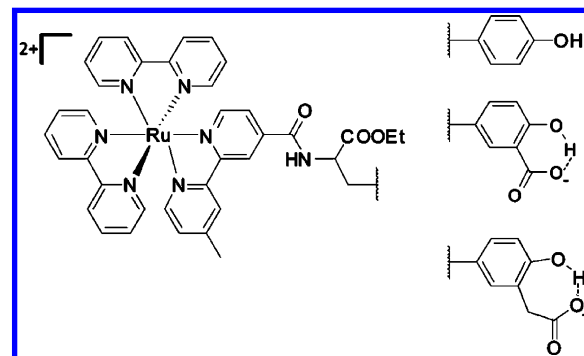


Figure 56. Structures of $\text{Ru}(\text{bpy})_2(\text{bpy}-\text{C}(\text{O})\text{NH}-\text{ArOH})^{2+}$ (RuY), a salicylic acid derivate (Ru-SA), and a 2-hydroxyphenylacetic acid derivate (Ru-PA). Reproduced with permission from ref 176. Copyright 2008 American Chemical Society.

oxide in WO_3 and MoO_3 .¹⁷⁷ Net photoinduction of hydrogen onto the metal oxide films (Figure 59) is induced by an electronic transition that triggers net charge transfer from the transferring H atom toward a surface M=O site, causing C–H bond rupture.¹⁷⁷

5.5. Biological Molecules

As noted in section 8.4, excited-state driven PCET plays an important role in photosynthetic oxygen production by Photosystem II (PSII) in the oxygen evolving complex (OEC).¹⁷⁸ To oxidize two water molecules to produce oxygen requires absorption of four photons.^{178,179} Understanding how the photosynthetic apparatus balances excitation energy from multiple photons to achieve PCET oxidation of water and reduction of CO_2 provides important lessons for the design of artificial photosynthetic devices. In the photosynthetic apparatus, excited-state energy is converted into transiently

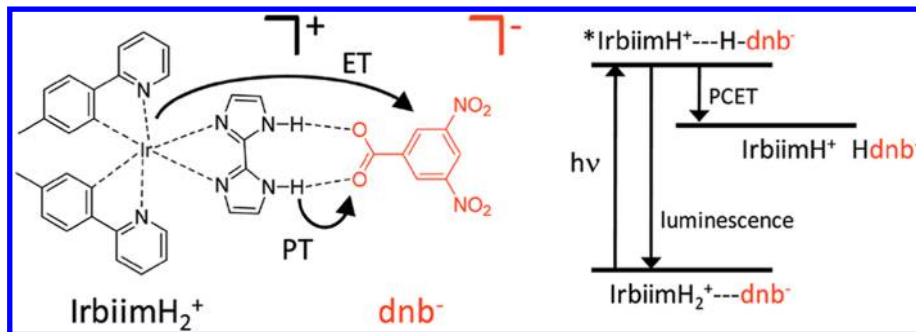


Figure 57. Illustrating the excited-state EPT quenching mechanism in the H-bonded adduct between IrbiimH_2^+ and the benzoate anion, dnb^- . Reproduced with permission from ref 165c. Copyright 2008 Royal Society of Chemistry.

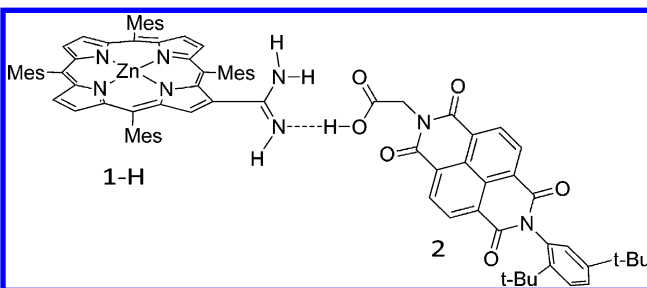


Figure 58. Illustrating the H-bonded amidinium–carboxylate salt-bridge assembly (1-H:2) between a Zn(II) porphyrin photoreductant (1-H) and a naphthalene diimide electron transfer acceptor (2). Reproduced with permission from ref 165e. Copyright 2006 American Chemical Society.

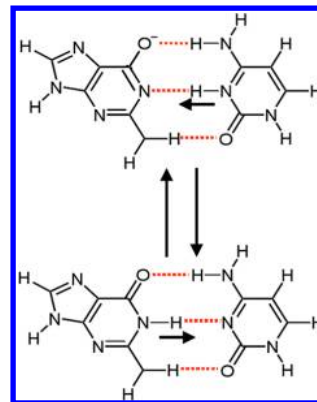


Figure 60. Watson–Crick ground-state guanine–cytosine base pair illustrating the direction of proton transfer following excitation (vertical arrow). Adapted with permission from ref 180. Copyright 2007 American Institute of Physics.

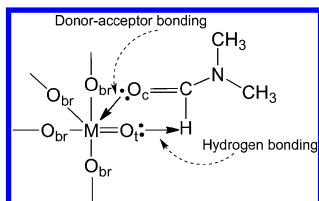


Figure 59. Photochemically induced net H-atom transfer from DMF to a surface $\text{M}=\text{O}$ site at MO_3 ($\text{M} = \text{Mo}, \text{W}$). Adapted with permission from ref 177. Copyright 2007 Taylor & Francis.

stored redox equivalents that drive PCET reactions for water oxidation and NADP^+ reduction.

Photochemically driven PCET in DNA base pairs is utilized to avoid photodamage.¹⁸⁰ The mechanisms by which coupled proton transfer events assist in excited-state energy dissipation and photostabilization in DNA molecule base pairs has been explored by ultrafast transient laser techniques.^{180,181} Proton transfer events in photoexcited Watson–Crick DNA base pairs occur on extremely rapid time scales. Calculations on guanine–cytosine (GC) base pairs predict conical intersections that connect the $\pi\pi^*$ excited state to the ground state.¹⁸⁰ The net proton transfer event is illustrated in Figure 60.

These charge transfer pathways connect excited states with ground states through conical intersections that lead to rapid decay, avoiding photodamage.^{180–182} Similar ultrafast deactivation through conical intersections is observed in Watson–Crick adenine (A)-thymine (T) base pairs.^{163b}

Hydrogen bonding is an integral feature in most biological structures and may play a general role in excited-state dynamics and reactivity following charge transfer excitation of peptides.¹⁸² Green fluorescent proteins (GFPs) offer an example where hydrogen bonding and proton transfer play important

roles in excited-state dynamics based on recent experimental and theoretical studies.¹⁸³ As noted above, prior hydrogen bonding ensures that proton transfer events triggered by photoexcitation can occur following light absorption. This conclusion is supported by computational studies.^{183b,f}

Ultrafast time-resolved fluorescence studies on GFP show that a neutral intermediate state (I^*) is formed very rapidly (<1 ps) following excitation to the initial excited state (A^*).^{183e} The rapid (sub-picosecond) time scale means the $\text{A}^* \rightarrow \text{I}^*$ transition occurs more rapidly “than excess energy can be dissipated, and intermediate state I^* is formed vibrationally hot”.^{183e} “Pre-existence of a low-barrier or barrierless H-bond between the phenol group of the chromophore and a side chain of aspartate” ensures facile proton transfer.^{183e} Figure 61 shows the initial configuration of GFP, A. Following excitation and the sequence, $\text{A} \rightarrow \text{A}^* \rightarrow \text{I}^*$. The intermediate state, I^* , either relaxes to the ground state and returns to A, or follows an alternate path to B^* , which decays to a long-lived B state.^{183d–f} This structure of GFP facilitates proton shifts through a hydrogen-bonding network by a proton wire effect. Figure 62 illustrates the proton wire effect following excitation in wild-type GFP.^{183c}

6. ELECTROCHEMICAL PCET

Electrochemical measurements have been applied to the study of PCET reactions, resulting in useful information on kinetics, thermodynamics, and mechanism. These studies have utilized cyclic voltammetry (CV), rotating disk electrodes (RDEs), electrochemical impedance spectroscopy (EIS), spectroelectrochemistry, and digital simulation (Digisim).

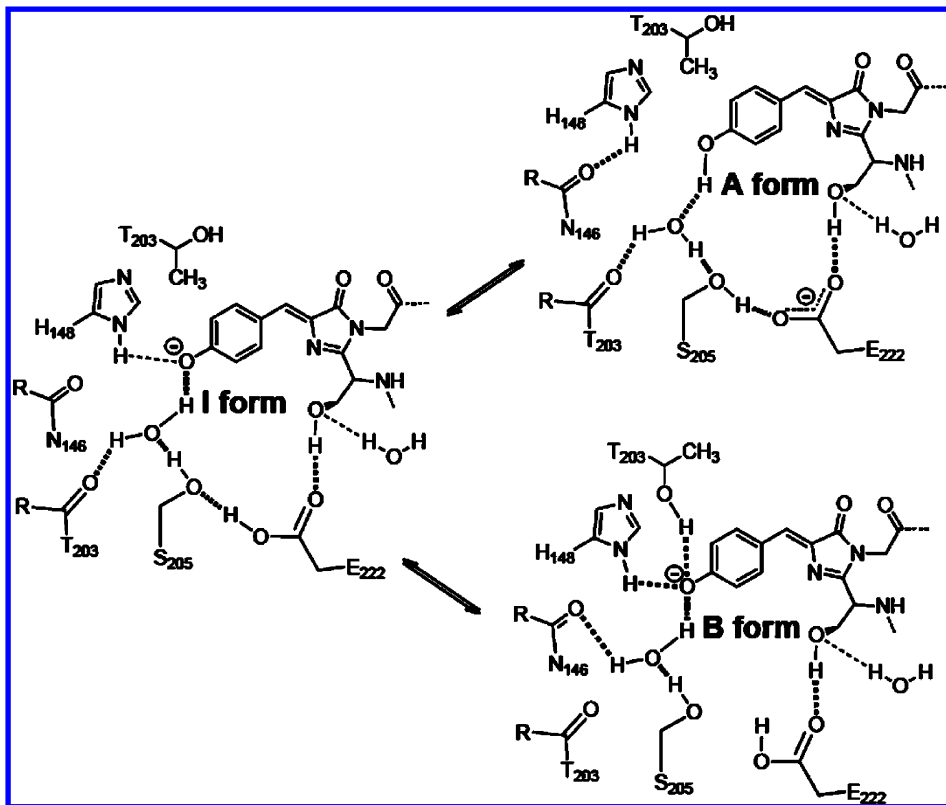


Figure 61. Illustration of interconversion between A and B forms of the green fluorescent protein (GFP) chromophore through intermediate state I*. Figure adapted from ref 184 and reproduced with permission from ref 183e. Copyright 2008 American Chemical Society.

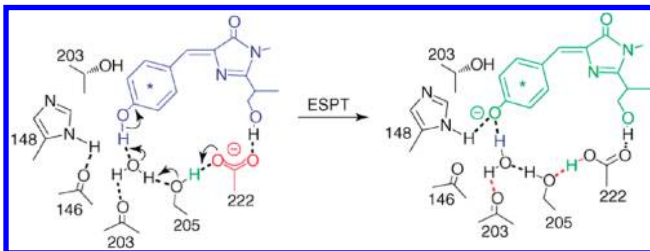


Figure 62. Proton wire effect leading to excited-state proton transfer (ESPT) following excitation in wild-type GFP. Excitation at 370–400 nm leads to stepwise proton transfer through the H-bonded network to Glu222. Reproduced with permission from ref 183c. Copyright 2006 Elsevier.

A major advance was made by Savéant, Evans, and co-workers in using electrochemistry to identify concerted electron–proton transfer (EPT) pathways in reactions previously thought to be stepwise, ET-PT or PT-ET. Their analyses of electrochemical data unambiguously established EPT mechanisms. Significant progress has also been made in unraveling the role of complex acid–base equilibria in PCET reactions.

6.1. Cyclic Voltammetry

Cyclic voltammetry (CV) has proven to be a powerful tool for identifying and studying PCET. For a chemically reversible half-reaction written as a reduction half-reaction, the pH dependence of a PCET couple is given by eq 56.

$$E = E^0 + \left(\frac{RT}{nF} \right) \ln \left(\frac{[\text{Ox}]}{[\text{Red}]} \right) - \frac{2.303mRT}{nF} \text{pH} \quad (56)$$

In this equation, $[\text{Ox}]$ is the concentration of the oxidized form of the couple, $[\text{Red}]$ is the concentration of the reduced form, and E^0 is the formal potential. The numbers of electrons and protons transferred are represented by n and m , respectively. E is the measured potential, while R , T , and F are the gas constant, temperature, and Faraday constant, respectively. According to this expression, the slope of a plot of E versus pH should be $-2.303mRT/nF$. If the number of electrons transferred is known, the number of protons transferred can be determined by use of eq 56.

Bond and co-workers¹⁸⁵ used this method to determine the number of protons transferred in the PCET reduction of highly charged lacunary anions, such as $[\alpha\text{-SiW}_{11}\text{O}_{39}]^{8-}$ and $[\alpha\text{-PW}_{11}\text{O}_{39}]^{7-}$. In aprotic solvents such as acetonitrile, they undergo simple 1e^- reduction; however, in protic media with added buffers, such as HOAc/OAc⁻ (acetic acid/acetate), noninteger values for m with $m \neq n$ were observed. As an example, for $[\alpha\text{-SiW}_{11}\text{O}_{39}]^{8-}$, $m = 2.4$ and $n = 2$. Incorporating a multisquare, multiple acid–base equilibria scheme utilizing experimentally determined E^0 and equilibrium constant (K) values (Scheme 32, simulated CVs were generated using Digisim which were in excellent agreement with experimentally obtained CVs. Noninteger values of m were explained by a multisquare, multiacid base equilibrium mechanism. Noninteger values for m were obtained because the numbers of protons and electrons involved are different in the interconnected square schemes. As shown in Scheme 32, 12 protons and 10 electrons are involved in the multiple equilibria. Recently, the same authors reported on the one-electron reduction of Keggin-type polyoxometalate anions (POMs) $[\text{XV}^{\text{V}}\text{M}_{11}\text{O}_{40}]^{4-}$, where X = P, As; M = Mo, W.¹⁸⁶ In aprotic solvents, the number of proton transfers associated with one-electron reduction was found to be 2. They observed noninteger values for m with $m \neq n$.

Determination of m and n for PCET reactions are routinely made from plots of half-wave potential ($E_{1/2}$) from voltammetric measurements as a function of pH, so-called Pourbaix diagrams.¹⁸⁷ In these measurements $E_{1/2}$ varies with a slope of 59 mV (m/n) per pH unit (at 25 °C) according to the Nernst equation with m/n calculated from the slope.

Pourbaix diagrams have also been used to determine pK_a values. Figure 63 illustrates the Pourbaix diagram for the μ -tri-

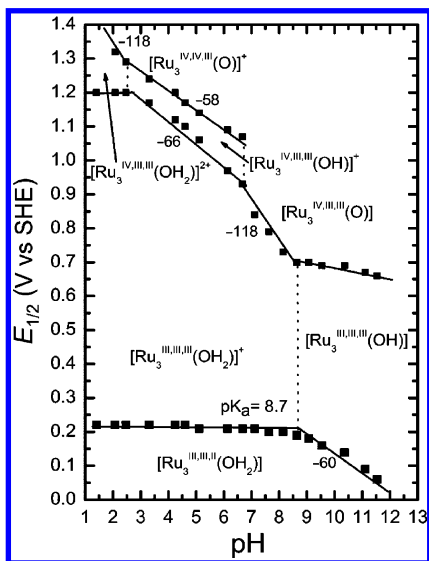


Figure 63. Pourbaix diagram for $[\text{Ru}_3\text{O}(\text{Ac})_6(\text{py})_2(\text{OH}_x)]^n$ in aqueous solution; pK_a values (vertical dotted lines) and slopes (in mV) are also noted in the figure. Reproduced with permission from ref 134b. Copyright 2006 Wiley.

Ru cluster $[\text{Ru}_3\text{O}(\text{Ac})_6(\text{py})_2(\text{OH}_x)]^n$.^{134b} The value $pK_a = 8.7$ for the equilibrium, $[\text{Ru}_3^{\text{III},\text{III},\text{III}}(\text{H}_2\text{O})]^+ = [\text{Ru}_3^{\text{III},\text{III},\text{III}}(\text{OH})] + \text{H}^+$, illustrated in the figure is in good agreement with the pK_a value determined by spectrophotometry.

Recently, Wang et al.¹⁸⁸ reported a Pourbaix diagram for $[\text{Fe}^{\text{IV}}\text{O}(\text{N}4\text{Py})]^{2+}$ ($\text{N}4\text{Py} = N,N\text{-bis}(2\text{-pyridylmethyl})\text{bis}(2\text{-pyridyl)methylamine}$). The $\text{Fe}^{\text{IV}/\text{III}}$ couple has a slope of 55 mV per pH unit, consistent with a $1\text{e}^-/\text{1H}^+$ PCET couple. This is the first instance where a $\text{Fe}^{\text{IV}}=\text{O}$ complex displays a reversible $\text{Fe}^{\text{IV}}=\text{O}/\text{Fe}^{\text{III}}-\text{OH}$ wave. The reactivity of the oxo complex was promising. It oxidizes dihydroanthracene (DHA) with a rate constant of $18 \text{ M}^{-1} \text{ s}^{-1}$.

Cyclic voltammetry is used extensively to determine diffusion coefficients for both irreversible (eq 57a) and reversible reactions (eq 57b) by application of the Randles–Sevcik equation.⁴³ In these experiments, the peak current (I_p) is measured as a function of scan rate (ν), while the diffusion coefficient is determined from a plot of I_p versus $\nu^{1/2}$. In these equations n , D_0 , C , A , and α are the number of electrons transferred, the diffusion coefficient, the concentration of diffusional species, the area of the electrode, and the charge transfer coefficient, respectively.

$$I_p = (2.99 \times 10^5) n^{3/2} \alpha^{1/2} A D_0^{1/2} C \nu^{1/2} \quad (57\text{a})$$

(irreversible reaction)

$$I_p = (2.69 \times 10^5) n^{3/2} \alpha^{1/2} A D_0^{1/2} C \nu^{1/2} \quad (57\text{b})$$

(reversible reaction)

This technique was used to determine the diffusion coefficient for protons in a ferrocyanide-incorporated solid electrolyte through a Nafion ion-exchange membrane. A linear relationship for I_p versus $\nu^{1/2}$ and application of eq 57a for irreversible reactions, yielded a diffusion coefficient of $4.8 \times 10^{-12} \text{ cm}^2/\text{s}$. This value is 7 orders of magnitude smaller than the diffusion coefficient in water, demonstrating slow proton transfer in the ion-exchange membrane.¹⁸⁹ Utilizing this value for the diffusion coefficient, the standard rate constant (k^0) was determined for the oxidation of absorbed hydrogen by eq 58 for reversible electron transfer.

$$E_p = E^0 - \frac{RT}{\alpha F} \left[0.78 + \ln \left(\frac{D_0^{1/2}}{k^0} \right) + \ln \left(\frac{\alpha F \nu}{RT} \right)^{1/2} \right] \quad (58)$$

CV has also been applied to the study of reaction kinetics at electrodes. For diffusion-controlled reactions that are chemically reversible, anodic (oxidative) and cathodic (reductive) peak potentials are independent of scan rate with a peak-to-peak separation ($\Delta E_p = E_{p,a} - E_{p,c}$) of 59/n mV at 25 °C.¹⁹⁰ If the kinetics of the heterogeneous reaction, including PCET, become comparable to the scan rate, ΔE_p increases with increasing scan rate and rate information can be extracted from its dependence on ν . On the basis of an analysis by Nicholson¹⁹⁰ for a quasi-reversible reaction, the surface rate constant (k^0) is related to a dimensionless parameter (ψ), defined by eq 59, where D_O and D_R are the diffusion coefficients for the oxidized and reduced forms of the couple, respectively.

$$\psi = \left(\frac{RT}{\pi D_O F \nu} \right) \left(\frac{D_O}{D_R} \right)^{\alpha/2} k^0 \quad (59)$$

ψ is related to the difference between the peak potential (E_p) and formal potential (E^0) in mV at different scan rates, ($\Delta E'_p = E_p - E^0$) as defined by eq 60.

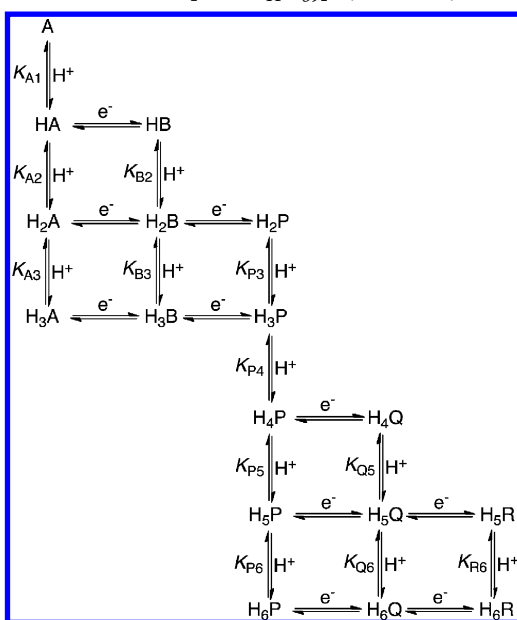
$$\ln \psi = 3.69 - 1.161 \ln(\Delta E'_p - 59) \quad (60)$$

Mayer and co-workers^{90a} applied this method to the determination of rate constants for the oxidation of phenols hydrogen bonded to various bases including the primary amine (HCPh_2NH_2), imidazole, and pyridine. Observed peak potentials for oxidation of these hydrogen-bonded phenols are lower than for non-hydrogen-bonded phenols, and the oxidation mechanism was deduced to be EPT as discussed in section 3.1.2. Nicholson's method was also applied by Evans and Compton¹⁹¹ for kinetic studies of *N,N*-dimethyl-*p*-toluidine (DMT) oxidation at room temperature in the ionic liquid *N*-methyl-*N*-butylpyrrolidinium bis(trifluoromethylsulfonyl)imide. Similar results were obtained to those previously reported in aprotic media.

For an irreversible PCET reaction, the peak potential shift relative to the formal potential ($E_p - E^0$) is given by eq 58. It allows the heterogeneous rate constant (k^0) to be determined from scan rate measurements, if the diffusion coefficient is known and certain assumptions are made about α .

As an example, Gupta and Sindal¹⁹² determined irreversible heterogeneous PCET rate constants for the reduction of five different Schiff bases based on 3-[5-phenylpyrazol-3-ylimino]-indol-2-ones in which the benzene ring was substituted by halogen atoms. The structure and proposed mechanism are shown in Scheme 33. Rate constants were similar ($1.3\text{--}8.4 \times 10^{-8} \text{ cm s}^{-1}$) throughout the series. For this series of halogen

Scheme 32. Illustrating the Multisquare, Multiple Acid–Base Equilibria Scheme for $[\alpha\text{-SiW}_{11}\text{O}_{39}]^{8-}$; $m = 2.4$, $n = 2^a$



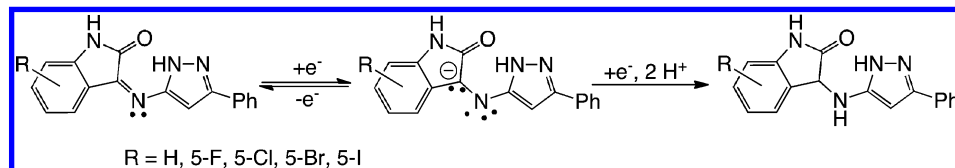
^aReproduced with permission from ref 185. Copyright 2006 American Chemical Society.

substituents, reduction peak potentials (E_p) decreased in the order I > Br > Cl > F > H, the order of decreasing electron-withdrawing ability of the substituent.

For an irreversible catalytic reaction followed by a reversible reaction, the catalytic rate constant (k_{cat}) can be determined from the slope of i_{cat}/i_p plotted against $\varphi^{1/2}$ (i_{cat} is the catalytic current at the catalytic peak potential; i_p is the peak current in the absence of substrate; and $\varphi = k_{\text{cat}}RT/nF\nu$). Nunes et al.^{134b} measured k_{cat} for catalytic benzyl alcohol oxidation by the Ru=O(IV,IV,III)/Ru-OH(IV,III,III) couple of $[\text{Ru}_3\text{O}(\text{Ac})_6(\text{Py})(\text{OH}_2)]^+$. The catalytic wave was associated with a ruthenium oxo-[IV,IV,III]/ruthenium hydroxo-[IV,III,III] PCET couple. The oxidation of benzyl alcohol proceeded by a two-electron transfer to generate benzaldehyde with $k = 2.2 \times 10^2 \text{ M}^{-1} \text{ s}^{-1}$. This rate constant is ~ 10 times higher than the previously reported rate constant for benzyl alcohol oxidation by $[\text{Ru}^{\text{IV}}(\text{tpy})(\text{bpz})(\text{O})]^{2+}$ (tpy = 2,2',2"-terpyridine, bpz = 2,2'-bipyrazine) at pH 11,¹⁹³ probably due to a greater driving force given the reduction potentials for $[\text{Ru}_3^{\text{IV},\text{IV},\text{III}}\text{O}(\text{Ac})_6(\text{py})_2(\text{O})]^+$ ($E^0 = 1.1 \text{ V}$ at pH 6.7) and $[\text{Ru}^{\text{IV}}(\text{tpy})(\text{bpz})(\text{O})]^{2+}$ ($E^0 = 0.90 \text{ V}$ at pH 11).

CV has also been used to measure formation constants for hydrogen-bonded adducts to $\text{O}_2^{\bullet-}$ in MeCN.¹⁹⁴ Reduction of O_2 by 1e^- gives $\text{O}_2^{\bullet-}$ ^{194a} which forms 1:1 and 1:2 complexes with weak acids (HA). Formation constants, K_1 and K_2 , have been determined for these complexes.

Scheme 33. Adapted from Ref 192

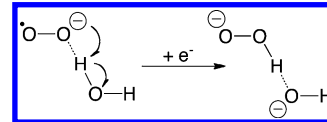


In this case, the observed formal potential with added HA ($E_{1,\text{HA}}^0$) is related to the standard potential with no HA added (E_1^0), the concentration of HA (C_{HA}), and the formation constant as shown in eq 61. Fits of formal potential with increasing HA concentration ($E_{1,\text{HA}}^0$ versus $\ln(C_{\text{HA}})$) were used to determine K values for the weak acids water, isopropanol, and methanol.

$$E_{1,\text{HA}}^0 = E_1^0 + \frac{RT}{F} \ln[1 + K_1 C_{\text{HA}} + K_1 K_2 C_{\text{HA}}^2] \quad (61)$$

Following formation of 1:1 or 1:2 complexes with HA, the complexed superoxide acts as a reactant for the second step. In the second step, both a proton from HA and an electron from the electrode are transferred to superoxide, generating HO_2^- and A^- , via an EPT pathway (Scheme 34, with HA = H_2O). A

Scheme 34. Electrochemical EPT with Proton Transfer from Added Water^{194a}



significant KIE was observed for this step varying from 2.4 (HA = isopropanol) to 5.6 (HA = methanol) at maximum acid concentrations. The KIEs support the proposed EPT mechanism.

Using CV measurements, Savéant and co-workers have unraveled the mechanisms of PCET reactions through detailed kinetic analyses with rate constants experimentally determined by the Nicholson method. For EPT pathways, they derived an expression for the electrochemical rate constant (k_s^{ap}) as a function of electrode potential.^{63c,195} This expression is shown in eq 62, where Z_{el} , χ , λ , and ΔZPE are the collision frequency, transmission coefficient, reorganization energy, and difference between the transferring proton zero-point energies at the transition state and at the reactant state, respectively.

$$k_s^{\text{ap}}(E) = Z_{\text{el}}\chi \exp\left[-\frac{\lambda}{4RT}\left(1 - F\frac{E - E^0}{\lambda}\right) - \frac{\Delta\text{ZPE}}{RT}\right] \quad (62)$$

Figure 64 is a schematic representation of an EPT pathway. In this representation four diabatic states are mixed to generate two states that are adiabatic toward proton transfer (upper inset). According to the Born–Oppenheimer approximation, because both the transferring electron and proton are light particles compared to the other atoms, their transfer requires reorganization of heavy atom motions, including solvent, to reach a transition state where both reactants and products have the same configuration. According to the authors, a second application of the Born–Oppenheimer approximation dictates that the electron transfers at the crossing intersection of the

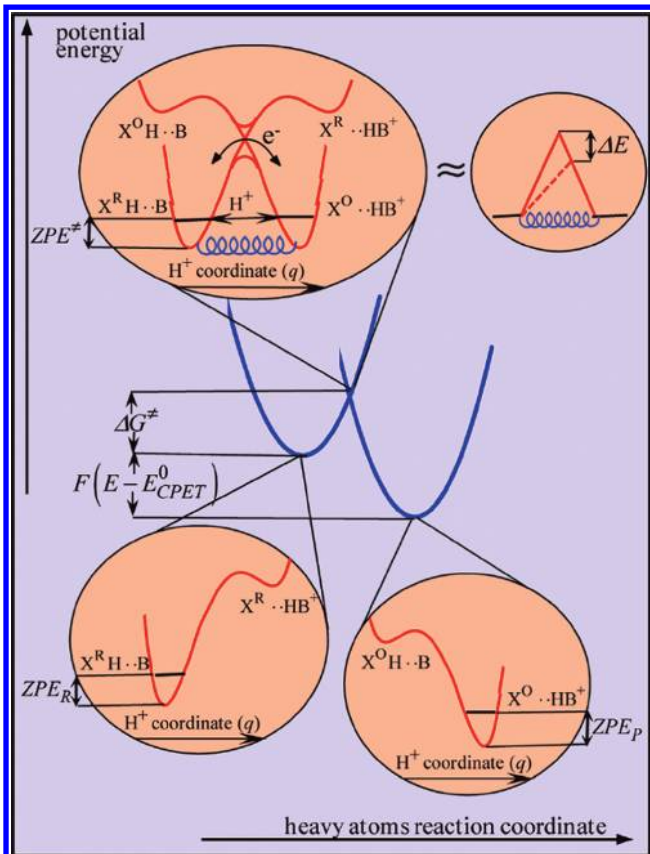


Figure 64. Schematic representation of the potential energy profiles for an EPT mechanism. Please note CPET in figure is described as EPT in the text. Reproduced with permission from ref 195. Copyright 2010 American Chemical Society.

potential energy profiles for the resulting two states, while the proton tunnels through the barrier (Figure 64).

Assuming that both collision frequencies and reorganization energies remain the same for both proton and deuterium transfer, eq 62 can be rewritten as eq 63, giving an expression for the kinetic isotope effect (KIE) for an EPT reaction.

$$\frac{k_{s,H}^{ap}}{k_{s,D}^{ap}} = \frac{\chi_H}{\chi_D} \exp \left[\frac{-\Delta ZPE_H + \Delta ZPE_D}{RT} \right] \quad (63)$$

According to eq 63, a significant KIE is expected for the EPT pathway, because $k_{s,H}^{ap}/k_{s,D}^{ap}$ essentially depends on the variation in the zero-point energies (ΔZPE) and on the transmission coefficient (χ) of proton versus deuterium. For adiabatic EPT, i.e., for $\chi = 1$, a typical KIE is on the order of 1.5, with larger values expected as the degree of nonadiabaticity increases. For example, the KIE in the case of *ortho*-substituted tertiary amine phenol oxidation was 1.6, indicating that an adiabatic EPT mechanism was operating,^{63d} whereas a KIE of 2.5 was observed for phenol oxidation in water, where water acts as a proton acceptor. This value indicates an adiabatic or quasi-adiabatic EPT mechanism.¹⁹⁶

In an interesting recent report, Savéant and co-workers studied long-distance EPT by inserting a hydrogen-bond relay between the group being oxidized and the distant proton acceptor (Figure 65).¹⁹⁷ In this case, proton movement over distances as large as 4.3 Å was possible. Moreover, a significant KIE indicated that EPT prevailed. This finding may provide

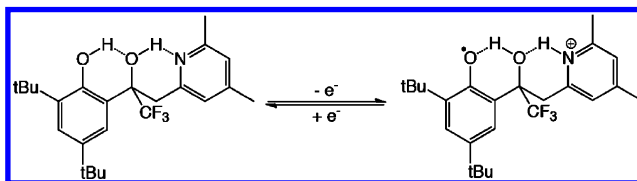


Figure 65. Long-distance proton-coupled electron transfer achieved by inserting a hydrogen-bonded relay. Reproduced with permission from ref 197. Copyright 2010 Wiley.

another clue to the involvement of EPT in biological EPT as a way to avoid high-energy intermediates, even at very long electron transfer distances.

Most of the recent reports by Savéant and co-workers for PCET reactions involve EPT mechanisms. However, for oxidation of $[\text{Os}^{II}(\text{bpy})_2(\text{py})(\text{OH}_2)]^{2+}$, they found that stepwise mechanisms (ET-PT and PT-ET) prevail.¹⁹⁸ As shown in Figure 66, the PCET rate constant for $\text{Os}^{II/III}$

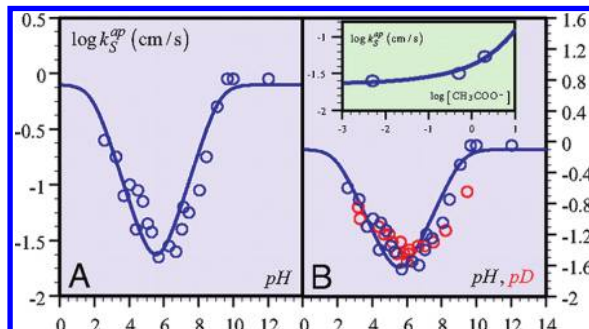
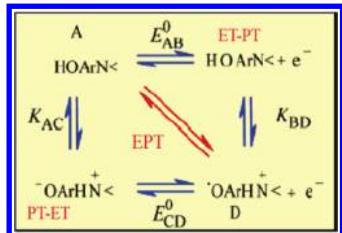


Figure 66. Variation of the apparent standard rate constant for the $\text{Os}^{III}(\text{bpy})_2(\text{py})(\text{OH}_2)^{3+}/\text{Os}^{II}(\text{bpy})_2(\text{py})(\text{OH}_2)^{2+}$ couple with pH. (A and B) Blue dots are experimental rate constants in 0.1 M Britton–Robinson buffers in water, and solid lines represent predicted variation of rate constants based on the stepwise ET-PT and PT-ET mechanisms. (B) Red dots are 0.1 M Britton–Robinson buffers in D_2O . Inset shows the dependence of the apparent standard rate constant with increasing buffer base concentration in an acetate buffer of pH 5 in water. Reproduced with permission from ref 198b. Copyright 2009 National Academy of Sciences (USA).

oxidation decreased with increasing pH below pH 6. Above pH 6, the PCET rate constant increased with increasing pH. These results support an acidic medium ET-PT mechanism and a basic medium PT-ET mechanism as expected from eq 64. Figure 66 also reveals that no KIE was observed, further supporting stepwise mechanisms. The onset of an EPT contribution was observed in only one instance. In this case, EPT was indicated by a slight enhancement of the PCET rate when the acetate concentration was raised to 2 M (inset Figure 66B).

$$k_{s,III/II}^{ap} = k_{s,III/II}^{\text{ET-PT}} \sqrt{\frac{[\text{H}^+]}{K_{\text{M}^{II}\text{OH}_2}}} + k_{s,III/II}^{\text{PT-ET}} \sqrt{\frac{K_{\text{M}^{II}\text{OH}_2}}{[\text{H}^+]}} \quad (64)$$

Simulation of cyclic voltammetry waveforms by Digisim has been applied by Savéant and co-workers to confirm EPT mechanisms of PCET reactions. In Scheme 35 are shown three different mechanistic pathways for electrochemical oxidation of *ortho*-substituted 4,6-di(*tert*-butyl)phenol. The ET-PT and PT-ET equilibrium constants in Scheme 35 are predicted to follow the relationship in eq 65. In the scheme, E_{CD}^0 , E_{AB}^0 , and E_{AD}^0 are known and eq 65 can be used to estimate K_{AC} and K_{BD} .

Scheme 35 ^a

^aReproduced with permission from ref 199; Copyright 2006 American Chemical Society.

Figure 67a shows that experimental voltammograms match with simulated voltammograms generated by assuming an EPT

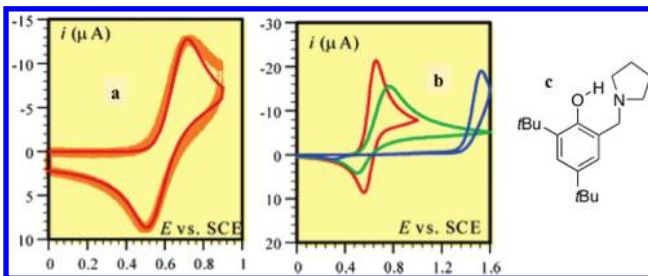


Figure 67. (a) CVs for an *ortho*-substituted phenol, structure shown in (c), at a scan rate of 0.2 V/s in a 0.1 M *n*-Bu₄NPF₆ acetonitrile solution at 20 °C. Dotted line is experimental and solid line is the simulated CV assuming an EPT pathway. (b) Red line is the experimental CV for (c); the blue and green lines are simulations based on the square scheme mechanism (Scheme 35), with $E_{AB}^0 = 1.59, 1.39$ V and $E_{CD}^0 = 0.23, 0.43$ V versus SCE, respectively, and $\lambda = 0.7$ eV, $K_{AC} = 3.5 \times 10^{-7}, 9.8 \times 10^{-4}$, $K_{BD} = 9 \times 10^{16}, 3.2 \times 10^{13}$ for both cases. λ is the reorganization energy. Note that PCET rate constant determinations for individual steps require assumption of a λ value (e.g., eq 62). Reproduced with permission from ref 199. Copyright 2006 American Chemical Society.

mechanism. By contrast, Figure 67b shows that simulated voltammograms generated by stepwise mechanisms ET-PT and PT-ET do not match the experimental results.

$$E_{AD}^0 = E_{AB}^0 - \left(\frac{RT}{F} \right) \ln K_{BD} = E_{BD}^0 - \left(\frac{RT}{F} \right) \ln K_{AC} \quad (65)$$

CV simulations of PCET reactions and PCET-catalyzed reactions have mainly utilized two commercial packages, Digisim²⁰⁰ and DigiElch.²⁰¹ Both are based on fast implicit finite difference (FIFD) algorithms. The programs construct matrices for carrying out simulations based on user-defined CV physical and chemical parameters. Some parameters are measured or estimated, and some parameters are automatically computed. The simulators allow the user to define mechanistic schemes, cyclic voltammetric parameters, concentrations of reactant species, kinetic rate constants, thermodynamic parameters, diffusion coefficients, double-layer capacitance, uncompensated cell resistance, and electrode geometry. The simulator creates concentration profiles of reacting species and their contribution to the CV response.

These simulations have allowed routine analysis of cyclic voltammetric responses and elucidation of complex electrochemical mechanisms. As noted above, they have been utilized to unravel complex PCET reaction mechanisms.^{63c,90a,95,194,198,202} However, there are limitations. Frumkin effects, arising from

potential drops across the diffuse double layer between the outer Helmholtz plane and the bulk solution, are not included. Also, this approach cannot simulate CVs for disk and band electrode geometries.

CV is the most widely used electrochemical technique for the kinetic study of PCET reactions, but there are fundamental limitations to its application. CV is a stationary technique, and slow mass transport can lead to insignificant currents and poorly defined waveforms. Because of uncompensated cell resistance, excess peak splitting equal to iR_s (i is the current and R_s is uncompensated cell resistance) is included. This complication leads to erroneous estimations of rate constants. A correction can be made by determination of uncompensated cell resistance by using EIS spectroscopy (section 6.3). Finally, an issue arises because double-layer charging increases linearly with increasing scan rate whereas peak current (due to the diffusion of reactive species) increases with the square root of the scan rate (eq 57). As a result, CV peak currents at high scan rates become small relative to double-layer charging, and this causes the determination of peak potentials to be difficult. Problems arising from iR_s drop and double-layer charging can be avoided by using ultramicroelectrodes (UMEs). They generate smaller currents, decreasing iR_s and double-layer charging to a significant degree.

6.2. Rotating-Disk Electrode Voltammetry

In applications using rotating-disk electrodes (RDEs), the working electrode is rotated at a constant rate, whereas the current–voltage (I – E) curve. Hydrodynamic techniques, such as RDE, have advantages over stationary techniques like CV. Because the electrode is rotating, the electrolyte solution at the working electrode is continuously renewed. This allows a steady state to be reached quickly, and double-layer charging is no longer important. Furthermore, rates of mass transfer are enhanced, resulting in larger currents and making uncompensated cell resistance insignificant.

In RDE, the limiting current (I_L) follows the Levich eq 66. The cathodic limiting current and the subscript “O” for D means that the relevant diffusion coefficient is for the oxidized species. If, instead, the reactant is being oxidized and the limiting current is anodic, then the relevant diffusion coefficient is the one for the reduced species. In this equation ω and γ are the rotation speed of the electrode and the kinematic viscosity of the solution, respectively. A plot of I_L versus ω is used to determine the diffusion coefficient. Direct application of the Levich equation by Guo et al. was used for the determination of diffusion coefficients for highly charged lacunary anions such as $[\alpha\text{-SiW}_{11}\text{O}_{39}]^{8-}$ and $[\alpha\text{-PW}_{11}\text{O}_{39}]^{7-}$.¹⁸⁵ Determination of diffusion coefficients by CV and RDE usually provides consistent values; however, if uncompensated cell resistance is high, diffusion coefficients determined by these two techniques can differ. In that case, RDE results are more accurate because they are unaffected by uncompensated cell resistance.

$$I_L = 0.62nFAD_0^{2/3}\omega^{1/2}\gamma^{-1/6}C \quad (66)$$

Similar to CV experiments, rate constants can be determined by RDE based on Koutecky–Levich plots. These plots are generated from eq 67.⁴³ Although RDE has advantages over CV, it also has limitations. Reproducible mass transfer conditions are more difficult to obtain. CV is more widely

used because of ease of use and interpretation of results by digital simulation.

$$\frac{1}{I} = \frac{1}{I_K} + \frac{1}{I_L} = \frac{1}{I_K} + \frac{1}{0.62nFAD_0^{2/3}\omega^{1/2}\gamma^{-1/6}C} \quad (67)$$

6.3. Electrochemical Impedance Spectroscopy

Electrochemical impedance spectroscopy (EIS) is a stationary electrochemical technique, like CV, but the current response is monitored with an AC potential, instead of a DC potential. Because of the AC input, the resulting current lags by a phase angle (ω) from the applied potential. On the basis of Ohm's law, resistances/impedances are calculated at different ω 's. The measured impedance has both imaginary and real components, and these are plotted against each other in a "Nyquist plot" (Figure 68). The electrochemical cell used is modeled as a

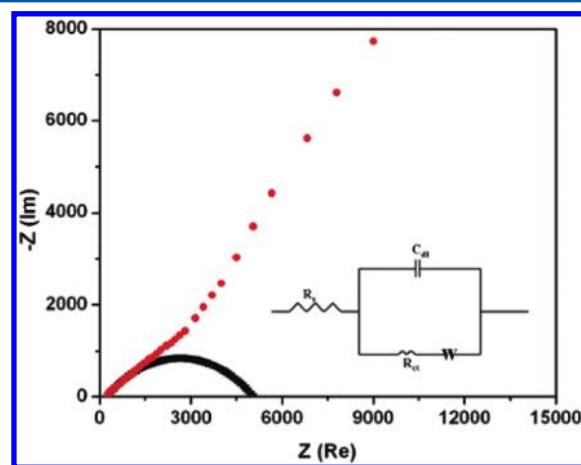


Figure 68. Impedance measurements in a Nafion membrane containing equal amounts of $K_3[Fe(CN)_6]$ and $K_4[Fe(CN)_6]$ (3.4×10^{-3} M) obtained by applying a 10 mV root-mean-squared (rms) AC signal in the frequency range 10–100 kHz. (Inset bottom right: equivalent circuit corresponding to the semicircle fitted with the high-frequency part of the response.) Reproduced with permission from ref 189. Copyright 2006 American Chemical Society.

Randles equivalent circuit (inset of Figure 68). In an EIS study, the impedance usually arises from a combination of four factors in the cell: (i) solution resistance (R_s), (ii) impedance due to electron transfer/PCET (R_{ct}), (iii) impedance due to mass transfer/Warburg impedance (W), and (iv) double-layer capacitance/charging (C_{dl}). The entire current passes through R_s ; hence, R_s is inserted as a series element. The sum of Faradaic impedances (R_{ct} and W) and double-layer capacitance (C_{dl}) are inserted in parallel in the circuit. From the intercept in the real part of impedance in the Nyquist plot (x -axis of Figure 68), R_{ct} and R_s can be calculated, because $\omega \rightarrow \infty$ corresponds to R_s and $\omega \rightarrow 0$ corresponds to the sum of R_{ct} and R_s . At these limits heterogeneous rate constants (k^0) can be calculated by eqs 68a and 68b, where E_{eq} is the equilibrium redox potential and C_0^* is the bulk concentration of the ions.

A typical Nyquist plot is shown in Figure 68 (taken from ref 189). Parthasarathy et al.¹⁸⁹ applied this technique to measure charge-transfer resistance across the polymer membrane Nafion in the PCET oxidation of $[Fe(CN)_6]^{4-}$ anion as mentioned previously. They used these EIS results to determine heterogeneous rate constants, i.e., 5.7×10^{-6} cm/s, and this value was in good agreement with results obtained by CV.

$$R_{ct} = \frac{RT}{nF^2 I_0} \quad (68a)$$

$$I_0 = nFAk^0 C_0^* \exp[-\alpha F(E_{eq} - E^0)] \quad (68b)$$

A major disadvantage of the EIS technique is the equivalent circuit modeling. Often equivalent circuits are more complicated than simple Randles circuits and may involve more than the four contributing factors listed above. For example, a constant phase element due to surface roughness may make a significant contribution to the electrochemical response. Under those circumstances, corresponding capacitance or resistance components have to be incorporated in the equivalent circuit. Incorporating contributors into the equivalent circuit can be challenging.

6.4. Spectroelectrochemistry

Spectroelectrochemistry is a powerful technique in which an electrochemical method such as CV is combined with a spectroscopic technique such as UV-vis or IR. Integration of electrochemistry and spectroscopy has proven to be extremely useful in identification of different oxidation states of inorganic complexes through spectral changes during electrochemical potential sweeps and has been applied to PCET studies. Recently Baitalik et al.²⁰³ reported spectroelectrochemical results on $[(bpy)_2Ru(H_2pzbzim)Ru(bpy)_2]^{3+}$ (pzbzim = pyrazolyl-3,5-bis(benzimidazole)) in which $Ru^{II}Ru^{II}$ is oxidized to $Ru^{III}Ru^{III}$ in two steps through PCET and stepwise proton loss. Figure 69a shows that, as $Ru^{II}Ru^{II}$ converts to $Ru^{II}Ru^{III}$, the intensity of metal-to-ligand charge transfer (MLCT) bands for $Ru^{II}Ru^{II}$ at 490 and 432 nm decreased with new bands appearing between 600 and 1100 nm. Deconvolution of spectral feature between 600 and 1100 nm (inset of Figure 69a) revealed near bands at 695 and 910 nm, respectively. The band at 695 nm arises from a ligand-to-metal charge transfer (LMCT) transition, and the band at 910 nm arises from intervalence transfer (IT) or intervalence charge transfer (IVCT). Further oxidation to $Ru^{III}Ru^{III}$ causes the 695 nm band to be blue-shifted; the band at 910 nm disappears, and a new band appears at 1100 nm, presumably due to a $\delta\pi-\delta\pi$ transition.

7. HETEROGENEOUS PCET

Since the 2007 review on PCET by Meyer and co-workers, the study of PCET in heterogeneous systems has continued and been extended.¹ Table 1 highlights important systems, covered in the current review, studied between 2006 and 2010. As can be seen from the results obtained, surface studies have facilitated acquisition of fundamental insights into PCET mechanisms and provided results of relevance to biology and catalysis.

7.1. Nonbiological

7.1.1. Liquid–Liquid Interfaces. Liquid–liquid interfaces can be used to control reactions involving PCET and function as models for soft interfaces, most notably membranes of importance to PCET in biology.²⁰⁴ The interface between two immiscible electrolyte solutions (ITIES) can provide a means for separating products from reactants and avoiding further undesired reactions. PCET can occur at these interfaces with a proton source on the aqueous acid side and lipophilic electron donors or acceptors on the organic side.^{204,205} Polarization at the interface can be used to influence interfacial proton or electron transfer rates and can be modulated by applying an

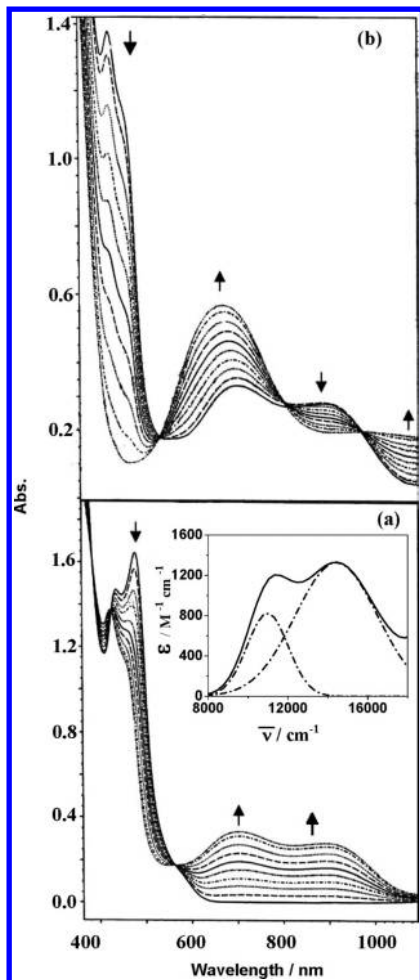


Figure 69. Spectroelectrochemical changes in acetonitrile during the oxidation of $[(\text{bpy})_2\text{Ru}(\text{H}_2\text{pbzim})\text{Ru}(\text{bpy})_2]^{3+}$: $\text{Ru}^{\text{II}}\text{Ru}^{\text{II}} \rightarrow \text{Ru}^{\text{II}}\text{Ru}^{\text{III}}$ (a) and $\text{Ru}^{\text{II}}\text{Ru}^{\text{III}} \rightarrow \text{Ru}^{\text{III}}\text{Ru}^{\text{III}}$ (b) with loss of a proton at each stage. Inset shows the intervalence charge transfer (IVCT) band obtained by spectral deconvolution. Reproduced with permission from ref 203. Copyright 2010 Wiley.

Table 1. Summary of Types of Heterogeneous PCET Investigations Between 2006 and 2010 Including Potential Applications; See Below for Details

solid state examples	solid–liquid interfaces	liquid–liquid interfaces
metal complexes in polymers	activated electrode surfaces absorbed species metal oxides ionic liquids surface functionalized electrodes excited-state semiconductor interfaces	aqueous–organic interfaces
applications	fuel cells solar cells	electrocatalysis photocatalysis protein film voltammetry
		isolation of reactive products mimicking membranes

external voltage or by controlling the distribution of a common ion between phases. The latter creates a Galvani potential

difference across the interface. A schematic design for controlling external voltage is shown in Figure 70.^{204,206}

Oxygen reduction by PCET has been studied at ITIES. The results obtained are applicable to development of fuel cells and for gaining insight into related biological processes such as respiration that occur at membrane-bound proteins.^{206b,207} Application of the biphasic approach can also provide a means for isolating H_2O_2 , a product that is often unstable due to its participation in redox reactions.^{206b}

Recent studies of O_2 reduction at ITIES have all utilized a polarized water/1,2-dichloroethane (DCE) interface, in which protons are supplied at the aqueous acidic side and electrons are supplied at the DCE side by decamethyl ferrocene (DMFc) or other ferrocene derivatives.^{204,205,206b,207b,208} Uncatalyzed reduction of O_2 to H_2O_2 was shown to occur at the ITIES with rate controlled by polarization of the interface. Interfacial polarization provides the driving force for proton transfer to the organic phase. On the basis of DFT calculations, it has been proposed that DMFc complexes with O_2 in the organic phase generate superoxide anion, which is protonated by water. Once produced, HO_2^\bullet is subsequently reduced by a second DMFc to generate H_2O_2 , and it diffuses across the interface into the aqueous phase.^{205a}

Both cobalt(II) porphine (CoP) and 5,10,15,20-tetr phenylporphyrinatocobalt(II) ($[\text{Co}(\text{TPP})]$) have been shown to catalyze the reduction of O_2 by ferrocenes at ITIES.^{204,208b} In both cases, O_2 is reduced, at least in part to H_2O_2 . Catalysis rates are dependent on both the reduction potential of the electron transfer donor and the rate at which protons are transported across the ITIES. The proposed mechanism is shown in Figure 71.

In the case of CoP catalysis, the major reduction product is water, which could be generated by either 2e^- or 4e^- interfacial PCET.²⁰⁴ Both pathways would occur by pH-dependent voltammetry, and the observed peak current for reduction shifts by $\sim 60 \text{ mV/pH}$ unit at $\sim 293 \text{ K}$, consistent with a PCET half-reaction involving equal numbers of protons and electrons with $m = n$ in eq 69. The observation of catalytic currents only at positive potentials relative to Ag/AgCl suggests a two-electron pathway because a four-electron pathway should allow catalysis at significantly more negative potentials, based on standard redox potentials; however, neither initial 2 or 4e^- reduction could be ruled out.

$$\Delta E = \frac{0.059m}{n} \text{pH} + \left(\frac{RT}{nF} \right) \ln \left(\frac{[\text{Ox}]}{[\text{Red}]} \right) \quad (69)$$

Platinum particles generated at ITIES have been shown to catalyze the reduction of oxygen by an overall 4e^- reduction.^{207b} It has been proposed that the particles behave as bipolar electrodes with reduction of O_2 on the aqueous side of the particles and oxidation of DMFc on the organic side. The rate-limiting step in catalytic reduction appears to involve one-electron reduction of platinum-adsorbed O_2 by DMFc. There is no evidence for concerted proton transfer. The rate of O_2 reduction is only slightly dependent on pH in the aqueous side below pH 9.7. Above this pH the rate of reduction decreases, perhaps due to a transition from the normal to the activationless electron transfer limit in terms of free-energy change as predicted by a semiphenomenological theory of electrode kinetics.

In an entirely different system, PCET has been studied at a liquid–liquid interface by electrogenerated chemiluminescence

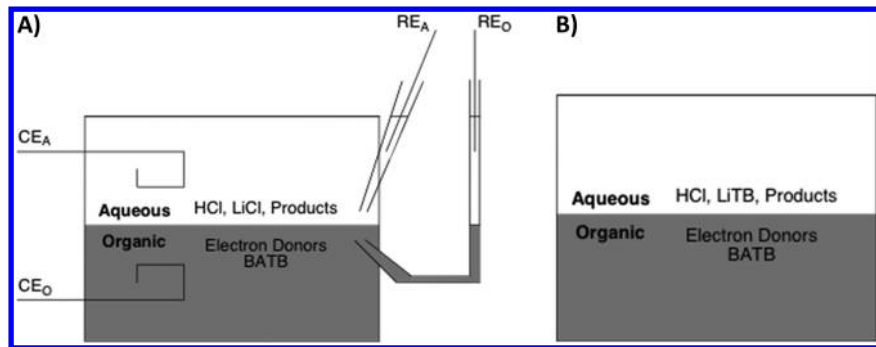


Figure 70. Experimental designs for polarizing liquid–liquid interfaces: (A) by applying an external voltage and (B) by using a common ion to generate a Galvani potential difference. CE_A = aqueous counter electrode; RE_O = reference electrode for the organic phase; BA^+ = bis(triphenylphosphoranylidene)ammonium cation; TB^- = tetrakis(pentafluorophenyl)borate anion.²⁰⁴

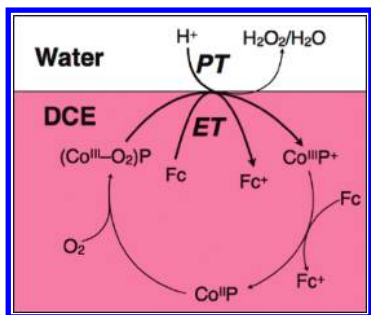


Figure 71. Proposed ITIES mechanism for O_2 reduction by a cobalt porphyrin catalyst.^{204,208b} Reproduced with permission from ref 204. Copyright 2009 American Chemical Society.

(ECL).²⁰⁹ In this system, femtoliter droplets of trioctylamine (Oc_3N) were immobilized on a glassy carbon electrode and immersed in an aqueous solution of $\text{Ru}(\text{bpy})_3^{2+}$, as depicted in Figure 72. Electrogeneration of $\text{Ru}^{\text{III}}(\text{bpy})_3^{3+}$ occurs where the aqueous phase directly interacts with the electrode. Reduction of $\text{Ru}^{\text{II}}(\text{bpy})_3^{2+}$ to $\text{Ru}^{\text{II}}(\text{bpy})_2(\text{bpy}^\bullet)^+$ occurs at the liquid–liquid interface. ECL is produced by ET between $\text{Ru}^{\text{III}}(\text{bpy})_3^{3+}$ and $\text{Ru}^{\text{II}}(\text{bpy})_2(\text{bpy}^\bullet)^+$, which gives the excited state: $\text{Ru}^{\text{III}}(\text{bpy})_3^{3+} + \text{Ru}^{\text{II}}(\text{bpy})_2(\text{bpy}^\bullet)^+ \rightarrow \text{Ru}^{\text{III}}(\text{bpy})_2(\text{bpy}^\bullet)^{2+*} + \text{Ru}^{\text{II}}(\text{bpy})_3^{2+}$. The extent of ECL was found to be dependent on the extent of Oc_3N protonation at the interface. Above the biphasic $\text{p}K_\text{a}$ (~ 11) outer-sphere, electron transfer occurs from Oc_3N to $\text{Ru}^{\text{III}}(\text{bpy})_3^{3+}$, whereas below the biphasic $\text{p}K_\text{a}$, PCET dominates. In the PCET reaction, Oc_3NH^+ transfers both a

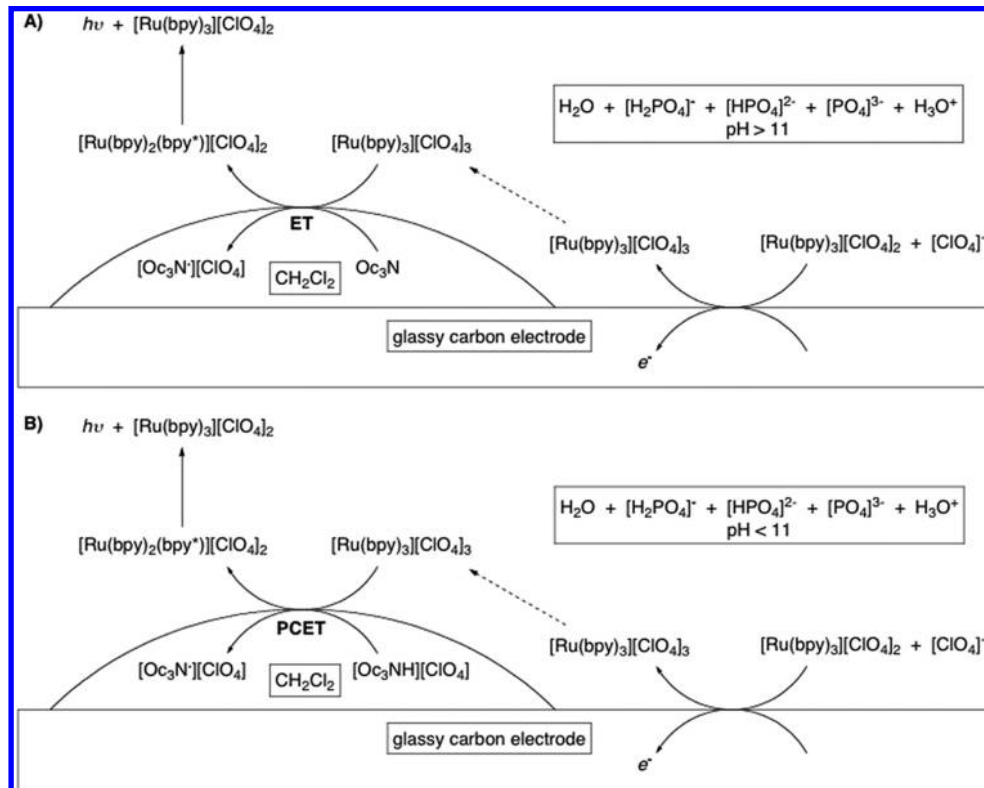


Figure 72. ECL at the liquid–liquid interface between the $[\text{Ru}(\text{bpy})_3]^{3+/2+}$ couple in an aqueous layer and droplets of trioctylamine in methylene chloride. (A) In aqueous solutions with $\text{pH} > 11$ with ET occurring at the liquid–liquid interface. (B) Below the biphasic $\text{p}K_\text{a}$ (~ 11), PCET occurs at the liquid–liquid interface.²⁰⁹

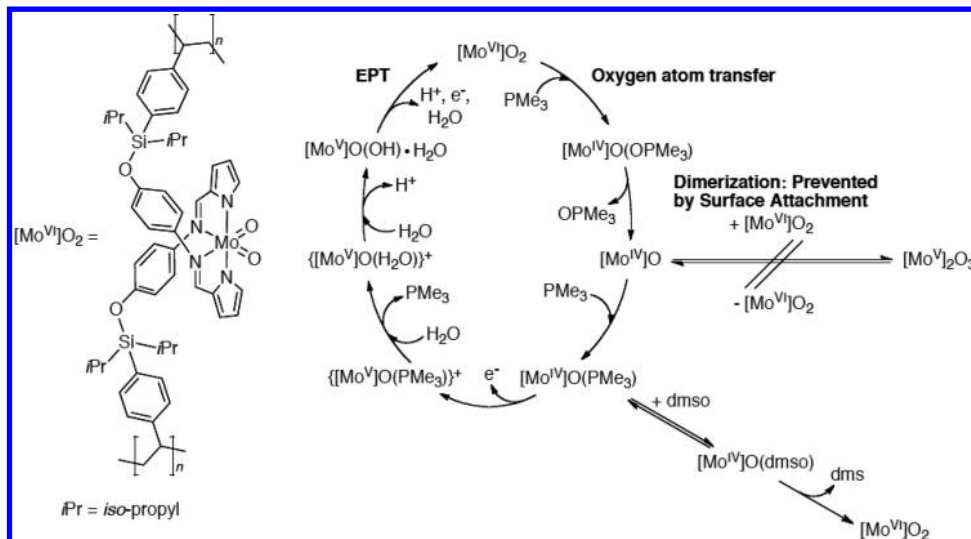


Figure 73. Polystyrene-supported molybdenum(VI) bisoxo catalyst for oxidation of trimethylphosphine. The proposed catalytic mechanism, involving EPT, is shown on the right. Diacetyl ferrocenium is the stoichiometric oxidant in this system. Adapted with permission from refs 89 and 213. Copyright 2007 Wiley and 2008 Elsevier.

proton and an electron to the aqueous phase, with $\text{Ru}^{\text{III}}(\text{bpy})_3^{3+}$ being the electron acceptor. Consistent with possible proton tunneling and EPT, the rate of the reaction is inhibited by increased reactant separation and a larger intrinsic barrier arising from N–H bond-dissociation and proton-reorganization energies.

7.1.2. Solid–Liquid Interfaces. PCET at solid–liquid interfaces plays an important role in electrochemistry as discussed in section 6. Closely related studies on PCET of molecules incorporated into, attached to, or adsorbed onto a solid have also been reported. Utilization of electrochemical monitoring in these cases can bypass complications arising from mass transfer effects. Surface attachment of catalysts on solid supports can have important implications for electrocatalysis and electroanalysis. This configuration also allows for flow-through operation and ready separation of products from reaction mixtures. In addition, surface attachment immobilizes the catalyst translationally, which can be important in controlling reactivity.⁸

7.1.2.1. Surface Activation of Electrodes. Oxidative activation of graphitic or glassy carbon electrodes produces surface phenolic and quinodal functional groups, which can markedly change electrochemical response to PCET couples by facilitating interfacial EPT.¹ Recently, it was reported that anodic pretreatment of a glassy carbon electrode appeared to increase rates for both electron and proton transfer steps in the oxidation of tripropylamine to *N,N*-dipropyl-1-propanaminium.²¹⁰ Oxygen-containing surface species may be directly involved in the deprotonation step.

Oxidative pretreatment has been extended to multiwalled carbon nanotubes (MWCNTs) for catalyzing the oxidation of enediols.²¹¹ Decreased overpotentials, between 80 and 380 mV, were observed in the oxidation of enediols at both MWCNTs and graphite following oxidative activation. With hydroquinone, a molecule commonly used to investigate PCET reactions (see the previous review on PCET by Meyer and co-workers and the earlier section on metal complex oxidations), the overpotential for oxidation decreased by ~200 mV with activated electrodes. The mechanism of enediol oxidation appears to be the same at both types of activated materials, presumably involving initial hydrogen

bonding between the enediol and an oxygen-containing surface species, followed by EPT at the interface.^{1,211,212}

7.1.2.2. Molecules Adsorbed or Tethered to a Solid Support. **7.1.2.2.1. Polymeric Supports.** As mentioned previously, potentially exploitable advantages of catalysis on solid-state supports are the physical separation of catalyst and solution reactants and the translational immobility of surface species. The latter was exploited in a PCET investigation of molybdenum(VI) bisoxo complexes on polystyrene supports (Figure 73).^{89,213} In this system, oxygen atom transfer to trimethylphosphine from the supported molybdenum(VI) bisoxo complex generates a molybdenum(IV) oxo species that can either react with the molybdenum(VI) bisoxo complex to generate an unreactive molybdenum(V) dimer or can undergo a series of steps to regenerate the molybdenum(VI) bisoxo, the last step of which is an oxidative EPT. By tethering the molybdenum complexes to a polystyrene support, dimerization is inhibited and the molybdenum(VI) bisoxo complex is regenerated.

7.1.2.2.2. Metal Oxides. Ruthenium(VII) oxide has proven to be capable of performing oxidations that could be useful in organic syntheses.²¹⁴ Unfortunately, its utility has been limited due to its instability under a variety of reaction conditions.^{214a} In acidic, aqueous solutions, ruthenium(VII) oxide is unstable and tends to decompose by a disproportionation.^{214a} To achieve increased stability, Kumar and Zen synthesized composite films containing ruthenium oxide mixed with a ruthenium Prussian blue analogue (K^+/H^+)_x $\text{Ru}_y[\text{Ru}(\text{CN})_6]_z \cdot n\text{H}_2\text{O}$ (RuPB).^{214a,215} The films were electrochemically grown on glassy carbon electrodes by repetitively cycling the potential between –0.5 and 1.25 V versus Ag/AgCl in acidic solutions of RuCl_3 and $[\text{Ru}(\text{CN})_6]^{3-}$. During this cycling, the increase in current of three redox couples was associated with the generation of the composite solid. While the exact structure of the composite solid has not yet been determined, a variety of electrochemical and physicochemical experiments have been utilized to determine the basic species responsible for the three redox couples. A redox couple for low spin—($\text{Ru}^{\text{III}/\text{II}}(\text{CN})_6$)—was observed at ~0.8 V versus Ag/AgCl. The cyano ligands at these sites bridge via nitrogen to high-spin $\text{Ru}^{\text{III}/\text{II}}$ sites that display a redox couple centered at ~0.1 V. Oxo bridges link the high-spin $\text{Ru}^{\text{III}/\text{II}}$ sites to high-valent ruthenium oxo species, which display a

$\text{Ru}^{\text{VII}/\text{VI}}$ wave at 1.0 V in aqueous solutions with a pH of 2. In addition to the oxo bridges, the high-valent ruthenium species are also associated with terminal oxo ($=\text{O}$), hydroxy ($-\text{OH}$), and aqua ($-\text{OH}_2$) functionalities. The $\text{Ru}^{\text{VII}/\text{VI}}$ couple is highly pH-dependent. Although the cathodic peak for this wave was masked by or coupled with other reductions in weakly acidic solutions, the $\text{Ru}^{\text{VII}/\text{VI}}$ redox couple was relatively reversible, allowing the anodic peak potential (E_{pa}) to be used as a reference for studying pH effects. In strong acid with $\text{pH} < 0$, E_{pa} decreases by $\sim 55 \text{ mV/pH}$ unit, consistent with a $1\text{e}^-/\text{1H}^+$ PCET couple. Above a pH of 0, E_{pa} decreases by 165 mV/pH unit, consistent with a $1\text{e}^-/\text{3H}^+$ couple. The authors speculated that the reactions shown in Figure 74 are

pH > 0: E_{pa} changes by $\sim 55 \text{ mV/pH}$ unit



pH < 0: E_{pa} changes by $\sim 165 \text{ mV/pH}$ unit



Figure 74. pH-dependent PCET oxidation of ruthenium(VI) oxide species in a composite ruthenium oxide/ruthenium Prussian blue (RuPB) surface.

responsible for these pH dependences. They proposed that the monoprotonated product is stabilized at $\text{pH} < 0$ by hydrogen bonding with other surface species, which are deprotonated under more basic conditions.

In the presence of glucose, the electrochemical PCET oxidation of Ru^{VI} to Ru^{VII} is coupled to the catalytic oxidation of glucose to gluconic acid (depicted in Figure 75). The anodic

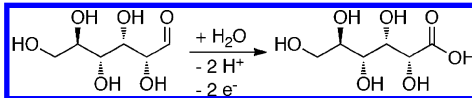
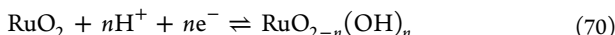


Figure 75. Electrochemical oxidation of glucose to gluconic acid.

peak current, E_{pa} , shows the same pH dependence as in the absence of glucose, and this results in increased driving force for glucose oxidation under increasingly acidic conditions. The catalytic current is relatively small in $0.01\text{--}1 \text{ M HClO}_4$, but it increases by a factor of ~ 200 as the concentration of HClO_4 is increased from 0.01 to 5 M.

7.1.2.2.3. Ionic Liquids. A role for PCET at RuO_2 electrodes in protic ionic liquids has been demonstrated.²¹⁶ RuO_2 and other metal oxide electrodes exhibit a pseudocapacitance arising from surface PCET in protic solvents (eq 70). Surface PCET reactivity was extended to RuO_2 in the protic ionic liquid 1:2 2-methylpyridine/trifluoroacetic acid. Pseudocapacitance was demonstrated, but high viscosity and slow proton transfer in the ionic liquid limit the charging rates.



7.1.2.2.4. Self-Assembled Monolayers. Self-assembled monolayers (SAMs) (note the examples in Figure 76) are useful for studying PCET because they allow substrates to be tethered at controlled distances from the electrode and physically separated from nearest neighbors by surface dilution.^{8,217} The tether can be used to minimize double-layer effects and to control the rate of electron transfer between the surface and redox-active sites.⁸

The oxidation of hydroquinones tethered to gold electrodes in SAMs—such as in the ones shown in Figure 76—has been used to study PCET in SAMs.^{8,217–219} The first pK_a of hydroquinone increases from 9.85 to 11.4–16.4 upon incorporation into the SAMs. The pK_a values of the SAM-incorporated hydroquinones are highly dependent on the specific linker connecting the hydroquinone to the gold electrode.²¹⁷ The SAM-incorporated hydroquinones display a $2\text{e}^-/2\text{H}^+$ redox couple whose $E^{\circ'}$ decreases by 60 mV/pH unit up to a pH of 12.6.^{217,218,219b} On the basis of surface rate constant measurements on tethers to the gold electrode with various degrees of conjugation, it was shown that enhanced electron tunneling can significantly increase the overall rate of PCET. Above the first pK_a for the surface hydroquinone, the tunneling effect on the overall rate is diminished. It was also noted that, at intermediate pHs, the apparent rate constants were independent of tether length.^{8,219b} The origin of this effect is unclear, but the involvement of counterion motion in the rate-limiting step could not be ruled out.

The temperature dependence of the apparent electron transfer rate constant (k_{app}) for oxidation of hydroquinones tethered to gold electrodes in SAMs ($\text{H}_2\text{Q}(\text{CH}_2)_n\text{SH}$; H_2Q = hydroquinone) has been investigated by application of eqs 71 and 72 from Laviron's formalism and eqs 73 and 74 from Marcus theory^{219a,220} (E_{pc} = potential at the peak cathodic current; E_{pa} = potential at the peak anodic current; $E_c^{\circ'}$ = formal potential of the cathodic wave; $E_a^{\circ'}$ = formal potential of the anodic wave; R = gas constant; T = temperature; α = transfer coefficient; n = number of electrons exchanged; v = sweep rate; d_1 and d_2 = different distances from the electrode surface; β = electron tunneling constant; and λ = reorganization energy).

$$E_{\text{pc}} = E_c^{\circ'} - (RT/\alpha nF) \ln[\alpha nFv_c/RTk_{\text{app}}] \quad (71)$$

$$E_{\text{pa}} = E_a^{\circ'} - (RT/(1-\alpha)nF) \ln[(1-\alpha)nFv_a/RTk_{\text{app}}] \quad (72)$$

$$k_{\text{app}}(d_2) = k_{\text{app}}(d_1) \exp[-\beta(d_2 - d_1)] \quad (73)$$

$$\lambda = -4.03d(\ln[k_{\text{app}}/T^{1/2}])/d[T^{-1}] \quad (74)$$

By plotting $\Delta E_p = E_{\text{pa}} - E_{\text{pc}}$ against $\log(v)$, k_{app} and the symmetry factors (αn and $(1-\alpha)n$) could be determined. They were shown to be temperature-independent.^{219a} This indicates that the geometry at the intersection of the free-energy curves for reactants and products remains the same over the temperature range explored.⁴³ Furthermore, n is calculated to be ~ 2 for all temperatures and lengths of alkyl chain tethers tested. This value for n accurately reflects the total number of electrons transferred in the hydroquinone/quinone redox reaction.

Using eq 73 and data collected with different lengths of the alkyl tether, β was shown to have values between 1.0 and 1.1 across the range of temperatures explored.^{219a} This indicates that the activation energy barrier for the elementary electron transfer step is insensitive to temperature change and that the structure of the monolayer does not change systematically with temperature.

The reorganization energy (λ) can be determined by using eq 74, with λ evaluated as the slope of plots of $\ln[k_{\text{app}}/T^{1/2}]$ versus T^{-1} . In these measurements, $\lambda = 1.3\text{--}1.4 \text{ eV}$, irrespective of tether length.^{219a} However, detailed interpretation of λ is

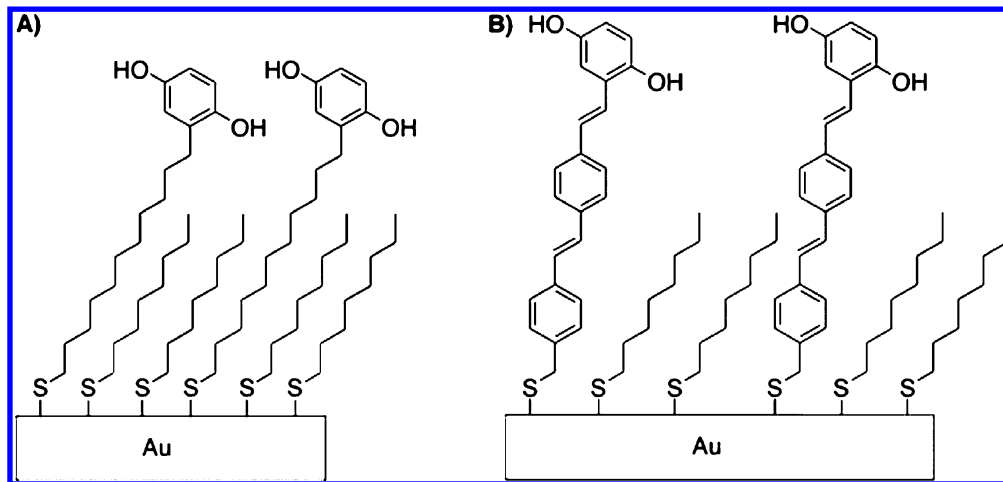


Figure 76. Two SAM structures on gold electrodes that undergo PCET. The hydroquinones involved in PCET are separated from each other by dilution with octane-1-thiol. The increased conjugation of the tether to the hydroquinone in (B) increases the rate of electron transfer to the surface, increasing the rate of $2e^-/2H^+$ oxidation to the quinone.²¹⁸

unclear because of possible contributions from competing electron transfer and pK_a effects.^{8,219a}

Burgess and co-workers used monolayers of mercaptoundecylamine diluted in 1-octanethiol to generate isolated 1,4-benzoquinone functional groups on gold surfaces as depicted in Figure 77.²²¹ Almost Nernstian behavior (without interactions

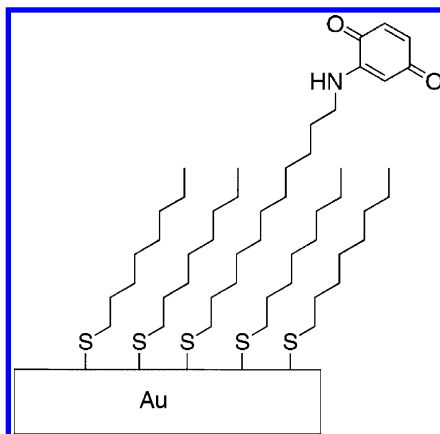


Figure 77. Isolated 1,4-benzoquinone site tethered to an alkanethiol monolayer on a gold surface studied by Burgess and co-workers.²²¹

between redox centers) was observed. This system was stable between pH 8.5 and 1, exhibiting pH-dependent PCET behavior over this range. From pH 8.5 to 4.5, the formal reduction potential of the quinone shifted by 58 mV per pH unit, indicative of the standard $2e^-/2H^+$ redox couple for quinone reduction to hydroquinone. However, the formal reduction potential shifted by 88 mV per pH unit upon decreasing the pH below 4.5. This reduction was shown to involve the transfer of $2e^-$ and was thus assigned to a $2e^-/3H^+$ process. The authors speculated that the third proton transfers to the amine group.

PCET was also investigated in SAMs of the 1-aminoanthroquinone derivative shown in Figure 78 on gold electrodes by Abhayawardhana and Sutherland.²²² In 0.1 M H_2SO_4 , the protonated ammonium-anthroquinone undergoes $2e^-/2H^+$ PCET reduction with $k_S = 7.4\text{ s}^{-1}$. Because of the disruption of an intramolecular hydrogen bond between the

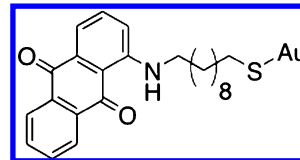


Figure 78. Surface-bound (Au) 1-aminoanthroquinone monomer SAM used to study PCET by Abhayawardhana and Sutherland.²²²

ammonium and anthroquinone sites, reduction occurs with a high activation energy (69 kJ/mol) with $\lambda = 2.7\text{ eV}$.

PCET has also been studied for metal complexes attached to gold in alkanethiol SAMs.^{53a,198a,223} By using a carbodiimide coupling reagent, the aqua complex $Os^{II}(bpy)_2(4\text{-AMP})(H_2O)^{2+}$ (4-AMP = 4-aminomethylpyridine) shown in Figure 79

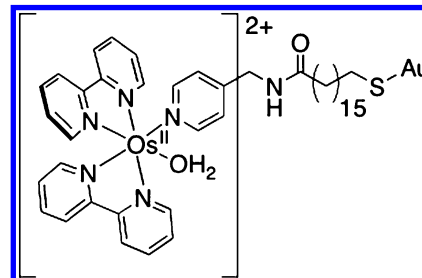


Figure 79. Structure of the $Os^{II}(bpy)_2(4\text{-AMP})(H_2O)^{2+}$ derivative imbedded in SAMs of $\sim 18\text{Au-S(CH}_2\text{)}_{15}\text{COOH:1 Au-S(CH}_2\text{)}_{16}\text{OH}$.^{223a}

was coupled to carboxylic acids in preformed alkanethiol SAMs, which contained an $\sim 18:1$ ratio of $\text{Au-S(CH}_2\text{)}_{15}\text{COOH}/\text{Au-S(CH}_2\text{)}_{16}\text{OH}$. This resulted in low osmium coverages with $\Gamma \approx 1 \times 10^{-11}\text{ mol/cm}^2$.^{53a,198a,223a} In homogeneous solution, oxidation of $Os^{II}(bpy)_2(\text{py})(H_2O)^{2+}$ to $Os^{III}(bpy)_2(\text{py})(OH)^{2+}$ is dominated by ET-PT below pH = 6 and by PT-ET above this pH. In contrast, the osmium complex in the SAMs undergoes oxidation by EPT in solutions at pH > 4.9, above the pK_a for the surface-bound carboxylate, with proton transfer occurring to the carboxylate and electron transfer occurring to the electrode. Further evidence for EPT is provided by $KIE(H_2O/D_2O) = 2$.

From electrochemical measurements and eq 75, a transfer coefficient (α_{PCET}) of ~ 0.46 was obtained at an overpotential

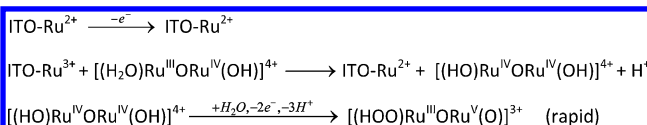
(η) of 0 with an asymmetric Tafel plot (a plot of $\log i$ versus η). Theory predicts that this asymmetry should be proportional to δR , the equilibrium proton donor–acceptor distance for the oxidized and reduced forms of the osmium complex.^{53a,224} Using DFT calculations on model systems, Hammes-Schiffer and co-workers calculated a proton donor–acceptor O–O distance of 2.49 Å in the reduced complex and 2.66 Å in the oxidized complex, giving a δR of ~0.17 Å.

$$\alpha_{\text{PCET}} = 0.5 - \alpha_{00} \delta R k_B T / \Lambda_{00} \quad (75)$$

The μ -oxo- μ -carboxylate-bridged ruthenium(III) dimer, $[\text{Ru}_2(\mu\text{-O})(\mu\text{-CH}_3\text{COO})_2(2,2'\text{-bipyridine})(\text{CH}_3\text{CN})_2]^{2+}$, was incorporated into pyridyl-terminated SAMs, by displacement of the CH_3CN ligands with the terminal pyridines of the SAMs.^{223b,c} The PCET reactivities of the dimer and of a related ruthenium trimer were studied electrochemically. Like the solution-phase dimer, $[\text{Ru}_2(\mu\text{-O})(\mu\text{-CH}_3\text{COO})_2(2,2'\text{-bipyridine})(\text{pyridine})_2]^{2+}$, the SAM-tethered dimer undergoes consecutive $1e^-/1\text{H}^+$ PCET reduction at moderately acidic pHs. These reductions arise from the couples $[\text{Ru}^{\text{III}}(\mu\text{-O})\text{Ru}^{\text{III}}]/[\text{Ru}^{\text{II}}(\mu\text{-OH})\text{Ru}^{\text{III}}]$ and $[\text{Ru}^{\text{II}}(\mu\text{-OH})\text{Ru}^{\text{III}}]/[\text{Ru}^{\text{II}}(\mu\text{-OH}_2)\text{Ru}^{\text{II}}]$. On increasing the pH, E° decreases, and the two couples shift negatively, eventually merging into a single $2e^-/\text{H}^+$ process for the couple $[\text{Ru}^{\text{III}}(\mu\text{-O})\text{Ru}^{\text{III}}]/[\text{Ru}^{\text{II}}(\mu\text{-OH})\text{Ru}^{\text{II}}]$.

7.1.2.2.5. Electrocatalysis. PCET and single-electron activation of multielectron catalysis play critical roles in water oxidation catalysis. The blue dimer, *cis,cis*- $[(\text{bpy})_2(\text{H}_2\text{O})\text{Ru}^{\text{III}}\text{ORu}^{\text{III}}(\text{H}_2\text{O})(\text{bpy})_2]^{4+}$ ($[(\text{H}_2\text{O})\text{Ru}^{\text{III}}\text{ORu}^{\text{III}}(\text{H}_2\text{O})]^{4+}$), was the first designed molecular catalyst for water oxidation.^{45a} Following $1e^-/1\text{H}^+$ oxidation to $[(\text{HO})\text{Ru}^{\text{IV}}\text{ORu}^{\text{III}}(\text{H}_2\text{O})]^{4+}$, further $3e^-/3\text{H}^+$ oxidation gives the transient intermediate $[(\text{O})\text{Ru}^{\text{V}}\text{ORu}^{\text{V}}(\text{O})]^{4+}$. It undergoes a rapid reaction with water to give the peroxidic intermediate $[(\text{HOO})\text{Ru}^{\text{III}}\text{ORu}^{\text{V}}(\text{O})]^{3+}$, which dominates at the catalytic steady state. Because of kinetic complications arising from PCET and proton loss, this key intermediate is kinetically inaccessible at metal oxide electrodes such as ITO ($\text{In}_2\text{O}_3:\text{Sn}$). Adsorption of $[\text{Ru}((4,4'\text{-}(\text{HO})_2\text{P}(\text{O})\text{CH}_2\text{bpy})_2(\text{bpy})]^{2+}$ (**ITO-Ru²⁺**) ($4,4'\text{-}(\text{HO})_2\text{P}(\text{O})\text{CH}_2\text{bpy}$ is $4,4'$ -bis-(methyl)phosphonato-2,2'-bipyridine) by chemical binding to the surface of ITO electrodes dramatically enhances the rate of water oxidation by the blue dimer in the external solution. As shown in Scheme 36, the reason for surface-

Scheme 36



enhanced rates is in the enhanced rate of oxidation of $[(\text{HO})\text{Ru}^{\text{IV}}\text{ORu}^{\text{III}}(\text{H}_2\text{O})]^{4+}$ to the high-energy intermediate $[(\text{HO})\text{Ru}^{\text{IV}}\text{ORu}^{\text{IV}}(\text{OH})]^{4+}$ at the electrode surface.²²⁵

In a related study, dramatic rate enhancements were reported for the oxidation of tyrosine and tyrosine methyl ester in acidic solution. As shown for tyrosine by the cyclic voltammograms in Figure 80, neither of the phenol derivatives is electroactive at ITO, but oxidation does occur at **ITO-Ru²⁺**. CVs with added bases—acetate ($\text{pK}_a = 4.7$); citrate ($\text{H}_3\text{C}_6\text{H}_5\text{O}_7/\text{H}_2\text{C}_6\text{H}_5\text{O}_7^-$, $\text{pK}_a = 6.4$); phosphate ($\text{H}_2\text{PO}_4^-/\text{HPO}_4^{2-}$, $\text{pK}_a = 7.2$)—provide direct evidence for concerted electron–proton transfer (EPT) pathways at these chemically modified interfaces (Figure 81).²²⁶

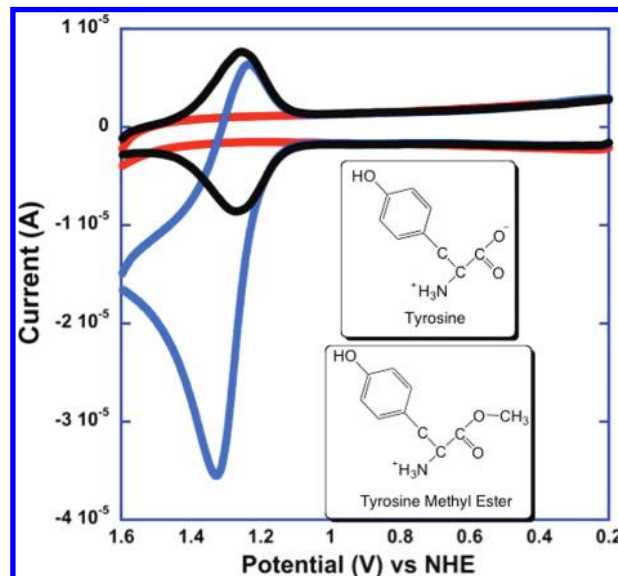


Figure 80. Cyclic voltammograms (CVs) of tyrosine (TyrOH , 0.1 mM) in 0.1 M $\text{HClO}_4/0.8 \text{ M LiClO}_4$ at 300 mV/s, at ITO (red), at ITO– Ru^{II} ($\Gamma = 1.2 \times 10^{-10} \text{ mol}/\text{cm}^2$, black), and at ITO– $\text{Ru}^{\text{II}} + \text{TyrOH}$ at 25 ± 2 °C (blue). Similar CVs were obtained with tyrosine methyl ester, which is also pictured. Reproduced with permission from ref 226. Copyright 2011 American Chemical Society.

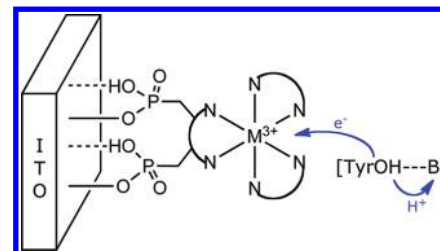


Figure 81. Illustrating surface MS-EPT with electron transfer to ITO– Ru^{3+} and proton transfer to an added buffer base, B, as proton acceptor. Reproduced with permission from ref 226. Copyright 2011 American Chemical Society.

7.1.2.3. Solid State. The effect of dielectric confinement on proton-coupled electron transfer was probed in an “all-solid-state” electrochemical cell for hydrogen oxidation.¹⁸⁹ In this cell, the working and reference electrodes were incorporated into the anionic polymer electrolyte membrane, Nafion, with the counter electrode, a Pt wire, encircling the membrane. Hydrogen gas was passed over the membrane, and oxidation of adsorbed hydrogen occurs at the membrane surface. Incorporation of $\text{K}_4[\text{Fe}^{\text{II}}(\text{CN})_6]^{4-}$ into the anionic polymer electrolyte catalyzes the oxidation, decreasing the overpotential. In probing the system electrochemically, it was determined that the rate of hydrogen oxidation ($9.1 \times 10^{-6} \text{ cm/s}$) is comparable to the rate of $[\text{Fe}^{\text{II}}(\text{CN})_6]^{4-}$ oxidation to $[\text{Fe}^{\text{III}}(\text{CN})_6]^{3-}$ ($5.4 \times 10^{-6} \text{ cm/s}$). It was also found that the rate of proton transport through the Nafion membrane ($4.8 \times 10^{-12} \text{ cm/s}$) closely matched the rate of $[\text{Fe}^{\text{II}}(\text{CN})_6]^{4-}$ diffusion through the membrane ($1.3 \times 10^{-12} \text{ cm}^2/\text{s}$). Proton transport in Nafion without $[\text{Fe}^{\text{II}}(\text{CN})_6]^{4-}$ is 2 orders of magnitude more rapid ($8.6 \times 10^{-10} \text{ cm}^2/\text{s}$). These data point to hydrogen oxidation as a proton-coupled electron transfer process, involving the $[\text{Fe}^{\text{II}}(\text{CN})_6]^{4-}/[\text{Fe}^{\text{III}}(\text{CN})_6]^{3-}$ couple with $[\text{Fe}^{\text{II}}(\text{CN})_6]^{4-}$ diffusion through the negatively charged sulfonate-containing Nafion membrane.¹⁸⁹

The results obtained for $[\text{Fe}^{\text{II}}(\text{CN})_6]^{4-}/[\text{Fe}^{\text{III}}(\text{CN})_6]^{3-}$ in Nafion are relevant to proton-exchange membrane (PEM) fuel cells that involve simultaneous electron transport and proton transport through an interconnecting membrane or solid-state proton transfer medium. In analysis of fuel cells, both experimental and theoretical studies have been used to probe the interdependence of proton and electron transfer rates as well as their overall effects on catalysis.²²⁷

7.1.2.4. Excited State. Heterogeneous excited-state PCET is potentially important in the development of photocatalysts and systems for solar energy conversion.^{109c,228} An approach to the latter involves dye-sensitized photoelectrosynthesis cells (DSPECs), which are based on TiO_2 and other high-band-gap semiconductors. These devices are driven by photoexcitation and electron injection by bound chromophores or by direct-band-gap excitation.

Laser excitation of electrons in a rutile TiO_2 (110) surface with a methanol overlayer state has been investigated.^{75,228,229} In these experiments methanol vapor was deposited at ~ 1 monolayer thickness on TiO_2 at 100 K. Methanol binds to five-coordinate titanium(IV) sites on the surface and undergoes partial deprotonation by surface oxygen atoms. Bandgap laser excitation leads to electron injection into an unoccupied electronic state (methanol-based antibonding level) of the methanol overlayer, 2.3 ± 0.2 eV above the Fermi level and mostly associated with the hydrogen atoms of the methyl groups. This drives the motion of protons in the methanol overlayer, whereas the creation of a hole in the TiO_2 substrate underlayer elicits changes in Ti–O bond stretching vibrations. These motions lead to a dielectric screening of the photo-generated electron–hole pair.

The excited electron thermalizes into the conduction band of TiO_2 by PCET, as evidenced by an isotope effect on the decay time of $\tau_{\text{H}}/\tau_{\text{D}} = 2.2$. On the basis of emission measurements and electronic structure theory, a methanol bound to a five-coordinate titanium site in the surface undergoes transfer of the excited electron to an unoccupied orbital associated with a bridging surface hydroxyl, while a proton on the same methanol molecule simultaneously migrates to a bridging surface oxo (Figure 82). Further decay of the electron into the conduction band of TiO_2 is facilitated by the unoccupied orbital associated with the bridging surface hydroxyls, as this orbital is strongly coupled to the conduction band.

Trapping of photogenerated holes in the valence band of TiO_2 also likely occurs by PCET from adsorbed methanol.^{229b} The HOMO of the methanol overlayer is only slightly lower in energy than the valence band maximum, and deprotonation of adsorbed methanol to give methoxide increases its propensity to donate an electron.

To model EPT involvement between P680^{•+} and the Tyr_z–His190 pair of Photosystem II (PSII; see sections 4.1 and 8.4), 2-(phenol)benzimidazole was incorporated into a porphyrin as illustrated in Figure 83.²³⁰ The porphyrin derivative was adsorbed onto TiO_2 nanoparticles and photoexcited to induce electron transfer from the porphyrin to the TiO_2 conduction band followed by ET from the 2-(phenol)benzimidazole functional group to the oxidized porphyrin to give a redox-separated intermediate. Electron transfer to the porphyrin was facilitated by intramolecular hydrogen bonding between the phenol and the benzimidazole and was demonstrated by ¹H NMR and Fourier transform infrared (FTIR) measurements. Although oxidation of phenols is typically irreversible and coupled to deprotonation, reversible oxidation of the

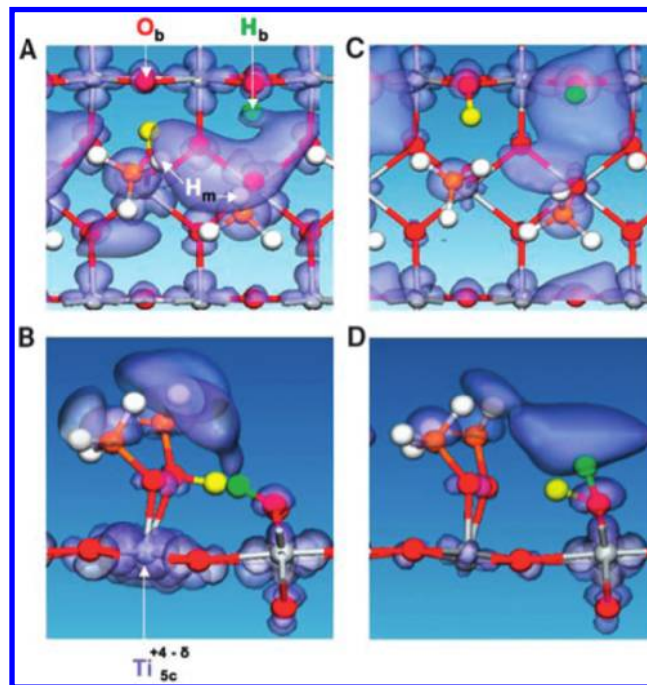


Figure 82. Band-gap injection of holes into a methanol overlayer on TiO_2 . (A and B) Top and side views, respectively, of the ground state and the associated lowest energy unoccupied orbital of the methanol overlayer. (C and D) The top and side views, respectively, of the structure and electron density, following electronic excitation and the resulting PCET. Ti is blue; O is red; C is orange; and H is white. Reproduced with permission from ref 228a. Copyright 2006 American Association for the Advancement of Science.

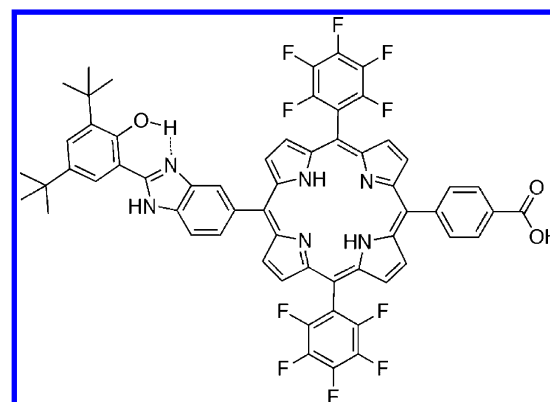


Figure 83. Illustration of intramolecular hydrogen bonding in a 2-(phenol)benzimidazole porphyrin.²³⁰

2-(phenol)benzimidazole derivative occurs at 0.95 V versus SCE in deoxygenated, anhydrous methylene chloride solutions containing 0.10 M tetrabutylammonium hexafluorophosphate. Under the same conditions, oxidation of 2,4,6-tri-*tert*-butylphenol is irreversible and occurs at 1.4 V. The reversibility of the 2-(phenol)benzimidazole porphyrin was attributed to facile proton shuttling between oxidized phenol and benzimidazole. The considerable decrease in potential for phenol oxidation enables intramolecular reduction of the initial porphyrin radical cation.

Studies have been performed on the occurrence of excited-state PCET during the formation of supramolecular layers of Cu complexes containing H_2O and hydroquinone intercalated between the layers (Figure 84).^{165d} The layers are composed of

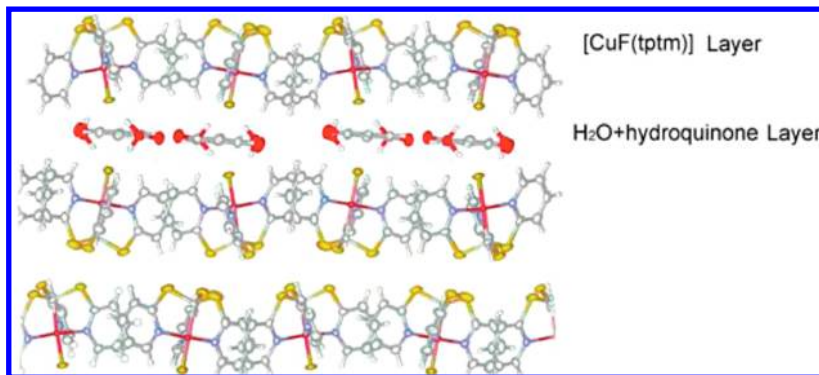


Figure 84. Illustrating the intercalated array of hydroquinone molecules between layers in $[\text{CuF}(\text{tptm})]$. Reproduced with permission from ref 165d. Copyright 2008 Springer.

$[\text{CuF}(\text{tptm})]$, where tptm is the tetradente ligand tri-(pyridylthio)methyl and there is a Cu–C bond. While quinone was used to form the layers, illumination during the generation of the layers leads to PCET reduction of quinone to hydroquinone. This process involves the oxidation of Cu(II) to Cu(III), while intercalated water molecules supply the protons. The strong hydrogen bonds formed between the Cu–ligand structures and the intercalated water molecules, as well as the ability of Cu to switch between divalent and trivalent states, facilitate the PCET reaction. This process has been proposed as a possible mimic of the PCET reaction taking place in Photosystem II.^{165d}

7.2. Biological

Protein immobilization on electrode surfaces can be beneficial both for studying PCET reactions in proteins and for the development of devices for electrochemical biocatalysis.²³¹ Direct electrochemical studies of proteins in solution are hindered by small diffusion coefficients, redox centers that are buried deeply within the protein structure, and protein denaturation due to adsorption on the electrode surface.²³² Denaturation can be avoided by immobilization on the electrode surface. This also overcomes mass transfer limitations while facilitating electron transfer between protein redox centers and the electrode. The resulting increase in electron transfer rates to the electrode facilitates investigation of protein redox reactions and can increase rates of protein-catalyzed electrochemical reactions. Increases in stability open the possibility of utilizing surface-bound proteins in device applications.

The results of recent studies on a chosen collection of proteins will be discussed below. Related results have been reported for horseradish peroxidase,^{232a,233,234} cytochrome *c* peroxidase,²³⁵ myoglobin,^{231a,232a,236} cytochrome P450 enzymes,²³⁷ and xanthine oxidase.²³⁸

7.2.1. Hemes. The role of PCET in many heme-containing proteins immobilized on electrodes has been probed electrochemically. In the absence of a reactive substrate, these proteins typically undergo quasi-reversible one-electron/one-proton PCET reactions, involving reduction of a heme Fe(III) with corresponding protonation of a *trans* ligand on the iron, an amino acid near the heme, or a water molecule coordinated to the heme.²³⁹ Heme-containing proteins have been shown to catalyze the reduction of a variety of natural and non-natural substrates via the delivery of both protons and electrons. Immobilization of the proteins on electrode surfaces has been a

critical element in studying heme electrochemistry and in utilizing enzymes for catalysis in devices, including biosensors.

7.2.1.1. Hemoglobin. PCET in hemoglobin has been studied extensively by direct voltammetry on a diverse set of substrates. Hemoglobin is of significant interest as the ubiquitous protein oxygen carrier. When attached to electrode surfaces, hemoglobin has been shown to catalyze the reduction of multiple substrates including hydrogen peroxide,^{232b,d,240} trichloroacetic acid,^{231a,240c} and nitrite anion.²⁴¹ Studies of hemoglobin are facilitated by its commercial availability and knowledge of its structure. Each hemoglobin molecule contains four redox-active iron hemes, but solution-phase electrochemical studies on hemoglobin are hindered by its adsorption and subsequent denaturation, which causes passivation of electrode surfaces.^{232a,240g} Also, the hemes are deeply buried in the polypeptide structure, which slows electron transfers to electrode surfaces.

To facilitate direct electron transfer, hemoglobin has been attached to electrode surfaces by direct adsorption,^{232a} by adsorption or entrapment in metal oxides on electrode surfaces,^{240f,241b} or by entrapment in polymer films on electrode surfaces.^{231a,232b-d,240-242} Many of these films incorporate conducting or semiconducting nanoparticles to facilitate electron transport.^{232b,c,240c-g,241b,242c} The method of attachment has a considerable impact on heme redox potentials (E°') with observed values between 0.129 and –0.376 V versus SCE. The pH dependence of E°' values is highly variable, ranging from –15.6 to –55.4 mV/pH unit. This is surprising because it is generally agreed that oxidation involves $1\text{e}^-/\text{1H}^+$ PCET couples. Large deviations from the ideal of –57 to –59 mV/pH unit (depending on temperature) have been attributed, in part, to slow electron transfer, but this is not the only factor affecting the nonideal slopes.

There have been extensive studies on the $2\text{e}^-/\text{2H}^+$ reduction of hydrogen peroxide catalyzed by hemoglobin. A variety of factors influence the catalytic rates including electron transfer and affinity of the immobilized enzyme for hydrogen peroxide.^{232b,243} Apparent Michaelis–Menten association constants ($K_{M,\text{app}}$) have been determined by application of the Lineweaver–Burk equation (eq 76) and used to compare electrochemical catalytic activities of enzymes.²⁴⁴

$$\frac{1}{I_{SS}} = \frac{1}{I_{\max}} + \frac{K_{M,\text{app}}}{I_{\max} C} \quad (76)$$

In this equation, I_{SS} is the steady-state current after the addition of substrate (e.g., H_2O_2), C is the bulk concentration

of substrate, and I_{\max} is the maximum current measured when the system is saturated in substrate. Smaller values for $K_{M,\text{app}}$ indicate increased catalytic activity.

7.2.1.2. Catalase. A variety of electrode surfaces have been explored for the direct PCET reduction of the hemes in catalase (Cat).^{239b,245} In a particularly interesting study, the effect of hydration on PCET reduction was studied electrochemically by exposing glassy carbon (GC)-supported agarose hydrogel films containing Cat to solutions with various concentrations of ethanol in water.^{239b} The use of increasingly hydrophobic solvent mixtures for enzymatic catalysis has attracted interest because it could conceivably increase rates for hydrophobic substrates and influence the thermodynamics of hydrolytic reactions.²⁴⁶ In addition, some enzymes have been shown to be more stable in water-poor environments.²⁴⁷

Agarose hydrogel is well-suited for this application because of its high turbidity and elasticity. Below 40 °C, the agarose polysaccharide coils into helices that aggregate into thick bundles with large pores containing water.²⁴⁸ When a GC-supported agarose film containing Cat was exposed to an aqueous phosphate-buffered solution (PBS) at pH = 7.0, $E^{\circ'} = -0.412$ V versus SCE for the PCET Fe(III/II) couple with a peak-to-peak splitting (ΔE_p) of 85 mV at a scan rate of 0.5 V/s.^{239b} Upon switching to a 1:1 mixture of PBS and ethanol, the peak currents increased, and the formal potential shifted to −0.441 V with a ΔE_p of 57 mV. The couple shows a pH dependence of −42 mV/pH unit in PBS and −54 mV/pH unit in the PBS/ethanol mixture, indicative of the expected 1e[−]/1H⁺ PCET couple. Increased reversibility and pH dependence in the PBS/ethanol mixture likely arises from partial dehydration of the distal heme pocket. Disruption of hydrogen-bonding networks in the heme pocket could facilitate electron transfer through attenuation of the reorganization energy. Disruption of hydrogen-bonding networks could also affect the pK_a's of the heme iron.^{236b} Similar results were obtained when ethanol was substituted with acetonitrile, N,N-dimethylformamide, or dimethylsulfoxide and were also obtained for myoglobin immobilized in konjac glucomannan on a glassy carbon electrode.^{236b} When the concentration of ethanol was increased beyond 50% for catalase, the peak currents began to decrease and shift to more negative potentials, possibly due to denaturation of the enzyme.

7.2.1.3. Cytochrome c Nitrite Reductase. Differences between protein film voltammograms taken in the presence and absence of the catalytic inhibitor, CO, were used to determine reduction potentials for catalytic hemes in cytochrome *c* nitrite reductase (ccNiR) over a wide pH range.²⁴⁹ A single subunit of ccNiR contains four six-coordinate, low-spin hemes, which are involved in intramolecular electron transfer, and one five-coordinate, high-spin heme, which performs the catalysis. The proteins from *Desulfovibrio desulfuricans* ATCC 27774 were purified as 2:1 complexes of the active subunit and the tetraheme, NrfH, which is the physiological electron donor for ccNiR. The number of hemes in this complex made it difficult to interrogate with EPR or UV-visible measurements, and comparisons of protein film voltammograms, before and after exposure to inhibitor, were used to determine the reduction potential of the active site.

Protein film voltammetry was performed by adsorbing the 2:1 complexes of the ccNiR active subunit and NrfH onto a freshly polished pyrolytic graphite edge (PGE) electrode. CO only binds to the two active, five-coordinate hemes in the complex, and the difference between protein film

voltammograms in the presence and absence of CO enabled determination of the redox potential for these hemes. It was concluded that, at pH = 7, the reduction potential occurs at -200 ± 20 mV versus SHE. This potential varies by -58 mV/pH unit, indicative of a 1e[−]/1H⁺ PCET couple. It was proposed that Histidine 299 in the active site undergoes protonation upon reduction of the active heme and that the proton is then delivered to the heme–substrate complex during catalytic turnover.

7.2.2. Biomimetic Membranes. PCET in membrane proteins plays an exceedingly important role in biology given its involvement in a variety of important cellular processes. Both photosynthesis and respiration involve membranal PCET.^{1,250} PCET is often utilized in membranal proteins to couple electron transport to the transfer of protons across the membrane. The membrane is critical to these processes, in part because it allows the buildup of proton gradients. In addition, membranal hydrophobicity and electrostatics impact protein conformations and redox processes. When studying PCET in membranal proteins *in vitro*, it is important that the proteins be incorporated into a structure that mimics their native membrane. To this end, membranal proteins have commonly been incorporated into phospholipid liposomes as depicted in Figure 85.^{250,251} The phospholipid liposomes are vesicles

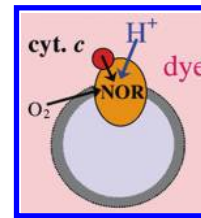


Figure 85. Schematic diagram of a system in which nitric oxide reductase (NOR) was incorporated into a liposome with the dye phenol red used to monitor pH changes outside the liposome during NOR-catalyzed oxygen reduction catalysis. Reprinted with permission from ref 251c. Copyright 2007 Elsevier.

composed of phospholipid bilayers self-assembled in aqueous solutions due to the aggregation of their hydrophobic tails. Liposomes resemble biological membranes in that there is aqueous solution on both sides of the phospholipid bilayer. Membranal proteins can sometimes be incorporated into liposomes in conformations similar to their native states due to differences in hydrophobicity; however, control over the orientation of proteins within liposomes remains a challenge.^{250,251c}

7.2.2.1. Nitric Oxide Reductase. Nitric oxide reductase (NOR) was incorporated into a liposome with ~90% of the protein in the proper conformation, with the hydrophilic portion directed toward the aqueous solution.^{251c} NOR is a heme–copper oxidase that catalyzes the reduction of NO to N₂O ($2\text{NO} + 2\text{e}^- + 2\text{H}^+ \rightarrow \text{N}_2\text{O} + \text{H}_2\text{O}$) as a part of overall denitrification. This particular system was used to confirm that NOR does not act as a proton pump, that it takes up both protons and electron donors from the same side of a membrane. To demonstrate this, the NOR-liposomes were exposed to a solution of O₂ (an alternative substrate to NO), reduced cytochrome *c* (the electron donor), and phenol red (a pH-sensitive dye). By monitoring absorbance changes for cytochrome *c* and phenol red, it was determined that the uptake of protons from outside the liposomes is coupled to the uptake

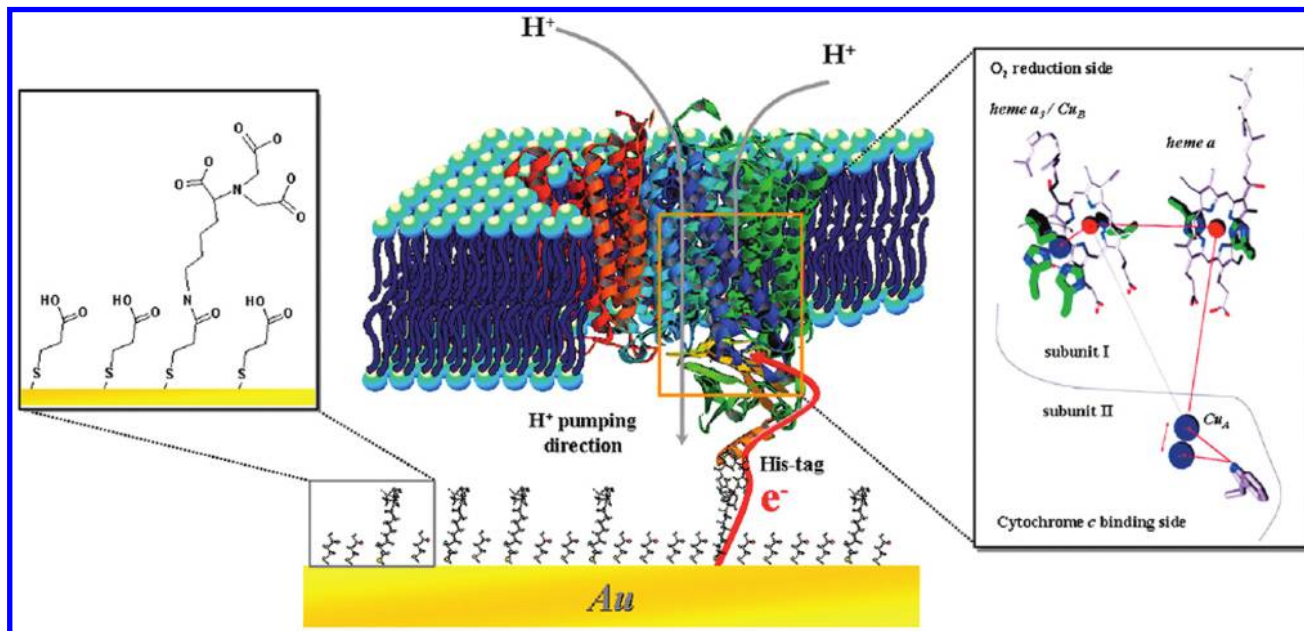


Figure 86. Illustration of CcO tethered to a gold electrode and embedded in a lipid bilayer membrane. Reproduced with permission from ref 250. Copyright 2008 Biophysical Society.

of electrons from cytochrome *c*. This was confirmed by optical measurements on single-turnover reduction of O₂.

7.2.2.2. Cytochrome *c* Oxidase. To gain better control over protein orientation in the phospholipid bilayer and to allow direct electron transfer between the protein and an electrode, a biomimetic system was developed in which the protein cytochrome *c* oxidase (CcO) was tethered to an electrode and used as a starting point for the assembly of a phospholipid bilayer around it (Figure 86).²⁵⁰ The tethers between the protein and electrode were of sufficient length and hydrophilicity to maintain a layer of aqueous solution between the protein bilayer and the electrode; the generation and maintenance of this layer was aided by the presence of a carboxylic acid-terminated alkanethiol SAM, surrounding the tethers.

CcO catalyzes the four-electron reduction of O₂ to water and couples this reduction to proton pumping across the membrane in which it resides. Driving dioxygen reduction electrochemically causes CcO to pump protons across the lipid bilayer into the aqueous layer between the membrane and the electrode. These protons can be detected electrochemically as they are reduced to hydrogen at the electrode. The pumping of protons across the bilayer was shown to be highly dependent on both the orientation of the proteins and the presence of O₂. No proton pumping occurred in the absence of O₂. Further details and mechanistic insight into catalysis by CcO will be presented in a later section of this review.

7.2.3. Glucose Oxidase. Because of its ability to oxidize glucose, glucose oxidase (GOD) has been used in biosensors for the quantitative determination of glucose in bodily fluids, food, beverages, and fermentation liquor.²⁵² Although there has been a large amount of research on the development of GOD-based biosensors, significantly less work has been invested in studying its direct electrochemistry. The electrochemical mechanism is of interest because the GOD-catalyzed oxidation of glucose involves two identical flavin adenine dinucleotide (FAD) redox centers in GOD.²⁵³ PCET reactions involving

FAD are common in biology and are discussed further in section 8.5.2 of this review.

Recently, GOD was immobilized on two different substrates, and each was used to study both direct electrochemistry and glucose oxidation catalysis by GOD.^{252,253} In one study, the enzyme was immobilized on colloidal gold nanoparticles on a glassy carbon electrode surface within a Nafion film.²⁵² In the other study, glassy carbon electrodes were used to support Nafion films, containing the enzyme adsorbed to mesoporous silica (MCM-41).²⁵³ In both films, the observed reduction potential for the FAD/FADH₂ couple occurred at a potential slightly positive of $E^{\circ'} = -0.46$ V (versus SCE) for the FAD/FADH₂ couple in solution at pH 7.0 (25.8 °C). In the gold nanoparticle films, $E^{\circ'} = -0.434$ V at pH = 7, while $E^{\circ'} = -0.417$ V at pH = 6.1. The positive shift in $E^{\circ'}$ for films containing MCM-41 was attributed to interaction of the protein with positively charged acidic SiOH groups on the surface of MCM-41. In both films, the pH dependence of the FAD/FADH₂ couple at 22 °C was that expected for a 2e⁻/2H⁺ couple (-58.6 mV/pH unit). A surface electron transfer rate constant, $k_s = 1.30$ s⁻¹, was determined for the gold nanoparticle films at a scan rate of 50 mV/s with a peak-to-peak splitting, $\Delta E_p = 21$ mV, assuming a charge transfer coefficient (α) of 0.5. Both films demonstrated relatively high stability and the ability to catalyze the electrochemical oxidation of glucose. Interestingly, both films showed the same degree of activity for glucose oxidation, with apparent $K_{M,app}$ values of ~5 mM.

7.2.4. Arsenite Oxidase. Arsenite oxidase from the chemolithoautotrophic bacterium, NT-26, was immobilized on an edge-oriented graphite disk, by using the nonredox-active peptide, polymixin sulfate, to promote binding.²⁵⁴ While adsorbed to the electrode, the enzyme functions natively in the oxidation of arsenite to arsenate. The catalytic electrochemical potential displayed a pH dependence of -33 mV/pH unit between pH 4.5 and 7. The authors claimed that this dependence was indicative of PCET; however, they were unable to assign it to a particular protonation reaction.

8. PCET IN BIOLOGY AND MODEL SYSTEMS

8.1. Introduction

PCET is a common phenomenon in biology, in signaling, and especially in bioenergetics, where transfer of both electrons and protons is key.^{9,255} The role of PCET in biological reactions has been explored at the molecular level by application of X-ray crystallography, a variety of spectroscopies, and site-directed mutagenesis, as well as by DFT calculations.^{7,53b,256} In the most recent crystallographic description of the oxygen-evolving complex, Shen and co-workers have presented the crystal structure of Photosystem II at a 1.9-Å resolution.²⁵⁷ This section highlights the role of PCET, and especially EPT, in a representative sample of biological systems.

8.2. Tyrosyl Radicals

PCET and EPT pathways are often essential steps in enzymatic catalytic reactions. In redox enzymes, the phenolic side-chain of tyrosine can participate in PCET with long-distance electron transfer coupled to local proton transfer. The most well-known example occurs in Photosystem II (PSII), where water oxidation is coupled to light absorption that occurs at a distant chlorophyll-accessory pigment antenna array.

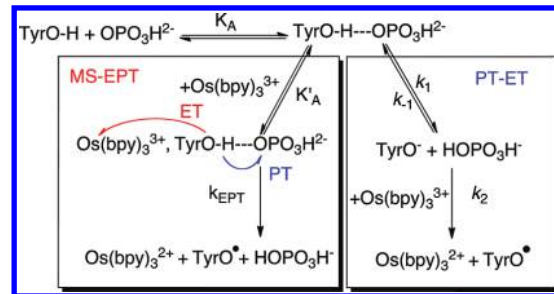
Excitation and electron transfer quenching at the chromophore P₆₈₀ gives the P₆₈₀^{•+} radical cation that subsequently oxidizes Y_Z to Y_Z[•], which serves as a redox relay. Y_Z consists of the hydrogen-bonded Tyr161--His190 pair, and it has been suggested that its oxidation to Y_Z[•] occurs by multisite-electron proton transfer (MS-EPT) with electron transfer from Tyr161 and proton transfer to His190: P₆₈₀^{•+} + TyrO-H--His190 → P₆₈₀ + TyrO^{•-}-H-His190.^{1,6,17a,20b,258,259}

Once formed, Y_Z[•] oxidizes the Mn₄Ca cluster in the oxygen-evolving complex (OEC). It has been suggested that this reaction occurs in reverse at Y_Z with electron transfer from the OEC occurring in concert with back proton transfer to tyrosyl radical—OEC + TyrO^{•-}-H-His190 → (OEC)⁺ + TyrO-H--His190—a mechanism described by Renger as “proton rocking”,^{20c,260} although numerous other descriptions exist. This coupling is a major area of PSII research and is discussed in section 8.4. Structure, mechanism, kinetics, and thermodynamics in PSII have all been reviewed in a number of accounts.^{1,9,90a,196,261}

Tyrosine has been proposed to participate in catalytically essential reactions in other biologically critical enzymes including prostaglandin H synthase,²⁵⁶ cytochrome c oxidase,²⁶² and class I ribonucleotide reductase.^{9,256} Its oxidation has also been investigated electrochemically and spectroscopically in the native amino acid^{15,263} and in model systems.^{38,90a,230} Electrocatalytic oxidation of tyrosine by M^{III}(bpy)₃³⁺ (M = Fe, Ru, Os) is catalyzed in buffered solutions containing a variety of proton-acceptor bases (sodium acetate, sodium succinate, histidine, sodium phosphate, and tris). Application of Digisim (section 6.1) to cyclic voltammograms (CVs) over a broad range of buffer concentrations and buffer ratios has been used to establish the mechanism in Scheme 37, consistent with the rate law in eq 77. Analogous mechanisms have been established for M^{III}(bpy)₃³⁺ oxidation of guanine, guanine derivatives and cysteine.²⁶⁴

$$\frac{-d[Os^{III}]}{dt} = \left[\frac{K_A[TyrOH]_T[HPO_4^{2-}]}{1 + K_A[HPO_4^{2-}]} \right] [Os^{III}] \left[K'_A k_{EPT} \right. \\ \left. + \frac{k_1 k_2}{k_2[Os^{III}] + k_{-1}[HB]} \right] \quad (77)$$

Scheme 37. Parallel Pathways for the Base-Catalyzed Oxidation of Tyrosine via Prior Association of Tyrosine (TyrOH) with HPO₄²⁻ as the Proton-Acceptor Base^a



^aPreassociation with the base form of the buffer (K_A) is followed by competitive multisite-electron proton transfer (MS-EPT) and deprotonation to $TyrO^-$ followed by electron transfer oxidation (PT-ET).¹⁵ Adapted with permission from refs 15, 226, and 263. Copyright 2007 American Chemical Society.

In the mechanism in Scheme 37, shown partly in Scheme 4 of the Introduction, the key step is initial H-bond preassociation by the buffer base, $TyrOH + B: = TyrOH-B:$ K_A , followed by oxidation via two competing pathways. In one pathway, a further preassociation occurs with the oxidant followed by MS-EPT with $k_{obs} = k_{EPT} K_A K_A'$. In MS-EPT, electron transfer occurs to $M^{III}(bpy)_3^{3+}$ in concert with proton transfer to the acceptor base. In the second pathway, proton transfer occurs to the H-bonded base to give tyrosine anion, $TyrO^-$, followed by its oxidation by $M^{III}(bpy)_3^{3+}$ via a PT-ET pathway (Scheme 37).^{15,263} Kinetic studies over an extended range of buffer concentrations and buffer acid/base ratios allowed the individual constants in Scheme 37 to be evaluated with K_A varying from 12 to 38 M⁻¹. The value for HPO₄²⁻ was in agreement with K_A values measured directly by ³¹P NMR.²⁶³

Given the extensive series of oxidants ($E^\circ' = 0.85\text{--}1.25$ V versus NHE) and proton-acceptor bases ($-RT \ln K_A = -0.15$ to -0.21 eV), it was possible to explore the role of free-energy change on EPT over an extended ΔG range under conditions where MS-EPT dominated. These studies revealed a systematic variation in k_{EPT} with $\Delta G^\circ'$ independent of whether ΔG was varied by varying E°' for the oxidant or pK_a for the base. As shown by the plot of $-RT \ln k_{EPT}$ versus $-\Delta G^\circ'$ in Figure 87,

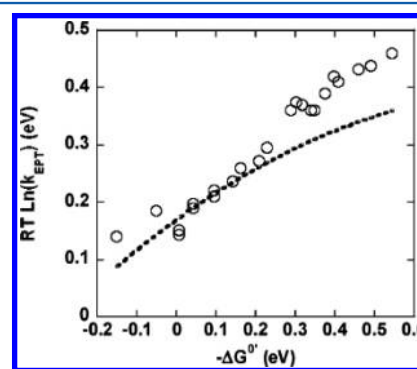


Figure 87. Variation of $RT \ln(k_{Red})$ versus $-\Delta G^\circ'$ in eV by varying both E°' for the oxidant and pK_a for the acceptor base; see text. The dashed line is a plot of $RT \ln k_{Red} = RT \ln k(0) + (\Delta G^\circ'/2)(1 + \Delta G^\circ'/2\lambda)$ with $k(0) = 8.9 \times 10^2$ s⁻¹, $\lambda = 0.90$ eV.¹⁵ Reproduced with permission from ref 15. Copyright 2007 American Chemical Society.

the variation with ΔG° provides evidence for a “quantum beat” effect arising from the high-frequency nature of the $-O-H-B$ stretching modes involved in the proton transfer part of the EPT reaction.¹⁵

DFT calculations by Hammes-Schiffer and co-workers on the association of dibasic phosphate with tyrosine, indicate that the donor–acceptor distance is ~ 0.2 Å shorter for HPO_4^{2-} as proton acceptor than for bulk water. The decrease in proton transfer distance is due to the increase in base strength for HPO_4^{2-} with $pK_a(HPO_4^{2-}) = 7.2$ compared to $pK_a(H_2O) = -1.7$. The decrease in proton transfer distance due to stronger H-bonding increases vibronic coupling between reactant and product wave functions, increasing k_{EPT} .²⁶⁵

The role of pH effects and EPT has been investigated in intramolecular oxidation of the phenol derivatives of the Ru and Re complexes shown in Figure 55 (section 5.4). In these experiments laser flash excitation and oxidative quenching of $Ru^{III}(bpy^{\bullet-})$ or $Re^{II}(bpy^{\bullet-})$ MLCT excited states was followed by intramolecular phenol \rightarrow Ru(III) or Re(II) electron transfer as monitored by transient absorption measurements. At high buffer concentrations, MS-EPT pathways were observed analogous to bimolecular tyrosine oxidation in Scheme 37, e.g., $Ru^{III}-ArOH-B \rightarrow Ru^{II}-ArO^{\bullet-}+H-B$. However, as shown by the data in the inset in Figure 88, at low

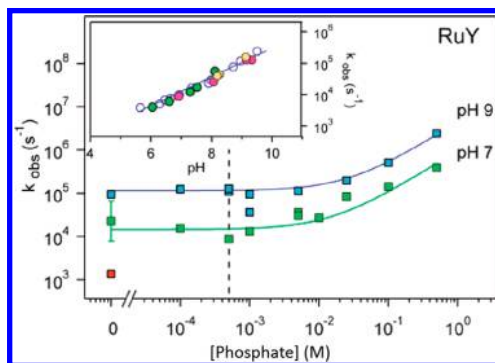


Figure 88. pH dependence of k_{obs} for intramolecular oxidation of Ru-Y, $Ru^{III}-TyrOH \rightarrow Ru^{II}-TyrO^{\bullet-} + H^+$, illustrating the appearance of a pH dependence below 0.5 mM added buffers, $H_2PO_4^-/HPO_4^{2-}$. The inset shows the pH dependence of k_{obs} over an extended pH range. Similar effects were observed for the complexes $Ru_{\text{ester}}Y$ and $Re(P-Y)$. Reproduced with permission from ref 165f. Copyright 2007 American Chemical Society.

concentrations of buffer where MS-EPT does not play a role, an apparent pH dependence remains.^{165f} Although ΔG for the intramolecular half-reaction $Ru^{III}-ArOH \rightarrow Ru^{II}-ArO^{\bullet-} + H$, is pH-dependent, as noted in section 5, this cannot be the origin of the pH effect: at the microscopic level, there is no basis for coupling a local gain or loss of protons in an elementary step to the surrounding ensemble of solvent, protons, buffer, etc. that define the final equilibrium state including the pH.²⁶⁶

Even given $pK_a = -1.7$ for H_3O^+ , a role for water acting as a proton acceptor in electrochemical phenol oxidation has been documented by Savéant and co-workers based on a kinetic analysis and the appearance of a H_2O/D_2O KIE in unbuffered solutions.^{95,196} At higher pH's, the authors also identified a pH dependence arising from proton loss, $TyrOH + OH^- \rightarrow TyrO^- + H_2O$, followed by oxidation of tyrosine anion.¹⁹⁶ Stopped-flow measurements on oxidation of phenols by hexachloroiridate ($IrCl_6^{2-}$) by Song and Stanbury suggested water as a proton acceptor in an EPT pathway with H_2O/D_2O KIEs as

large as 3.5 ± 0.3 observed.¹⁴¹ However, the physical basis for a pH dependence observed in these reactions was not fully resolved.^{53a}

8.3. PCET in Designed Peptides and Redox Cofactors

8.3.1. Peptides. Radical transfer between redox-active amino acids is a common reaction in enzymes.²⁵⁶ This phenomenon has been explored extensively in synthetic peptides to mimic related intramolecular phenomena in Photosystem II, RNR, and cytochrome c peroxidase.²⁶⁷

The role of oxidatively induced PT from tyrosine and histidine was investigated in a small β -loop 18 amino acid peptide.²⁶⁸ Oxidation was induced by pulse radiolysis and investigated by using EPR and ^{14}N And ^{15}N electron spin-echo envelope modulation (ESEEM). The results suggest not only that histidine acts as a proton acceptor but also that the protein environment alters EPT.²⁶⁹ The role of base and protonation state was further verified by studies on non-natural amino acids and quinones in tyrosine oxidation.^{259g,270}

Electron transfer between tyrosine and tryptophan radical cation ($TrpNH^{\bullet+}$) plays a significant role in long-range electron transfer and, with it, signaling and enzyme function. Examples of this type of reactivity are found in ribonucleotide reductase.²⁷¹ Electron transfer between tyrosine and $TrpNH^{\bullet+}$ was investigated in a series of bridged donor–acceptor assemblies, $Tyr-(Gly)_n-Trp$ ($n = 0-5$), with methylamine added to mimic amino acid side chains. The peptide reactions were studied by density functional theory (DFT) and ab initio molecular dynamics (AIMD). The combined methods provided information on how electrons and protons might transfer cooperatively in peptides. The most essential feature of the cooperative mechanism for proton and electron transfer is either direct or proton-regulated transfer.²⁶⁸ In assemblies with the redox sites in close proximity, $n = 0, 1$, and 2 , prior proton loss from $TrpNH^{\bullet+}$ followed by EPT from $-TyrOH$ to $TrpN^{\bullet}$ dominates (Figure 89). At longer distances, $n > 2$, the mechanism shifts to MS-EPT with an external base acting as proton acceptor (Figure 89). The switch in mechanism underlines the importance of position and availability of proton acceptors in the utilization of EPT pathways in protein oxidation.²⁶⁸ In related studies, the formation of tyrosyl radicals with cysteine placed at intermediate distances point to water, not buffer base, as the proton acceptor.²⁷²

8.3.2. Metal-Binding Heme Proteins. A role for PCET was investigated in an electrochemical study on metal-binding heme proteins in 4-helix α bundles in an attempt to model proton-pumping mechanisms. Electrochemically determined redox potentials of the heme proteins for oxidation from Fe(II) to Fe(III) occur with a pH-dependent midpoint potential as studied by redox potentiometry. Two heme maquettes were prepared based on the structure in Figure 90. The first is heme b-[$\Delta 7$ -His]₂. This shows a pH-dependent reduction potential of 120 mV/pH unit consistent with a $2H^+/1e^-$ transfer between pH 4.0 and pH 8.0. A second protein maquette, heme b-[H10A24], has a pH-dependent reduction potential between 4.2 and 7.0, which was fit to two distinct $1H^+/1e^-$ transfers. One at $pK_{a,\text{eff}} = 1.7$ makes b-[H10A24] more resistant to changes in the protonation state of the heme in both the oxidized and reduced states than in b-[$\Delta 7$ -His] with $pK_{a,\text{eff}} = 5.7$. The relative ratios of Fe(II) to Fe(III) were investigated by UV/visible spectrophotometry. Stronger binding is correlated with less-structured proteins.^{270c} Tighter binding is correlated to axial histidines and stabilization of Fe(II). It also binds the

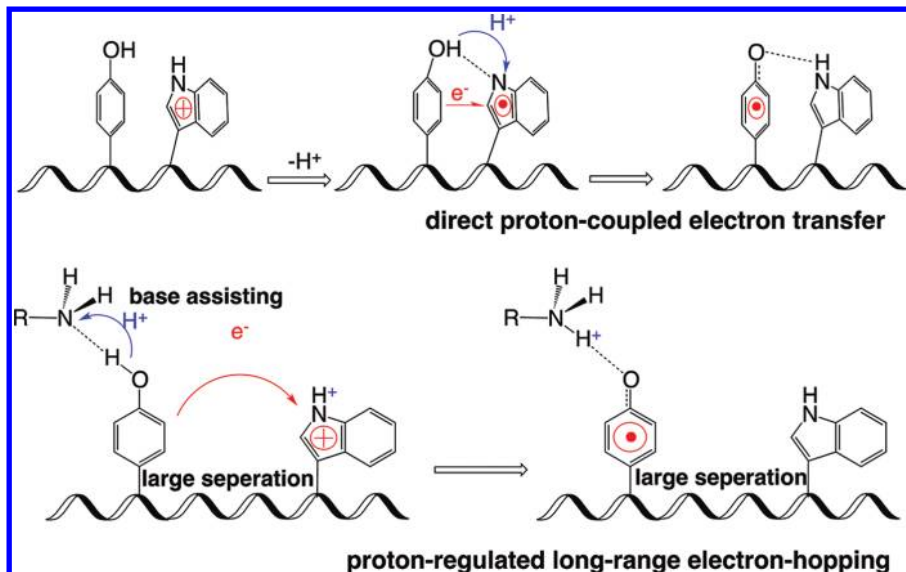


Figure 89. Proposed mechanisms for electron transfer from tyrosine to tryptophan radical cation (TrpNH^{2+}) in a series of synthetic peptides. With $n < 2$, the mechanism involves prior proton loss from TrpNH^{2+} followed by concerted EPT from TyrOH to TrpN^{\bullet} . With $n > 2$, the mechanism involves an external base and MS-EPT with electron transfer to TrpNH^{2+} and proton transfer to the base. Reproduced with permission from ref 268. Copyright 2009 American Chemical Society.

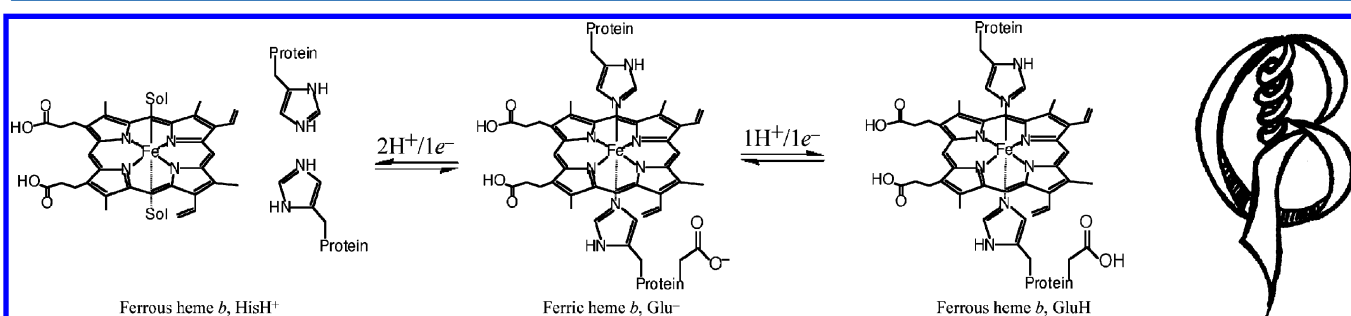


Figure 90. Proton-coupled electron transfer (PCET) mechanisms proposed for heme protein maquettes. The structure of the protein maquette is reported in the figure on the right and consists of both beta sheets and an α -helix. Reproduced with permission from ref 270c. Copyright 2007 American Chemical Society.

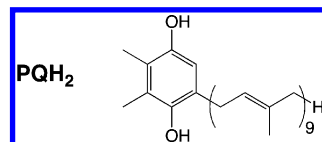
ferric state with flexible binding, allowing for dissociation of ligands.

The two protein maquettes were used to investigate the effects on the protein scaffold of pH modulation of reduction potential. Investigation of protein thermodynamics for these two scaffolds reveals that the sites and mechanisms of proton-coupled electron transfer are distinct. It shows that redox kinetics in the protein are affected by porphyrin–protein hydrophobic interactions, histidine coordination, and electrostatics. The mechanisms of PCET are reported in Figure 91. The redox kinetics of *b*-[H10A24] are associated with a glutamate residue and result in destabilization of the ferrous state. In the case of *b*-[Δ 7-His], the pH-dependent reduction potential is attributed to histidine ligand loss from the ferric state.

8.4. Photosystem II

8.4.1. Introduction. Oxygenic photosynthetic organisms use the oxygen-evolving complex (OEC) in Photosystem II to catalyze the photooxidation of water to dioxygen (eq 78). Sequential and cumulative oxidation steps occur by the Kok cycle, where four photons result in the accumulation of 4 oxidizing equivalents in the OEC, at which point O_2 is released. An extended version of the Kok cycle (Scheme 38) was

recently proposed by Dau accommodating sequential proton release throughout the cycle (see later), a modified version of this is shown in Scheme 38. PSII is one of four key functional elements embedded in the hydrophobic thylakoid membrane in chloroplasts. Oxygen production is coupled to the reduction of plastoquinone (PQ), to plastoquinol (PQH_2) by the net reaction in eq 78.^{21,109d,273} The overall process is energetically demanding (0.884 V at pH 7), requiring four photons to produce a single molecule of O_2 . O_2 production is coupled with transport of four protons across the thylakoid membrane from the stroma to the lumen creating a proton gradient, which is used to convert ~ 7 ADP molecules to ATP. The mechanism for production of the pH gradient discussed in section 7.2.2. PSII is a spectacular example of PCET in action, requiring the precise management of protons and electrons over long distances through multiple steps.^{6,274}



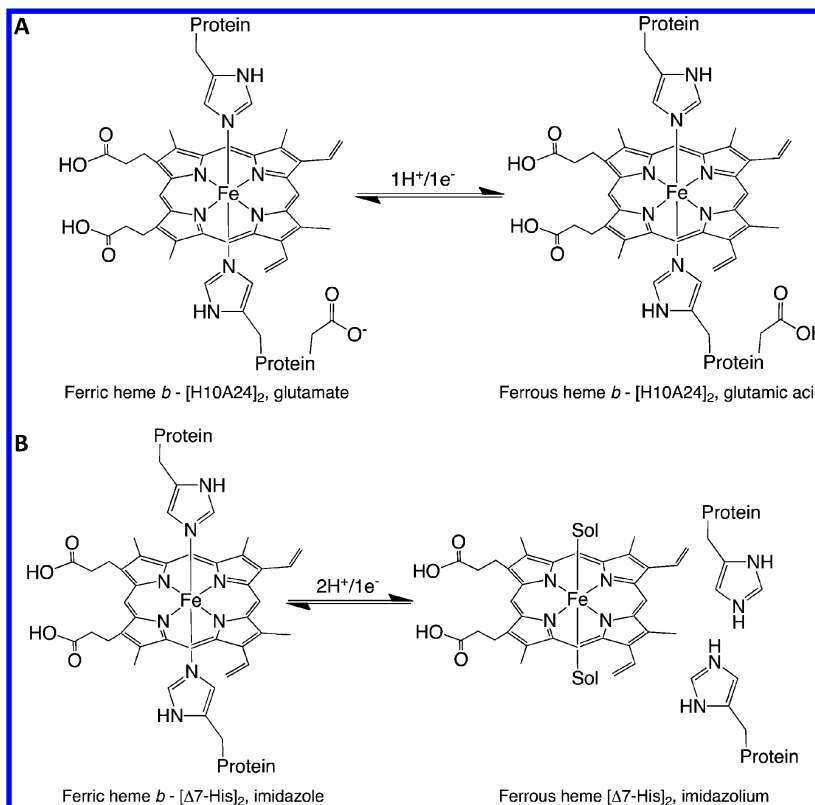


Figure 91. Mechanism of proton-coupled electron transfer for two related protein maquettes. (A) Mechanism for redox kinetics at the iron heme center for *b*-[H10A24] where PCET reactivity is associated with the glutamate residue. (B) Mechanism for redox kinetics for *b*-[Δ 7-His] where PCET is associated with a histidine. Reproduced with permission from ref 270c. Copyright 2007 American Chemical Society.

Water oxidation is driven by light absorption by a distant chlorophyll-accessory pigment antenna array, which sensitizes formation of the lowest singlet excited state of chlorophyll P_{680} (Chl_{D1}), $^1P_{680}^*$. $^1P_{680}^*$ undergoes electron transfer quenching by adjacent pheophytin $_{D1}$ to give P_{680}^+ , which is a powerful oxidant with $E^\circ/(P_{680}^+/P_{680}) = 1.25$ V. As seen in Figure 92, this triggers a cascade of coupled electron–proton transfer reactions.

As shown in Figure 92, taken from ref 18, electron transfer quenching triggers a cascade of five coupled electron transfer events with time scales ranging from ps to ms. Electron transfer is driven by spatially directed free-energy gradients between intermediate redox carriers in the membrane. Electron transfer leads to separated oxidative and reductive equivalents, the former at the OEC and the latter at quinone Q_B as semiquinone, $Q_B^{\bullet-}$, separated by ~ 50 Å from the nearest Mn site in the OEC. The long separation distance is essential for slowing down back electron transfer, which occurs on the \sim ms time scale over the Kok cycle, allowing charge and a potential high enough for water oxidation to accumulate in the OEC.

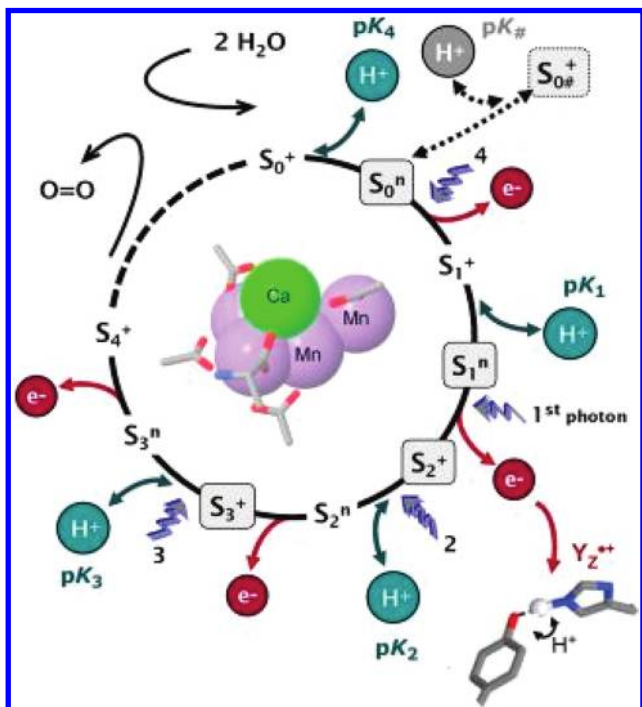
Following a second photon-electron cycle, further PCET reduction of $Q_B^{\bullet-}$ occurs to give plastoquinol (H_2Q_B) with its reductive equivalents ultimately transferred, via cytochrome b_6f , to Photosystem I and the Calvin cycle, where CO_2 is reduced to glucose.²⁷⁷ Protons released by oxidative activation of the OEC during the Kok cycle are transferred through a proton transfer channel to the lumen in $\sim 10 \mu\text{s}$. Protons enter the membrane from the stroma driven by PCET reduction of PQ to PQH_2 , as discussed in section 1.4.S. The protons gained at PQ upon reduction to PQH_2 are later released to the lumen when PQH_2 is reoxidized to PQ.

The role of PCET in the OEC is a long-standing problem of broad interest that has been studied from the standpoint of enzymes hosting native PSII, the synthesis of model complexes, and theoretical studies.^{6,13,109,278} Still, no consensus has been reached about the exact mechanism of water oxidation; this enormous body of literature is briefly reviewed only as far as it relates to emerging consensus and barriers to understanding PCET. We anticipate that this field will continue to grow at a fast pace, specifically in the area of joint experimental and theoretical studies, which are still much needed. As shown in Figure 93, EPT has been proposed as a $1\text{e}^-/2\text{H}^+$ MS-EPT step for the initial $S_0 \rightarrow S_1$ stage in the Kok cycle with electron transfer from the Mn(4) site in the Mn_4Ca cluster to Y_Z^{\bullet} . In this step (Figure 93), it has been proposed that two coupled EPT events occur in concert: (i) EPT at $\text{Mn}(4)\text{-OH}_2$ with electron transfer to TyrO^{\bullet} and proton transfer to neighboring base Asp61; and (ii) EPT at $\text{TyrO}^{\bullet}\cdots\text{H}-\text{His190}$ with electron transfer from $\text{Mn}(4)\text{-OH}_2$ and proton transfer to TyrO^{\bullet} from the H-bonded $\text{H}-\text{His190}$. The Asp61 involved in (i) is the entryway to a long-range proton exit channel to the lumen.

In a final stage in the $S_0 \rightarrow S_1$ conversion, it has been proposed that proton transfer to the lumen from Asp61-COO $^-$ is followed by proton equilibration at $\text{Mn}(4)\text{-OH}_2$ by intracoordination sphere proton transfer (Figure 94). This resets the $\text{Mn}(4)\text{-OH}_2$ position in the coordination sphere at $\text{Mn}(4)\text{-OH}_2$ with a hydrogen bond to Asp61-COO $^-$ for use in further stages in the Kok cycle.

In general, PCET is currently invoked to describe three aspects of PSII: (i) oxidation of and proton loss in the OEC and subsequent formation of Mn-OH_2 , Mn-OH (or bridging species), Mn-OOH , and Mn=O around the Mn cluster, (ii)

Scheme 38. Modified Version of the Kok Cycle for Oxidative Activation and O₂ Evolution at the Oxygen-Evolving Complex (OEC) of Photosystem II^a



^aIn the cycle, light absorption and excited-state electron transfer result in stepwise oxidation of the OEC ($S_0 \rightarrow S_1$, etc.) with transmembrane proton transfer occurring from the stroma to the lumen. Reproduced from ref 275. Copyright 2011 The American Society for Biochemistry and Molecular Biology.

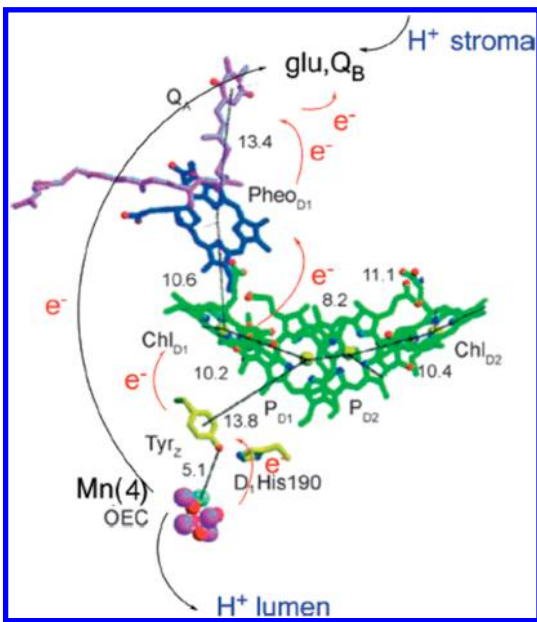


Figure 92. Structure of the reaction center in PSII illustrating the sequence of e^-/H^+ events that occur in the $S_0 \rightarrow S_1$ transition following single photon absorption. Reproduced in part with permission from ref 18. Copyright 2004 American Association for the Advancement of Science.

the oxidation and reduction reactions of the Y_z and Y_D tyrosine residues, and, to a lesser extent, (iii) reactions around the

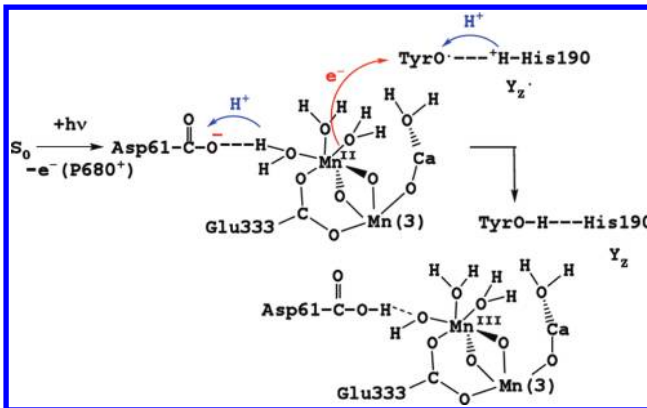


Figure 93. Illustrating the proposed $1e^-/2H^+$ EPT oxidation of $Mn(4)-OH_2$ to $Mn-OH$ in the first stage of the Kok cycle.

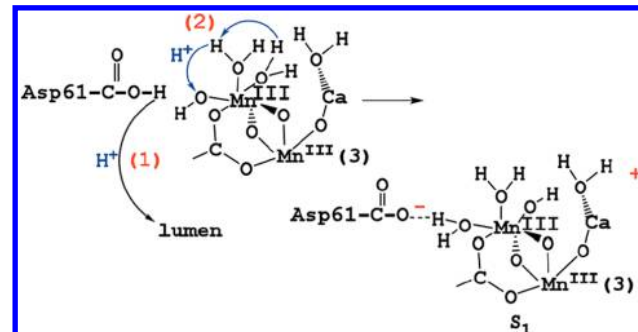


Figure 94. Illustration of the proposed intracoordination sphere proton transfer step in the first step of the Kok cycle.

quinone species Q_A and Q_B . An enormous body of literature describing the structure and mechanistic proposals for PSII already exists.^{6,274b,283} We have therefore highlighted recent advances in these three main areas.

8.4.2. Structural Updates Related to Water Oxidation and PCET.

8.4.2.1. Structural Background. PSII is a ca. 650 kDa homodimer embedded in the thylakoid membrane of oxygenic photosynthetic organisms (cyanobacteria, algae, and most green plants). Each monomer is further made up of polypeptide units. Some are used for light absorption and photonic energy transfer based on chlorophyll and carotenoid absorbers located in subunits CP43 and CP47, whereas others are used in electron transfer (subunits D1 and D2). As discussed below, both monomers are essential for water oxidation and utilize PCET for proton and electron transport. The oxygen-evolving complex (OEC) is a Mn_4CaO_4 cluster that probably contains Cl^- and interacts with all protein subunits.²¹ Subunit D1, which contains P680 and Y_z , undergoes photooxidation and drives the Kok cycle in Scheme 38 by repeated oxidative cycling with electron transfer to $P680^+$. Progression through the Kok cycle occurs through a sequence of “S states” from S_0 to S_4 with the subscript indicating the number of electrons lost. The “dark” resting state is S_0 , and oxygen evolution occurs when the S_4 state is reached.²⁸⁴ Long-range proton transfer from the OEC to the lumen is thought to be aided by the remaining protein subunits. Calcium is thought to play a critical role in the O–O bond-forming step. Chloride is a necessary cofactor, although it can be replaced by other anions.^{285,286}

8.4.2.2. Recent Structural Findings. A major obstacle to understanding the exact structure of PSII and the OEC in its

various S states is radiative damage to the crystalline protein samples used in EXAFS and XRD data collection due to X-ray irradiation.^{287,274b,283a,b} This severely limits the resolution (ca. 3.8–3.0 Å) of the information that is obtained by these methods. Structural changes induced by X-ray damage have been investigated and are a known phenomenon.²⁸⁸

Since 2007, the end date for coverage by PCET1,¹ there have been several new structural findings: a 2.9-Å resolution crystal structure for cyanobacterial *Thermosynechococcus elongatus*²⁸⁹, a 3.5-Å eukaryotic structure for red algae,²⁹⁰ and a 1.9-Å resolution structure from the cyanobacterium *T. vulcanus*.²⁵⁷ A separate crystal structure containing bromide in place of chloride was also obtained at 4.2-Å resolution.²⁹¹ The coordination sphere of the OEC is thought to be bridged by carboxylates at Asp170, Glu189, His332, Glu333, Asp342, Ala344, and Glu354; Gln165, His337, and Asp61 may be close enough to have electrostatic interactions with the OEC and exhibit structural effects. The structural assignments are still debatable: results from FTIR and direct mutation studies have shown that residues Asp342 and Glu189 do not show the expected spectroscopic changes as the S states progress and appear not to be ligands in the OEC.^{283g,292}

New XRD data have allowed Q_A , the precursor electron donor to Q_B , to be modeled completely, along with a new quinone, Q_C . On the basis of this new data, Guskov et al. have proposed a new mechanism for the quinone and quinol “flux” within the quinone–quinol exchange cavity.²⁹³ The putative location of chloride is agreed, experimentally and theoretically, to be 5–7 Å from the Mn–Ca vector of the OEC. The degree of interaction between the OEC, bound H_2O , and chloride is still debated (see below).²⁷⁷ The possibility of a second chloride-binding site has also been proposed.²⁹¹

The use of X-ray methods that are less damaging to the protein have also led to new structural insights.^{274b,283a,b,294–296} Data collected using polarized EXAFS, with data refinement to ~0.15 Å, show metal–metal distances that differ slightly from the crystallographic data.^{296b,a,c} The same technique provides information on the formal oxidation states of the manganese ions in the various S states. Both S1 and S2 are thought to contain Mn^{III} and Mn^{IV} , in agreement with current models of the early S states (see later for S state mechanisms).²⁹⁷ The Mn–Ca distance was found to be 3.4 Å, and Mn–Mn distances were 2.7, 2.8, and 3.2 Å.^{296a} Because of the differences in the angular distances of the manganese atoms, there is still some discrepancy in their exact coordinates within the OEC. A recent series of papers suggests that bicarbonate is not a ligand to the OEC.²⁹⁸

Rapid progress on structure and mechanism in the OEC has been made by using DFT and QM/MM computational methods. A number of calculated structures of the OEC have appeared; most emphasize the energetic stability of a particular structure for the Mn_4O_4Ca cluster and are in agreement with available structural information by XRD.^{262a,b,282d,299} The preferred OEC model is a cubane Mn_3O_4Ca core tethered to a “dangler” Mn by a di- μ -oxo bridge.¹⁸ Lower-energy structures are obtained if the metal positions are not fixed, showing that theoretical and experimental structures do not completely agree. As an example, calculations on the location of the chloride cofactor optimize its position 5.6 Å from the nearest Mn atom by DFT.^{282d} It is modeled nearly 6.5 Å away in crystal structures.³⁰⁰ These structural details have mechanistic implications that are discussed in the next section.

8.4.3. Mechanism, Kinetics, and Thermodynamics.

8.4.3.1. Background and Thermodynamics. The major function of the OEC is the transfer of oxidizing equivalents from photo-oxidized P680 to water molecules bound to the Mn core in the OEC. As noted above, to oxidize water to dioxygen, the OEC advances through a series of “S states”, known collectively as the Kok cycle (Scheme 38), which involve the sequential loss of protons and electrons following the repeated photoexcitation of P680.^{278a–j,l–n,284} Five S states, $S_0–S_4$, were initially proposed,²⁸⁴ with the O–O bond being formed in the second half of the cycle.²¹ Because of the limited structural information about the detailed ligation pattern of amino acids and water molecules in the primary and secondary coordination spheres of the OEC, a number of variations to the Kok cycle have been proposed based on theoretical (DFT and QM/MM) and experimental evidence that vary in oxidation states at the Mn ions.^{6,301} Regardless of structural considerations, inspection of the Frost diagram in Figure 95 shows that involvement of

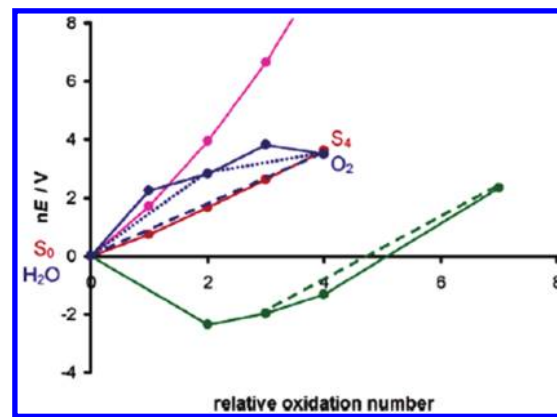


Figure 95. Frost diagram (nE versus relative oxidation number) showing the cumulative reduction potentials of four species: the OEC in red (pH = 6, referenced to S_0); a single manganese ion in green (pH = 6, referenced to Mn^0); a hypothetical manganese tetramer, without PCET, in magenta (see text for details, referenced to $Mn^{III} Mn^{IV}$); oxygen in blue (pH 6, referenced to $2H_2O$; the species shown on the solid blue line are $2H_2O$ (0), $H_2O + OH^-$ (1), H_2O_2 (2), O_2^- (3), and O_2 (4)). The blue long-dashed line represents the four-electron S_4/S_0 couple. The two blue short-dashed lines represent the two two-electron couples, S_4/S_2 and S_2/S_0 . The green dashed line represents the Mn^{VII}/Mn^{III} couple. All reduction potentials are given versus the standard hydrogen electrode (SHE). Reproduced with permission from ref 21. Copyright 2006 American Chemical Society.

PCET is certain.^{21,274b,283} The magenta and red lines show water oxidation in the absence and presence of PCET, respectively. PCET provides the lowest ΔG route (smallest slope in Figure 95) for the four-electron, four-proton oxidation of water to dioxygen. The most recent experimental findings related to PCET are reviewed below.

Redox potentials for couples in the P680/ Q_B redox chain governing the thermodynamics of water oxidation in PSII are not yet clear because of the difficulty of making direct measurements. In recent developments, Kato et al.³⁰² measured $E^\circ' = -261 \pm 6$ mV (NHE) for the Phe a /Phe a^- couple, and Shibamoto et al.³⁰³ measured -140 ± 2 mV (NHE) for the Q_A/Q_A^- couple at physiological pH by application of spectroelectrochemical techniques (see section 6.4). These values are significantly different from previously reported values, and will undoubtedly be debated for years

to come: the Q_A/Q_A^- couple was reported in 2007 to be 84 ± 24 mV by Fufezan et al.,^{277a} which is significantly different from the previously accepted value of -604 mV.³⁰⁴ These new values significantly affect the free-energy difference between the donor Phe a^- and the acceptor Q_A (the donor to Q_B), which is determined to be -330 to -370 mV, as shown in Figure 96.

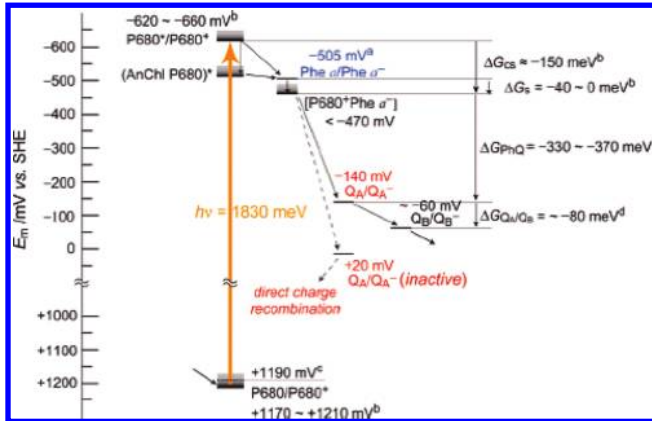


Figure 96. Energetics in PS II based on midpoint redox potentials, $E_m(Q_A/Q_A^-)$ and $E_m(\text{Phe } a^-/\text{Phe } a^-)$, together with free-energy differences estimated in the literature. The value of $E_m(\text{Phe } a^-/\text{Phe } a^-)$ is from ref 302 for the values of $E_m(\text{P}_{680}^+/\text{P}_{680}^*)$, $E_m(\text{P}_{680}^+/\text{P}_{680})$, ΔG_{CS} , and ΔG_S , and the gray boxes indicate uncertainties; see discussion in ref 302. The value of $E_m(\text{P}_{680}/\text{P}_{680}^+)$ was calculated from a kinetic analysis (ref 305) on the basis of the $E_m(Q_A/Q_A^-)$ value determined by Shibamoto and co-workers;³⁰³ the value of $\Delta G_{Q_A/Q_B}$ is from the literature.^{304,306} The solid arrows denote the forward electron transfer in oxygen-evolving PS II complexes, whereas the broken arrows denote reverse (charge-recombination) electron transfer for photoprotection of inactivated PS II. Reproduced with permission from ref 303. Copyright 2009 American Chemical Society.

Good theoretical agreement with the measured pK_a values has recently been reported by Ishikita and Knapp^{299c} and is discussed in the next section. The evolving thermodynamic picture remains consistent with the kinetic analysis by Rappaport et al. on Phe a^{277c} and with charge-recombination studies by Dau and co-workers on Q_A .^{274b,305}

Only limited values for S state energies, energy barriers, and standard free-energy changes (ΔG°) are available by direct measurement and can only be calculated. Differences in free energies between S states have been calculated based on eq 79 and free-energy differences for formation of the cation radical $\text{P}_{680}^{+\bullet}$, oxidation of Y_Z by $\text{P}_{680}^{+\bullet}$, and S_i -state transitions, respectively.

$$\Delta G^\circ \left/ \frac{S_i + 1}{S_i} \right. = \Delta G^\circ \left(\frac{\text{P}_{680}^{+\bullet}}{\text{P}_{680}} \right) + \Delta G^\circ \left(\frac{\text{P}_{680} Y_X^{\text{Ox}} S_i}{\text{P}_{680} Y^{+\bullet} Y_Z S_i} \right) + \Delta G^\circ \left(\frac{Y_Z S_{i+1}}{Y_Z^{\text{Ox}} S_i} \right) \quad (79)$$

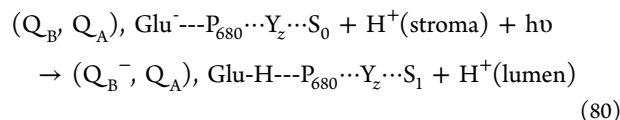
Messinger and Renger^{274a,307} have calculated the thermodynamic scheme for the Kok cycle shown in Figure 97, which draws on their interpretation of the water oxidation mechanism (see section 8.4.3.2).^{274a,278j,307}

8.4.3.2. Mechanism of Catalytic Water Oxidation and the S State Cycle. As shown in Scheme 38, protons are lost from the OEC as the S state increases to compensate for increased charge due to the higher oxidation state at Mn or associated

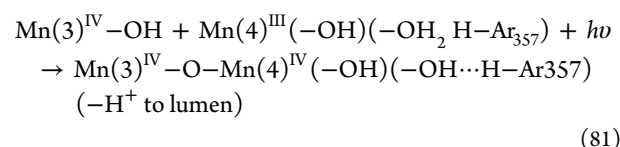
ligands. For the thermodynamic reasons described above, simultaneous release of protons is likely to involve PCET and MS-EPT pathways.^{9,274b,278c-h,j,l-n,283a-e,i} The key function of PSII in the photosynthetic apparatus is water oxidation at the OEC. As discussed in sections 1.4.5 and 8.4.1, water oxidation is coupled to an elaborate reaction scheme in which protons are transferred from the stroma to the lumen though a proton exit channel originating at Asp61 and driven by a free-energy gradient.

There are continuing debates about how the individual reactions occur, the precise pathways by which protons are released, the ligation patterns around Mn, and the location of the 4 electron “holes” or oxidative equivalents for water oxidation within the OEC. There is emerging consensus on the following points: (i) protons released following 4 consecutive light flashes required to produce dioxygen follow a 1:0:1:2 pattern, (ii) the oxidative steps between S_0 and S_3 are Mn-centered (as opposed to ligand-centered, see later),²¹ and (iii) Y_Z oxidizes the OEC and uses His190, a H-bond acceptor, for the phenolic Y_Z proton. However, the identities of the Mn ions oxidized, the location of the final reducing equivalent for Y_Z , whether O–O bond formation occurs in S_3 (“peroxidic mechanism”)⁶ or S_4 (“ S_4 Mechanism”),^{299a} and the exact mechanism of proton removal remain key points of controversy. Substantial insight into the S state mechanism has been gained by calculations on the S states, most notably by Batista, Messinger, and Siegbahn and their co-workers (see later).^{299a,308} Because S state semantics are somewhat confusing and may contribute to the ongoing O–O bond-formation debate, Renger and Renger recently proposed a “MWLY” (manganese, water, ligand, tyrosine) framework formulated to include reducing equivalents on the ligands and water and oxidizing equivalents at Y_Z .^{278j} The S states are only discussed here insofar as they illustrate recent contributions to the role of PCET in water oxidation. The reader is referred to previous reviews for the individual steps in the Kok cycle as a reference.^{6,274b,283}

As noted above, in the net reaction for $S_0 \rightarrow S_1$ in eq 80, illustrated in Figure 92, absorption of a single photon results in electron transfer over 50 Å from the OEC to Q_B by a sequence of five steps. Intramembrane H^+ transfer occurs from $Mn-\text{OH}_2$ to the lumen, and a second H^+ is transferred from the stroma to glu. This causes proton translocation across the membrane from the stroma to the lumen, which contributes to the pH gradient for ATP production.



In a recent application of PCET theory, Batista et al.’s QM/MM model predicts that oxidation in the S_2 to S_3 transition of the dangler Mn(4) occurs with transfer of a proton to the lumen from an aqua ligand bound to Mn(4), while an OH^- ligand on Mn(4) deprotonates, an OH^- ligand on Mn(3), forming a Mn(4)–O–Mn(3) bridge (eq 81).^{299a,b} This results in conformational H-bond changes that effect O–O bond formation in the S_4 state.



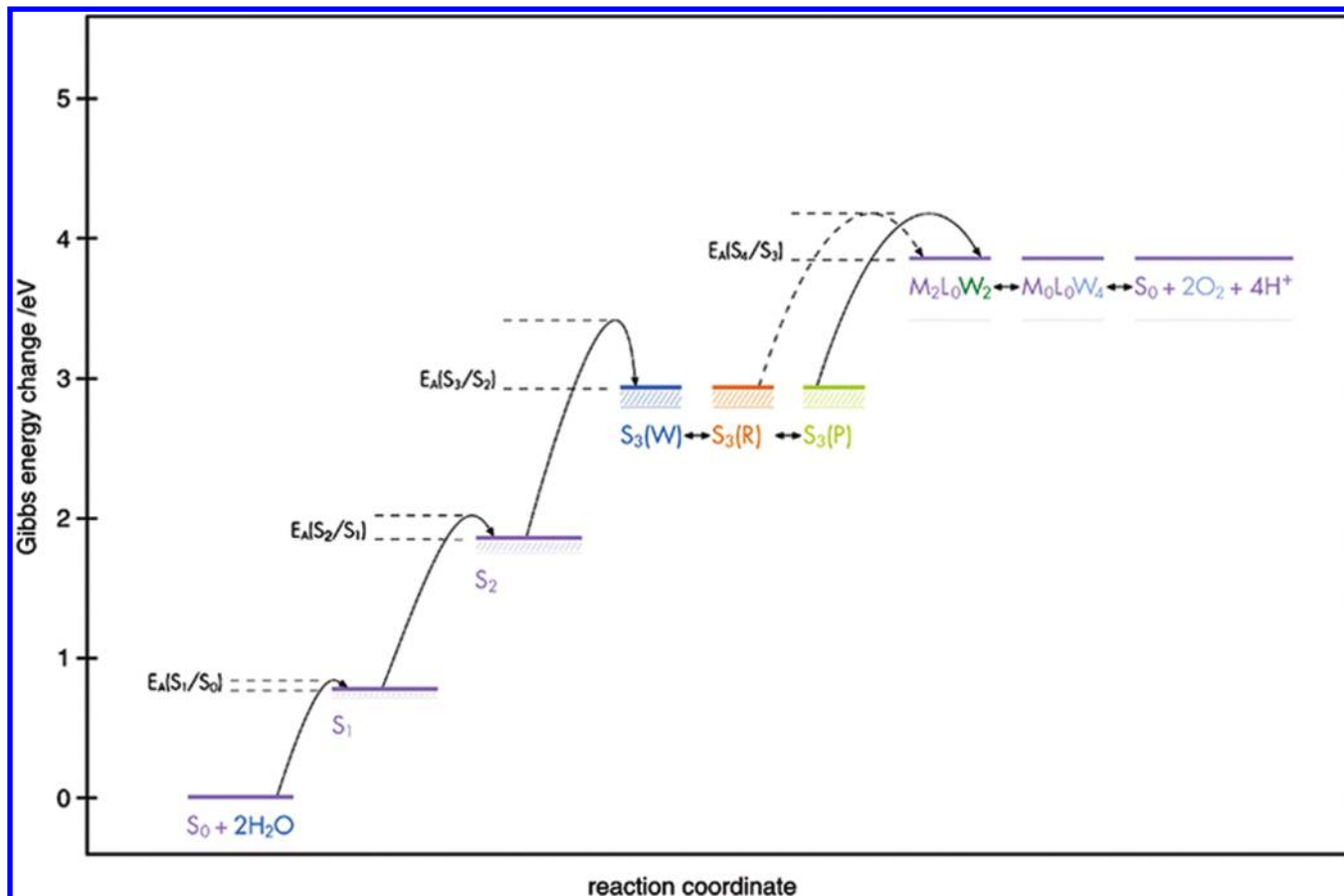


Figure 97. Generalized reaction coordinate for four-step oxidative water cleavage in the photosynthetic apparatus. Reproduced with permission from ref 307. Copyright 2007 Elsevier.

Brudvig et al. propose the formation of an OH^- ligand on Mn(4) via an ET-PT pathway directly involving H^+ abstraction by Y_Z .²⁷³ Meyer et al. also propose the involvement of Y_Z , but via a $1\text{e}^-/2\text{H}^+$ MS-EPT pathway that ultimately releases a single proton to the lumen.⁶ MS-EPT is supported by the pH-dependence³⁰⁹ of the rate constant for this step.

The subsequent S_3 to S_4 and S_4 to S_0 transitions are the focus of two competing views for the key O–O bond-forming step. Interest in and understanding of this step is bolstered by the large number of recent biomimetic “water-oxidation catalysts” that have been published, some of which are reviewed in section 4.^{109c,115,119,121,310,311,312,313} In the “ S_4 Mechanism” interpretation, formation of a high oxidation state metal oxo intermediate is invoked in the $\text{S}_3 \rightarrow \text{S}_4$ step as either a low-spin $\text{Mn}^{\text{V}}=\text{O}$ or a high-spin oxy, $\text{Mn}^{\text{IV}}-\text{O}^\bullet$, which is sufficiently electrophilic to forge an O–O bond followed by O_2 release.

MS-EPT is invoked in the recent QM/MM model of Batista et al., where the $\text{Mn}^{\text{III}}\text{OH}$ formed in the $\text{S}_2 \rightarrow \text{S}_3$ transition is subsequently deprotonated by CP43-R357 to give a transient $\text{Mn}^{\text{III}}-\text{O}^\bullet$ intermediate, which is further oxidized by the tyrosyl radical Y_Z^\bullet to $\text{Mn}^{\text{IV}}-\text{O}^\bullet$, in the $\text{S}_3 \rightarrow \text{S}_4$ step. This is in agreement with Siegbahn and Crabtree’s proposal³¹⁴ that $\text{Mn}^{\text{IV}}-\text{O}^\bullet$, not $\text{Mn}^{\text{V}}=\text{O}$, is the oxidant. By analogy, an “oxy” $\text{Ir}^{\text{IV}}-\text{O}^\bullet$, as opposed to $\text{Ir}^{\text{V}}=\text{O}$, was proposed to be essential to O–O bond formation.³¹²

In this sequence, in the $\text{S}_4 \rightarrow \text{S}_0$ transition, two water molecules, or one bicarbonate anion,^{296a,297} are proposed to displace dioxygen with addition of one proton to regenerate the OEC in its resting state. O–O bond formation occurs by attack

of a neighboring hydroxyl- or aquo-ligand bound to Ca, a μ -oxo bridge, or other nearby ligand on the high-valent $\text{Mn}^{\text{IV}}-\text{O}^\bullet$ species. Supporting this suggestion are studies on model complexes of the OEC. They provide evidence against attack on a bridging ligand,^{315,17b,316,112,317} and also against the presence of bicarbonate in the vicinity of the OEC.^{298a}

The other “peroxidic”¹¹⁷ interpretation involves an Mn–OOH intermediate, named $\text{S}3'$, formed in the $\text{S}_3 \rightarrow \text{S}_4$ transition, so that the O–O bond formation is preformed before the S_4 state is reached.^{6,318} It has been suggested that fourth oxidation is ligand-centered with Mn(4) remaining in the +3 oxidation state with reduction of Y_Z^\bullet being rate-limiting. Evidence for this line of reasoning is based on the slow kinetics (millisecond)^{274a,307} that occur after S_3 is formed. A 250 μs lag time between the light pulse and the final change in oxidation state in Mn has been attributed to a proton transfer step, possibly to the loss of the Mn–OOH proton, or to a redox isomer equilibrium.³⁰⁷ Similarly, high pressures of O_2 were found to suppress the reduction of Y_Z^\bullet and O_2 release,³¹⁹ suggesting an equilibrium between the final S states and a precursor intermediate. The details of O–O bond formation will likely be in debate for some time to come.

8.4.3.3. Tyrosine Z and Tyrosine D. Two redox-active tyrosine residues, Y_Z and Y_D , are known to function in PSII. They can be distinguished spectroscopically by the half-lives of their radicals. Once formed, Y_Z^\bullet decays on a subsecond time scale, whereas Y_D^\bullet decays over a time scale of minutes.^{267a,320} A ΔpK_a of ~ 10 –12 units is observed upon oxidation of Y to Y^\bullet by $\text{P}680^+$ (Table 2), with a reduction potential for the couple

Table 2. Redox Potentials for Tyrosine Couples and Associated pK_a Values

reaction	couple	E_m (mV vs NHE)	estimated pK_a^a
$Y^- \rightarrow Y^\bullet + e^-$	Y^\bullet/Y^-	+680	
$YH \rightarrow Y^\bullet + H^+ + e^-$ (pH7)	Y^\bullet/YH	+970	9.6–12
$YH \rightarrow YH^{*+} + e^-$	YH^{*+}/YH	+1380	-2

^aOn the basis of measurements on a model tyrosine compound in aqueous solution. See ref 321 for a review.³¹⁸

estimated to be 1.0 – 1.2 V (NHE).²¹ The OEC is thought to be directly oxidized by Y_Z^\bullet , which can accept an electron and a proton from the OEC, and its function has become a prototypical example of PCET in biology. The $P_{680}^+ + Y_Z \rightarrow P_{680} + Y_Z^\bullet$ reaction also provides a spectroscopic basis for monitoring the kinetics of the Kok cycle. The multiphasic kinetics of Y_Z^\bullet reduction, characterized by slower reduction after S_2 , has implications for structural assignments in the S states as discussed above. A recent report suggests that the rate of oxidation at the OEC is limited by an EPT step at Y_Z .^{259d}

Ishikita and Knapp^{299c} have been able to calculate the pK_a 's of Y_Z and Y_D with good accuracy and have proposed the PT-ET mechanism shown in Figure 98 for the oxidation of Y_Z by cytochrome P_{680}^+ . A short-lived species, Y_Z^- is stabilized by a calcium-bound water molecule following initial proton transfer from Y_Z to His190-D2. Y_Z^- , shown in Figure 98, is rapidly oxidized by reductive quenching of the P_{680} excited state, yielding Y_Z^\bullet . Y_Z^\bullet is generated by a PT-ET mechanism. In the next step the protonated histidine ($pK_a = 2.2$) transfers a proton back to Y_Z^\bullet , accompanied by electron transfer from the OEC restoring the hydroxyl functionality to Y_Z . In agreement

with some mechanistic proposals, this mechanism shows CP43-Arg357 to be deprotonated beyond the S_2 state and to be responsible for the similar reduction potentials calculated for the S_0 and S_2 states (+932 and +936 mV, respectively).

In contrast to Y_Z , Y_D is not thought to be directly involved in water oxidation, although it does help equilibrate the redox potential between the OEC and P_{680}^+ .^{267a,299c,320} Crystal structures reveal that Y_D and the nearby D2-His189 residue in the D2 subunit share a hydrogen bond. Upon reduction, the tyrosyl radical, Y_D^\bullet , is thought to accept a proton from D2-His198, although other donors are possible. Jenson and co-workers^{267a,282a} have recently found that PCET involving this pair occurs during water oxidation and have proposed multiple PT pathways due to the pH-dependent kinetics (Figure 99) at pH values > 7, where KIEs as high as 2.2 were accompanied by a first-order rate constant of < 2.8 s⁻¹; at pH values < 7, KIEs as low as 1.2 were observed with higher rate constants (10.3 s⁻¹ at pH = 5.5). From these data, a PT-ET mechanism was inferred at lower pH values. A more recent study^{282a} proposed that multiple PCET pathways operate at pH 8 and that at least three protons are transferred. Other residues that could act as donors to Y_D are D2-Arg294 and CP47-Glu364.

8.4.3.4. Proton Removal from the OEC. Although electrons can travel significant distances within proteins (~50 Å in PS II),⁶ proton-tunneling distances are far more restricted (<1 Å).³²² This is due to the higher proton mass and much less extended proton wave functions. To overcome this limitation, proteins use hydrogen-bonding networks that allow protons to move in sequential steps over short distances driven by pH gradients or, in EPT, coupled with the movements of electrons. Recently there have been important theoretical contributions to this area, especially for CcO and RNR.^{262b,282d} Different types of biological proton transfer reactions were studied by quantum

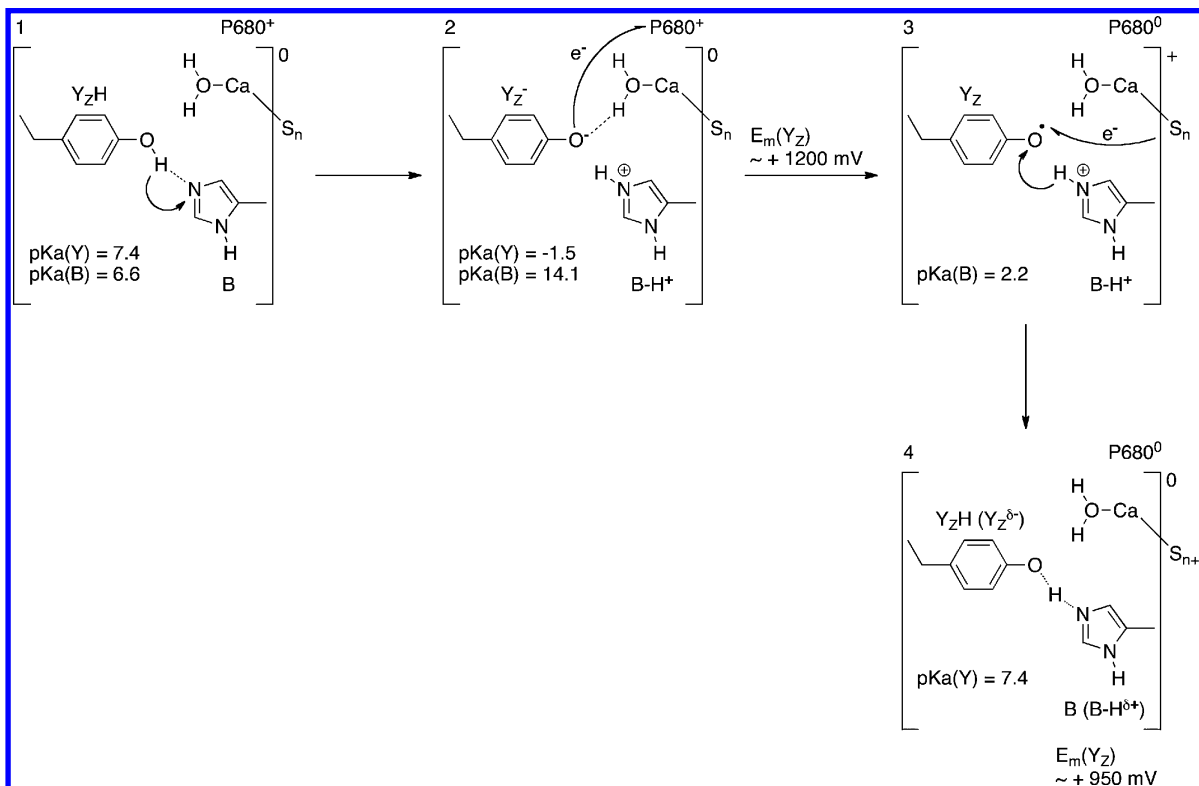


Figure 98. Scheme for ET from Y_Z to P_{680}^* . Y and B are Y_Z and D1-His,¹⁸⁸ respectively, and the calculated pK_a values of Y and B for these residues at each step are listed in the scheme. Reproduced with permission from ref 299c. Copyright 2006 Elsevier.

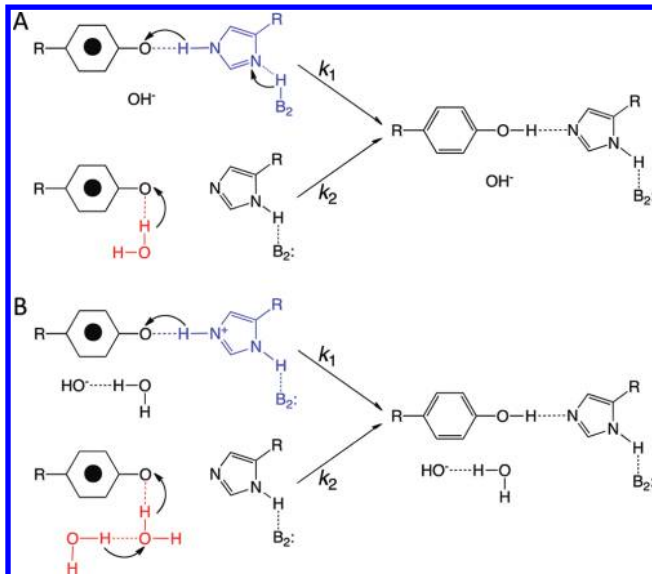


Figure 99. Two possible proton-donor pathways for $\text{Y}_{\text{D}}^{\bullet}$. The straight arrows indicate electron transfer. The curved arrows indicate proton transfer. In (A), His189D2 (reaction k_1 , blue) is involved in a multiple-proton pathway that must include three or more protons of which two are shown. An internal water molecule (reaction k_2 , red) acts as a single-proton donor. Alternatively, in (B), His189D2 (reaction k_1 , blue) acts as a single-proton donor, and a chain of internal water molecules (reaction k_2 , red), of which two are shown, is involved in a multiple-proton pathway. Reproduced with permission from ref 282a. Copyright 2009 American Chemical Society.

chemical methods.^{262a} In the OEC, the “proton exit channel” is proposed to begin at the aspartate D1-D61 residue and end at the PsbO-Asp224.^{299c} The CP43-R357 residue may mediate the interaction between the OEC and the proton exit channel; see later.^{6,21} The driving force for moving protons along hydrogen-bonded networks through these proton transfer channels is thought to be governed by a pK_a gradient and is triggered by oxidation of the OEC.^{299c} The possible involvement of MS-EPT and local proton movement in water oxidation at the OEC is discussed in section 1.1.2 and has been reviewed elsewhere.^{6,109d,257,274b,283,323}

Several recent theoretical results are relevant to proton removal and delivery to the lumen. Batista and co-workers^{299a} have shown that arginine residue CP43-R357 aids in proton abstraction from the OEC through hydrogen-bonding interactions with two aqua ligands bound to the dangler manganese ($\text{Mn}(4)$) and to calcium. There is additional evidence for hydrogen-bonding networks that link CP43-R357 to $\text{Mn}(3)$ and $\text{Mn}(4)$. It has been suggested that the OH^- ligand on $\text{Mn}(3)$ removes protons during the $\text{S}_2 \rightarrow \text{S}_3$ and $\text{S}_3 \rightarrow \text{S}_4$ transitions by utilization of additional hydrogen-bond interactions with the same arginine and alanine 344. Proton management at this level is required for formation of the reactive $\text{Mn}^{\text{V}}=\text{O}/\text{Mn}^{\text{IV}}-\text{O}^{\bullet}$ precursor to $\text{O}-\text{O}$ coupling and for removal of protons produced by water oxidation.

Ishikita and Knapp also propose CP43-Arg357 as the beginning of a PT channel terminating at the CP43-Asp360/D1-His92 pair on the luminal surface (Figure 100).^{299c} Another proton transfer channel involves D1-D61, D1-E65, D2-E312, D2-K317, PsbO-D158, PsbO-D222, PsbO-D223, PsbO-D224, PsbO-His228, and PsbO-E229 with a total proton transfer distance of ~ 35 Å. It is important to note that neither proton exit channel involves Y_z , consistent with the growing consensus

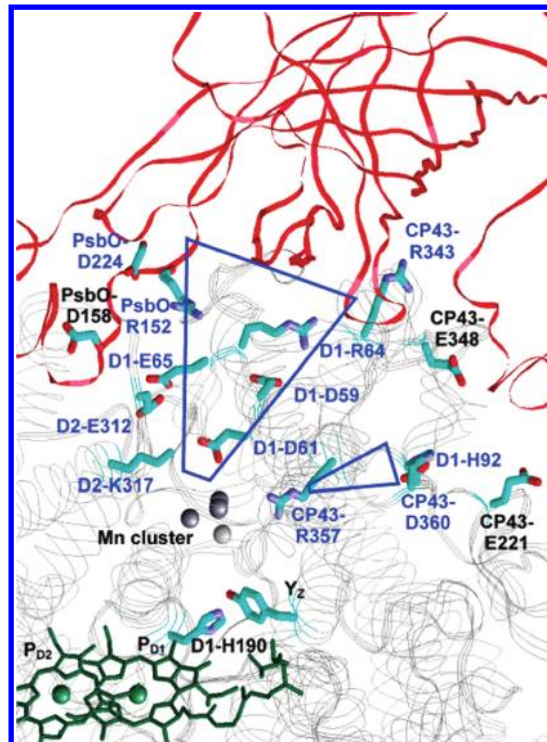


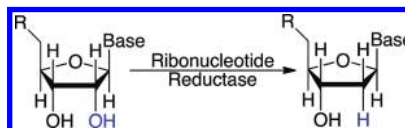
Figure 100. Proposed proton exit channel beginning at aspartate D1-61. See also references by Voth and co-workers.¹⁹ Reproduced with permission from ref 22b. Copyright 2006 American Chemical Society.

that its function is an oxidizing electron transfer relay.^{21,299a} However, other proposals are known and should be considered.^{109d,323}

8.5. Proton-Coupled Electron Transfer in Enzymes

8.5.1. Class I Ribonucleotide Reductase. Class I RNRs are found in *E. coli* and consist of complexed subunits R1 and R2. They catalyze the reduction of nucleosides to deoxynucleosides (Scheme 39). The enzyme initiates the reactions at a

Scheme 39



dihydro tyrosyl radical site (Y_{122}) with radical transfer occurring over 35 Å through a chain of amino acids with termination at cysteine C439^{256,271} (Figure 101). Radical transfer is thought to occur by a long-range EPT “shuttle” mechanism with electron transfer occurring between amino acids coupled with a double concerted proton transfer, e.g., $(\text{TyrO}^{\bullet}-\text{H}-\text{His}) \cdots (\text{TyrOH}-\text{His})' \rightarrow (\text{TyrO}-\text{H}-\text{His}) \cdots (\text{TyrO}^{\bullet}-\text{H}-\text{His})'$. Radical transport sites have been isolated at Y_{122} , W_{48} , and Y_{356} on the R2 unit and at Y_{731} , Y_{730} , and C_{439} at the R1 unit.²⁵⁶ An impressive number of techniques have been applied to the investigation of radical transport including pulse radiolysis, EPR, and UV/visible measurements combined with site-directed mutagenesis, X-ray crystallography, magnetic circular dichroism (MCD), DFT, and native protein chemical ligation and dipeptide model proteins.^{9,266,271,324} Re(bpy)(CO)₃(CN)-derivatized peptide models of RNR β 2 adducts were developed to investigate site-specific radical transfer, which is activated

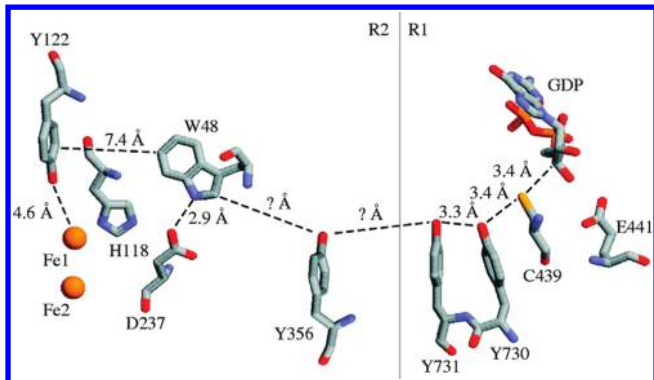


Figure 101. Schematic diagram of amino acid residues along the catalytic chain of class I RNR. The crystal structure suggests that the protein exists as a homodimer and that radical transport from subunit R2 to subunit R1 involves electron transfers over a 35-Å distance, originating at Y122 on the R2 subunit of RNR and terminating at C439 on the R1 subunit. Reproduced with permission from ref 271. Copyright 2006 American Chemical Society.

photochemically. In these experiments, $\text{Re}(\text{bpy})(\text{CO})_3\text{CN}$ was appended next to Y356 on a 20-mer peptide, YBC19, created to mimic the $\beta 2$ binding domain. It was determined that emission radically increases after peptide bonding, indicating that conformational dynamics and the protonation state of Y356 influence the enzyme's catalytic turnover.⁹

The role of Y356 is of particular interest because of its position at the interface between R1 and R2.^{324h} Pulse radiolysis has been used to explore radical transport through the interface between peptides modified by site-directed mutagenesis and chemical ligation.^{266,324h} Chemical ligation has also been used to incorporate fluorinated tyrosine derivatives (F_nY , Figure 102) having potential shifts in the

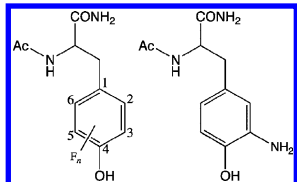


Figure 102. Structure of non-natural amino acids incorporated into ribonucleotide reductase.

range -50 to 270 mV compared to Y356 and with pK_a 's from 5.6 to 9.9. Decreasing the reduction potential has the effect of completely inhibiting RNR activity. Incorporating amino-dermatized tyrosines (NH_2Y , Figure 102) at Y730 and Y731 results in radical trapping due to decreases in reduction potential. This supports an EPT model.^{324b,c} The results of these studies were consistent with important roles for EPT in RNR radical transport.

8.5.2. DNA Photolyase. The indole group of tryptophan has also been demonstrated to be involved in PCET. For example, in the mechanism of photoactivation in *Escherichia coli* DNA photolyase, the excited-state flavin adenine dinucleotide undergoes reductive quenching by adjacent tryptophan W382 to give the semiquinoidal radical anion ($\text{FADH}^{\bullet-}$) and $\text{TrpNH}^{\bullet+}$.^{325,326d} The reaction was studied by laser flash photolysis and EPR spectroscopy. Radical formation and charge hopping were found to occur on the picosecond time scale, and the isolation of intermediates was not possible. Site-directed

mutagenesis studies demonstrated the importance of tryptophan residues located at W306, W359, and W382. Subsequent long-range electron transfer occurs by site-to-site electron transfer hopping through tryptophan residue W359 from the terminal tryptophan W306 located 13.4 Å from the flavin. Long-range electron transfer is followed by loss of a proton (Figure 103).³²⁶

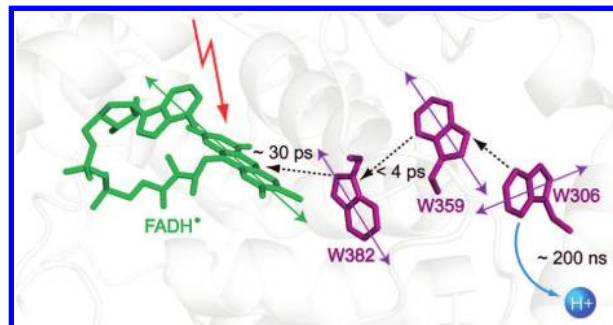


Figure 103. Structural arrangement of the $\text{FADH}^{\bullet-}$ -W382-W359-W306 chain in DNA photolyase following laser flash photolysis at 500 nm with time scales for subsequent electron transfer hopping indicated on the figure. The axes in the figure highlight the different orientations of the ring systems. Reproduced with permission from ref 326c. Copyright 2008 American Chemical Society.

The initial quenching step occurs by rapid (<10 ns) electron transfer to give $\text{FADH}^{\bullet-}$, the catalytically active form of the cofactor (Figure 103).^{326c,327} The triple tryptophan redox relay in DNA photolyase has been explored thoroughly by spectroscopic and mutagenic studies.³²⁵⁻³²⁸ On the basis of XRD, the indolyl N1 N atom of W306⁺ is directly exposed to a shallow pocket open to solvent. Deprotonation is proposed to occur to solvent water within 300 ns after excitation in a net, stepwise ET-PT reaction even though proton transfer from $\text{TrpNH}^{\bullet+}$ to water in water is disfavored by ~0.3 eV.^{326c} In the XRD structure there is no potential proton acceptor within 5 Å of the indolic nitrogen atom. W382 and W559 are surrounded by hydrophobic and polar amino acids but are proposed to be hydrogen bound to a buried water molecule.^{328a}

8.5.3. Azurin. Recently, Gray and co-workers used nanosecond laser flash photolysis with visible transient absorption monitoring to explore the possible role of an intervening tryptophan residue in facilitating electron transfer in a mutant *Pseudomonas aeruginosa* azurin protein. The azurin derivative is illustrated in Figure 104. As shown in Figure 105, in these experiments MLCT excitation of $[\text{Re}^{\text{I}}(\text{CO})_3(\text{dmp})]^+$ ($\text{dmp} = 4,7\text{-dimethyl-1,10-phenanthroline}$) bound to His124 was used to initiate long-range (19 Å) electron transfer from Cu(I) through intervening tryptophan (W122).³²⁹ The two-step electron-hopping mechanism with migration of the photogenerated hole through W122⁺ is $\sim 10^2$ times faster than single-step electron tunneling. Replacement of W122 by tyrosine (Y) or phenylalanine (F) inhibits the initial ET event because $E^{\circ'}$ values for the $\text{Y}^{\bullet+/\circ}$ and $\text{F}^{\bullet+/\circ}$ couples are >200 mV above $E^{\circ'}$ for the excited-state $\text{Re}^{\text{II}}(\text{CO})_3(\text{dmp}^{\bullet-})(\text{His})^{+\bullet}/\text{Re}^{\text{I}}(\text{CO})_3(\text{dmp}^{\bullet-})(\text{H124})^{\circ}$ couple. Concerted EPT involving Y122 and $\text{Re}^{\text{II}}(\text{CO})_3(\text{dmp}^{\bullet-})(\text{His})^{+\bullet}$ is thermodynamically favored but postulated not to occur because of a significant activation barrier.^{329,330}

8.5.4. Soybean Lipoxygenase. Soybean lipoxygenase (SLO) is a nonheme iron metalloprotein that catalyzes the oxidation of unsaturated fatty acids. A combination of a

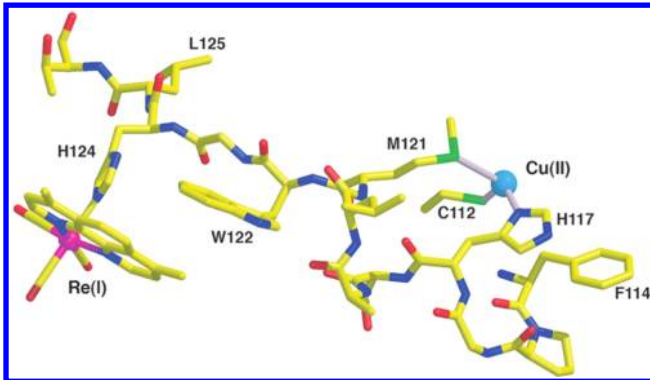


Figure 104. Structure of the Re–W122–Cu(II) azurin derivative from a 1.5-Å resolution XRD structure. The Re complex is $\text{Re}^{\text{I}}(\text{CO})_3(\text{dmp})(\text{His124})^+$. Distances: Cu to W122 (aromatic centroid) = 11.1 Å, W122 to Re = 8.9 Å, Cu to Re = 19.4 Å. Reproduced with permission from ref 329. Copyright 2008 American Association for the Advancement of Science.

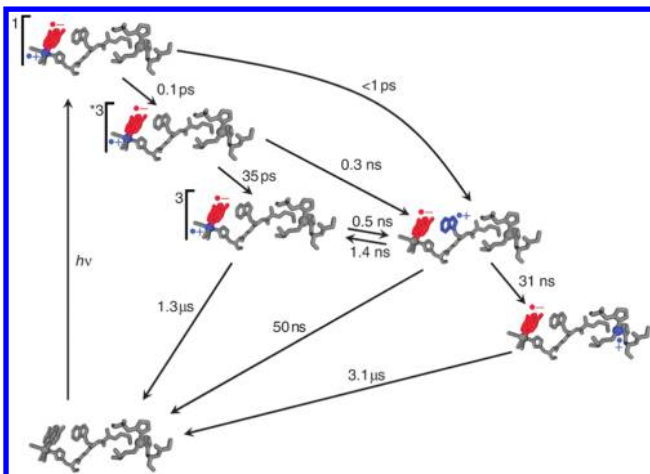


Figure 105. Kinetic events following laser flash excitation to the MLCT excited state of the $\text{Re}^{\text{I}}(\text{dmp})$ chromophore ($\text{Re}^{\text{II}}(\text{dmp}\cdot^-)$) in $\text{Re}^{\text{I}}(\text{CO})_3(\text{dmp})(\text{His124})^+(\text{W122})|\text{AzCu}^{\text{I}}$. The excited electron (red)–hole (blue) pair in the MLCT excited state is illustrated. MLCT excitation is followed by W122 reductive quenching to give the redox-separated state $\text{Re}^{\text{I}}(\text{dmp}\cdot^-)-\text{TrpNH}^{\cdot+}$ in <50 ns. Back electron transfer occurs on the microsecond time scale. Reproduced with permission from ref 329. Copyright 2008 American Association for the Advancement of Science.

high-resolution crystal structure by XRD, results from a number of spectroscopic studies, and results of quantum calculations have given considerable insight into the mechanism by which this enzyme functions.^{9,331} A key step is thought to involve net hydrogen atom transfer by EPT (Figure 106). In the proposed

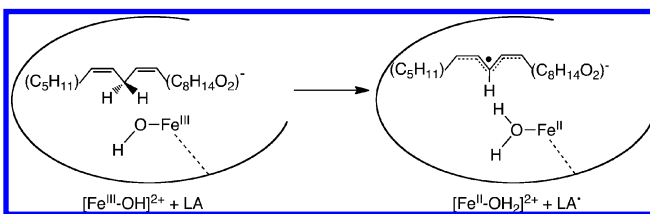


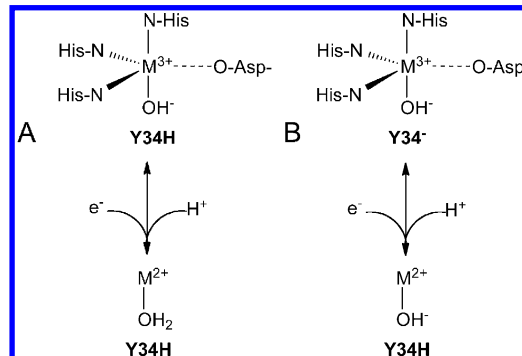
Figure 106. Chemical reaction of soybean lipoxygenase-catalyzed oxidation of linoleic acid. Reproduced with permission from ref 331d. Copyright 2002 American Chemical Society.

pathway, the electron is thought to transfer from the π -system of the substrate to the iron cofactor while proton transfer occurs from the C11 carbon.^{9,331a–c,e}

With linoleic acid as the substrate, a number of mechanistic conclusions were reached. The concerted process is exothermic by ~5 kcal/mol and nonadiabatic toward electron transfer because of weak electron coupling between the electron donor and acceptor. Recent advances in dynamic calculations on SLO have discerned the importance of protein motion, its effects on substrate position and donor–acceptor distance, and the role it plays in hydrogen tunneling.^{331b} Protein motion results in a decrease in proton transfer distance relative to the equilibrium state, resulting in more efficient proton tunneling due to better vibrational overlap.^{331b}

8.5.5. Superoxide Dismutase. The superoxide dismutases (SODs) are a family of metalloenzymes that catalyze disproportionation of superoxide to molecular oxygen and peroxide. Their main role is in defending against oxidative stress. In bacteria, the main SODs are FeSOD and MnSOD, which contain a mononuclear active site coordinated by two histidines and an aspartate in the equatorial plane forming a trigonal bipyramidal geometry with a histidine and a solvent molecule along the trigonal bipyramidal axis (Scheme 40).³³² In

Scheme 40. Possible Schemes for Proton Uptake upon Reduction of the SOD Active Site^a



^aIn (A), the redox-coupled H^+ acceptor would be coordinated solvent, whereas in (B), the redox-coupled H^+ acceptor would be nearby Tyr34 (Y34). The upper end of each equilibrium includes short-hand notation for the four amino acid ligands to the metal ion (M). These are still present in the reduced state of SOD but are omitted for simplicity.³³³ Reproduced with permission from ref 333. Copyright 2003 Elsevier.

the dismutation mechanism it is thought that reduction at the metal is coupled to proton transfer with protein structure playing a significant role in redox tuning. There are two halves of the catalytic cycle with each half involving a $\text{O}_2^{\cdot-}/-$ binding step with subsequent proton binding (Scheme 40).

A recent investigation into the redox mechanisms of FeSOD and MnSOD enzymes have led to the conclusion that reduction from M(III) to M(II) occurs via a PCET mechanism (the proton donor is unclear). There was no change in ^{13}C NMR at Tyr34 over the course of the reaction at neutral pH. This showed that Tyr34[–] is not the proton acceptor, implicating coordinated water as the probable proton acceptor.^{332,333} Site-directed mutagenesis and DFT calculations were used to examine second-sphere amino acid effects, and it was found that the protein matrix plays a role in both tuning the redox

potential of the protein and in defining proton transfer distance between enzyme and solvent.³³⁴

8.5.6. Cytochrome c Peroxidase. (CcP) is a diiron heme protein that plays a role in cellular detoxification and catalysis of hydrogen peroxide reduction. The overall reaction is shown in eq 82. CcP catalyzes the oxidation of cytochrome *c* by H₂O₂, which reacts with two nonequivalent ferric heme (Fe⁴⁺=O) centers and cation radical tryptophan (W191 in eukaryotes and W97 in bacteria). The high-potential heme acts as an electron transfer center, accepting electrons and shuttling them to the low-potential heme. The main difference between the two is the amino acid residues that ligate the iron. In the high-potential heme, the axial position is filled by a methionine (M118), whereas the low-potential heme binds a histidine (H74) reversibly in the axial site and can bind substrates for catalysis.³³⁵ The two iron centers are separated by 20 Å, and during catalysis electron transfer occurs from the C-terminal, high-potential heme to the *n*-terminal low-potential heme (Figure 107) through the intervening tryptophan W97.³³⁵

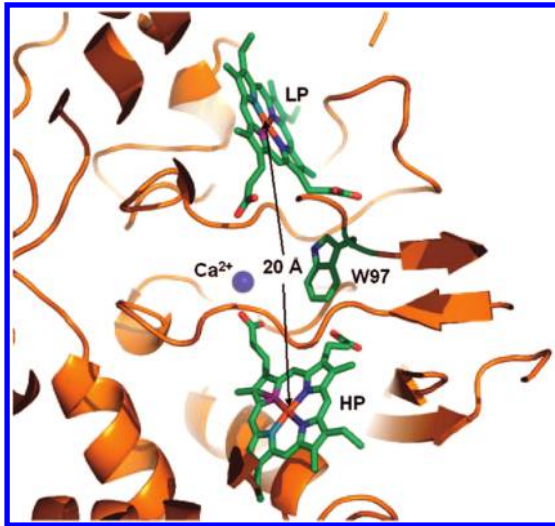
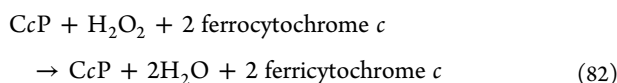


Figure 107. XRD structure of cytochrome *c* peroxidase. In the enzyme, electron transfer originates at high-potential (HP) heme and terminates 20 Å away at a low-potential (LP) heme with tryptophan W97 as an electron transfer mediator located 20 Å from both iron hemes. Reproduced with permission from ref 335. Copyright 2006 American Society for Biochemistry and Molecular Biology.



As shown in Figure 108, the activation mechanism for CcP involves electron movement from the high-potential heme to the low-potential heme with catalytic reduction of H₂O₂.³³⁵ In the catalytic cycle, cleavage of an Fe^{III}–O–OH peroxide bond occurs with oxidation of the Fe^{III}–heme to a Fe^{IV}oxyl porphyrin radical cation, O=Fe^{IV}(por^{•+}). During the O–O bond-cleavage step, electrons are transferred from both Fe^{III} and porphyrin (por) with proton transfer from His75.

In a following step, electron transfer occurs from W191 to por^{•+}, to give O=Fe^{IV}(por). The Trp191 radical is formed at the high-potential heme and is hydrogen-bonded to D235. The D286 group acts to stabilize the indole radical. High-potential heme and W191 are reduced in subsequent steps. Active-site mutations at Asp286 point to its role as a critical proton

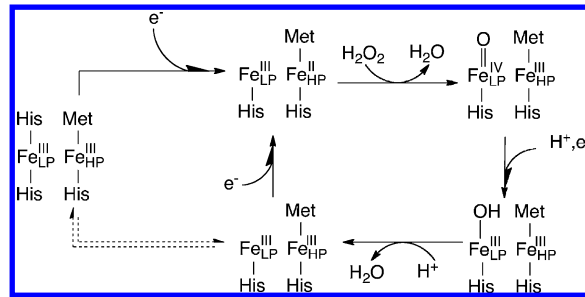


Figure 108. Proposed mechanism of CcP activation for the reduction of H₂O₂. Reproduced with permission from ref 235. Copyright 2009 American Chemical Society.

acceptor in this reaction, suggesting a MS-EPT pathway with electron transfer to the porphyrin cation and proton transfer to Asp286, TrpN–H---OOC–Asp286···O=Fe^{IV}(por^{•+}) → TrpN···HOOC–Asp286···O=Fe^{IV}(por). Trp191 (W191) was further stabilized toward oxidation by the presence of Met residues at sites 230, 231, and 172.³³⁶ Once electron transfer has occurred at the high-potential heme, electrons are shuttled to the low-potential heme where hydrogen peroxide is reduced.

Spectroscopic and mutagenesis studies have provided convincing evidence that long-range electron transfer occurs through a radical-hopping mechanism through a radical amino acid pathway and the pathway outlined in Figure 108.³³⁵ Trp97 (W97) is located at a distance of ~10 Å from both hemes. Its mutagenesis with either Ala or Phe renders the enzyme inactive, trapping the radical at the high-potential heme site, consistent with a role for Trp97 as an electron transfer conduit for long-range electron transfer in CcP.³³⁵ Similarly, replacement of Trp97 with *N*-benzimidazolepropionic acid inhibited electron transfer, consistent with long-range electron transfer mediated by a tryptophan radical.^{267b} Redox potentiometry combined with UV/visible spectroscopic studies are consistent with a proposed electron transfer mechanism.³³⁵ There is evidence that participation by Trp97 as an electron shuttle also involves EPT along with associated proton-acceptor propionate groups along the electron transfer pathway. The results of computational studies indicate that the propionic groups play a critical role in the electron transfer process.³³⁷

Electrochemical studies on CcP confirm a role for PCET at the heme sites with appearance of pH-dependent electrochemistry over the range pH = 5–11 (Figure 109).^{235,338} Protein film voltammetry (PFV) was used to investigate the pH dependence of CcP (Figures 109 and 110). The data in Figure 109 were fit to a two pK_a model in which the oxidized and reduced states can be protonated independently. The 64 mV/pH unit dependence of *E*_{cat} at extreme pH values is consistent with a 1H⁺/1e[−] step.^{235,338b,340} Electrochemical and single-crystal absorption spectroscopy were used to investigate solvent isotope effects in CcP.³³⁹ No variation in reduction potential was observed with a change in solvent; however, spectroscopic studies revealed solvent isotope effects of 1.5 for the redox process in CcP.^{338a}

8.6. Proton-Gated Electron Transfer in Cytochrome *c* Oxidase

Cytochrome *c* oxidase (CcO) is a membrane-bound protein that catalyzes the 1e[−] reduction of four cytochrome *c* units, ultimately with 4e[−] reduction of oxygen (Figure 111).³⁴¹ It is the terminal member of the respiratory redox chain.³⁴² Electron transfer through the enzyme is linked to proton pumping from one side of the membrane to the other, producing a free-energy gradient used to drive ATP synthesis.³⁴³ Elucidation of the

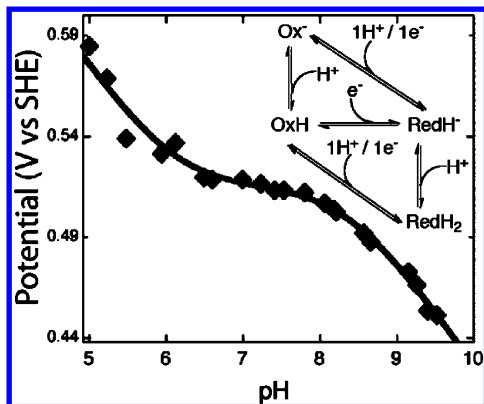


Figure 109. pH dependence of E_{cat} determined for voltammograms of *Nitrosomonas europaea* CcP in the presence of 100 μM substrate. Reproduced with permission from ref 340. Copyright 2004 American Society for Biochemistry and Molecular Biology.

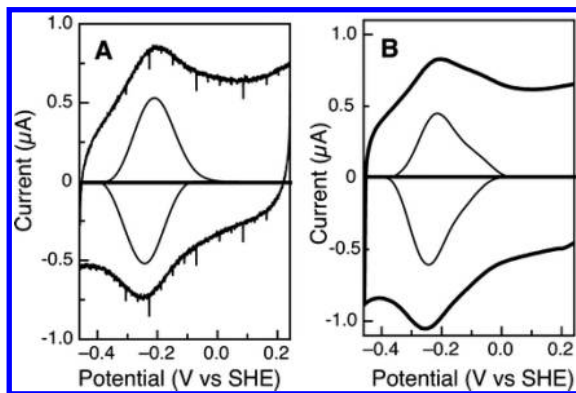
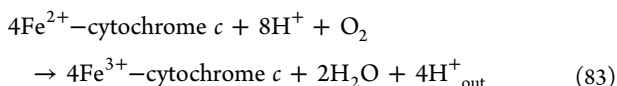


Figure 110. Raw and baseline-subtracted cyclic voltammograms for protein films of *Psa* CcP at pH 7 (A) on a 1-octanethiol-modified gold electrode at a scan rate of 2 V/s and (B) on a pyrolytic graphite edge electrode at a scan rate of 100 mV/s. Reproduced with permission from ref 235. Copyright 2009 American Chemical Society.

mechanisms of proton pumping and oxygen reduction are deeply fundamental issues in bioenergetics, and multiple mechanisms have been proposed to account for both.^{342,344}

CcO has four redox centers: a binuclear CuA center bound to heme *a*, heme *a*, heme *a*₃, and CuB.¹ In CcO, oxidation and reduction at heme *a*/CuA and heme *a*₃/CuB are linked to proton transfer with acid/base groups in the enzyme.³⁴⁶ The overall reaction is outlined in eq 83. In the overall oxidation mechanism, 2e⁻/1H⁺ reduction at CcO occurs between Cu_B and Fe(III)heme, resulting in the reduction of O₂ in cellular respiration.³⁴⁷



DFT calculations have been performed based on known distances from the XRD structure of CcO. Molecular oxygen binds reversibly to the reduced binuclear center (BNC).^{262b} In the cleavage mechanism associated with CcO, the BNC provides three electrons with Fe(III) \rightarrow Fe(IV) and Cu(II) \rightarrow Cu(I) changes occurring over the course of the reaction. The fourth electron needed to cleave molecular oxygen is probably derived from Tyr288.^{262a,b} The O–O bond-cleavage reaction occurs in two steps, the first of which involves proton transfer of the hydroxyl proton to the distal oxygen with electron transfer to the oxygen forming FeOOH. Concerted

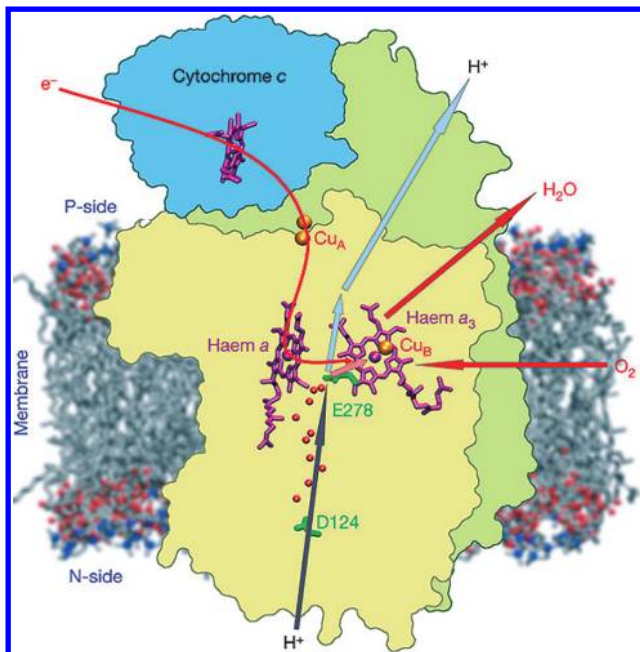


Figure 111. XRD structure of cytochrome *c* oxidase showing the net movement of electrons and protons during enzyme turnover. Reproduced with permission from ref 345. Copyright 2006 Nature Publishing Group.

EPT has been proposed to occur between the resulting Fe^{IV}=O center and Tyr288 with proton transfer from the phenolic proton to the oxo ligand and electron transfer from tyrosine to iron, TyrOH---O=Fe^{IV}(por or por^{•+}) \rightarrow TyrO[•]---H---OFe^{III}(por) (Figure 112). Tyr288 is believed to provide both a proton and a fourth electron in the overall 4e⁻ catalytic reduction of O₂. Redox titrations, pH studies from electrochemical investigation, and EPR studies point to the formation of a tyrosyl radical. Mutagenesis studies point to the importance of a Tyr244 His 240 cross-link, which stabilizes the amino acid radical (Figure 113). Replacement of His240 results in decreased catalytic activity.³⁴⁶

O₂ reduction by CcO is coupled to pumping of one proton across the membrane for every electron transferred.³⁴⁸ In addition, a single substrate proton is transferred to produce a molecule of water.³⁴⁵ Protons are transferred through CcO by the D channel named after the solvent-exposed Asp124, and protons are transferred to Glu278 in the center of the membrane-bound protein.³⁴⁵ High-resolution XRD, site-directed mutagenesis, EPR, and stopped-flow studies have been applied to the investigation of the proton-pumping mechanism and the relationship between proton pumping and the redox state of the enzyme (Figure 112).^{344a,346,349}

A recent higher-resolution structure has provided new insights into proton pumping and points to the importance of a carboxylate Glu278 in the proton transfer pathway.³⁵⁰ The carboxylate group prevents back electron transfer and is deprotonated upon heme oxidation. The exact nature of the carboxylate is unclear because it is not conserved in the superfamily of heme copper oxidases. Siegbahn and Blomberg have presented quantum calculations that support Glu278's role in preventing back proton transfer due to its high pK_a.^{262a,b} DFT calculations confirm the role of a low-spin heme in the proton-pumping mechanism and point to an instrumental role for Glu 278 as a redox “gate” for controlling proton transfer. A proton

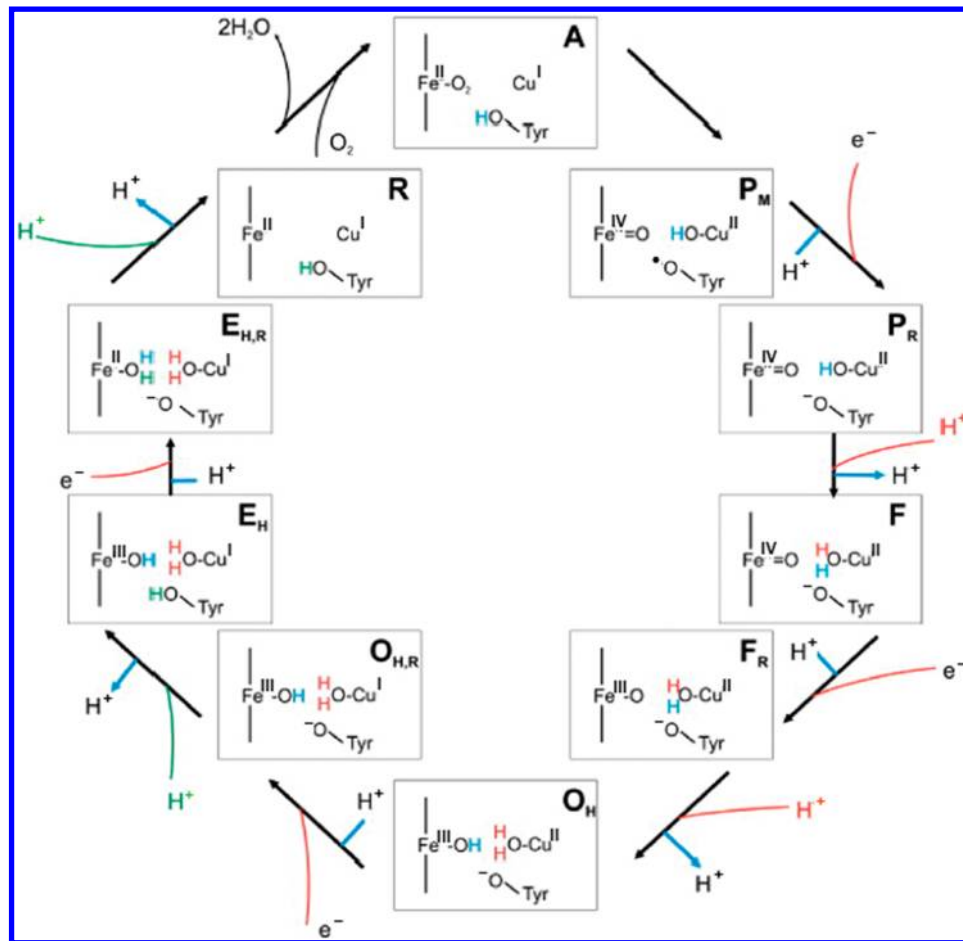


Figure 112. Proposed reaction cycle for CcO. The cycle begins by cleavage of the O–O bond. One proton is transferred from E242 to the proton-loading site (blue arrow, H^+) while an electron is transferred to the binuclear site. Reproduced with permission from ref 346. Copyright 2009 Elsevier.

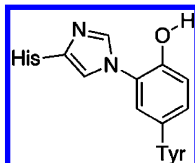


Figure 113. Structure of the tyrosine histidine adduct formed in cytochrome *c* oxidase (CcO). The histidine acts to support radical formation at the tyrosine hydroxyl group.

begins to move from Glu278 to the pump site for transfer to the P-side as a proton moves from the N-side to the Glu278. The $Glu278^+$ becomes immediately reprotonated and does not permit back proton flux.^{262a} On the basis of the modeling studies, Glu 278 has an on and off state that allows proton transfer to occur. Initial proton transfer is thought to occur from Glu 278 to heme *a*, which prevents back proton transfer from the metal center.^{19b,349a,351}

Results of crystallographic and spectroscopic studies suggest a mechanism for this proton-gated electron transfer. In this mechanism Glu 278 exists in an up and down position dictated by the amount of water present. In its resting state, Glu 278 is positioned downward toward the D channel, but an increase in water concentration causes the residue to point upward toward a hydrophobic channel, allowing proton transfer from water to heme *a*.^{344a,351b,352}

Overall, cytochrome *c* oxidase undergoes multiple electron and proton transfer events. The electron transfer between Fe–O and CuB as well as the transfer between Tyr244 and Fe–O utilize

an EPT mechanism. Electron transfer between Tyr244 and Fe–O allows CcO to join an ever-growing group of redox enzymes that invoke amino acid radicals to mediate charge transfer in enzymes.³⁵³ Interestingly, CcO also undergoes a distinctive mechanism, protonated electron transfer, in which electron transfer from heme *a* is coupled to proton transfer from the D channel and is regulated by Glu242.^{350b} Proton-gated electron transfer is characterized by a pH-dependent reduction potential for the heme and a small deuterium isotope effect.^{235,354} Further investigation of this novel mechanism is needed to elucidate the specific details of the mechanism. Further investigation of CcO will allow for a better understanding of bioenergetics and charge transfer in the respiratory chain and of the generation of proton gradients across membranes.

8.7. PCET in Biology is Everywhere

PCET plays a critical role in many enzymatic pathways that control life such as photosynthesis, respiration, and DNA repair. There is increasing evidence that its role may be far more extensive than previously thought. Recently, pH-dependent reduction potentials and solvent kinetic isotope effects have been reported for catalase peroxidases in nitrate reductase,²⁴⁹ nitrite reductase,³⁵⁵ catalase peroxidase,³⁵⁶ and ATP synthase³⁵⁷ indicating that these enzymes may also use PCET to avoid formation of high-energy intermediates and to transfer electrons and protons over long distances.^{79,249,326a,328b,358} Although the exact mechanism(s) by which PCET operates in these enzymes is currently under investigation, the underlying

principles of PCET are no doubt at work coupling electron and proton transfer both thermodynamically and mechanistically in order to avoid high-energy intermediates and enable enzyme turnover with high rates and efficiencies.

AUTHOR INFORMATION

Corresponding Author

*E-mail: tjmeyer@email.unc.edu.

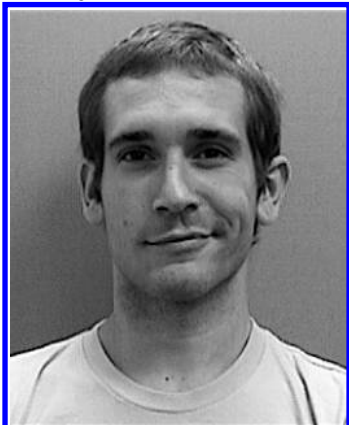
Notes

The authors declare no competing financial interest.

Biographies



David R. Weinberg was born in 1979 near Algonquin, Illinois, where he received his primary and secondary education. He followed the sun to California in 1997 and received his bachelor's degree in chemistry via a biochemistry pathway at the University of San Diego. A stint as a summer undergraduate research assistant with Professor James M. Meyer at the University of Washington inspired him to pursue graduate studies in organometallic chemistry with Professor John E. Bercaw and Dr. Jay A. Labinger at California Institute of Technology. In 2009, he received his Ph.D. for *Investigations into the Requirements for Homogeneous Platinum- and Iridium-Catalyzed Oxidative C–H Bond Functionalization*. By studying nanostructured electrocatalytic films for carbon dioxide reduction as a postdoctoral associate in the laboratories of Professor Thomas J. Meyer at The University of North Carolina at Chapel Hill, he continued to specialize in energy conversion chemistry and to bridge homogeneous and heterogeneous catalysis. He is currently an assistant professor at Colorado Mesa University in Grand Junction, Colorado. Inspired by discussions with Professor Jonathan Scharle Owen at Columbia University, he firmly believes that all students can be successful if they work hard and are willing to ask questions.



Christopher J. Gagliardi was born in 1984 and grew up in Hillsborough, New Jersey. He received his B.S. in Chemistry and

Biology with high honors from Roger Williams University in Bristol, RI, in 2007. At Roger Williams, he worked in the laboratory of Prof. Cliff Timpson where his interests in proton-coupled electron transfer began. In the fall of 2007, he went to work in the laboratories of Thomas J. Meyer and H. Holden Thorp at the University of North Carolina at Chapel Hill. His Ph.D. work has involved studying the kinetics and thermodynamics of proton-coupled electron transfer reactions of amino acids, with a particular emphasis on the fundamental underpinnings of PCET.



Jonathan F. Hull was born in 1981 in Miami, FL, and grew up in Santa Fe, NM, and Geneva, Switzerland. He received a B.S. in Philosophy and Chemistry from Haverford College in 2004 and a Ph.D. in Bioinorganic and Organometallic Chemistry from Yale University in 2009 under the supervision of Professors Robert H. Crabtree and Gary W. Brudvig. He subsequently completed postdoctoral research with Professor Thomas J. Meyer in 2010 at the University of North Carolina at Chapel Hill. He joined Brookhaven National Lab in Upton, NY, in the fall of 2010 after receiving a Goldhaber Distinguished Fellowship to explore strategies to electrocatalytically store renewable energy. Jonathan has worked at 3M, Inc., and as a personal trainer, and enjoys the weight room and volunteering when he's not in lab.



Christine Fecenko Murphy was born in 1981 in Blackwood, NJ. She graduated with honors from Ursinus College in 2004. She received her Ph.D. from the University of North Carolina at Chapel Hill in 2009. At UNC, where her research included investigation of base effects in amino acid oxidation, her research advisors were H. Holden Thorp and Thomas J. Meyer. In 2009, she began a postdoctoral fellowship at Duke University in Durham, NC, with Dewey G. McCafferty. Her current research interests include investigation of electron transfer mechanisms in proteins and the development of electrochemical techniques to investigate redox-active enzymes. Currently, Christine is

the Assistant Academic Dean of STEM fields at The College of Global Studies at Arcadia University in Glenside, PA.



Caleb A. Kent attended Kalamazoo College as a Heyl Scholar and received a B.A. in chemistry in 2007. He is currently a Ph.D. candidate under the direction of Thomas Meyer and Wenbin Lin and a Carolina Energy Fellow. His research is focused on energy-related topics including excited-state PCET reactions of metal complexes and also energy and electron transfer studies of metal-organic frameworks.



Brittany C. Westlake received a B.S. in chemistry in 2004 from the University of Georgia, where she carried out undergraduate work with Michael A. Duncan. She completed her Ph.D. at the University of North Carolina at Chapel Hill in 2010, under the mentorship of John M. Papanikolas and Thomas J. Meyer, studying proton-coupled electron transfer systems using ultrafast spectroscopy techniques. Currently, she is the Science Policy Fellow for the American Chemical Society in Washington, DC.



Amit Paul received his B.Sc. from Jadavpur University, Kolkata, India, his M.Sc. from IIT Bombay, Mumbai, India, and his Ph.D. from

Department of Chemistry, University of Pittsburgh, under the supervision of Prof. David H. Waldeck. He was a postdoctoral research associate at Department of Chemistry, University of North Carolina, Chapel Hill, under the supervision of Prof. Thomas J. Meyer. Currently, He is an Assistant Professor at Indian Institute of Science Education and Research (IISER), Bhopal. His research interests include electron transfer through molecular bridges, proton-coupled electron transfer, catalysis, and hydrocarbon activation.



Daniel H. Ess was born in California in 1981. He was raised in Southern California and Utah. After graduation from Brigham Young University in 2000, he served as a full-time volunteer from 2001–2003 for the Church of Jesus Christ of Latter-day Saints. From 2003–2007 he did graduate work in computational chemistry under the direction of K. N. Houk at the University of California, Los Angeles. Afterwards he was a postdoctoral scholar at the California Institute of Technology with William A. Goddard III and at the Scripps Research Institute in Florida with Roy A. Periana. From 2009–2010 he was a postdoctoral researcher at the University of North Carolina at Chapel Hill at the UNC Energy Frontier Research Center directed by Thomas J. Meyer. Currently he is an assistant professor at Brigham Young University in Provo Utah. He is also principal investigator in the Center for Catalytic Hydrocarbon Functionalization, a DOE energy frontier research center.



Dewey Granville McCafferty was born in 1967 in Raleigh, North Carolina. He received his B.S. in Chemistry from North Carolina State University in 1990. He subsequently received his Ph.D. in Organic Chemistry from the University of North Carolina at Chapel Hill in 1995, conducting his thesis research in synthetic peptide chemistry, de novo redox protein design, and photoinitiated electron transfer with Profs. Bruce W. Erickson and Thomas J. Meyer. He then moved to Harvard Medical School and became the National Hemophilia Foundation Judith Graham Pool Postdoctoral Fellow, studying the enzymology of vancomycin resistance and post-translational carboxylation of blood coagulation proteins with Christopher T. Walsh.

In 1997, Prof. McCafferty joined the faculty of the University of Pennsylvania in the Department of Biochemistry and Biophysics, where he held Assistant and Associate Professor positions and studied the enzymology of bacterial cell wall protein anchoring, mechanisms of chromatin post-translational modification, and antibiotic synthesis, resistance, and mechanism of action. In 2005 he was awarded the Eli Lilly Award in Biological Chemistry from the American Chemical Society Division of Biological Chemistry. In 2006 he joined the faculty of the Department of Chemistry at Duke University as Professor of Chemistry. His current research interests in chemical biology include investigating the molecular mechanisms of redox-active enzymes, protein design, epigenetics enzymology, peptidoglycan recycling, antibiotic synthesis, biosynthesis and mechanism of action, and role of hydrolytic enzymes in staphylococcal and chlamydial pathogenesis.



Thomas J. Meyer first identified proton-coupled electron transfer and designed the first molecular water catalyst. He was an early pioneer in the field of artificial photosynthesis and solar fuels beginning with research published in the 1970s. He has gained an international reputation in photochemistry, mechanisms, and chemical reactivity and catalysis. He is currently Arey Professor of Chemistry at UNC—Chapel Hill and Director of the UNC Energy Frontier Research Center. In addition to PCET, his group is focused on water oxidation, carbon dioxide reduction, and photochemical and photoelectrochemical water splitting and reduction of carbon dioxide.

ACKNOWLEDGMENTS

The authors thank John M. Papanikolas, who supported B.C.W. (excited-state PCET) through the National Science Foundation Grant CHE0809045. The National Science Foundation Grant CHE0957215 supported organic and biological PCET as well as overall preparation by C.J.G (T.J.M.). The authors D.R.W (heterogeneous PCET, overall preparation), C.A.K (metal complex PCET) and D.H.E (theory) were supported by T.J.M. as part of the UNC EFRC: Center for Solar Fuels, an Energy Frontier Research Center funded by the U.S. Department of Energy, Office of Science, Office of Basic Energy Sciences, under Award Number DE-SC0001011. In addition, C.A.K. (T.J.M.) was a Carolina Energy Fellow. The authors J.F.H (biological PCET and model systems, overall preparation) and A.P. (electrochemical PCET) were supported by T.J.M. as part of the UVA EFRC: Center for Catalytic Hydrocarbon Functionalization, an Energy Frontier Research Center funded by the U.S. Department of Energy, Office of Science, Office of Basic Energy Sciences, under Award Number DE-SC0001298. D.G.M. and C.F.M. (biological PCET and model systems) were kindly supported by Duke University and by the National Institutes of Health research grant R01GM087566 for studies on Bioorganic Mechanisms of Chromatin Modifying Enzymes.

D.G.M. was also supported by the National Institutes of Health research grant R01AI46611 for studies on bioorganic mechanisms of peptide antibiotics. In addition, D.G.M. and C.F.M. thank the members of the McCafferty laboratory for their helpful discussions during the preparation of this manuscript.

REFERENCES

- (1) Huynh, M. H. V.; Meyer, T. J. *Chem. Rev.* **2007**, *107*, 5004.
- (2) Costentin, C.; Robert, M.; Savéant, J.-M. *Chem. Rev.* **2010**, *110*, PR1.
- (3) Hammes-Schiffer, S.; Stuchebrukhov, A. A. *Chem. Rev.* **2010**, *110*, 6939.
- (4) Dempsey, J. L.; Winkler, J. R.; Gray, H. B. *Chem. Rev.* **2010**, *110*, 7024.
- (5) Warren, J. J.; Tronic, T. A.; Mayer, J. M. *Chem. Rev.* **2010**, *110*, 6961.
- (6) Meyer, T. J.; Huynh, M. H. V.; Thorp, H. H. *Angew. Chem., Int. Ed.* **2007**, *46*, 5284.
- (7) Hammes-Schiffer, S.; Hatcher, E.; Ishikita, H.; Skone, J. H.; Soudackov, A. V. *Coord. Chem. Rev.* **2008**, *252*, 384.
- (8) Costentin, C. *Chem. Rev.* **2008**, *108*, 2145.
- (9) Reece, S. Y.; Nocera, D. G. *Annu. Rev. Biochem.* **2009**, *78*, 673.
- (10) Gagliardi, C. J.; Westlake, B. C.; Kent, C. A.; Paul, J. J.; Papanikolas, J. M.; Meyer, T. J. *Coord. Chem. Rev.* **2010**, *254*, 2459.
- (11) (a) Iordanova, N.; Hammes-Schiffer, S. *J. Am. Chem. Soc.* **2002**, *124*, 4848. (b) Binstead, R. A.; Meyer, T. J. *J. Am. Chem. Soc.* **1987**, *109*, 3287. (c) Farrer, B. T.; Thorp, H. H. *Inorg. Chem.* **1999**, *38*, 2497. (d) Moyer, B. A.; Meyer, T. J. *J. Am. Chem. Soc.* **1978**, *100*, 3601. (e) Binstead, R. A.; Moyer, B. A.; Samuels, G. J.; Meyer, T. J. *J. Am. Chem. Soc.* **1981**, *103*, 2897. (f) Meyer, T. J.; Huynh, M. H. V. *Inorg. Chem.* **2003**, *42*, 8140.
- (12) Cukier, R. I.; Nocera, D. G. *Annu. Rev. Phys. Chem.* **1998**, *49*, 337.
- (13) Sjodin, M.; Styring, S.; Wolpher, H.; Xu, Y. H.; Sun, L. C.; Hammarström, L. *J. Am. Chem. Soc.* **2005**, *127*, 3855.
- (14) (a) Carra, C.; Iordanova, N.; Hammes-Schiffer, S. *J. Am. Chem. Soc.* **2003**, *125*, 10429. (b) Sjodin, M.; Irebo, T.; Utas, J. E.; Lind, J.; Merenyi, G.; Åkermark, B.; Hammarström, L. *J. Am. Chem. Soc.* **2006**, *128*, 13076. (c) Dixon, W. T.; Murphy, D. *J. Chem. Soc., Faraday Trans. 2* **1976**, *72*, 1221.
- (15) Fecenko, C. J.; Thorp, H. H.; Meyer, T. J. *J. Am. Chem. Soc.* **2007**, *129*, 15098.
- (16) (a) Biczok, L.; Linschitz, H. *J. Phys. Chem.* **1995**, *99*, 1843. (b) Biczok, L.; Gupta, N.; Linschitz, H. *J. Am. Chem. Soc.* **1997**, *119*, 12601.
- (17) (a) Hoganson, C. W.; Lydakis-Simantiris, N.; Tang, X.-S.; Tommos, C.; Warncke, K.; Babcock, G. T.; Diner, B. A.; McCracken, J.; Styring, S. *Photosynth. Res.* **1995**, *46*, 177. (b) Brudvig, G.; Cady, C.; Tagore, R.; Crabtree, R. *Photosynth. Res.* **2007**, *91*, 177. (c) Biesiadka, J.; Loll, B.; Kern, J.; Irrgang, K.-D.; Zouni, A. *Phys. Chem. Chem. Phys.* **2004**, *6*, 4733. (d) Penner-Hahn, J. *Met. Sites Proteins Models* **1998**, *1*.
- (18) Ferreira, K. N.; Iverson, T. M.; Maghlaoui, K.; Barber, J.; Iwata, S. *Science* **2004**, *303*, 1831.
- (19) (a) Lee, H. J.; Svahn, E.; Swanson, J. M. J.; Lepp, H.; Voth, G. A.; Brzezinski, P.; Gennis, R. B. *J. Am. Chem. Soc.* **2010**, *132*, 16225. (b) Xu, J.; Voth, G. A. *Biochim. Biophys. Acta, Bioenerg.* **2008**, *1777*, 196.
- (20) (a) Junge, W.; Haumann, M.; Ahlbrink, R.; Mulkidjianian, A.; Clausen, J. *Philos. Trans. R. Soc., B* **2002**, *357*, 1407. (b) Hays, A.; Vassiliev, I.; Golbeck, J.; Debus, R. *Biochemistry* **1999**, *38*, 11851. (c) Eckert, H. J.; Renger, G. *FEBS Lett.* **1988**, *236*, 425. (d) Christen, G.; Renger, G. *Biochemistry* **1999**, *38*, 2068. (e) Schilstra, M.; Rappaport, F.; Nugent, J.; Barnett, C.; Klug, D. *Biochemistry* **1998**, *37*, 3974.
- (21) McEvoy, J. P.; Brudvig, G. W. *Chem. Rev.* **2006**, *106*, 4455.
- (22) (a) Barber, J.; Ferreira, K.; Maghlaoui, K.; Iwata, S. *Phys. Chem. Chem. Phys.* **2004**, *6*, 4737. (b) Ishikita, H.; Saenger, W.; Loll, B.; Biesiadka, J.; Knapp, E. W. *Biochemistry* **2006**, *45*, 2063. (c) Iwata, S.;

- Barber, J. *Curr. Opin. Struct. Biol.* **2004**, *14*, 447. (d) De Las Rivas, J.; Barber, J. *Photosynth. Res.* **2004**, *81*, 329.
- (23) Gagliardi, C. J.; Binsteader, R. A.; Thorp, H. H.; Meyer, T. J. *J. Am. Chem. Soc.* **2011**, *133*, 19594.
- (24) Zundel, G. *Adv. Chem. Phys.* **2000**, *111*, 1.
- (25) (a) Eigen, M. *Angew. Chem., Int. Ed.* **1964**, *3*, 1. (b) Markovitch, O.; Agmon, N. *J. Phys. Chem. A* **2007**, *111*, 2253.
- (26) (a) Vuilleumier, R.; Borgis, D. *J. Chem. Phys.* **1999**, *111*, 4251. (b) Lapid, H.; Agmon, N.; Petersen Matt, K.; Voth Gregory, A. *J. Chem. Phys.* **2005**, *122*, 14506. (c) Marx, D.; Tuckerman, M. E.; Hutter, J.; Parrinello, M. *Nature* **1999**, *397*, 601.
- (27) (a) Park, S.-Y.; Lee, Y.-S.; Kwon, O.-H.; Jang, D.-J. *Chem. Commun.* **2009**, 926. (b) Mohammed, O. F.; Pines, D.; Dreyer, J.; Pines, E.; Nibbering, E. T. *J. Science* **2005**, *310*, 83.
- (28) (a) Schowen, K. B.; Limbach, H. H.; Denisov, G. S.; Schowen, R. L. *Biochim. Biophys. Acta, Bioenerg.* **2000**, *1458*, 43. (b) Jencks, W. P. *Catalysis in Chemistry and Enzymology*; McGraw-Hill: New York, 1969.
- (29) Chen, Z.; Concepcion, J.; Luo, H.; Hull, J.; Paul, A.; Meyer, T. J. *Am. Chem. Soc.* **2010**, *132*, 17670.
- (30) Chen, Z.; Concepcion, J.; Hu, X.; Yang, W.; Hoertz, P.; Meyer, T. *Proc. Natl. Acad. Sci. U.S.A.* **2010**, *107*, 7225.
- (31) Huynh, M. H. V.; Baker, R. T.; Morris, D. E.; White, P. S.; Meyer, T. J. *Angew. Chem., Int. Ed.* **2002**, *41*, 3870.
- (32) Ess, D.; Schauer, C.; Meyer, T. J. *Am. Chem. Soc.* **2010**, *132*, 16318.
- (33) (a) Knowles, W. S.; Noyori, R. *Acc. Chem. Res.* **2007**, *40*, 1238. (b) Ikariya, T.; Blacker, A. *J. Acc. Chem. Res.* **2007**, *40*, 1300. (c) Jessop, P. G.; Ikariya, T.; Noyori, R. *Chem. Rev.* **1995**, *95*, 259. (d) Noyori, R.; Hashiguchi, S. *Acc. Chem. Res.* **1997**, *30*, 97.
- (34) Simon, L.; Goodman, J. *J. Am. Chem. Soc.* **2008**, *130*, 8741.
- (35) Chakraborty, A.; Pak Michael, V.; Hammes-Schiffer, S. *Phys. Rev. Lett.* **2008**, *101*, 153001.
- (36) (a) Concepcion, J. J.; Dattelbaum, D. M.; Meyer, T. J.; Rocha, R. C. *Philos. Trans. R. Soc., A* **2008**, *366*, 163. (b) Demadis, K. D.; Hartshorn, C. M.; Meyer, T. J. *Chem. Rev.* **2001**, *101*, 2655.
- (37) Chen, P.; Meyer, T. J. *Chem. Rev.* **1998**, *98*, 1439.
- (38) Johannissen, L.; Irebo, T.; Sjodin, M.; Johansson, O.; Hammarstrom, L. *J. Phys. Chem. B* **2009**, *113*, 16214.
- (39) (a) Ram, M. S.; Skeens-Jones, L. M.; Johnson, C. S.; Zhang, X. L.; Stern, C.; Yoon, D.; Selmarthen, D.; Hupp, J. T. *J. Am. Chem. Soc.* **1995**, *117*, 1411. (b) Pipes, D. W.; Meyer, T. J. *Inorg. Chem.* **1986**, *25*, 3256. (c) Baes, C. F., Jr.; Mesmer, R. E. *The Hydrolysis of Metal Cations*; Krieger Publishing Co.: Malabar, FL, 1986.
- (40) (a) Pipes, D. W.; Bakir, M.; Vitols, S. E.; Hodgson, D. J.; Meyer, T. J. *J. Am. Chem. Soc.* **1990**, *112*, 5507. (b) El-Samanody, E.-S.; Demadis, K. D.; Meyer, T. J.; White, P. S. *Inorg. Chem.* **2001**, *40*, 3677. (c) Coia, G. M.; Demadis, K. D.; Meyer, T. J. *Inorg. Chem.* **2000**, *39*, 2212. (d) Huynh, M. H. V.; White, P. S.; John, K. D.; Meyer, T. J. *Angew. Chem., Int. Ed.* **2001**, *40*, 4049.
- (41) (a) Thompson, M. S.; Meyer, T. J. *J. Am. Chem. Soc.* **1981**, *103*, 5577. (b) Murphy, W.; Rorer, J.; Takeuchi, K. J.; Meyer, T. J. *J. Am. Chem. Soc.* **1982**, *104*, 5817.
- (42) Kuehn, C. C.; Taube, H. *J. Am. Chem. Soc.* **1976**, *98*, 689.
- (43) Bard, A. J.; Faulkner, L. R. *Electrochemical Methods: Fundamentals and Applications*, 2nd ed.; Wiley: New York, 2004.
- (44) Moyer, B. A.; Meyer, T. J. *Inorg. Chem.* **1981**, *20*, 436.
- (45) (a) Gilbert, J. A.; Eggleston, D. S.; Murphy, W. R.; Geselowitz, D. A.; Gersten, S. W.; Hodgson, D. J.; Meyer, T. J. *J. Am. Chem. Soc.* **1985**, *107*, 3855. (b) Dobson, J. C.; Takeuchi, K. J.; Pipes, D. W.; Geselowitz, D. A.; Meyer, T. J. *Inorg. Chem.* **1986**, *25*, 2357.
- (46) Lyon, L. A.; Hupp, J. T. *J. Phys. Chem. B* **1999**, *103*, 4623.
- (47) (a) Heath, G. A.; Moock, K. A.; Sharp, D. W. A.; Yellowlees, L. J. *J. Chem. Soc., Chem. Commun.* **1985**, 1503. (b) Eggleston, D. S.; Goldsby, K. A.; Hodgson, D. J.; Meyer, T. J. *Inorg. Chem.* **1985**, *24*, 4573.
- (48) Cotton, F. A.; Wilkinson, G.; Murillo, C. A.; Bochmann, M. *Advanced Inorganic Chemistry*, 6th ed.; Wiley & Sons: New York, 1999.
- (49) Endicott, J. F. *Charge-Transfer Photochemistry*; Wiley: New York, 1975.
- (50) (a) Laviron, E. *J. Electroanal. Chem., Interfacial Electrochem.* **1984**, *164*, 213. (b) Laviron, E. *J. Electroanal. Chem., Interfacial Electrochem.* **1984**, *169*, 29. (c) Laviron, E. *J. Electroanal. Chem., Interfacial Electrochem.* **1986**, *208*, 357.
- (51) Okayama, S. *Biochim. Biophys. Acta, Bioenerg.* **1976**, *440*, 331.
- (52) Perrin, D. D. *Dissociation Constants of Inorganic Acids and Bases in Aqueous Solution*; Butterworths: London, 1969.
- (53) (a) Hammes-Schiffer, S. *Acc. Chem. Res.* **2009**, *42*, 1881. (b) Hammes-Schiffer, S.; Soudakov Alexander, V. *J. Phys. Chem. B* **2008**, *112*, 14108. (c) Han, W.; Liu, T.; Lovell, T.; Noddleman, L. *J. Inorg. Biochem.* **2006**, *100*, 771.
- (54) (a) Andrieux, C.; Gamby, J.; Hapiot, P.; Savéant, J. *J. Am. Chem. Soc.* **2003**, *125*, 10119. (b) Peters, K.; Cashin, A.; Timbers, P. *J. Am. Chem. Soc.* **2000**, *122*, 107. (c) Peters, K.; Kim, G. *J. Phys. Chem. A* **2004**, *108*, 2598. (d) Peters, K. *Acc. Chem. Res.* **2009**, *42*, 89.
- (55) Edwards, S.; Soudakov, A.; Hammes-Schiffer, S. *J. Phys. Chem. B* **2009**, *113*, 14545.
- (56) (a) Soudakov, A.; Hammes-Schiffer, S. *J. Chem. Phys.* **2000**, *113*, 2385. (b) Ulstrup, J.; Jortner, J. *J. Chem. Phys.* **1975**, *17*, 4358.
- (57) Zwickl, J.; Shenvi, N.; Schmidt, J.; Tully, J. *J. Phys. Chem. A* **2008**, *112*, 10570.
- (58) Edwards, S. J.; Soudakov, A. V.; Hammes-Schiffer, S. *J. Phys. Chem. A* **2009**, *113*, 2117.
- (59) Nelsen, S. F.; Blackstock, S. C.; Kim, Y. *J. Am. Chem. Soc.* **1987**, *109*, 677.
- (60) Wander, M.; Kubicki, J.; Clark, A.; Schoonen, M. *J. Phys. Chem. A* **2009**, *113*, 1020.
- (61) Navrotskaya, I.; Hammes-Schiffer, S. *J. Chem. Phys.* **2009**, *131*, 24112.
- (62) Venkataraman, C.; Soudakov, A. V.; Hammes-Schiffer, S. *J. Phys. Chem. C* **2008**, *112*, 12386.
- (63) (a) Costentin, C.; Evans, D.; Robert, M.; Savéant, J.; Singh, P. *J. Am. Chem. Soc.* **2005**, *127*, 12490. (b) Costentin, C.; Robert, M.; Savéant, J. *J. Am. Chem. Soc.* **2006**, *128*, 8726. (c) Costentin, C.; Robert, M.; Savéant, J. *J. Electroanal. Chem.* **2006**, *588*, 197. (d) Costentin, C.; Robert, M.; Savéant, J. *M. J. Am. Chem. Soc.* **2007**, *129*, 9953.
- (64) Navrotskaya, I.; Soudakov, A. V.; Hammes-Schiffer, S. *J. Chem. Phys.* **2008**, *128*, 244712.
- (65) Tishchenko, O.; Truhlar, D. G.; Ceulemans, A.; Nguyen, M. T. *J. Am. Chem. Soc.* **2008**, *130*, 7000.
- (66) (a) DiLabio, G.; Ingold, K. *J. Am. Chem. Soc.* **2005**, *127*, 6693. (b) DiLabio, G.; Johnson, E. *J. Am. Chem. Soc.* **2007**, *129*, 6199.
- (67) Li, P.; Xie, X.; Bu, Y.; Wang, W.; Wang, N.; Shi, J.; Mou, Z. *J. Theor. Comput. Chem.* **2008**, 435.
- (68) Vaidya, V.; Ingold, K.; Pratt, D. *Angew. Chem., Int. Ed.* **2009**, *48*, 157.
- (69) Mayer, J. *Annu. Rev. Phys. Chem.* **2004**, *55*, 363.
- (70) Chen, X.; Bu, Y. *J. Am. Chem. Soc.* **2007**, *129*, 9713.
- (71) Chen, X. H.; Xing, D. X.; Zhang, L.; Cukier, R. I.; Bu, Y. X. *J. Comput. Chem.* **2009**, *30*, 2694.
- (72) Singh, N.; O'Malley, P. J.; Popelier, P. L. A. *Phys. Chem. Chem. Phys.* **2005**, *7*, 614.
- (73) de Lucas, N. C.; Elias, M. M.; Firme, C. L.; Correa, R. J.; Garden, S. J.; Netto-Ferreira, J. C.; Nicodem, D. E. *J. Photochem. Photobiol. A* **2009**, *201*, 1.
- (74) Venkataraman, C.; Soudakov, A.; Hammes-Schiffer, S. *J. Chem. Phys.* **2009**, *129*, 154502.
- (75) Venkataraman, C.; Soudakov, A. V.; Hammes-Schiffer, S. *J. Phys. Chem. C* **2010**, *114*, 487.
- (76) Cape, J.; Bowman, M.; Kramer, D. *J. Am. Chem. Soc.* **2005**, *127*, 4208.
- (77) Yamamoto, T.; Kato, S. *J. Chem. Phys.* **2007**, *126*, 224514.
- (78) Ludlow, M. K.; Soudakov, A. V.; Hammes-Schiffer, S. *J. Am. Chem. Soc.* **2009**, *131*, 7094.
- (79) Kumar, M.; Kozlowski, P. M. *J. Phys. Chem. B* **2009**, *113*, 9050.
- (80) Yanai, T.; Mori, S. *Chem.—Eur. J.* **2009**, *15*, 4464.
- (81) Hewitt, N.; Rauk, A. *J. Phys. Chem. B* **2009**, *113*, 1202.

- (82) Shimizu, M.; Katsuda, N.; Katsurada, T.; Mitani, M.; Yoshioka, Y. *J. Phys. Chem. B* **2008**, *112*, 15116.
- (83) (a) Wang, Y.; Chen, H.; Makino, M.; Shiro, Y.; Nagano, S.; Asamizu, S.; Onaka, H.; Shaik, S. *J. Am. Chem. Soc.* **2009**, *131*, 6748. (b) Wang, Y.; Hirao, H.; Chen, H.; Onaka, H.; Nagano, S.; Shaik, S. *J. Am. Chem. Soc.* **2008**, *130*, 7170.
- (84) Cho, K.; Carvajal, M.; Shaik, S. *J. Phys. Chem. B* **2009**, *113*, 336.
- (85) Tureček, F.; Chen, X.; Hao, C. *J. Am. Chem. Soc.* **2008**, *130*, 8818.
- (86) Iyengar, S.; Sumner, I.; Jakowski, J. *J. Phys. Chem. B* **2008**, *112*, 7601.
- (87) dos Santos, A.; Silva, D.; Bolzani, V.; Santos, L.; Schmidt, T.; Baffa, O. *J. Braz. Chem. Soc.* **2009**, 1483.
- (88) Young, E. R.; Rosenthal, J.; Hodgkiss, J. M.; Nocera, D. G. *J. Am. Chem. Soc.* **2009**, *131*, 7678.
- (89) Heinze, K.; Marano, G.; Fischer, A. *J. Inorg. Biochem.* **2008**, *102*, 1199.
- (90) (a) Rhile, I. J.; Markle, T. F.; Nagao, H.; DiPasquale, A. G.; Lam, O. P.; Lockwood, M. A.; Rotter, K.; Mayer, J. M. *J. Am. Chem. Soc.* **2006**, *128*, 6075. (b) Markle, T.; Mayer, J. *Angew. Chem., Int. Ed.* **2008**, *47*, 738.
- (91) Tsai, M.; Rochford, J.; Polyansky, D.; Wada, T.; Tanaka, K.; Fujita, E.; Muckerman, J. *Inorg. Chem.* **2009**, *48*, 4372.
- (92) Mak, A.; Whiteman, M.; Wong, M. *J. Phys. Chem. A* **2007**, *111*, 8202.
- (93) Lingwood, M.; Hammond, J. R.; Hrovat, D. A.; Mayer, J. M.; Borden, W. T. *J. Chem. Theory Comput.* **2006**, *2*, 740.
- (94) Ludlow, M. K.; Skone, J. H.; Hammes-Schiffer, S. *J. Phys. Chem. B* **2008**, *112*, 336.
- (95) Costentin, C.; Louault, C.; Robert, M.; Savéant, J. M. *J. Am. Chem. Soc.* **2008**, *130*, 15817.
- (96) Litwinienko, G.; Ingold, K. U. *Acc. Chem. Res.* **2007**, *40*, 222.
- (97) Musialik, M.; Kuzmicz, R.; Pawłowski, T. S.; Litwinienko, G. *J. Org. Chem.* **2009**, *74*, 2699.
- (98) Valgimigli, L.; Amorati, R.; Petrucci, S.; Pedulli, G. F.; Hu, D.; Hanthorn, J. J.; Pratt, D. A. *Angew. Chem., Int. Ed.* **2009**, *48*, 8348.
- (99) Vuina, D.; Pilepic, V.; Ljubas, D.; Sankovic, K.; Sajenko, I.; Ursic, S. *Tetrahedron Lett.* **2007**, *48*, 3633.
- (100) Sajenko, I.; Pilepic, V.; Brala, C.; Ursic, S. *J. Phys. Chem. A* **2010**, *114*, 3423.
- (101) Warren, J. J.; Mayer, J. M. *J. Am. Chem. Soc.* **2008**, *130*, 7546.
- (102) Markle, T. F.; Rhile, I. J.; DiPasquale, A. G.; Mayer, J. M. *Proc. Natl. Acad. Sci. U.S.A.* **2008**, *105*, 8185.
- (103) Baciocchi, E.; Calcagni, A.; Lanzalunga, O. *J. Org. Chem.* **2008**, *73*, 4110.
- (104) Wu, A.; Mader, E. A.; Datta, A.; Hrovat, D. A.; Borden, W. T.; Mayer, J. M. *J. Am. Chem. Soc.* **2009**, *131*, 11985.
- (105) Chatgilialoglu, C.; D'Angelantonio, M.; Kaloudis, P.; Mulazzani, Q.; Guerra, M. *J. Phys. Chem. Lett.* **2010**, *1*, 174.
- (106) Zhu, X.-Q.; Zhang, M.-T.; Yu, A.; Wang, C.-H.; Cheng, J.-P. *J. Am. Chem. Soc.* **2008**, *130*, 2501.
- (107) Rajapakshe, A.; Snyder, R. A.; Astashkin, A. V.; Bernardson, P.; Evans, D. J.; Young, C. G.; Evans, D. H.; Enemark, J. H. *Inorg. Chim. Acta* **2009**, *362*, 4603.
- (108) Sugimoto, H.; Tsukube, H. *Chem. Soc. Rev.* **2008**, *37*, 2609.
- (109) (a) Dismukes, G. C.; Brimblecombe, R.; Felton, G. A. N.; Pryadun, R. S.; Sheats, J. E.; Spiccia, L.; Swiegers, G. F. *Acc. Chem. Res.* **2009**, *42*, 1935. (b) Magnuson, A.; Anderlund, M.; Johansson, O.; Lindblad, P.; Lomoth, R.; Polivka, T.; Ott, S.; Stensjo, K.; Styring, S.; Sundstrom, V.; Hammarström, L. *Acc. Chem. Res.* **2009**, *42*, 1899. (c) Concepcion, J. J.; Jurss, J. W.; Brennaman, M. K.; Hoertz, P. G.; Patrocinio, A. O. T.; Iha, N. Y. M.; Templeton, J. L.; Meyer, T. J. *Acc. Chem. Res.* **2009**, *42*, 1954. (d) Kern, J.; Renger, G. *Photosynth. Res.* **2007**, *94*, 183. (e) Mayer, J. M.; Rhile, I. J.; Larsen, F. B.; Mader, E. A.; Markle, T. F.; DiPasquale, A. G. *Photosynth. Res.* **2006**, *87*, 3. (f) Lomoth, R.; Magnuson, A.; Sjodin, M.; Huang, P.; Styring, S.; Hammarström, L. *Photosynth. Res.* **2006**, *87*, 25.
- (110) Magnuson, A.; Liebisch, P.; Hogblom, J.; Anderlund, M. F.; Lomoth, R.; Meyer-Klaucke, W.; Haumann, M.; Dau, H. *J. Inorg. Biochem.* **2006**, *100*, 1234.
- (111) Anderlund, M. F.; Hogblom, J.; Shi, W.; Huang, P.; Eriksson, L.; Weihe, H.; Styring, S.; Åkermark, B.; Lomoth, R.; Magnuson, A. *Eur. J. Inorg. Chem.* **2006**, 5033.
- (112) Wang, T.; Brudvig, G.; Batista, V. S. *J. Chem. Theory Comput.* **2010**, *6*, 755.
- (113) Yang, X.; Baik, M. H. *J. Am. Chem. Soc.* **2006**, *128*, 7476.
- (114) (a) Cape, J.; Siems, W.; Hurst, J. *Inorg. Chem.* **2009**, *48*, 8729. (b) Jurss, J. W.; Concepcion, J. J.; Butler, J. M.; Omberg, K. M.; Baraldo, L. M.; Thompson, D. G.; Lebeau, E. L.; Hornstein, B.; Schoonover, J. R.; Jude, H.; Thompson, J. D.; Dattelbaum, D. M.; Rocha, R. C.; Templeton, J. L.; Meyer, T. J. *Submitted for publication*. (c) Jurss, J. W.; Concepcion, J. J.; Templeton, J. L.; Meyer, T. J. *Manuscript in preparation*. (d) Jurss, J. W.; Templeton, J. L.; Meyer, T. J. *Manuscript in preparation*. (e) Jurss, J. W.; Concepcion, J. J.; Norris, M. R.; Binstead, R. A.; Templeton, J. L.; Meyer, T. J. *Manuscript in preparation*.
- (115) Bozoglian, F.; Romain, S.; Ertem, M. Z.; Todorova, T. K.; Sens, C.; Mola, J.; Rodriguez, M.; Romero, I.; Benet-Buchholz, J.; Fontrodona, X.; Cramer, C. J.; Gagliardi, L.; Llobet, A. *J. Am. Chem. Soc.* **2009**, *131*, 15176.
- (116) Liu, F.; Concepcion, J. J.; Jurss, J. W.; Cardolaccia, T.; Templeton, J. L.; Meyer, T. J. *Inorg. Chem.* **2008**, *47*, 1727.
- (117) Concepcion, J. J.; Jurss, J. W.; Templeton, J. L.; Meyer, T. J. *J. Am. Chem. Soc.* **2008**, *130*, 16462.
- (118) Concepcion, J. J.; Jurss, J. W.; Norris, M. R.; Chen, Z. F.; Templeton, J. L.; Meyer, T. J. *Inorg. Chem.* **2010**, *49*, 1277.
- (119) Tseng, H. W.; Zong, R.; Muckerman, J. T.; Thummel, R. *Inorg. Chem.* **2008**, *47*, 11763.
- (120) Wasyleンko, D.; Ganeshamoorthy, C.; Koivisto, B.; Henderson, M.; Berlinguet, C. *Inorg. Chem.* **2010**, *49*, 2202.
- (121) Concepcion, J. J.; Jurss, J. W.; Templeton, J. L.; Meyer, T. J. *Proc. Natl. Acad. Sci. U.S.A.* **2008**, *105*, 17632.
- (122) Nyhlen, J.; Duan, L.; Åkermark, B.; Sun, L.; Privalov, T. *Angew. Chem., Int. Ed.* **2010**, *49*, 1773.
- (123) Balcells, D.; Clot, E.; Eisenstein, O. *Chem. Rev.* **2010**, *110*, 749.
- (124) Gunay, A.; Theopold, K. *Chem. Rev.* **2010**, *110*, 1060.
- (125) Nam, W. *Acc. Chem. Res.* **2007**, *40*, 522.
- (126) Lee, Y. M.; Dhuri, S. N.; Sawant, S. C.; Cho, J.; Kubo, M.; Ogura, T.; Fukuzumi, S.; Nam, W. *Angew. Chem., Int. Ed.* **2009**, *48*, 1803.
- (127) Bhattacharyya, J.; Mukhopadhyay, S. *Trans. Met. Chem. (Dordrecht, Neth.)* **2006**, *31*, 256.
- (128) Mandal, P. C.; Bhattacharyya, J.; Das, S.; Mukhopadhyay, S.; Kirschenbaum, L. *J. Polyhedron* **2009**, *28*, 3162.
- (129) Goldsmith, C. R.; Stack, T. D. P. *Inorg. Chem.* **2006**, *45*, 6048.
- (130) Parsell, T. H.; Yang, M.-Y.; Borovik, A. S. *J. Am. Chem. Soc.* **2009**, *131*, 2762.
- (131) Prokop, K.; de Visser, S.; Goldberg, D. *Angew. Chem., Int. Ed.* **2010**, *49*, 5091.
- (132) Hirai, Y.; Kojima, T.; Mizutani, Y.; Shiota, Y.; Yoshizawa, K.; Fukuzumi, S. *Angew. Chem., Int. Ed.* **2008**, *47*, 5772.
- (133) Cheung, W. M.; Ng, H. Y.; Williams, I. D.; Leung, W. H. *Inorg. Chem.* **2008**, *47*, 4383.
- (134) (a) Nunes, G. S.; Alexiou, A. D. P.; Toma, H. E. *J. Catal.* **2008**, *260*, 188. (b) Nunes, G. S.; Alexiou, A. D. P.; Araki, K.; Formiga, A. L. B.; Rocha, R. C.; Toma, H. E. *Eur. J. Inorg. Chem.* **2006**, 1487.
- (135) Herres-Pawlis, S.; Verma, P.; Haase, R.; Kang, P.; Lyons, C. T.; Wasinger, E. C.; Florke, U.; Henkel, G.; Stack, T. D. P. *J. Am. Chem. Soc.* **2009**, *131*, 1154.
- (136) Matsumoto, T.; Ohkubo, K.; Honda, K.; Yazawa, A.; Furutachi, H.; Fujinami, S.; Fukuzumi, S.; Suzuki, M. *J. Am. Chem. Soc.* **2009**, *131*, 9258.
- (137) Ribas, X.; Calle, C.; Poater, A.; Casitas, A.; Gomez, L.; Xifra, R.; Parella, T.; Benet-Buchholz, J.; Schweiger, A.; Mitrikas, G.; Sola, M.; Llobet, A.; Stack, T. *J. Am. Chem. Soc.* **2010**, *132*, 12299.

- (138) Halime, Z.; Kieber-Emmons, M.; Qayyum, M.; Mondal, B.; Gandhi, T.; Puiu, S.; Chufan, E.; Sarjeant, A.; Hodgson, K.; Hedman, B.; Solomon, E.; Karlin, K. *Inorg. Chem.* **2010**, *49*, 3629.
- (139) Ohde, C.; Limberg, C. *Chem.—Eur. J.* **2010**, *16*, 6892.
- (140) Waidmann, C. R.; Zhou, X.; Tsai, E. A.; Kaminsky, W.; Hrovat, D. A.; Borden, W. T.; Mayer, J. M. *J. Am. Chem. Soc.* **2009**, *131*, 4729.
- (141) Song, N.; Stanbury, D. M. *Inorg. Chem.* **2008**, *47*, 11458.
- (142) Makarycheva-Mikhailova, A. V.; Stanbury, D. M.; McKee, M. L. *J. Phys. Chem. B* **2007**, *111*, 6942.
- (143) (a) Esswein, M.; Nocera, D. *Chem. Rev.* **2007**, *107*, 4022. (b) Fujishima, A.; Honda, K. *Nature* **1972**, *238*, 37. (c) Maeda, K.; Domen, K. *J. Phys. Chem. C* **2007**, *111*, 7851.
- (144) Capon, J.-F.; Gloaguen, F.; Petillon, F. Y.; Schollhammer, P.; Talarmin, J. *Coord. Chem. Rev.* **2009**, *253*, 1476.
- (145) Dubois, M. R.; Dubois, D. L. *Acc. Chem. Res.* **2009**, *42*, 1974.
- (146) Barton, B. E.; Rauchfuss, T. B. *Inorg. Chem.* **2008**, *47*, 2261.
- (147) Yang, J. Y.; Bullock, R. M.; Shaw, W. J.; Twamley, B.; Fraze, K.; DuBois, M. R.; DuBois, D. L. *J. Am. Chem. Soc.* **2009**, *131*, 5935.
- (148) (a) DuBois, M. R.; DuBois, D. L. *C. R. Chim.* **2008**, *11*, 805. (b) Dubois, M.; Dubois, D. *Acc. Chem. Res.* **2009**, *42*, 1974. (c) Yang, J. Y.; Bullock, R. M.; Shaw, W. J.; Twamley, B.; Fraze, K.; DuBois, M. R.; DuBois, D. L. *J. Am. Chem. Soc.* **2009**, *131*, 5935.
- (149) Dempsey, J. L.; Brunschwig, B. S.; Winkler, J. R.; Gray, H. B. *Acc. Chem. Res.* **2009**, *42*, 1995.
- (150) Dempsey, J.; Winkler, J.; Gray, H. *J. Am. Chem. Soc.* **2010**, *132*, 1060.
- (151) Soo, H. S.; Komor, A. C.; Iavarone, A. T.; Chang, C. J. *Inorg. Chem.* **2009**, *48*, 10024.
- (152) Shook, R.; Borovik, A. *Inorg. Chem.* **2010**, *49*, 3646.
- (153) Snir, O.; Wang, Y.; Tuckerman, M.; Geletii, Y.; Weinstock, I. J. *Am. Chem. Soc.* **2010**, *132*, 11678.
- (154) Mader, E.; Davidson, E.; Mayer, J. *J. Am. Chem. Soc.* **2007**, *129*, 5153.
- (155) Lancaster, K. M.; Gerken, J. B.; Durrell, A. C.; Palmer, J. H.; Gray, H. B. *Coord. Chem. Rev.* **2010**, *254*, 1803.
- (156) Wu, A.; Mayer, J. M. *J. Am. Chem. Soc.* **2008**, *130*, 14745.
- (157) Christian, G.; Llobet, A.; Maseras, F. *Inorg. Chem.* **2010**, *49*, 5977.
- (158) Warren, J. J.; Mayer, J. M. *J. Am. Chem. Soc.* **2008**, *130*, 2774.
- (159) (a) Miyazaki, S.; Kojima, T.; Sakamoto, T.; Matsumoto, T.; Ohkubo, K.; Fukuzumi, S. *Inorg. Chem.* **2008**, *47*, 333. (b) Miyazaki, S.; Kojima, T.; Mayer, J. M.; Fukuzumi, S. *J. Am. Chem. Soc.* **2009**, *131*, 11615.
- (160) Manner, V. W.; Mayer, J. M. *J. Am. Chem. Soc.* **2009**, *131*, 9874.
- (161) Ding, F. Z.; Smith, J. M.; Wang, H. B. *J. Org. Chem.* **2009**, *74*, 2679.
- (162) (a) Cox, M. J.; Siwick, B. J.; Bakker, H. J. *ChemPhysChem* **2009**, *10*, 236. (b) Nunes, R. M. D.; Pineiro, M.; Arnaut, L. G. *J. Am. Chem. Soc.* **2009**, *131*, 9456.
- (163) (a) Frutos, L. M.; Markmann, A.; Sobolewski, A. L.; Domcke, W. *J. Phys. Chem. B* **2007**, *111*, 6110. (b) Perun, S.; Sobolewski, A. L.; Domcke, W. *J. Phys. Chem. A* **2006**, *110*, 9031. (c) Samoylova, E.; Radloff, W.; Ritze, H.-H.; Schultz, T. *J. Phys. Chem. A* **2009**, *113*, 8195.
- (164) Balzani, V.; Bergamini, G.; Ceroni, P. *Coord. Chem. Rev.* **2008**, *252*, 2456.
- (165) (a) Lan, Z. G.; Frutos, L. M.; Sobolewski, A. L.; Domcke, W. *Proc. Natl. Acad. Sci. U.S.A.* **2008**, *105*, 12707. (b) Prashanthi, S.; Bangal, P. R. *Chem. Commun.* **2009**, 1757. (c) Freys, J. C.; Bernardinelli, G.; Wenger, O. S. *Chem. Commun.* **2008**, 4267. (d) Kinoshita, I.; Hashimoto, H.; Nishioka, T.; Miyamoto, R.; Kuwamura, N.; Yoshida, Y. *Photosynth. Res.* **2008**, *95*, 363. (e) Hodgkiss, J. M.; Damrauer, N. H.; Presse, S.; Rosenthal, J.; Nocera, D. G. *J. Phys. Chem. B* **2006**, *110*, 18853. (f) Irebo, T.; Reece, S. Y.; Sjodin, M.; Nocera, D. G.; Hammarström, L. *J. Am. Chem. Soc.* **2007**, *129*, 15462. (g) Skone, J. H.; Soudakov, A. V.; Hammes-Schiffer, S. *J. Am. Chem. Soc.* **2006**, *128*, 16655. (h) Rosenthal, J.; Young, E. R.; Nocera, D. G. *Inorg. Chem.* **2007**, *46*, 8668. (i) Hodgkiss, J. M.; Krivokapic, A.; Nocera, D. G. *J. Phys. Chem. B* **2007**, *111*, 8258.
- (166) Sobolewski, A. L.; Domcke, W. *J. Phys. Chem. A* **2007**, *111*, 11725.
- (167) (a) Shi, X.; Abbyad, P.; Shu, X.; Kallio, K.; Kanchanawong, P.; Childs, W.; Remington, S. J.; Boxer, S. G. *Biochemistry* **2007**, *46*, 12014. (b) Shu, X.; Kallio, K.; Shi, X.; Abbyad, P.; Kanchanawong, P.; Childs, W.; Boxer, S. G.; Remington, S. J. *Biochemistry* **2007**, *46*, 12005. (c) Leiderman, P.; Genosar, L.; Huppert, D.; Shu, X.; Remington, S. J.; Solntsev, K. M.; Tolbert, L. M. *Biochemistry* **2007**, *46*, 12026.
- (168) Westlake, B. C.; Brennaman, K. M.; Concepcion, J. J.; Paul, J. J.; Bettis, S. E.; Hampton, S. n. D.; Miller, S. A.; Lebedeva, N. V.; Forbes, M. D. E.; Moran, A. M.; Meyer, T. J.; Papanikolas, J. M. *Proc. Natl. Acad. Sci. U.S.A.* **2011**, *21*, 8554.
- (169) (a) Silverman, L. N.; Spry, D. B.; Boxer, S. G.; Fayer, M. D. *J. Phys. Chem. A* **2008**, *112*, 10244. (b) Nishikubo, Y.; Kanzaki, S.; Matsumura, S.; Toshima, K. *Tetrahedron Lett.* **2006**, *47*, 8125.
- (170) (a) Gepshtain, R.; Leiderman, P.; Huppert, D.; Project, E.; Nachliel, E.; Gutman, M. *J. Phys. Chem. B* **2006**, *110*, 26354. (b) Spry, D. B.; Fayer, M. D. *J. Chem. Phys.* **2007**, *127*, 204501. (c) Spry, D. B.; Fayer, M. D. *J. Chem. Phys.* **2008**, *128*, 084508.
- (171) Chen, X. H.; Tureček, F. *J. Am. Chem. Soc.* **2006**, *128*, 12520.
- (172) (a) Catalan, J.; Diaz, C.; de Paz, J. L. *G. Chem. Phys. Lett.* **2006**, *419*, 164. (b) Sekiya, H.; Sakota, K. *J. Photochem. Photobiol., C* **2008**, *9*, 81. (c) Takeuchi, S.; Tahara, T. *Proc. Natl. Acad. Sci. U.S.A.* **2007**, *104*, 5285.
- (173) Yamada, H.; Tanabe, K.; Ito, T.; Nishimoto, S. *Chem.—Eur. J.* **2008**, *14*, 10453.
- (174) (a) Concepcion, J. J.; Brennaman, M. K.; Deyton, J. R.; Lebedeva, N. V.; Forbes, M. D. E.; Papanikolas, J. M.; Meyer, T. J. *J. Am. Chem. Soc.* **2007**, *129*, 6968. (b) Sun, H.; Hoffman, M. Z. *J. Phys. Chem.* **1993**, *97*, 5014. (c) Rugge, A.; Clark, C.; Hoffman, M.; Rillema, D. *Inorg. Chim. Acta* **1998**, *279*, 200.
- (175) Zhang, H.; Rajesh, C. S.; Dutta, P. K. *J. Phys. Chem. A* **2008**, *112*, 808.
- (176) Irebo, T.; Johansson, O.; Hammarström, L. *J. Am. Chem. Soc.* **2008**, *130*, 9194.
- (177) Gavrilyuk, A.; Tritthart, U.; Gey, W. *Philos. Mag.* **2007**, *87*, 4519.
- (178) Barry, B. A.; Cooper, I. B.; De Riso, A.; Brewer, S. H.; Vu, D. M.; Dyer, R. B. *Proc. Natl. Acad. Sci. U.S.A.* **2006**, *103*, 7288.
- (179) Cooper, I. B.; Barry, B. A. *Biophys. J.* **2008**, *95*, 5843.
- (180) Markwick, P. R. L.; Doltsinis, N. L. *J. Chem. Phys.* **2007**, *126*, 175102.
- (181) de La Harpe, K.; Crespo-Hernandez, C. E.; Kohler, B. *J. Am. Chem. Soc.* **2009**, *131*, 17557.
- (182) Sobolewski, A. L.; Domcke, W. *ChemPhysChem* **2006**, *7*, 561.
- (183) (a) Leiderman, P.; Huppert, D.; Agmon, N. *Biophys. J.* **2006**, *90*, 1009. (b) Manca, C. *Chem. Phys. Lett.* **2007**, *443*, 173. (c) Remington, S. J. *Curr. Opin. Struct. Biol.* **2006**, *16*, 714. (d) Stoner-Ma, D.; Melief, E. H.; Nappa, J.; Ronayne, K. L.; Tonge, P. J.; Meech, S. R. *J. Phys. Chem. B* **2006**, *110*, 22009. (e) Stoner-Ma, D.; Jaye, A. A.; Ronayne, K. L.; Nappa, J.; Meech, S. R.; Tonge, P. J. *J. Am. Chem. Soc.* **2008**, *130*, 1227. (f) Vendrell, O.; Gelabert, R.; Moreno, M.; Lluch, J. M. *J. Am. Chem. Soc.* **2006**, *128*, 3564.
- (184) Brejc, K.; Sixma, T. K.; Kitts, P. A.; Kain, S. R.; Tsien, R. Y.; Ormo, M.; Remington, S. J. *Proc. Natl. Acad. Sci. U.S.A.* **1997**, *94*, 2306.
- (185) Guo, S.-X.; Mariotti, A. W. A.; Schlipf, C.; Bond, A. M.; Wedd, A. G. *Inorg. Chem.* **2006**, *45*, 8563.
- (186) Nambu, J.-i.; Ueda, T.; Guo, S.-X.; Boas, J. F.; Bond, A. M. *Dalton Trans.* **2010**, *39*, 7364.
- (187) Pourbaix, M. In *Atlas of Electrochemical Equilibria in Aqueous Solution*, 2nd ed.; Franklin, J. A., Ed.; Pergamon: New York, 1974.
- (188) Wang, D.; Zhang, M.; Buhlmann, P.; Que, L., Jr. *J. Am. Chem. Soc.* **2010**, *132*, 7638.
- (189) Parthasarathy, M.; Gopinath, C. S.; Pillai, V. K. *Chem. Mater.* **2006**, *18*, 5244.
- (190) Nicholson, R. S. *Anal. Chem.* **1965**, *37*, 1351.
- (191) Evans, R. G.; Compton, R. G. *ChemPhysChem* **2006**, *7*, 488.
- (192) Gupta, A. K.; Sindal, R. S. *J. Chem. Sci.* **2009**, *121*, 347.

- (193) Gerli, A.; Reedijk, J.; Lakin, M. T.; Spek, A. L. *Inorg. Chem.* **1995**, *34*, 1836.
- (194) (a) Singh, P.; Evans, D. *J. Phys. Chem. B* **2006**, *110*, 637. (b) Wang, S. H.; Singh, P. S.; Evans, D. H. *J. Phys. Chem. C* **2009**, *113*, 16686.
- (195) Costentin, C.; Robert, M.; Savéant, J.-M. *Acc. Chem. Res.* **2010**, *43*, 1019.
- (196) Costentin, C.; Louault, C.; Robert, M.; Savéant, J.-M. *Proc. Natl. Acad. Sci. U.S.A.* **2009**, *106*, 18143.
- (197) Costentin, C.; Robert, M.; Savéant, J.-M.; Tard, C. *Angew. Chem., Int. Ed.* **2010**, *49*, 3803.
- (198) (a) Costentin, C.; Robert, M.; Savéant, J.-M.; Teillout, A.-L. *ChemPhysChem* **2009**, *10*, 191. (b) Costentin, C.; Robert, M.; Savéant, J. M.; Teillout, A. L. *Proc. Natl. Acad. Sci. U.S.A.* **2009**, *106*, 11829.
- (199) Costentin, C.; Robert, M.; Savéant, J.-M. *J. Am. Chem. Soc.* **2006**, *128*, 4552.
- (200) Rudolph, M.; Reddy, D. P.; Feldberg, S. W. *Anal. Chem.* **1994**, *66*, A589.
- (201) Rudolph, M. *J. Electroanal. Chem.* **2003**, *543*, 23.
- (202) Savéant, J. M. *J. Phys. Chem. C* **2007**, *111*, 2819.
- (203) Baitalik, S.; Dutta, S.; Biswas, P.; Floerke, U.; Bothe, E.; Nag, K. *Eur. J. Inorg. Chem.* **2010**, *570*.
- (204) Hatay, I.; Su, B.; Li, F.; Mendez, M. A.; Khouri, T.; Gros, C. P.; Barbe, J.-M.; Ersöz, M.; Samec, Z.; Girault, H. H. *J. Am. Chem. Soc.* **2009**, *131*, 13453.
- (205) (a) Li, F.; Su, B.; Salazar, F. C.; Nia, R. P.; Girault, H. H. *Electrochim. Commun.* **2009**, *11*, 473. (b) Kelly, A. M.; Katif, N.; James, T. D.; Marken, F. *New J. Chem.* **2010**, *34*, 1261.
- (206) (a) Jensen, H.; Devaud, V.; Josserand, J.; Girault, H. H. *J. Electroanal. Chem.* **2002**, *537*, 77. (b) Su, B.; Nia, R. P.; Li, F.; Hojeij, M.; Prudent, M.; Corminboeuf, C.; Samec, Z.; Girault, H. H. *Angew. Chem., Int. Ed.* **2008**, *47*, 4675.
- (207) (a) Rosenthal, J.; Nocera, D. G. *Acc. Chem. Res.* **2007**, *40*, 543. (b) Trojanek, A.; Langmaier, J.; Samec, Z. *Electrochim. Commun.* **2006**, *8*, 475.
- (208) (a) Trojanek, A.; Marecek, V.; Janchenova, H.; Samec, Z. *Electrochim. Commun.* **2007**, *9*, 2185. (b) Partovi-Nia, R.; Su, B.; Li, F.; Gros, C.; Barbe, J.; Samec, Z.; Girault, H. *Chem.—Eur. J.* **2009**, *15*, 2335.
- (209) Lledo-Fernandez, C.; Hatay, I.; Ball, M. J.; Greenway, G. M.; Wadhawan, J. *New J. Chem.* **2009**, *33*, 749.
- (210) Chen, Z.; Zu, Y. *J. Phys. Chem. C* **2008**, *112*, 16663.
- (211) Creville, A. G.; Pumera, M.; Gonzalez, M. C.; Escarpa, A. *Analyst* **2009**, *134*, 657.
- (212) (a) McCreery, R. *Chem. Rev.* **2008**, *108*, 2646. (b) Cabaniss, G. E.; Diamantis, A. A.; Murphy, W. R.; Linton, R. W.; Meyer, T. J. *J. Am. Chem. Soc.* **1985**, *107*, 1845. (c) DuVall, S.; McCreery, R. *J. Am. Chem. Soc.* **2000**, *122*, 6759.
- (213) Heinze, K.; Fischer, A. *Eur. J. Inorg. Chem.* **2007**, *1020*.
- (214) (a) Kumar, A.; Zen, J. *ChemPhysChem* **2004**, *5*, 1227. (b) Ciriminna, R.; Pagliaro, M. *Chem.—Eur. J.* **2003**, *9*, 5067.
- (215) Kumar, A. S.; Zen, J.-M. *J. Mol. Catal. A: Chem.* **2006**, *252*, 63.
- (216) Rochefort, D.; Pont, A. *Electrochim. Commun.* **2006**, *8*, 1539.
- (217) Trammell, S. A.; Lebedev, N. *J. Electroanal. Chem.* **2009**, *632*, 127.
- (218) Trammell, S. A.; Lowy, D. A.; Seferos, D. S.; Moore, M.; Bazan, G. C.; Lebedev, N. *J. Electroanal. Chem.* **2007**, *606*, 33.
- (219) (a) Park, W.; Hong, H. *Bull. Korean Chem. Soc.* **2006**, *27*, 381. (b) Trammell, S. A.; Seferos, D. S.; Moore, M.; Lowy, D. A.; Bazan, G. C.; Kushmerick, J. G.; Lebedev, N. *Langmuir* **2007**, *23*, 942.
- (220) (a) Laviron, E. *J. Electroanal. Chem.* **1979**, *99*, 19. (b) Marcus, M. A. *J. Chem. Phys.* **1965**, *43*, 679.
- (221) Zhang, W.; Rosendahl, S.; Burgess, I. *J. Phys. Chem. C* **2010**, *114*, 2738.
- (222) Abhayawardhana, A. D.; Sutherland, T. C. *J. Phys. Chem. C* **2009**, *113*, 4915.
- (223) (a) Madhiri, N.; Finklea, H. O. *Langmuir* **2006**, *22*, 10643. (b) Uehara, H.; Abe, M.; Hisaeda, Y.; Uosaki, K.; Sasaki, Y. *Chem. Lett.* **2006**, *35*, 1178. (c) Uehara, H.; Inomata, T.; Abe, M.; Uosaki, K.; Sasaki, Y. *Chem. Lett.* **2008**, *37*, 684.
- (224) Ludlow, M.; Soudackov, A.; Hammes-Schiffer, S. *J. Am. Chem. Soc.* **2010**, *132*, 1234.
- (225) Jurss, J. W.; Concepcion, J. C.; Norris, M. R.; Templeton, J. L.; Meyer, T. J. *Inorg. Chem.* **2010**, *49*, 3980.
- (226) Gagliardi, C. J.; Jurss, J. W.; Thorp, H. H.; Meyer, T. J. *Inorg. Chem.* **2011**, *50*, 2076.
- (227) (a) Sui, P. C.; Djilali, N. *J. Power Sources* **2006**, *161*, 294. (b) Lee, S.-J.; Pyun, S.-I. *Electrochim. Acta* **2007**, *52*, 6525. (c) Janik, M.; Taylor, C.; Neurock, M. *Top. Catal.* **2007**, *46*, 306. (d) Yang, W. W.; Zhao, T. S.; He, Y. L. *J. Power Sources* **2008**, *185*, 765.
- (228) (a) Li, B.; Zhao, J.; Onda, K.; Jordan, K. D.; Yang, J.; Petek, H. *Science* **2006**, *311*, 1436. (b) Zhao, J.; Onda, K.; Li, B.; Petek, H. *Proc. SPIE—Int. Soc. Opt. Eng.* **2006**, *6325*, 63250W/1.
- (229) (a) Zhao, J.; Li, B.; Onda, K.; Feng, M.; Petek, H. *Chem. Rev.* **2006**, *106*, 4402. (b) Zhao, J.; Yang, J.; Petek, H. *Phys. Rev. B* **2009**, *80*, 235416.
- (230) Moore, G. F.; Hamberger, M.; Gervaldo, M.; Poluektov, O. G.; Rajh, T.; Gust, D.; Moore, T. A.; Moore, A. L. *J. Am. Chem. Soc.* **2008**, *130*, 10466.
- (231) (a) Sun, Y.-X.; Wang, S.-F. *Bioelectrochemistry* **2007**, *71*, 172. (b) Leger, C.; Bertrand, P. *Chem. Rev.* **2008**, *108*, 2379.
- (232) (a) Xu, Y.; Wang, F.; Chen, X.; Hu, S. *Talanta* **2006**, *70*, 651. (b) Ma, G.-X.; Wang, Y.-G.; Wang, C.-X.; Lu, T.-H.; Xia, Y.-Y. *Electrochim. Acta* **2008**, *53*, 4748. (c) Zhang, Y.; Cheng, W.; Li, S.; Li, N. *Colloids Surf. A* **2006**, *286*, 33. (d) Zeng, X.; Wei, W.; Li, X.; Zeng, J.; Wu, L. *Bioelectrochemistry* **2007**, *71*, 135.
- (233) (a) Huang, J.; Tsai, Y. *Sens. Actuators, B* **2009**, *140*, 267. (b) Wang, Y.; Ma, X.; Wen, Y.; Duan, G.; Ren, W.; Zhang, Z.; Yang, H. *Microchim. Acta* **2009**, *166*, 283. (c) Li, Y.-M.; Liu, G.-D.; Zhang, Z.-L. *Yingyong Huaxue* **2006**, *23*, 399.
- (234) Wang, Q.; Zheng, J. *Chem. Pap.* **2010**, *56*.
- (235) Becker, C.; Watmough, N.; Elliott, S. *Biochemistry* **2009**, *48*, 87.
- (236) (a) Yang, W.; Li, Y.; Bai, Y.; Sun, C. *Sens. Actuators, B* **2006**, *B115*, 42. (b) Liu, H.-H.; Wan, Y.-Q.; Zou, G.-L. *J. Electroanal. Chem.* **2006**, *594*, 111. (c) Li, Y.-m.; Liu, G.-d.; Zhang, Z.-l. *Sichuan Shifan Daxue Xuebao, Ziran Kexueban* **2006**, *29*, 364.
- (237) Fleming, B. D.; Bell, S. G.; Wong, L.-L.; Bond, A. M. *J. Electroanal. Chem.* **2007**, *611*, 149.
- (238) Shan, D.; Wang, Y.-N.; Xue, H.-G.; Cosnier, S.; Ding, S.-N. *Biosens. Bioelectron.* **2009**, *24*, 3556.
- (239) (a) Yamazaki, I.; Araiso, T.; Hayashi, Y.; Yamada, H.; Makino, R. *Adv. Biophys.* **1978**, *11*, 249. (b) Liu, H.; Huang, X.-L.; Wang, Q.-H. *Int. J. Chem. React. Eng.* **2008**, *6*, no pp given.
- (240) (a) Shan, D.; Wang, S.; Zhu, D.; Xue, H. *Bioelectrochemistry* **2007**, *71*, 198. (b) Zheng, W.; Li, J.; Zheng, Y. *Biosens. Bioelectron.* **2008**, *23*, 1562. (c) Sun, W.; Wang, D.; Zhai, Z.; Gao, R.; Jiao, K. *J. Iran. Chem. Soc.* **2009**, *6*, 412. (d) Chen, L.; Lu, G. *J. Electroanal. Chem.* **2006**, *597*, 51. (e) Sun, W.; Wang, D.; Li, G.; Zhai, Z.; Zhao, R.; Jiao, K. *Electrochim. Acta* **2008**, *53*, 8217. (f) Salimi, A.; Hallaj, R.; Soltanian, S. *Biophys. Chem.* **2007**, *130*, 122. (g) Zheng, N.; Zhou, X.; Yang, W.; Li, X.; Yuan, Z. *Talanta* **2009**, *79*, 780.
- (241) (a) Xu, J.; Zhao, J.; Wang, F.; Lu, Q.; Xu, Y.; Hu, S. *Russ. J. Electrochem.* **2008**, *44*, 1002. (b) Zhao, S.; Zhang, K.; Sun, Y.; Sun, C. *Bioelectrochemistry* **2006**, *69*, 10.
- (242) (a) Shan, D.; Cheng, G.; Zhu, D.; Xue, H.; Cosnier, S.; Ding, S. *Sens. Actuators, B* **2009**, *B137*, 259. (b) Song, M.; Ge, L.; Wang, X. *J. Electroanal. Chem.* **2008**, *617*, 149. (c) Dai, Z.; Bai, H.; Hong, M.; Zhu, Y.; Bao, J.; Shen, J. *Biosens. Bioelectron.* **2008**, *23*, 1869.
- (243) Yu, C.; Guo, J.; Gu, H. *Microchim. Acta* **2009**, *166*, 215.
- (244) Kamin, R. A.; Wilson, G. S. *Anal. Chem.* **1980**, *52*, 1198.
- (245) (a) Jiang, H.-J.; Yang, H.; Akins, D. L. *J. Electroanal. Chem.* **2008**, *623*, 181. (b) Zhou, B.; Wang, J.; Gao, X.; Tian, Y. *Anal. Lett.* **2008**, *41*, 1832.
- (246) (a) Azevedo, A. M.; Prazeres, D. M. F.; Cabral, J. M. S.; Fonseca, L. P. *J. Mol. Catal. B: Enzym.* **2001**, *15*, 147. (b) Saini, S.; Hall, G. F.; Downs, M. E. A.; Turner, A. P. F. *Anal. Chim. Acta* **1991**, *249*, 1. (c) Wang, J.; Rivas, G.; Liu, J. *Anal. Lett.* **1995**, *28*, 2287.

- (247) Ayala, G.; Degomezpuyou, M. T.; Gomezpuyou, A.; Darszon, A. *FEBS Lett.* **1986**, *203*, 41.
- (248) Aymard, P.; Martin, D.; Plucknett, K.; Foster, T.; Clark, A.; Norton, I. *Biopolymers* **2001**, *131*.
- (249) Almeida, M. G.; Silveira, C. M.; Guiigliarelli, B.; Bertrand, P.; Moura, J. J. G.; Moura, I.; Leger, C. *FEBS Lett.* **2007**, *581*, 284.
- (250) Friedrich, M. G.; Robertson, J. W. F.; Walz, D.; Knoll, W.; Naumann, R. L. C. *Biophys. J.* **2008**, *94*, 3698.
- (251) (a) Pilotelle-Bunner, A.; Beaunier, P.; Tandori, J.; Maroti, P.; Clarke, R. J.; Sebban, P. *Biochim. Biophys. Acta, Bioenerg.* **2009**, *1787*, 1039. (b) Ohnishi, T.; Ohnishi, S.; Shinzawa-Ito, K.; Yoshikawa, S. *Biofactors* **2008**, *32*, 13. (c) Reimann, J.; Flock, U.; Lepp, H.; Honigmann, A.; Aedelroth, P. *Biochim. Biophys. Acta, Bioenerg.* **2007**, *1767*, 362.
- (252) Zhao, S.; Zhang, K.; Bai, Y.; Yang, W.; Sun, C. *Bioelectrochemistry* **2006**, *69*, 158.
- (253) Dai, Z. H.; Ni, J.; Huang, X. H.; Lu, G. F.; Bao, J. C. *Bioelectrochemistry* **2007**, *70*, 250.
- (254) Bernhardt, P. V.; Santini, J. M. *Biochemistry* **2006**, *45*, 2804.
- (255) (a) Pujols-Ayala, I.; Barry, B. *Biochim. Biophys. Acta* **2004**, *1655*, 205. (b) Anderson, R.; Shinde, S.; Maroz, A. *J. Am. Chem. Soc.* **2006**, *128*, 15966. (c) von Feilitzsch, T.; Tuma, J.; Neubauer, H.; Verdier, L.; Haselsberger, R.; Feick, R.; Gurzadyan, G.; Voityuk, A.; Griesinger, C.; Michel-Beyerle, M. *J. Phys. Chem. B* **2008**, *112*, 973.
- (256) Reece, S. Y.; Hodgkiss, J. M.; Stubbe, J.; Nocera, D. G. *Philos. Trans. R. Soc., B* **2006**, *361*, 1351.
- (257) Umena, Y.; Kawakami, K.; Shen, J.-R.; Kamiya, N. *Nature* **2011**, *473*, 55.
- (258) McEvoy, J. P.; Brudvig, G. W. *Biochemistry* **2008**, *47*, 13394.
- (259) (a) Faller, P.; Debus, R.; Brettel, K.; Sugiura, M.; Rutherford, A.; Boussac, A. *Proc. Natl. Acad. Sci. U.S.A.* **2001**, *98*, 14368. (b) Hammarström, L.; Styring, S. *Energy Environ. Sci.* **2011**, *4*, 2379. (c) Ioannidis, N.; Zahariou, G.; Petrouleas, V. *Biochemistry* **2006**, *45*, 6252. (d) Keough, J.; Jenson, D.; Zuniga, A.; Barry, B. *J. Am. Chem. Soc.* **2011**, *133*, 11084. (e) Rappaport, F.; Boussac, A.; Force, D.; Peloquin, J.; Brynda, M.; Sugiura, M.; Un, S.; Britt, R.; Diner, B. *J. Am. Chem. Soc.* **2009**, *131*, 4425. (f) Rappaport, F.; Lavergne, J. *Biochim. Biophys. Acta, Bioenerg.* **2001**, *1503*, 246. (g) Sibert, R.; Josowicz, M.; Porcelli, F.; Veglia, G.; Range, K.; Barry, B. *A. J. Am. Chem. Soc.* **2007**, *129*, 4393. (h) Sugiura, M.; Rappaport, F.; Brettel, K.; Noguchi, T.; Rutherford, A.; Boussac, A. *Biochemistry* **2004**, *43*, 13549. (i) Zhang, C.; Boussac, A.; Rutherford, A. *Biochemistry* **2004**, *43*, 13787.
- (260) Diner, B. A.; Nixon, P. J. In *Photosynthesis: Mechanisms and Effects*. Garab, G.; Kluwer: Dordrecht, 1998; Vol. II, 11771180.
- (261) Reece, S. Y.; Lutterman, D. A.; Seyedsayamdst, M. R.; Stubbe, J.; Nocera, D. G. *Biochemistry* **2009**, *48*, 5832.
- (262) (a) Siegbahn, P. E. M.; Blomberg, M. R. A. *J. Phys. Chem. A* **2008**, *112*, 12772. (b) Blomberg, M. R. A.; Siegbahn, P. E. M. *Biochim. Biophys. Acta, Bioenerg.* **2006**, *1757*, 969. (c) Kim, Y. C.; Wikstrom, M.; Hummer, G. *Proc. Natl. Acad. Sci. U.S.A.* **2009**, *106*, 13707.
- (263) Fecenko, C.; Meyer, T.; Thorp, H. *J. Am. Chem. Soc.* **2006**, *128*, 11020.
- (264) Murphy, C. F. Ph.D. Thesis, University of North Carolina at Chapel Hill, 2009.
- (265) Ishikita, H.; Soudakov, A. V.; Hammes-Schiffer, S. *J. Am. Chem. Soc.* **2007**, *129*, 11146.
- (266) Reece, S. Y.; Seyedsayamdst, M. R.; Stubbe, J.; Nocera, D. G. *J. Am. Chem. Soc.* **2007**, *129*, 13828.
- (267) (a) Jenson, D. L.; Evans, A.; Barry, B. A. *J. Phys. Chem. B* **2007**, *111*, 12599. (b) Hays Putnam, A.-M. A.; Lee, Y.-T.; Goodin, D. B. *Biochemistry* **2009**, *48*, 1. (c) Vassiliev, I.; Offenbacher, A.; Barry, B. *J. Phys. Chem. B* **2005**, *109*, 23077.
- (268) Chen, X. H.; Zhang, L. B.; Zhang, L.; Wang, J.; Liu, H. Y.; Bu, Y. X. *J. Phys. Chem. B* **2009**, *113*, 16681.
- (269) McCracken, J.; Vassiliev, I.; Yang, E.; Range, K.; Barry, B. *J. Phys. Chem. B* **2007**, *111*, 6586.
- (270) (a) Lichtenstein, B.; Cerda, J.; Koder, R.; Dutton, P. *Chem. Commun.* **2009**, *168*. (b) Nara, S.; Valgimigli, L.; Pedulli, G.; Pratt, D. *J. Am. Chem. Soc.* **2010**, *132*, 863. (c) Reddi, A. R.; Reedy, C. J.; Mui, S.; Gibney, B. R. *Biochemistry* **2007**, *46*, 291.
- (271) Reece, S. Y.; Seyedsayamdst, M. R.; Stubbe, J.; Nocera, D. G. *J. Am. Chem. Soc.* **2006**, *128*, 13654.
- (272) Wang, M.; Gao, J.; Muller, P.; Giese, B. *Angew. Chem., Int. Ed.* **2009**, *48*, 4232.
- (273) Brudvig, G.; Hillier, W.; Batista, V.; Ho, F. *Philos. Trans. R. Soc., B* **2008**, *363*, 1234.
- (274) (a) Renger, G. *Photosynth. Res.* **2007**, *92*, 407. (b) Dau, H.; Zaharieva, I. *Acc. Chem. Res.* **2009**, *42*, 1861.
- (275) Zaharieva, I.; Wichmann, J.; Dau, H. *J. Biol. Chem.* **2011**, *286*, 18222.
- (276) Barber, J.; Siegbahn, P. E. M.; Nocera, D.; Dau, H.; Armstrong, F.; Rich, P. *Philos. Trans. R. Soc., B* **2008**, *363*, 1228.
- (277) (a) Fufezan, C.; Gross, C. M.; Sjodin, M.; Rutherford, A. W.; Krieger-Liszka, A.; Kirillovsky, D. *J. Biol. Chem.* **2007**, *282*, 12492. (b) Fufezan, C.; Zhang, C.; Krieger-Liszka, A.; Rutherford, A. *Biochemistry* **2005**, *44*, 12780. (c) Rappaport, F.; Guergova-Kuras, M.; Nixon, P. J.; Diner, B. A.; Lavergne, J. *Biochemistry* **2002**, *41*, 8518. (d) Sedoud, A.; Cox, N.; Sugiura, M.; Lubitz, W.; Boussac, A.; Rutherford, A. *Biochemistry* **2011**, *50*, 6012.
- (278) (a) Chu, H.; Sackett, H.; Babcock, G. *Biochemistry* **2000**, *39*, 14371. (b) Clausen, J.; Junge, W.; Dau, H.; Haumann, M. *Biochemistry* **2005**, *44*, 12775. (c) Dau, H.; Haumann, M. *Science* **2006**, *312*, 1471. (d) Haumann, M.; Liebisch, P.; Muller, C.; Barra, M.; Grabolle, M.; Dau, H. *Science* **2005**, *310*, 1019. (e) Havelius, K.; Su, J.; Feyziyev, Y.; Mamedov, F.; Styring, S. *Biochemistry* **2006**, *45*, 9279. (f) Hillier, W.; Babcock, G. *Biochemistry* **2001**, *40*, 1503. (g) Ioannidis, N.; Nugent, J.; Petrouleas, V. *Biochemistry* **2002**, *41*, 9589. (h) McEvoy, J.; Gascon, J.; Batista, V.; Brudvig, G. *Photochem. Photobiol. Sci.* **2005**, *4*, 940. (i) Pushkar, Y.; Long, X.; Glatzel, P.; Brudvig, G.; Dismukes, G.; Collins, T.; Yachandra, V.; Yano, J.; Bergmann, U. *Angew. Chem., Int. Ed.* **2010**, *49*, 800. (j) Renger, G.; Renger, T. *Photosynth. Res.* **2008**, *98*, 53. (k) Sjodin, M.; Styring, S.; Akermark, B.; Sun, L.; Hammarström, L. *J. Am. Chem. Soc.* **2000**, *122*, 3932. (l) Sjoholm, J.; Havelius, K.; Mamedov, F.; Styring, S. *Biochemistry* **2009**, *48*, 9393. (m) Su, J.; Havelius, K.; Ho, F.; Han, G.; Mamedov, F.; Styring, S. *Biochemistry* **2007**, *46*, 10703. (n) Zhang, C.; Styring, S. *Biochemistry* **2003**, *42*, 8066.
- (279) Barry, B. A.; Babcock, G. T. *Proc. Natl. Acad. Sci. U.S.A.* **1987**, *84*, 7099.
- (280) Debus, R. J.; Barry, B. A.; Babcock, G. T.; McIntosh, L. *Proc. Natl. Acad. Sci. U.S.A.* **1988**, *85*, 427.
- (281) Barry, B. A.; Byrne, J. J.; Fergusonmiller, S.; McIntosh, L.; Yocom, C. F.; Babcock, G. T. *Biophys. J.* **1988**, *53*, A616.
- (282) (a) Jenson, D. L.; Barry, B. A. *J. Am. Chem. Soc.* **2009**, *131*, 10567. (b) Evans, A. Y.; Jenson, D. L.; Barry, B. A. Abstracts of Papers, 233rd ACS National Meeting, Chicago, IL, March 25–29, 2007; CHED: 2007. (c) Qiu, H.; Xue, L.; Ji, G.; Zhou, G.; Huang, X.; Qu, Y.; Gao, P. *Biosens. Bioelectron.* **2009**, *24*, 3014. (d) Siegbahn, P. E. M. *J. Am. Chem. Soc.* **2009**, *131*, 18238.
- (283) (a) Dau, H.; Haumann, M. *Coord. Chem. Rev.* **2008**, *252*, 273. (b) Dau, H.; Limberg, C.; Reier, T.; Risch, M.; Roggan, S.; Strasser, P. *ChemCatChem* **2010**, *2*, 724. (c) Rappaport, F.; Diner, B. *Coord. Chem. Rev.* **2008**, *252*, 259. (d) Barber, J. *Biochim. Soc. Trans.* **2006**, *34*, 619. (e) Barber, J. *Chem. Soc. Rev.* **2009**, *38*, 185. (f) Barber, J.; Murray, J. *Coord. Chem. Rev.* **2008**, *252*, 233. (g) Debus, R. J. *Coord. Chem. Rev.* **2008**, *252*, 244. (h) Herrero, C.; Lassalle-Kaiser, B.; Leibl, W.; Rutherford, A.; Aukauloo, A. *Coord. Chem. Rev.* **2008**, *252*, 456. (i) Sproviero, E.; Gascon, J.; McEvoy, J.; Brudvig, G.; Batista, V. *Coord. Chem. Rev.* **2008**, *252*, 395.
- (284) Kok, B.; Forbush, B.; McGloin, M. *Photochem. Photobiol.* **1970**, *11*, 457.
- (285) Sinclair, J. *Biochim. Biophys. Acta* **1984**, *764*, 247.
- (286) Wincencjusz, H.; Yocom, C. F.; van Gorkom, H. J. *Biochemistry* **1999**, *38*, 3719.
- (287) Murata, M.; Yano, K.; Kuroki, S.; Suzutani, T.; Katayama, Y. *Anal. Sci.* **2003**, *19*, 1569.

- (288) Grabolle, M.; Haumann, M.; Muller, C.; Liebisch, P.; Dau, H. *J. Biol. Chem.* **2006**, *281*, 4580.
- (289) Balaban, T. S.; Braun, P.; Hattig, C.; Hellweg, A.; Kern, J.; Saenger, W.; Zouni, A. *Biochim. Biophys. Acta, Bioenerg.* **2009**, *1787*, 1254.
- (290) Adachi, H.; Umena, Y.; Enami, I.; Henmi, T.; Kamiya, N.; Shen, J. R. *Biochim. Biophys. Acta, Bioenerg.* **2009**, *1787*, 121.
- (291) Murray, J. W.; Maghlaoui, K.; Kargul, J.; Ishida, N.; Lai, T. L.; Rutherford, A. W.; Sugiura, M.; Boussac, A.; Barber, J. *Energy Environ. Sci.* **2008**, *1*, 161.
- (292) Strickler, M. A.; Hillier, W.; Debus, R. J. *Biochemistry* **2006**, *45*, 8801.
- (293) Guskov, A.; Gabdulkhakov, A.; Broser, M.; Glockner, C.; Hellmich, J.; Kern, J.; Frank, J.; Muh, F.; Saenger, W.; Zouni, A. *ChemPhysChem* **2010**, *11*, 1073.
- (294) Yano, J.; Yachandra, V. K. *Photosynth. Res.* **2009**, *102*, 241.
- (295) Sauer, K.; Yano, J.; Yachandra, V. K. *Coord. Chem. Rev.* **2008**, *252*, 318.
- (296) (a) Pushkar, Y.; Yano, J.; Glatzel, P.; Messinger, J.; Lewis, A.; Sauer, K.; Bergmann, U.; Yachandra, V. J. *Biol. Chem.* **2007**, *282*, 7198. (b) Pushkar, Y. L.; Yano, J.; Sauer, K.; Boussac, A.; Yachandra, V. K. *Proc. Natl. Acad. Sci. U.S.A.* **2008**, *105*, 1879. (c) Yano, J.; Robblee, J.; Pushkar, Y.; Marcus, M. A.; Bendix, J.; Workman, J. M.; Collins, T. J.; Solomon, E. I.; George, S. D.; Yachandra, V. K. *J. Am. Chem. Soc.* **2007**, *129*, 12989.
- (297) Yano, J.; Kern, J.; Sauer, K.; Latimer, M. J.; Pushkar, Y.; Biesiadka, J.; Loll, B.; Saenger, W.; Messinger, J.; Zouni, A.; Yachandra, V. K. *Science* **2006**, *314*, 821.
- (298) (a) Ulas, G.; Olack, G.; Brudvig, G. W. *Biochemistry* **2008**, *47*, 3073. (b) Aoyama, C.; Suzuki, H.; Sugiura, M.; Noguchi, T. *Biochemistry* **2008**, *47*, 2760. (c) McConnell, I. L.; Badger, M. R.; Wydrzynski, T.; Hillier, W. *Biochim. Biophys. Acta, Bioenerg.* **2007**, *1767*, 639. (d) Hillier, W.; McConnell, I.; Badger, M. R.; Boussac, A.; Klimov, V. V.; Dismukes, G. C.; Wydrzynski, T. *Biochemistry* **2006**, *45*, 2094.
- (299) (a) Sproviero, E. M.; Gascon, J. A.; McEvoy, J. P.; Brudvig, G. W.; Batista, V. S. *J. Am. Chem. Soc.* **2008**, *130*, 3428. (b) Batista, V.; Sproviero, E.; Gascon, J.; McEvoy, J.; Brudvig, G. *Photosynth. Res.* **2007**, *91*, PS42. (c) Ishikita, H.; Knapp, E. W. *Biophys. J.* **2006**, *90*, 3886.
- (300) Guskov, A.; Kern, J.; Gabdulkhakov, A.; Broser, M.; Zouni, A.; Saenger, W. *Nature Struct. Mol. Biol.* **2009**, *16*, 334.
- (301) Dau, H.; Haumann, M. *Photosynth. Res.* **2007**, *92*, 327.
- (302) Kato, Y.; Sugiura, M.; Oda, A.; Watanabe, T. *Proc. Natl. Acad. Sci. U.S.A.* **2009**, *106*, 17365.
- (303) Shibamoto, T.; Kato, Y.; Sugiura, M.; Watanabe, T. *Biochemistry* **2009**, *48*, 10682.
- (304) Rutherford, A. W.; Mullet, J. E.; Crofts, A. R. *FEBS Lett.* **1981**, *123*, 235.
- (305) Grabolle, M.; Dau, H. *Biochim. Biophys. Acta, Bioenerg.* **2005**, *1708*, 209.
- (306) Minagawa, J.; Narusaka, Y.; Inoue, Y.; Satoh, K. *Biochemistry* **1999**, *38*, 770.
- (307) Renger, G.; Kuehn, P. *Biochim. Biophys. Acta, Bioenerg.* **2007**, *1767*, 458.
- (308) Sproviero, E. M.; Gascon, J. A.; McEvoy, J. P.; Brudvig, G. W.; Batista, V. S. *J. Am. Chem. Soc.* **2008**, *130*, 6728.
- (309) Haumann, M.; Bogershausen, O.; Cherepanov, D.; Ahlbrink, R.; Junge, W. *Photosynth. Res.* **1997**, *51*, 193.
- (310) McDaniel, N. D.; Coughlin, F. J.; Tinker, L. L.; Bernhard, S. J. *Am. Chem. Soc.* **2008**, *130*, 210.
- (311) Sala, X.; Romero, I.; Rodriguez, M.; Escriche, L.; Llobet, A. *Angew. Chem., Int. Ed.* **2009**, *48*, 2842.
- (312) Hull, J. F.; Balcells, D.; Blakemore, J. D.; Incarvito, C. D.; Eisenstein, O.; Brudvig, G. W.; Crabtree, R. H. *J. Am. Chem. Soc.* **2009**, *131*, 8730.
- (313) Deng, Z. P.; Tseng, H. W.; Zong, R. F.; Wang, D.; Thummel, R. *Inorg. Chem.* **2008**, *47*, 1835.
- (314) Siegbahn, P. E. M.; Crabtree, R. H. *J. Am. Chem. Soc.* **1999**, *121*, 117.
- (315) Tagore, R.; Crabtree, R. H.; Brudvig, G. W. *Inorg. Chem.* **2008**, *47*, 1815.
- (316) Tagore, R.; Crabtree, R. H.; Brudvig, G. W. *Inorg. Chem.* **2007**, *46*, 2193.
- (317) Tagore, R.; Chen, H. Y.; Crabtree, R. H.; Brudvig, G. W. *J. Am. Chem. Soc.* **2006**, *128*, 9457.
- (318) Renger, G. *Biochim. Biophys. Acta, Bioenerg.* **2004**, *1655*, 195.
- (319) Clausen, J.; Junge, W. *Nature* **2004**, *430*, 480.
- (320) (a) Faller, P.; Rutherford, A.; Debus, R. *Biochemistry* **2002**, *41*, 12914. (b) Rutherford, A.; Boussac, A.; Faller, P. *Biochim. Biophys. Acta, Bioenerg.* **2004**, *1655*, 222.
- (321) Tommos, C.; Babcock, G. T. *Biochim. Biophys. Acta, Bioenerg.* **2000**, *1458*, 199.
- (322) Kohen, A.; Klinman, J. P. *Chem. Biol.* **1999**, *6*, R191.
- (323) (a) Gabdulkhakov, A.; Guskov, A.; Broser, M.; Kern, J.; Muh, F.; Saenger, W.; Zouni, A. *Structure* **2009**, *17*, 1223. (b) Ho, F. *Photosynth. Res.* **2008**, *98*, 503. (c) Ho, F.; Styring, S. *Biochim. Biophys. Acta, Bioenerg.* **2008**, *1777*, 140.
- (324) (a) Artin, E.; Wang, J.; Lohman, G.; Yokoyama, K.; Yu, G.; Griffin, R.; Bar, G.; Stubbe, J. *Biochemistry* **2009**, *48*, 11622. (b) Minnihan, E. C.; Seyedsayamdst, M. R.; Stubbe, J. *Biochemistry* **2009**, *48*, 12125. (c) Offenbacher, A. R.; Vassiliev, I. R.; Seyedsayamdst, M. R.; Stubbe, J.; Barry, B. A. *J. Am. Chem. Soc.* **2009**, *131*, 7496. (d) Seyedsayamdst, M. R.; Argirevic, T.; Minnihan, E. C.; Stubbe, J.; Bennati, M. *J. Am. Chem. Soc.* **2009**, *131*, 15729. (e) Shanmugam, M.; Doan, P.; Lees, N.; Stubbe, J.; Hoffman, B. *J. Am. Chem. Soc.* **2009**, *131*, 3370. (f) Wang, S.; Lu, L.; Yang, M.; Lei, Y.; Shen, G.; Yu, R. *Anal. Chim. Acta* **2009**, *651*, 220. (g) Hristova, D.; Wu, C.; Jiang, W.; Krebs, C.; Stubbe, J. *Biochemistry* **2008**, *47*, 3989. (h) Seyedsayamdst, M. R.; Chan, T. Y. C.; Reece, S. Y.; Xie, J.; Schultz, P. G.; Nocera, D. G.; Stubbe, J. *Abstracts of Papers*, 234th ACS National Meeting, Boston, MA, August 19–23, 2007; INOR: 2007.
- (325) Byrdin, M.; Villette, S.; Espagne, A.; Eker, A. P. M.; Brettel, K. *J. Phys. Chem. B* **2008**, *112*, 6866.
- (326) (a) Langenbacher, T.; Immeln, D.; Dick, B.; Kottke, T. *J. Am. Chem. Soc.* **2009**, *131*, 14274. (b) Sancar, A. *Chem. Rev.* **2003**, *103*, 2203. (c) Lukacs, A.; Eker, A. P. M.; Byrdin, M.; Brettel, K.; Vos, M. H. *J. Am. Chem. Soc.* **2008**, *130*, 14394. (d) Aubert, C.; Vos, M. H.; Mathis, P.; Eker, A. P. M.; Brettel, B. *Nature* **2000**, *405*, 586.
- (327) (a) Byrdin, M.; Villette, S.; Eker, A. P. M.; Brettel, K. *Biochemistry* **2007**, *46*, 10072. (b) Byrdin, M.; Lukacs, A.; Thiagarajan, V.; Eker, A. P. M.; Brettel, K.; Vos, M. H. *J. Phys. Chem. A* **2010**, *114*, 3207.
- (328) (a) Lukacs, A.; Eker, A. P. M.; Byrdin, M.; Villette, S.; Pan, J.; Brettel, K.; Vos, M. H. *J. Phys. Chem. B* **2006**, *110*, 15654. (b) Kao, Y.-T.; Tan, C.; Song, S.-H.; Oztuerk, N.; Li, J.; Wang, L.; Sancar, A.; Zhong, D. *J. Am. Chem. Soc.* **2008**, *130*, 7695. (c) Chen, H.-Y.; Kao, C.-L.; Hsu, S. C. N. *J. Am. Chem. Soc.* **2009**, *131*, 15930. (d) Sancar, A. *J. Biol. Chem.* **2008**, *283*, 32153. (e) Kao, Y.-T.; Saxena, C.; Wang, L.; Sancar, A.; Zhong, D. *Cell Biochem. Biophys.* **2007**, *48*, 32. (f) Prytkova, T. R.; Beratan, D. N.; Skourtis, S. S. *Proc. Natl. Acad. Sci. U.S.A.* **2007**, *104*, 802. (g) Sancar, A. *Annu. Rev. Biochem.* **2000**, *69*, 31. (h) Sancar, G. B. *Mutat. Res.* **2000**, *451*, 25.
- (329) Shih, C.; Museth, A. K.; Abrahamsson, M.; Blanco-Rodriguez, A. M.; Di Bilio, A. J.; Sudhamsu, J.; Crane, B. R.; Ronayne, K. L.; Towrie, M.; Vlcek, A., Jr.; Richards, J. H.; Winkler, J. R.; Gray, H. B. *Science* **2008**, *320*, 1760.
- (330) Blanco-Rodriguez, A. M.; Busby, M.; Ronayne, K.; Towrie, M.; Grdinaru, C.; Sudhamsu, J.; Sykora, J.; Hof, M.; Zalis, S.; Di Bilio, A. J.; Crane, B. R.; Gray, H. B.; Vlcek, A. *J. Am. Chem. Soc.* **2009**, *131*, 11788.
- (331) (a) Hatcher, E.; Soudackov, A.; Hammes-Schiffer, S. *J. Am. Chem. Soc.* **2004**, *126*, 5763. (b) Hatcher, E.; Soudackov, A.; Hammes-Schiffer, S. *J. Am. Chem. Soc.* **2007**, *129*, 187. (c) Huang, Y.; Yu, D.; Hua, Y.; Qiu, A. *J. Agric. Food Chem.* **2006**, *54*, 9216. (d) Knapp, M. J.; Rickert, K.; Klinman, J. P. *J. Am. Chem. Soc.* **2002**, *124*, 3865.

- (e) Rickert, K.; Klinman, J. *Biochemistry* **1999**, *38*, 12218. (f) Glickman, M. H.; Klinman, J. P. *Biochemistry* **1995**, *34*, 14077.
- (332) Miller, A.-F. *Acc. Chem. Res.* **2008**, *41*, 501.
- (333) Miller, A.-F.; Padmakumar, K.; Sorkin, D. L.; Karapetian, A.; Vance, C. K. *J. Inorg. Biochem.* **2003**, *93*, 71.
- (334) (a) Yikilmaz, E.; Porta, J.; Grove, L. E.; Vahedi-Faridi, A.; Bronshteyn, Y.; Brunold, T. C.; Borgstahl, G. E. O.; Miller, A. F. *J. Am. Chem. Soc.* **2007**, *129*, 9927. (b) Noddleman, L.; Han, W.-G. *J. Biol. Inorg. Chem.* **2006**, *11*, 674. (c) Smirnov, V. V.; Roth, J. P. *J. Am. Chem. Soc.* **2006**, *128*, 16424.
- (335) De Smet, L.; Savvides, S. N.; Van Horen, E.; Pettigrew, G.; Van Beeumen, J. *J. Biol. Chem.* **2006**, *281*, 4371.
- (336) Barrows, T.; Bhaskar, B.; Poulos, T. *Biochemistry* **2004**, *43*, 8826.
- (337) Guallar, V.; Wallrapp, F. *J. R. Soc. Interface* **2008**, *5*, S233.
- (338) (a) Kang, S. A.; Hoke, K. R.; Crane, B. R. *J. Am. Chem. Soc.* **2006**, *128*, 2346. (b) Elliott, S. J.; Bradley, A. L.; Arciero, D. M.; Hooper, A. B. *J. Inorg. Biochem.* **2007**, *101*, 173.
- (339) Kang, S.-K.; Lee, J.-H.; Lee, Y.-C.; Kim, C.-H. *Biochim. Biophys. Acta, Gen. Subj.* **2006**, *1760*, 724.
- (340) Bradley, A. L.; Chobot, S. E.; Arciero, D. M.; Hooper, A. B.; Elliott, S. J. *J. Biol. Chem.* **2004**, *279*, 13297.
- (341) Sharpe, M.; Ferguson-Miller, S. *J. Bioenerg. Biomembr.* **2008**, *40*, 541.
- (342) Verkhovsky, M. I.; Belevich, I.; Bloch, D. A.; Wikstroem, M. *Biochim. Biophys. Acta, Bioenerg.* **2006**, *1757*, 401.
- (343) Richter, O.; Ludwig, B. *Biochim. Biophys. Acta* **2009**, *1787*, 626.
- (344) (a) Kim, Y. W.; Shin, J.-C.; An, Y.-s. *Clin. Neuropharmacol.* **2009**, *32*, 335. (b) Papa, S.; Capitanio, G.; Luca Martino, P. *Biochim. Biophys. Acta, Bioenerg.* **2006**, *1757*, 1133. (c) Busenlehner, L. S.; Salomonsson, L.; Brzezinski, P.; Armstrong, R. N. *Proc. Natl. Acad. Sci. U.S.A.* **2006**, *103*, 15398. (d) Shimokata, K.; Katayama, Y.; Murayama, H.; Suematsu, M.; Tsukihara, T.; Muramoto, K.; Aoyama, H.; Yoshikawa, S.; Shimada, H. *Proc. Natl. Acad. Sci. U.S.A.* **2007**, *104*, 4200.
- (345) Belevich, I.; Verkhovsky, M. I.; Wikstroem, M. *Nature* **2006**, *440*, 829.
- (346) Kaila, V. R. I.; Johansson, M. P.; Sundholm, D.; Laakkonen, L.; Wikstrom, M. *Biochim. Biophys. Acta, Bioenerg.* **2009**, *1787*, 221.
- (347) Quenneville, J.; Popovic, D. M.; Stuchebrukhov, A. A. *Biochim. Biophys. Acta, Bioenerg.* **2006**, *1757*, 1035.
- (348) Belevich, I.; Tuukkanen, A.; Wikstroem, M.; Verkhovsky, M. I. *Biochemistry* **2006**, *45*, 4000.
- (349) (a) Lepp, H.; Brzezinski, P. *Biochim. Biophys. Acta, Gen. Subj.* **2009**, *1790*, 552. (b) Parul, D.; Palmer, G.; Fabian, M. *J. Biol. Chem.* **2010**, *285*, 4536. (c) Siletsky, S. A.; Belevich, I.; Wikstroem, M.; Soulimate, T.; Verkhovsky, M. I. *Biochim. Biophys. Acta, Bioenerg.* **2009**, *1787*, 201. (d) Zara, V.; Conte, L.; Trumppower, B. L. *Biochim. Biophys. Acta, Mol. Cell Res.* **2009**, *1793*, 89. (e) Brzezinski, P.; Reimann, J.; Adelroth, P. *Biochem. Soc. Trans.* **2008**, *36*, 1169. (f) Busenlehner, L. S.; Braenden, G.; Namslauer, I.; Brzezinski, P.; Armstrong, R. N. *Biochemistry* **2008**, *47*, 73. (g) Fadda, E.; Yu, C.-H.; Pomes, R. *Biochim. Biophys. Acta, Bioenerg.* **2008**, *1777*, 277. (h) Lepp, H.; Svahn, E.; Faxen, K.; Brzezinski, P. *Biochemistry* **2008**, *47*, 4929. (i) Pisliakov, A. V.; Sharma, P. K.; Chu, Z. T.; Haranczyk, M.; Warshel, A. *Proc. Natl. Acad. Sci. U.S.A.* **2008**, *105*, 7726.
- (350) (a) Koepke, J.; Olkhova, E.; Angerer, H.; Mueller, H.; Peng, G.; Michel, H. *Biochim. Biophys. Acta, Bioenerg.* **2009**, *1787*, 635. (b) Tuukkanen, A.; Kaila, V. R. I.; Laakkonen, L.; Hummer, G.; Wikstroem, M. *Biochim. Biophys. Acta, Bioenerg.* **2007**, *1767*, 1102.
- (351) (a) Lee, H.; Ojemyr, L.; Vakkasoglu, A.; Brzezinski, P.; Gennis, R. *Biochemistry* **2009**, *48*, 7123. (b) Popovic, D. M.; Stuchebrukhov, A. A. *Photochem. Photobiol. Sci.* **2006**, *5*, 611. (c) Namslauer, A.; Lepp, H.; Braenden, M.; Jasaitis, A.; Verkhovsky, M. I.; Brzezinski, P. *J. Biol. Chem.* **2007**, *282*, 15148.
- (352) Egawa, T.; Lee, H. J.; Ji, H.; Gennis, R. B.; Yeh, S.-R.; Rousseau, D. L. *Anal. Biochem.* **2009**, *394*, 141.
- (353) (a) Voicescu, M.; El Khoury, Y.; Martel, D.; Heinrich, M.; Hellwig, P. *J. Phys. Chem. B* **2009**, *113*, 13429. (b) Voicescu, M.; Heinrich, M.; Hellwig, P. *J. Fluoresc.* **2009**, *19*, 257.
- (354) (a) Iwaki, M.; Rich, P. *J. Am. Chem. Soc.* **2007**, *129*, 2923. (b) Mills, D. A.; Xu, S.; Geren, L.; Hiser, C.; Qin, L.; Sharpe, M. A.; McCracken, J.; Durham, B.; Millett, F.; Ferguson-Miller, S. *Biochemistry* **2008**, *47*, 11499.
- (355) Brenner, S.; Heyes, D. J.; Hay, S.; Hough, M. A.; Eady, R. R.; Hasnain, S. S.; Scrutton, N. S. *J. Biol. Chem.* **2009**, *284*, 25973.
- (356) Colin, J.; Wiseman, B.; Switala, J.; Loewen, P. C.; Ivancich, A. J. *Am. Chem. Soc.* **2009**, *131*, 8557.
- (357) Sharp, R. E.; Chapman, S. K. *Biochim. Biophys. Acta, Protein Struct. Mol. Enzymol.* **1999**, *1432*, 143.
- (358) (a) Cerqueira, N. M. F. S. A.; Gonzalez, P. J.; Brondino, C. D.; Romao, M. J.; Romao, C. C.; Moura, I.; Moura, J. J. G. *J. Comput. Chem.* **2009**, *30*, 2466. (b) Gonzalez, P. J.; Rivas, M. G.; Brondino, C. D.; Bursakov, S. A.; Moura, I.; Moura, J. J. G. *J. Biol. Inorg. Chem.* **2006**, *11*, 609. (c) Flock, U.; Watmough, N. J.; Aedelroth, P. *Biochemistry* **2005**, *44*, 10711. (d) Crane, B. R.; Siegel, L. M.; Getzoff, E. D. *Biochemistry* **1997**, *36*, 12120. (e) Stiefel, E. I. *Proc. Natl. Acad. Sci. U.S.A.* **1973**, *70*, 988. (f) Pipirou, Z.; Guallar, V.; Basran, J.; Metcalfe, C. L.; Murphy, E. J.; Bottrill, A. R.; Mistry, S. C.; Raven, E. L. *Biochemistry* **2009**, *48*, 3593.